frontiers | Research Topics

Insight into plant spatial omics: Mass spectrometry imaging

Edited by
Xiaodong Wang, Liangyu Liu, Jun Han, Zhili Li, Bin Li and Yinglang Wan

Published in
Frontiers in Plant Science

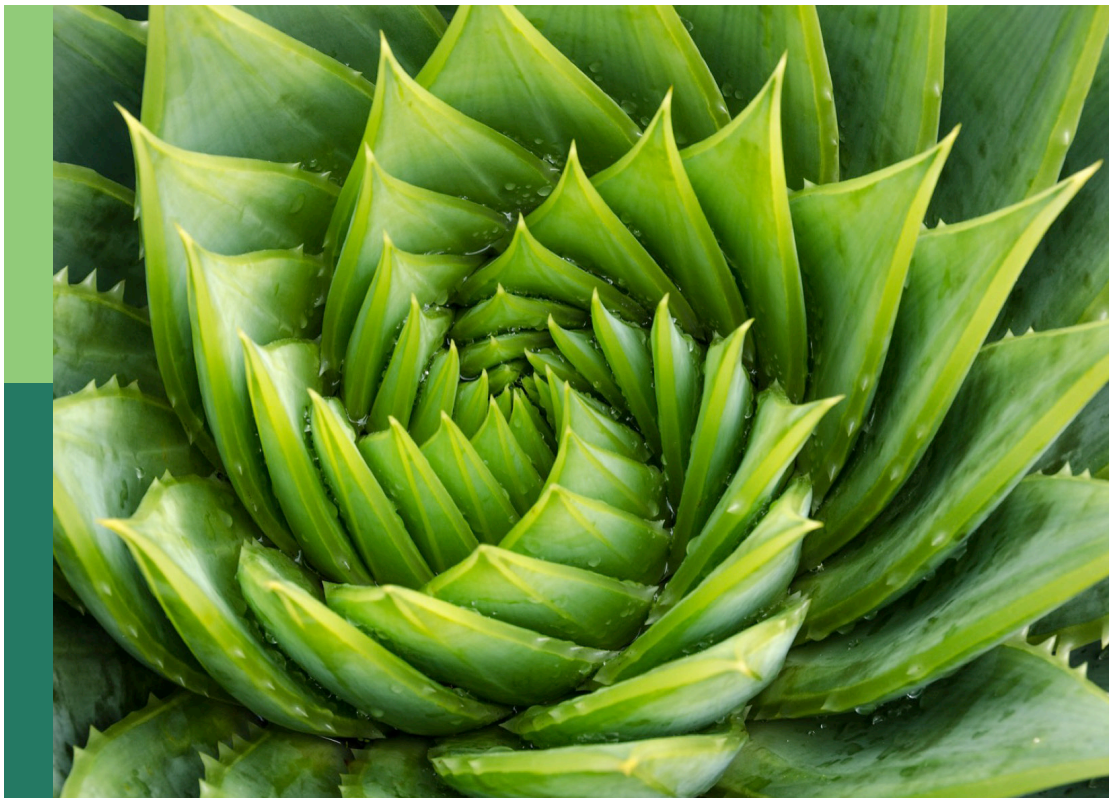

ISSN 1664-8714
ISBN 978-2-8325-3403-8
DOI 10.3389/978-2-8325-3403-8

About Frontiers

Frontiers is more than just an open access publisher of scholarly articles: it is a pioneering approach to the world of academia, radically improving the way scholarly research is managed. The grand vision of Frontiers is a world where all people have an equal opportunity to seek, share and generate knowledge. Frontiers provides immediate and permanent online open access to all its publications, but this alone is not enough to realize our grand goals.

Frontiers journal series

The Frontiers journal series is a multi-tier and interdisciplinary set of open-access, online journals, promising a paradigm shift from the current review, selection and dissemination processes in academic publishing. All Frontiers journals are driven by researchers for researchers; therefore, they constitute a service to the scholarly community. At the same time, the *Frontiers journal series* operates on a revolutionary invention, the tiered publishing system, initially addressing specific communities of scholars, and gradually climbing up to broader public understanding, thus serving the interests of the lay society, too.

Dedication to quality

Each Frontiers article is a landmark of the highest quality, thanks to genuinely collaborative interactions between authors and review editors, who include some of the world's best academicians. Research must be certified by peers before entering a stream of knowledge that may eventually reach the public - and shape society; therefore, Frontiers only applies the most rigorous and unbiased reviews. Frontiers revolutionizes research publishing by freely delivering the most outstanding research, evaluated with no bias from both the academic and social point of view. By applying the most advanced information technologies, Frontiers is catapulting scholarly publishing into a new generation.

What are Frontiers Research Topics?

Frontiers Research Topics are very popular trademarks of the *Frontiers journals series*: they are collections of at least ten articles, all centered on a particular subject. With their unique mix of varied contributions from Original Research to Review Articles, Frontiers Research Topics unify the most influential researchers, the latest key findings and historical advances in a hot research area.

Find out more on how to host your own Frontiers Research Topic or contribute to one as an author by contacting the Frontiers editorial office: frontiersin.org/about/contact

Insight into plant spatial omics: Mass spectrometry imaging

Topic editors

Xiaodong Wang — Minzu University of China, China
Liangyu Liu — Capital Normal University, China
Jun Han — University of Victoria, Canada
Zhili Li — Institute of Basic Medical Sciences, Chinese Academy of Medical Sciences and Peking Union Medical College, China
Bin Li — China Pharmaceutical University, China
Yinglang Wan — Hainan University, China

Citation

Wang, X., Liu, L., Han, J., Li, Z., Li, B., Wan, Y., eds. (2023). *Insight into plant spatial omics: Mass spectrometry imaging*. Lausanne: Frontiers Media SA. doi: 10.3389/978-2-8325-3403-8

Table of contents

frontiers | Frontiers in Plant Science

TYPE Editorial
PUBLISHED 21 August 2023
DOI 10.3389/fpls.2023.1273010

OPEN ACCESS

EDITED AND REVIEWED BY
Roger Deal,
Emory University, United States

*CORRESPONDENCE
Xiaodong Wang
Xiaodong@muc.edu.cn

RECEIVED 05 August 2023
ACCEPTED 16 August 2023
PUBLISHED 21 August 2023

CITATION
Wang X, Han J, Li Z, Li B, Wan Y and Liu L (2023) Editorial: Insight into plant spatial omics: mass spectrometry imaging. *Front. Plant Sci.* 14:1273010. doi: 10.3389/fpls.2023.1273010

Editorial: Insight into plant spatial omics: mass spectrometry imaging

Xiaodong Wang[1,2]*, Jun Han[3,4], Zhili Li[5], Bin Li[6], Yinglang Wan[7] and Liangyu Liu[8]

[1]College of Life and Environmental Sciences, Minzu University of China, Beijing, China, [2]Key Laboratory of Mass Spectrometry Imaging and Metabolomics (Minzu University of China), State Ethnic Affairs Commission, Beijing, China, [3]Genome British Columbia Proteomics Centre, University of Victoria, Victoria, BC, Canada, [4]Division of Medical Sciences, University of Victoria, Victoria, BC, Canada, [5]Institute of Basic Medical Sciences, Chinese Academy of Medical Sciences and Peking Union Medical College, Beijing, China, [6]State Key Laboratory of Natural Medicines, China Pharmaceutical University, Nanjing, China, [7]Hainan Key Laboratory for Sustainable Utilization of Tropical Bioresources, College of Tropical Crops, Hainan University, Haikou, China, [8]Beijing Key Laboratory of Plant Gene Resources and Biotechnology for Carbon Reduction and Environmental Improvement, and College of Life Sciences, Capital Normal University, Beijing, China

KEYWORDS

mass spectrometry imaging, plant science, spatial omics, *in situ* analysis, tissue imaging, endogenous compounds

Editorial on the Research Topics
Insight into plant spatial omics: mass spectrometry imaging

Plant spatial omics, initiated by mass spectrometry imaging (MSI), is an analytically advanced, label-free technology that is capable of simultaneous determination of the abundances and distribution patterns of endogenous molecules (*e.g.*, proteins, peptides, lipids, primary metabolites and secondary metabolites) directly from the surfaces of thinly-sectioned plant tissues. Accurate characterization of the structure, abundance, and spatial location of these naturally occurring molecules in plants is of paramount importance for comprehensive understanding of plant development, growth, and the interactions between plants and their environment under physiological and pathological conditions or under perturbations caused by stress. Consequently, MSI has gained significant popularity and is increasingly being applied in various areas of plant science such as plant physiology, pathology, resistance to biotic/abiotic stresses, as well as plant-microbe/insect interactions, among others. This Research Topic aims to present a collection of 9 articles that focuses on methodology and application studies related to MSI techniques in plant science, thereby facilitating the dissemination of innovative and groundbreaking insights in the field of MSI-driven plant spatial omics.

The optimization of the process for preparing samples plays a pivotal role in ensuring the achievement of high sensitivity, high spatial resolution, and high-quality signals of MSI. In a groundbreaking study, Qin et al. have described an innovative tissue pretreatment protocol, which is specifically designed for matrix-assisted laser desorption/ionization (MALDI)-MSI analysis of endogenous peptide molecules in castor bean tissues, which are known for their abundance of lipids. Through the utilization of a modified sample washing protocol, the researchers successfully visualized and quantified *Ricinus communis*

biomarkers (RCBs) in the tissue sections of castor beans obtained from nine different geographical sources. These findings represent a significant advancement in our understanding of castor bean-related intoxication events, which will shed light on a new research perspective on traceability within this domain.

In a typical MALDI-MSI experiment, it is crucial to select the appropriate MALDI matrix to facilitate the process of analyte ionization. Building upon this premise, Shen et al. have introduced a new approach in which a pre-coated matrix comprised of platinum nanomaterials were prepared in quantities. It was achieved by sputtering platinum nanoparticles onto glass slides using an ion sputterer. By employing the innovative pre-coated matrix of this type, the researchers successfully obtained high-resolution ionic images to depict the spatial distribution of oligosaccharides and lipids in germinating wheat and corn tissue sections through MALDI-MSI. The methodology that Shen et al. proposed presents a fundamental technique that serves as an indispensable tool for exploring the intricate distribution patterns of oligosaccharides and lipids within plant tissues.

The characterization of bioactive secondary metabolites such as alkaloids, sesquiterpenes, and flavonoids using MSI techniques is experiencing substantial growth. This phenomenon can be attributed to the pivotal role of MSI, which plays a crucial role in unraveling the intricacies of plant metabolism, as highlighted by recent findings in the field. In this vein, Liu et al. have made a significant stride by employing a combined approach of ultra-performance liquid chromatography/quadrupole time-of-flight mass spectrometry (UPLC-QTOF-MS) and MALDI-TOF-MSI to analyze the metabolite profiles, spatial distributions, and biosynthetic pathways of various functional metabolites within the stem of *Dendrobium nobile* (*D. nobile*). The investigation successfully identified and relatively quantitated a set of bioactive metabolites, including 11 alkaloids, 10 sesquiterpenes, and 13 other metabolites. It has shed light on the biosynthetic pathways and accumulation patterns of dendrobine in the *D. nobile* stem. Concurrently, Wu et al. have delved into the spatiotemporal distributions of alkaloids in *Gelsemium elegans*, utilizing desorption electrospray ionization MSI. Notably, the study has visualized 23 alkaloids in roots, stems, and leaves of the plant during the seedling stage, while 19 alkaloids were imaged by MS during the mature stage. It has showcased the intriguing phenomena of multiple alkaloid diffusion and transfer within tissues, which correlates with their developmental and maturation processes. Likewise, Liu et al. have successfully undertaken the *in-situ* detection and imaging of the distribution of flavonoids in litchi (*Litchi chinensis*) seed tissue sections via MALDI-MSI, pioneering a groundbreaking work in this field. Notably, the investigation has successfully detected and imaged 15 flavonoid ion signals in the positive ion mode of MS detection. Overall, these studies present essential methodologies for comprehensively understanding the physiological changes occurring in bioactive metabolites and effectively harnessing the potential of plant tissues.

Profiling and imaging strategies using MS techniques have made great contributions to the identification of distinct compounds that exhibit inter- and intra-species differences. In this respect, Liu et al. have made significant advancements by employing MALDI-TOF-MSI to achieve rapid and effective identification at the species level of *Pterocarpus santalinus* and *Pterocarpus tinctorius*. The conducted study successfully screened and identified 15 potential chemical markers, thereby overcoming the limitations caused by traditional methods of identification. The findings of this research hold immense promise in providing vital technical support for conservation of the endangered and valuable wood species. Simultaneously, Liu et al. have also provided insight into the chemical changes of protein-related metabolites derived from *Bombyx batryticatus* (*B. batryticatus*) before and after undergoing the stir-frying process with wheat bran. Their investigations have substantiated that the process of frying not only reduces the toxicity of *B. batryticatus* but also potentially enhances specific biological activities. This highlights the significance of Chinese medicine processing technology. These studies collectively contribute to our understanding of species identification and the chemical transformations that take place during the processing of medicinal substances, thereby paving the way for future advancements in both fields.

The field of plant science has witnessed remarkable progress in recent years, which is primarily driven by advances in rapid and non-destructive optical imaging technology. Notably, these advancements have revolutionized the detection of seed quality, offering unprecedented insights and opportunities. Building upon this trend, Jia et al. have leveraged optical imaging techniques alongside cutting-edge machine learning algorithms to develop a robust model for effectively categorizing the maturity stages and locations of Siberian wild rye (*Elymus sibiricus* L.) seeds. Remarkably, this study has demonstrated that the integration of feature filtering algorithms with machine learning methods yields a highly performant and cost-effective approach for accurately identifying seed maturity statuses. Furthermore, the implementation of the k-means technique to address variations in maturity among plant seeds has further augmented the classification accuracy. These pioneering findings not only contribute to the field of seed quality detection but also showcase the remarkable potential of optical imaging and machine learning in enhancing our understanding of plant development and optimizing agricultural practices.

The investigation of plant-pathogenic microbe interactions utilizing MSI is a burgeoning field in plant sciences. In this context, Maia et al. conducted a detailed MSI analysis of *Vitis vinifera* L. (*V. vinifera*) leaf discs that were infected by *Plasmopara viticola* (*P. viticola*), with the aim to unravel and localize bioactive molecules crucial to the initial stages of pathogen contact with the leaf surface. Notably, the researchers meticulously optimized the preparation of the plant material to overcome the challenges posed by the non-flat nature of *V. vinifera* leaves and the presence of trichomes, which hindered the MS detection. Furthermore, they systematically evaluated different matrices and solvents to acquire high-quality MALDI-MS images. The outcomes of their study unveiled a compelling finding, indicating a conspicuous accumulation of identified sucrose with a non-homogeneous distribution in the infected leaf discs, contrasting with the control samples. Intriguingly, the accumulation of sucrose was predominantly observed around the veins, leading the researchers to develop a hypothesis suggesting the manipulation of sucrose

metabolism by the developmental structures of *P. viticola*. This research not only sheds light on the intricacies of plant-microbe interactions but also underscores the significance of MSI in elucidating the dynamic processes underlying host-pathogen relationships in plants. The findings pave the way for further investigations to comprehend the molecular mechanisms at play, which can contribute to the development of innovative strategies for disease control and plant protection.

In summary, this Research Topic presents valuable insights into plant spatial omics through the method development and application of MSI. The articles featured within this Research Topic highlight a wide range of practical or promising applications that are being explored in this field of research and development. Most of the contributors in this Research Topic have concentrated on investigating the spatial distributions of pivotal or distinctive compounds within plant samples through analysis using MSI. It is our earnest desire that these studies will not only improve our understanding of plant spatial omics but also provide groundwork to conduct more extensive investigations on the physiological and biochemical processes of plants.

Author contributions

XW: Conceptualization, Supervision, Writing – original draft, Writing – review & editing. JH: Conceptualization, Supervision, Writing – review & editing. ZL: Conceptualization, Supervision, Writing – review & editing. BL: Conceptualization, Supervision, Writing – review & editing. YW: Conceptualization, Supervision, Writing – review & editing. LL: Conceptualization, Supervision, Writing – review & editing.

Acknowledgments

We thank all authors and reviewers for their contributions to this Research Topic and for the support of the editorial office.

Conflict of interest

The authors declare that the research was conducted in the absence of any commercial or financial relationships that could be construed as a potential conflict of interest.

Publisher's note

frontiers | Frontiers in Plant Science

TYPE Original Research
PUBLISHED 10 October 2022
DOI 10.3389/fpls.2022.1012636

OPEN ACCESS

EDITED BY
Xiaodong Wang,
Minzu University of China, China

REVIEWED BY
Mo Zhang,
Chinese Academy of Medical Sciences and Peking Union Medical College, China
Weiwei Tang,
China Pharmaceutical University, China

*CORRESPONDENCE
Marisa Maia
mrmaia@fc.ul.pt
Marta Sousa Silva
mfsilva@fc.ul.pt

†These authors share senior authorship

SPECIALTY SECTION
This article was submitted to Technical Advances in Plant Science, a section of the journal Frontiers in Plant Science

RECEIVED 05 August 2022
ACCEPTED 20 September 2022
PUBLISHED 10 October 2022

CITATION
Maia M, McCann A, Malherbe C, Far J, Cunha J, Eiras-Dias J, Cordeiro C, Eppe G, Quinton L, Figueiredo A, De Pauw E and Sousa Silva M (2022) Grapevine leaf MALDI-MS imaging reveals the localisation of a putatively identified sucrose metabolite associated to *Plasmopara viticola* development. *Front. Plant Sci.* 13:1012636. doi: 10.3389/fpls.2022.1012636

Grapevine leaf MALDI-MS imaging reveals the localisation of a putatively identified sucrose metabolite associated to *Plasmopara viticola* development

Marisa Maia[1,2*], Andréa McCann[3], Cédric Malherbe[3], Johann Far[3], Jorge Cunha[4], José Eiras-Dias[4], Carlos Cordeiro[1,5], Gauthier Eppe[3], Loïc Quinton[3], Andreia Figueiredo[2], Edwin De Pauw[3†] and Marta Sousa Silva[1,5*†]

[1]Laboratório de FTICR e Espectrometria de Massa Estrutural, Faculdade de Ciências da Universidade de Lisboa, Lisboa, Portugal, [2]Grapevine Pathogen Systems Lab (GPS Lab), Biosystems and Integrative Sciences Institute (BioISI), Faculdade de Ciências da Universidade de Lisboa, Lisboa, Portugal, [3]Mass Spectrometry Laboratory (MolSys), University of Liège, Liège, Belgium, [4]Estação Vitivinícola Nacional, Instituto Nacional de Investigação Agrária e Veterinária (INIAV), Torres-Vedras, Portugal, [5]MARE - Marine and Environmental Sciences Centre, Faculdade de Ciências da Universidade de Lisboa, Lisboa, Portugal

Despite well-established pathways and metabolites involved in grapevine-*Plasmopara viticola* interaction, information on the molecules involved in the first moments of pathogen contact with the leaf surface and their specific location is still missing. To understand and localise these molecules, we analysed grapevine leaf discs infected with *P. viticola* with MSI. Plant material preparation was optimised, and different matrices and solvents were tested. Our data shows that trichomes hamper matrix deposition and the ion signal. Results show that putatively identified sucrose presents a higher accumulation and a non-homogeneous distribution in the infected leaf discs in comparison with the controls. This accumulation was mainly on the veins, leading to the hypothesis that sucrose metabolism is being manipulated by the development structures of *P. viticola*. Up to our knowledge this is the first time that the localisation of a putatively identified sucrose metabolite was shown to be associated to *P. viticola* infection sites.

KEYWORDS

***Vitis vinifera*, metabolomics, pathogen response, sucrose metabolism, mass spectrometry imaging**

Introduction

The development of matrix-assisted laser desorption-ionisation (MALDI) mass spectrometry imaging (MSI) was first reported in 1994 and has been applied to visualise different biomolecules, since 1997 (Spengler et al., 1994; Caprioli et al., 1997). MALDI-MSI has the unique ability to analyse the sample surface directly by combining powerful raster-scan of the sample surface with lasers shots with high mass resolution mass spectrometry (Grassl et al., 2011; Bjarnholt et al., 2014; Boughton et al., 2016). This technique has not only the ability to identify specific molecules, but also to reveal the distribution of a wide range of biological compounds across the sample section in a label-free and non-targeted mode. Considering that the complexity of biochemical processes occurring in cells, tissues, organs and whole systems is not only determined by their timing, but also by the localisation of certain molecular events (Kaspar et al., 2011), MALDI-MSI has the advantage to provide high spatial resolution (Grassl et al., 2011; Kaspar et al., 2011; Bjarnholt et al., 2014; Boughton et al., 2016; Schulz et al., 2019). Moreover, MALDI-MSI is a very sensitive technique with the ability to analyse complex samples (Laugesen and Roepstorff, 2003a). The analysis of compounds in MALDI-MSI ranges from large biomolecules, such as proteins and peptides, to small molecule compounds such as lipids, sugars, amino acids, phosphorylated compounds and pharmacological and chemical compounds (Puolitaival et al., 2008; Francese et al., 2009; Goodwin et al., 2010; Solon et al., 2010; Carter et al., 2011; Goodwin et al., 2011a; Goodwin et al., 2011b; Grassl et al., 2011; Kaspar et al., 2011; Gorzolka et al., 2014a; Takahashi et al., 2015; Sarabia et al., 2018a; Alcantara et al., 2020a). MALDI-MSI is also a suitable analytical technique for both polar and nonpolar biomolecules (Rubakhin and Sweedler, 2010b).

To date, the literature of MALDI-MSI in plants is limited when compared to animal studies (Bjarnholt et al., 2014; Boughton et al., 2016). MALDI-MSI has the potential to bring new insights into the molecular analysis of plants by providing high spatial resolution information about metabolic processes and potentially determine changes during plant development or induced by environmental variation. It will provide a means of identifying the localisation of metabolites associated with tissue types, development, disease, genetic variations or following genetic manipulation (Bjarnholt et al., 2014; Boughton et al., 2016). Some reports have used MALDI-MSI to evaluate the surface distribution of sugars, metabolites and lipids in different plant tissues and organs (Bunch et al., 2004; Burrell et al., 2007; Ng et al., 2007; Li et al., 2008; Shroff et al., 2008a; Goto-Inoue et al., 2010). For instance, the distribution and profiles of metabolites were studied in barley seeds and roots to investigate the compounds associated to seed germination (Gorzolka et al., 2014a). This technique has also been used to highlight the uneven distribution of specific biological compounds in wheat grains at various developmental stages (Veličković et al., 2014). Moreover, different studies have also used this technique to better understand plant biotic and abiotic stresses (Shroff et al., 2008a; Hamm et al., 2010; Shroff et al., 2015; Soares et al., 2015; Sarabia et al., 2018b). As an example, MALDI-MSI was used in barley roots to uncover metabolites in response to salinity stress (Sarabia et al., 2018b). Also, with the increasing demands for a more sustainable agriculture practice, this technique has been used to identify specific agrochemical compounds that are present in the plant or in specific organs of the plant (Alcantara et al., 2020a).

In every mass spectrometry imaging-based analysis, the measurement of an analyte intensity is influenced by several factors including analyte extraction efficiency, ionisation efficiency and consistency of co-crystallisation with the MALDI matrix (Schwartz et al., 2003a; Schulz et al., 2019). Sample handling and preparation are crucial to obtain high quality MALDI mass spectra in a reproducible manner (Laugesen and Roepstorff, 2003a; Schwartz et al., 2003a; Grassl et al., 2011). However, the selection of the MALDI matrix and the optimisation of the preparation protocol are still empirical procedures. The composition of the solvent in which the MALDI matrix is applied on the sample influences the desorption-ionisation of molecules from the tissues. Also, the selection of the optimal matrix, including its crystallisation parameters, for the experiment depends on the type of biological molecules to be analysed. A homogeneous layer of matrix solution, followed by a fast drying of the matrix film should be preferred to avoid the formation of large matrix crystals, that are responsible for critical signal fluctuation in MALDI-MSI profile (known as the matrix effects) (Francese et al., 2009; Rubakhin and Sweedler, 2010b; Grassl et al., 2011; Kaspar et al., 2011). By its ultra-high mass resolving power, Fourier Transform Ion Cyclotron Resonance mass spectrometry (FT-ICR-MS) imaging analysis enables small molecule separation from the complex background of tissue constituents and matrix ions (Bjarnholt et al., 2014; Boughton et al., 2016), which is a very important asset when analysing complex samples such as plant tissues.

Vitis vinifera L. (grapevine) is one of the most important and cultivated fruit plants in the world with a highly economic impact in several countries. Unfortunately, the domesticated *V. vinifera* cultivars frequently used for wine production are highly susceptible to fungal diseases, being the downy mildew, caused by the biotrophic oomycete *Plasmopara viticola* (Berk. et Curt.) Berl.et de Toni, one of the most destructive vineyard diseases. *Plasmopara viticola* is an obligatory biotrophic pathogen. It feeds on the living tissue (grapevine) and develops specific structures to invade the cell and to obtain metabolism products, without killing the plant (Gessler et al., 2011). So far, several potential metabolic biomarkers were identified by comparing the constitutive accumulation of specific metabolites not only in the leaf tissue of different *Vitis* genotypes (Maia et al., 2020), but also in grapevine-pathogen interaction (Batovska et al., 2008; Batovska et al., 2009; Becker

et al., 2013; Adrian et al., 2017; Nascimento et al., 2019). Their accumulation reflects however the all-leaf tissue metabolome composition/modulation and not the molecules that contribute for the first contact with pathogens at leaf surface. Some studies in grapevine leaves with MSI are starting to appear to identify the main biological compounds in the leaf surface during the interaction with *Plamopara viticola* (Hamm et al., 2010; Becker et al., 2014; Becker et al., 2017). However, these studies are only focused on the detection of specific compounds already described to have a defence role on grapevine after pathogen infection, e.g., resveratrol, pterostilbene and viniferins. Also, previous studies have reported that the lower side surface of leaves of *Vitis* genotypes differ distinctively with respect to trichomes. The distribution of these structures appears to be very characteristic of each genotype ranging from complete absence to dense coverage (Konlechner and Sauer, 2016).

The present work aimed at analysing *V. vinifera* 'Trincadeira' leaf surface with and without *P. viticola* infection, using MALDI FT-ICR-MS imaging approach. Sample preparation, including trichomes removal, the choice of the MALDI matrix and the matrix deposition solvent, were optimised to uncover the localisation of biological compounds present after pathogen infection.

Materials and methods

P. viticola propagation

Plasmopara viticola sporangia were collected from infected plants from the vineyard at the Portuguese Ampelographic Grapevine Collection (CAN, international code PRT051, established in 1988) at INIAV-Estação Vitivinícola Nacional (Dois Portos), using a vacuum pump (Millipore) at 10 kPa and stored at -20°C. Inoculum was propagated in *V. vinifera* 'Carignan' (susceptible cultivar) leaves by spreading a sporangia solution on the lower side surface of the leaf using a sterilized laboratory spreader, with an undefined concentration of *P. viticola* sporangia. After infection, leaves were kept in the dark for the first 8 to 12 hours and then kept in a climate chamber with controlled conditions (25°C; 16/8 hours with light/dark; 90% humidity) until sporulation appeared in all leaf surface. Sporangiophores with sporangia were collected with a vacuum pump (Millipore) at 10 kPa and stored at -20°C until further use.

Plant material harvesting and *P. viticola* infection assay

The third to fifth fully expanded leaves, from shoot to apex, of *Vitis vinifera* 'Trincadeira' (VIVC variety number: 15685) at the veraison stage, susceptible to *P. viticola*, were collected at the Portuguese Ampelographic Grapevine Collection. CAN is located at Quinta da Almoinha, 60 km north of Lisbon (9° 11′ 19″ W; 39° 02′ 31″ N; 75 m above sea level), and occupies nearly 2 ha of area with homogeneous modern alluvial soils (lowlands) as well as drained soil. All accessions are grafted on a unique rootstock variety (Selection Oppenheim 4–SO4) and each accession come from one unique plant collected in the field. The climate of this region is temperate with dry and mild summer. The best possible health status was guaranteed for all accessions

For leaf infections, sporangia viability was confirmed by microscopic observations as described by Kortekamp and co-workers (Kortekamp et al., 2008), prior to inoculation. One mL of a suspension containing 50 000 spores/mL was spread all-over the lower side of the leaf using a sterilized laboratory spreader. After inoculation, plants were kept for 8 to 12 hours in the dark and kept under natural light conditions at 25°C (90% humidity) for 96 hours. Two types of inoculated leaves were obtained for analysis: leaves infected with *P. viticola* without visible sporulation and with visible sporulation. Leaf discs of 1 cm were then cut using a cork-borer and lyophilised at -50°C between 2 glass slides, to obtain a planar surface once dried. Mock inoculations (controls) were performed by rinsing *Vitis vinifera* 'Trincadeira' leaves with water and keeping them for 8 to 12 hours in the dark. After that, control leaves were kept under natural light conditions at 25°C for 96 hours. Leaf discs of 1 cm were cut using a cork-borer and lyophilised at -50°C between 2 glass slides, to obtain a planar surface once dried. Infection control was accessed 8 days after inoculation with the appearance of typical disease symptoms (Figure S1).

Matrix coating optimisation

MALDI matrices α-cyano-4-hydroxycinnamic acid (HCCA), 2,5-dihydroxybenzoic acid (DHB) and 9-aminoacridine (9-AA) were purchased from Sigma-Aldrich (Overijse, Belgium). Trifluoracetic acid (TFA) was from Sigma-Aldrich, and LC-MS grade acetonitrile (ACN) and methanol (MeOH), were purchase from Biosolve (Valkenswaard, Netherlands). Indium tin oxide (ITO)-coated glass slides were purchased from Bruker Daltonics (Bremen, Germany).

For matrix coating optimization on leaf discs with and without trichomes, lyophilised control *Vitis vinifera* 'Trincadeira' leaf discs were carefully removed from the plates and transferred to the target ITO-glass slide, previously covered with a double-sided adhesive copper tape (StructureProbe INC, West Chester, PA, USA), with the lower side surface of the leaf facing up. For the analysis of trichome-free leaf discs, after mounting, trichomes were carefully removed using tweezers under a magnifying lens. After trichomes removal, microscope images (obtained at the magnification 10 x with an Olympus BX40 microscope) of the leaf discs were performed to visualise the leaf discs for possible damages. Only not damaged and flat areas of the microscopic images were selected for MSI analysis.

Both leaf discs were sprayed with HCCA matrix at 5 mg/mL using a solution of 70:30 (v:v) ACN:H_2O (Table 1).

After optimization, *Vitis vinifera* 'Trincadeira' leaf discs: control (mock inoculated), 96 hpi (hours post-inoculation) with *P. viticola* without visible sporulation and 96 hpi with *P. viticola* visible sporulation were transferred to ITO-glass slides and trichomes were removed. ITO-glass slides were stored in a desiccator until matrix deposition. Leaf discs were sprayed with the different matrices in different concentrations and solvents (Table 1). HCCA matrices of 5 mg/mL were prepared using 70:30 (v:v) ACN:H_2O and 70:30 (v:v) MeOH:H_2O with 0.1% (v/v) TFA. In total, 20 layers of this matrix solution were sprayed on the ITO slide using the SunCollect instrument (SunChrom, Friedrichsdorf, Germany). The first layer was sprayed at a flow rate of 10 µL/min. Flow rate was increased by 10 µL/min after each layer until reaching 60 µL/min. DHB matrix was prepared in 50:50 (v:v) ACN:H_2O with 0.1% (v/v) TFA to reach a final concentration of 20 mg/mL according to Seaman and co-workers (Seaman et al., 2014) and fifty matrix layers were sprayed on the ITO slide, as previously described. Solution of 9-AA was prepared at 15 mg/mL in methanol with 0.1% (v/v) TFA according to Rohit Shroff and co-workers (Shroff et al., 2008a). Leaves were spray-coated by using a commercial sprayer. The target plate was kept at around 45° angle and the sprayer held at 20 cm from the plate. This insured that the cone of the spray reaching the target covered the entire leaf. Each spray was followed by 10 seconds of warm air drying. This process was typically carried out 15 times to give maximal signal strength.

MALDI FT-ICR-MS imaging analysis

Microscope images (obtained at the magnification 10 x with an Olympus BX40 microscope) of leaf discs onto ITO-glass slides were acquired to better visualise and select areas of interest in the discs. Also, since the leaf surface is not entirely flat, only the flat areas of the microscopic images were selected for MSI analysis. Small areas of each leaf disc were selected to be analysed (Figure S2). Analysis was performed using a SolariX XR 9.4T FT-ICR-MS (Bruker Daltonics, Bremen, Germany), fitted with the dual ESI/MALDI ion sources and SmartBeam laser. For each mass spectrum, a 355 nm wavelength laser was used and the following parameters were used: 200 laser shots at a repetition rate of 1000 Hz, 60% of power. The raster step size was set at 200 µm. Mass spectrometry images were acquired in positive ionisation mode, in the mass range of 200 to 1000 m/z. A mass resolution of 1 million at the *m/z* 365 was achieved and a data reduction factor of 97% was considered. Peaks were considered at a minimum signal-to-noise ratio of 3. Red phosphorus solution in pure acetone spotted directly onto the ITO Glass slide was used to calibrate the mass spectrometer before each analysis.

Data analysis

Data were analysed using the MSI software SCiLS™ Lab 2016b (Bruker Daltonics, Bremen, Germany) for unsupervised spatial identification of discriminative features between control, 96 hpi, and 96 hpi with visible sporulation of *P. viticola* sporangiophores. For each pixel, data was normalised by the total ion count. MALDI FT-ICR-MS chemical images were generated from a colour scale, which represents the normalised intensity of specific ions. Each pixel of the image is associated with the original mass spectrum that is acquired in a particular position. A spatial localisation of the analytes is provided as a function of the *m/z* values. For metabolite identification, selected *m/z* values were submitted to MassTRIX 3 (Suhre and Schmitt-Kopplin, 2008) server (http://masstrix.org, accessed in March 2022) considering the following parameters: positive scan mode; the adducts $[M+H]^+$, $[M+K]^+$ and $[M+Na]^+$ were considered; a maximum *m/z* deviation of 2 ppm was considered; *Vitis vinifera* was selected; search was performed in the databases "KEGG (Kyoto Encyclopaedia of Genes and Genomes)/HMDB (Human Metabolome DataBase)/LipidMaps without isotopes".

Results

Preparation of grapevine leaves for analysis: The influence of trichomes

Grapevine leaves have trichomes in the lower side surface (Konlechner and Sauer, 2016), which may hamper the analysis and influence the MSI results (Bjarnholt et al., 2014). Hence, we started by analysing grapevine control leaf discs with and

TABLE 1 Different matrices, concentrations and layers used in *Vitis vinifera* 'Trincadeira' leaf discs.

	Matrix	Concentration	Solvent (% v/v)	Matrix application method	Number of layers
(1)	HCCA	5 mg/mL	70% ACN 30% H2O 0.1% TFA	SunChrom	20
(2)	HCCA	5 mg/mL	70% MeOH 30% H2O 0.1% TFA	SunChrom	20
(3)	DHB	20 mg/mL	50% ACN 50% H2O 0.1% TFA	SunChrom	50
(4)	9-AA	15 mg/mL	100% MeOH 0.1% TFA	Commercial spray	15

without trichomes to understand if these structures influence the coating of the matrix and to select the leaf discs leading to the best matrix coating. For this analysis, α-cyano-4-hydroxycinnamic acid (HCCA) was chosen as the matrix as it has been described in the literature to form small crystals, producing a more homogeneous matrix coating (Laugesen and Roepstorff, 2003a; Schwartz et al., 2003). HCCA was prepared according to (1) in Table 1 (Materials and Methods section).

V. vinifera 'Trincadeira' leaf discs' areas analysed with and without trichomes are presented in Figure 1. In positive-ion mass spectrum, the global intensity of the peaks detected was higher in the leaf disc without trichomes and with a more homogenous intensity detection. These results demonstrate that the matrix was better distributed in the leaf disc without trichomes and consequently a better signal was detected. For further analyses, trichomes were removed from all leaf discs using a tweezer under a magnifying lens. Moreover, to avoid leaf topological interference with the laser, only flat areas of the microscopic images (i.e., corresponding to flat regions on the microscopic image) were selected for MSI analysis.

Different matrix analysis and metabolite detection

After plant material preparation optimisation, and to detect molecules related to the grapevine-*P. viticola* interaction, we tested different matrices already described for MALDI FT-ICR MS imaging analysis of plant tissues (Table 1).

Matrices α-cyano-4-hydroxycinnamic acid (HCCA), 2,5-dihydroxybenzoic acid (DHB) and 9-aminoacridine (9-AA) were prepared according to Table 1 and applied by spraying on the different *V. vinifera* 'Trincadeira' leaf discs: control (mock inoculated), 96 hpi (hours post-inoculation) with *P. viticola* without visible sporulation and 96 hpi with *P. viticola* visible sporulation. HCCA was prepared into two different solvents: MeOH and ACN. HCCA is the most commonly used matrix for metabolites and different MALDI imaging studies in plant tissues were reported using that matrix in both solvents (Costa et al., 2013; Becker et al., 2014; Seaman et al., 2014; Soares et al., 2015). Microscope images (10x) of leaf discs were taken for a better selection of the leaf discs areas to be analysed (Figure S2). Selected areas were analysed with an FT-ICR-MS and ion images were reconstructed from the absolute intensities of the mean mass spectra, showing the exact location of ions on the extension of the leaf area analysed.

The mass spectra of grapevine leaf discs areas obtained from HCCA matrix with MeOH and ACN as solvents were very similar (Figure S3). These results demonstrate that both solvents can be used for MALDI analysis of grapevine leaf discs. Comparing all spectra, the intensity of the peaks, within the 800 to 900 *m/z* range, was lower for the matrices DHB and 9-AA (Figure S3).

These results also confirm our previous analysis. Removing the physical barrier from the grapevine leaves, trichomes, allows for a better MSI analysis independently of the matrix and solvents used.

Reconstructed MS images by MS data of all matrices, demonstrated that the ion intensity at *m/z* 365.105 (< 1 ppm) and 381.079 (< 1 ppm) is higher in the leaf discs infected by *P. viticola* than in the control discs (Figure 2 and Figure S4). The highest signals for both ions were observed with HCCA in MeOH and, to a lower extent with HCCA in ACN. For DHB, the signal was higher than HCCA in ACN for the *m/z* 365.105 but lower than HCCA matrix in both solvents for the *m/z* 381.07. For 9-AA, the signal was found much lower and less detectable than with the other matrices (Figure S4).

For compound annotation, MassTRIX database was used and *m/z* 365.105 and 381.079 ions were putatively identified as the $[M+Na]^+$ and $[M+K]^+$ adducts, respectively, of a disaccharide with a molecular formula of $C_{12}H_{22}O_{11}$. Being sucrose the most common disaccharide in plants and given our previous results (Nascimento et al., 2019) showing that sucrose increased in *Plasmopara viticola*-infected grapevine leaves 24h post-inoculation, we can attribute the ion images of *m/z* 365.105 and 381.079 to putatively identified sucrose. In a recent study based on the accurate mass measurements by Taylor and co-workers, these masses were also detected and correspond to different adducts of disaccharides (Taylor et al., 2021).

In a more detailed analysis, it was visible that the spatial distribution of putatively identified sucrose in the infected grapevine leaf discs is non-homogeneous, as observed in Figure 2. To evaluate this distribution, the accumulation of these ions was further investigated in the network of small veins and more precisely in the dense parenchyma tissue (Figure 3 and Figure S5). Images of the 96 hpi without visible *P. viticola* sporulation and 96 hpi with visible *P. viticola* sporulation leaf discs were reconstructed from the putatively identified sucrose *m/z* 365.105 ($[M+Na]^+$) as the distribution for *m/z* 381.079 ($[M+K]^+$) was similar but less intense. Our results suggest that putatively identified sucrose, *m/z* 365.105 ($[M+Na]^+$) and *m/z* 381.079 ($[M+K]^+$), are mainly located around the veins, which is an indicator of putatively identified sucrose at *P. viticola* infection sites (Figure 3 and Figure S5).

Discussion

Mass spectrometry imaging has been applied to study several plant tissues. However, sample preparation of plant tissues is not easy and continuously seems to be the bottleneck of this technique (Dong et al., 2016). This topic has been the major area of interest with the goal to improve sensitivity, specificity and obtain good quality images in a reproducible manner (Schulz et al., 2019).

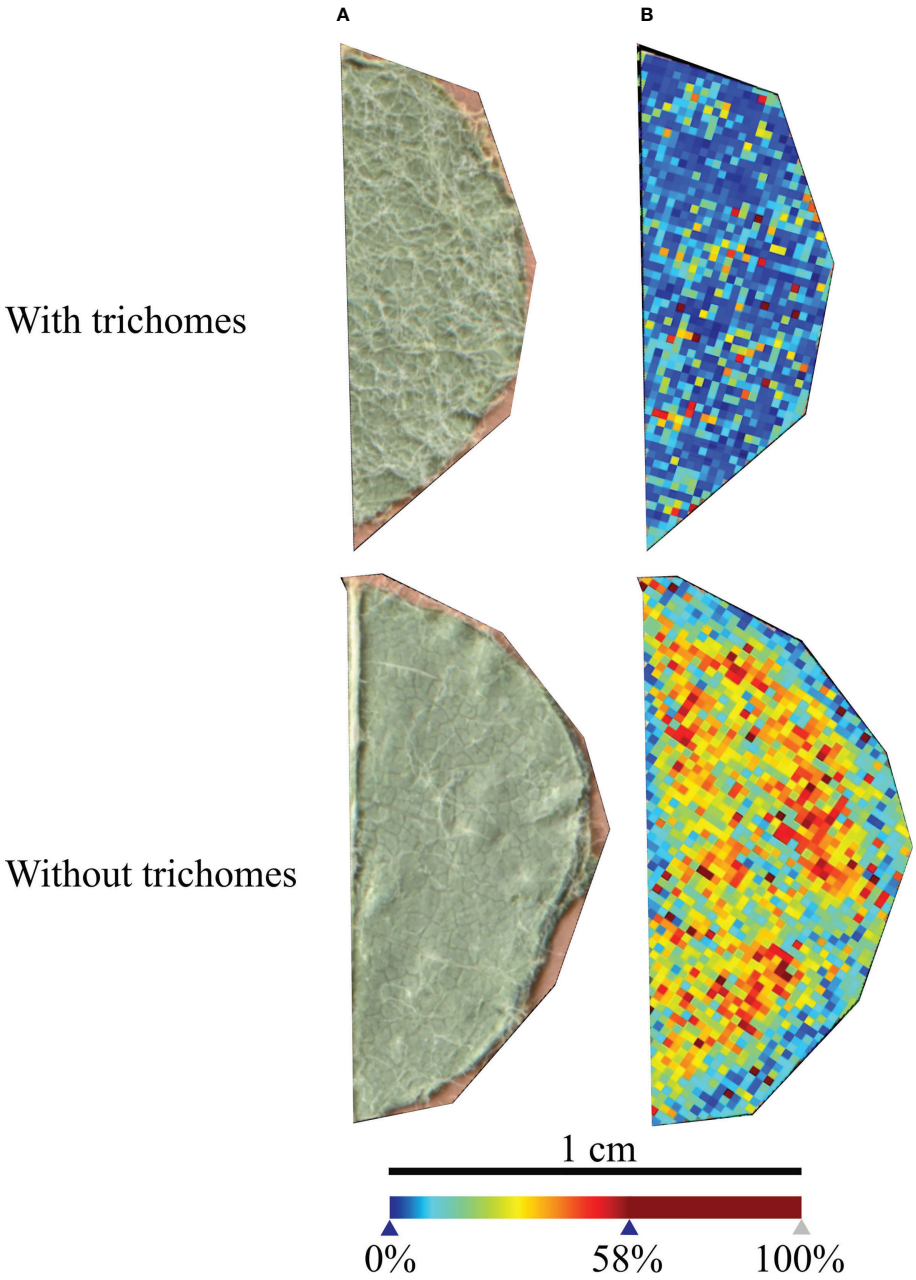

FIGURE 1
Vitis vinifera 'Trincadeira' leaf discs analysed with and without trichomes. **(A)** Microscopy images of the leaf disc sections analysed. **(B)** MALDI-FT-ICR-MS images reconstructed from all the peaks detected in the leaf discs. Spatial resolution: 30μm.

Sample preparation is a particular challenge, because the visualisation of certain classes of compound relies on specific conditions for optimal ionisation. Careful sample treatment is essential for signal quality and the avoidance of lateral displacement of the analytes (Rubakhin and Sweedler, 2010a). Artefacts can arise at any stage between sample collection and MSI analysis (Rubakhin and Sweedler, 2010a). Although different methodologies have been published through the years to limit these issues, the optimisation of sample preparation is still sample dependent, because of inherent differences in the composition of plant tissues (Grassl et al., 2011; Kaspar et al., 2011).

In our work, we focused our analysis on *V. vinifera* 'Trincadeira' leaves. The morphological leaf details for this genotype are already described for young and mature leaves

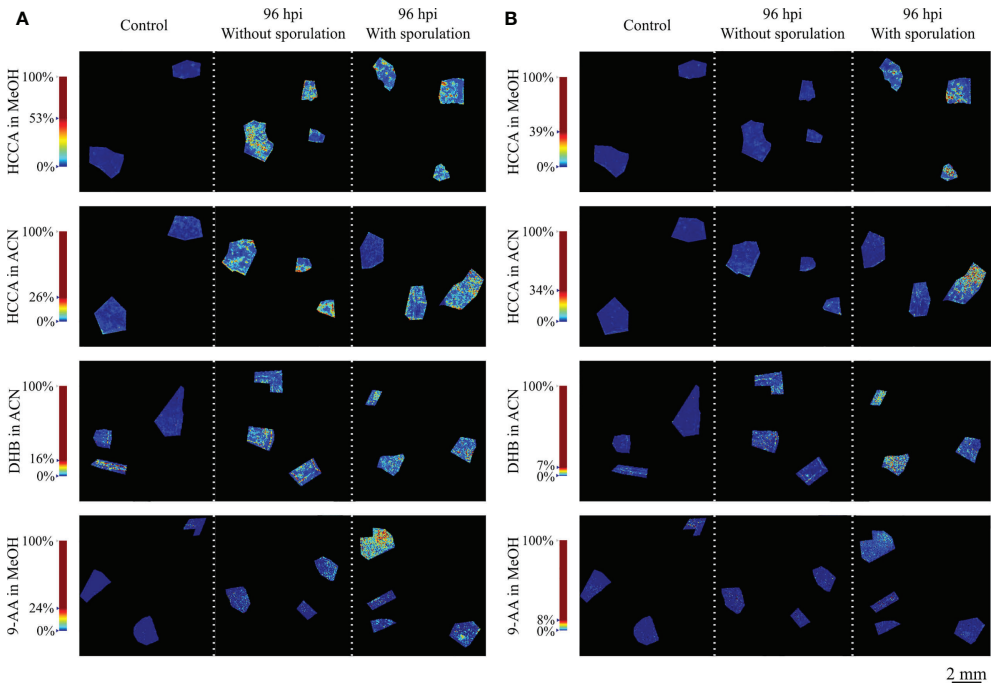

FIGURE 2
Reconstructed ion images of putatively identified sucrose. **(A)** (m/z 365.105, $[M+Na]^+$) and **(B)** (m/z 381.079, $[M+K]^+$) adducts, detected with MALDI–FT-ICR-MS imaging using HCCA matrix with MeOH and ACN, DHB matrix and 9-AA matrix. Leaf disc areas analysed from control (mock inoculated), 96 hpi without visible *P. viticola* sporulation and 96 hpi with visible *P. viticola* sporulation are presented. The colour scale of the leaf disc areas indicates the absolute intensity of each pixel (arbitrary units). Spatial resolution: 30µm.

according to the OIV descriptor list for grape varieties and *Vitis* species (Organisation of Vine and Wine, 2009). Young 'Trincadeira' leaves possess a yellow colour of the upper side of blade according to OIV descriptor 051. For mature leaves, 'Trincadeira' leaves present a pentagonal shape of blade (OIV descriptor 067), five lobes (OIV descriptor 068), absent area of anthocyanin coloration of main veins on upper side of blade (OIV descriptor 070), a weak goffering of blade (OIV descriptor 072), a twisted profile of blade in cross section (OIV descriptor 075), and a medium blistering of upper side of blade (OIV descriptor 076). Additionally, both sides convex for the shape of the teeth (OIV descriptor 076), a closed degree of opening/overlapping of the petiole sinus (OIV descriptor 076), a U-shaped for the shape of base of petiole sinus (OIV descriptor 080), present teeth in the petiole sinus (OIV descriptor 081-1), and a not limited petiole sinus base limited by the veins (OIV descriptor 081-2). Leaves also present teeth in the upper lateral sinuses (OIV descriptor 083-2) and a medium depth of upper lateral sinuses (OIV descriptors 094). Trichomes are essential epidermal outgrowths in plants, covering most aerial plant tissues and found in a very large number of plant species (Huchelmann et al., 2017), including grapevine (Konlechner and Sauer, 2016). Albeit one of the main functions of these structures is to protect the plant from, e.g., herbivorous, insects and fungi, the presence of trichomes in the leaf may inhibit the deposition of a homogeneous coating of the matrix. This may lead to an inaccurate ionisation of the ions present on the leaf and consequently a misleading detection/identification of the compounds (Bjarnholt et al., 2014).

Our genotype of study ('Trincadeira') possess a medium density of prostrate hairs between main veins on lower side of blade (OIV descriptor 053) in young leaves and a medium density of prostrate hairs between the main veins on lower side of Blade (OIV descriptor 084) and none or very low density of erect hairs on main veins on lower side of blade (OIV descriptor 087) in mature leaves. Having this in mind, and since trichomes could interfere with the analysis, our first approach was to analyse leaf discs with and without trichomes. Our results showed that leaf discs with no trichomes provide a more accurate analysis of the site-specific compounds.

Another important point in sample preparation for MALDI imaging is the matrix. Despite numerous matrices are available to analyse a wide range of biological compounds, it is important to consider the compounds of interest to be analysed in the sample. Selection of an appropriate matrix is a critical point to obtain a high quality MALDI imaging mass spectrum. For metabolomics analysis, the choice of matrices for metabolite

10.3389/fpls.2022.1012636

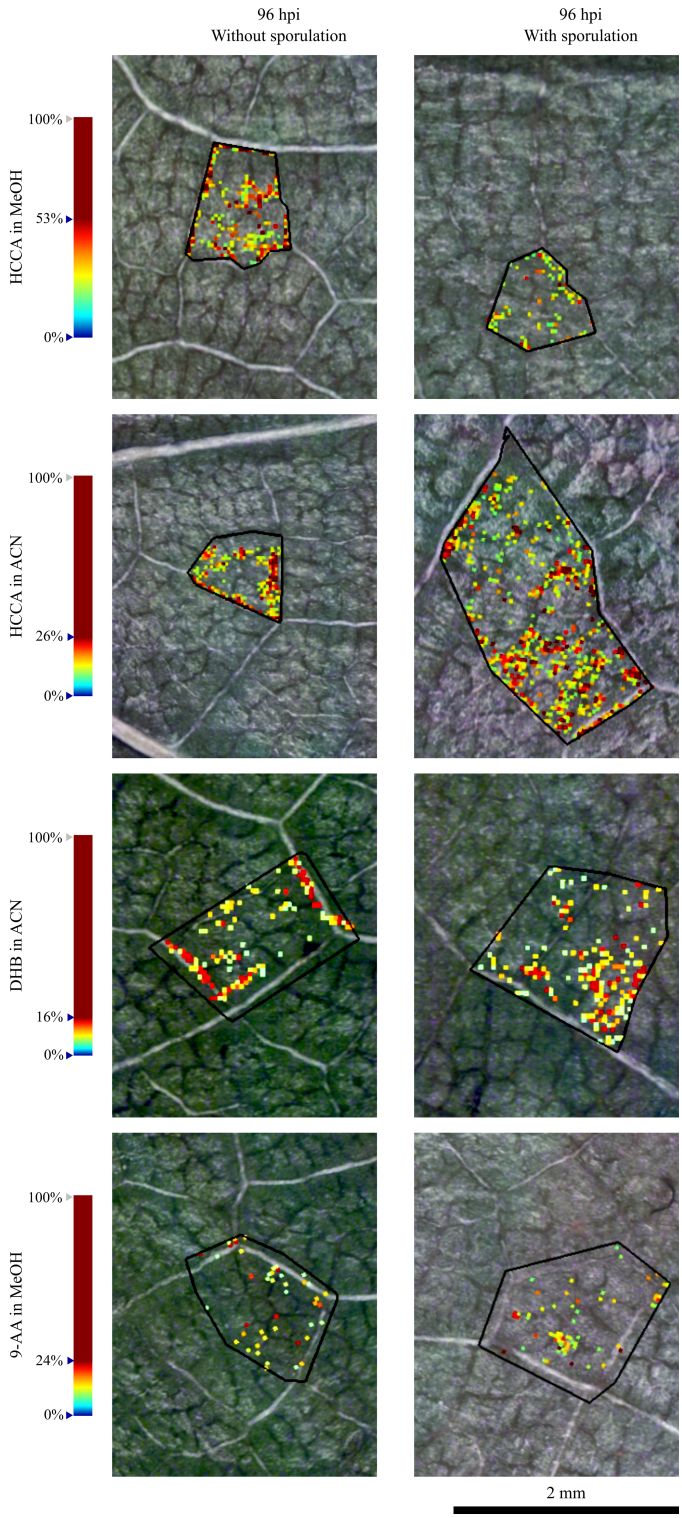

FIGURE 3
Reconstructed ion images of one selected region of putatively identified sucrose (*m/z* 365.105, $[M+Na]^+$) in 96 hpi without visible *P. viticola* sporulation and 96 hpi with visible *P. viticola* sporulation. Leaf disc areas detected *via* MALDI–FT-ICR-MS imaging using HCCA matrix with MeOH and ACN, DHB matrix and 9-AA matrix. The colour scale indicates the absolute intensity of each pixel (arbitrary units). Spatial resolution: 30µm.

analysis is even more complex, since matrix ions often crowd the low-mass range, limiting confident detection of low-molecular weight analyte ions. For the detection of low-weight molecules, α-cyano-4-hydroxycinnamic acid (HCCA), 2,5-dihydroxybenzoic acid (DHB) and 9-aminoacridine (9-AA) have been found to be the better suited (Laugesen and Roepstorff, 2003a; Calvano et al., 2018; Leopold et al., 2018). Although MALDI matrix 9-AA is mainly used in negative ionization mode, several recent studies have used this matrix to study some metabolites in positive mode, mainly from the lipid class (Chen et al., 2016; Leopold et al., 2018; Perry et al., 2020). Besides matrix itself, matrix application, solvent composition (typically methanol or acetonitrile) and mode of application, e.g., sprayer device, movement speed, solvent flow rate, distance between sample and target and/or nozzle temperature, influence the analysis of target molecules from the sample. These parameters are directly related to the size of the matrix crystals formed (Laugesen and Roepstorff, 2003a; Leopold et al., 2018; Schulz et al., 2019). The crystallisation between the matrix and the analyte leads to co-crystals which should be as homogeneous as possible, to assure reproducibility and highest sensitivity. Hence, spray is currently the most widespread matrix application technique. Taking this information into account, in this work, HCCA, DHB and 9-AA were tested with MeOH and ACN as solvents. Our results demonstrate that both solvents can be used for grapevine leaf discs. Also, all matrices appear to be suitable for grapevine leaf disc analysis, within the range of analysis. However, it is important to consider that the intensity of the peaks may be altered according to the matrix used. The obtained molecular mass and the deviation obtained for the ion images of the *m/z* values 365.105 and 381.079 make them identified as a sodiated ($[M+Na]^+$) and potasiated ($[M+K]^+$), respectively, disaccharide with a molecular formula of $C_{12}H_{22}O_{11}$, putatively assigned to sucrose.

In our previous studies, we investigated *Plasmopara viticola*-infected grapevine leaves 24h post-inoculation. Sucrose was identified by FT-ICR-MS, through direct injection, with a deviation between 0.2 and 1 ppm as differentially accumulated in inoculated leaves and was further quantified in the homogenised leaves (Nascimento et al., 2019). Therefore, we can attribute the reconstructed ion images of the *m/z* values 365.105 and 381.079 to sucrose. In this study, the *m/z* values were commonly identified in all of the matrices and solvents tested presenting high levels of abundance in grapevine leaf discs infected with *P. viticola* when comparing with mock inoculated leaf discs.

There are different hypothesis regarding the roles of sugar transporters in pathogen defence (Bezrutczyk et al., 2018), but all point out to a carbohydrate metabolic shift upon pathogen interaction. Indeed, plants use sugars as the main source of carbon and energy for defence responses (Morkunas and Ratajczak, 2014). In *Vitis vinifera* L. 'Modra frankinja' leaves infected with Flavescence Dorée phytoplasma, was observed an increase of sucrose concentration, as well as a higher activity of sucrose synthase (Prezelj et al., 2016). In this interaction, phloem transport is inhibited, resulting in the accumulation of carbohydrates and secondary metabolites that cause a source-sink transition (Prezelj et al., 2016). Also in grapevine, there is an accumulation of sucrose in leaves infected with phytoplasma (Hren et al., 2009). Moreover, upon grapevine-*P. viticola* interaction, the visible putatively identified sucrose accumulation is in accordance with our previously results on leaf metabolite profiling by NMR, where we reported higher accumulation of sucrose in *V. vinifera* 'Trincadeira' in the first 48 hours after inoculation with *P. viticola* (Ali et al., 2012). Also, we have previously shown an increase of sucrose in *Plasmopara viticola*-infected grapevine leaves 24 hpi (Nascimento et al., 2019) and in another study an increase of sugars was observed after 96 hpi with *P. viticola* (Chitarrini et al., 2020). Moreover, Gamm and co-workers have previously reported an overall alteration of the carbohydrate metabolism with an abnormal starch accumulation associated with an increase of starch synthesis in the all-leaf tissue analysis of *Vitis vinifera* L. 'Marselan', after 7 dpi (days post-inoculation) (Gamm et al., 2011).

To achieve the carbohydrate metabolic shift and to ensure plants surpass pathogen attacks, sugars are imported to the infected tissue from adjacent or distal healthy source leaves, *via* long-distance translocation, in the form of sucrose (Liu et al., 2022). This is quite important for grapevine upon *P. viticola* inoculation since for the infection to occur., *P. viticola* zoospores germinate and penetrate the stomatal cavity on the lower side of the leaf, forming a substomatal vesicle. This vesicle gives rise to the primary hyphae and mycelium, which grows through intercellular spaces, enclosed by the veins of the leaf (Fröbel and Zyprian, 2019). The haustorium penetrated the parenchyma cell walls, allowing the contact between the pathogen (*P. viticola*) and the host (grapevine leaves) (Gessler et al., 2011; Yin et al., 2017). Also, this structure function as a site of molecular exchange of effectors and nutrients between the grapevine and *P. viticola* and block grapevine defence signalling pathways (Yin et al., 2017). Sucrose is the main sugar-transport molecule in grapevine, as it is exported from leaves in the phloem (Walker et al., 2021). Hence, our results suggest a link between putatively identified sucrose and the development of *P. viticola* infection structures due to its higher intensity around the veins.

Up to our knowledge, our results are the first evidence of a metabolite putatively identified as sucrose near to *P. viticola* infection site areas, which lead us to hypothesise that the pathogen, through mycelium development, has gained access to this plant resource, and it is using it to complete its lifecycle (Aked and Hall, 1993; Sutton et al., 1999; Gebauer et al., 2017; Bezrutczyk et al., 2018). The specific location of sucrose needs to be better understood according to the involved biosynthesis pathways and their isomeric composition. Also, sucrose localisation in different *Vitis* genotypes, with different resistance degrees towards pathogens, should be further investigated to understand its role in grapevine defence against pathogens.

The results presented in this article clearly demonstrate the potential of MALDI-FT-ICR-MSI to gain more knowledge on the grapevine-*P.viticola* interaction particularly through the localisation and visual tracking of specific compounds in leaf tissue. Furthermore, our MSI results demonstrate that the analysis methodology works for complex samples, such as grapevine leaves, showing a great potential for application to other plant leaves.

Conclusion

Grapevine leaves are quite challenging in obtaining high quality MALDI mass spectra images, as leaves are not entirely flat and possess trichomes, influencing the detection of ions. In this work, we have shown that higher ion signal is achieved in leaf discs without trichomes. Three different matrices were selected (HCCA, DHB and 9-AA), whether dissolved in MeOH or ACN, for leaf discs coating and analysis. HCCA showed the highest signal intensity, independently of the solvent.

Reconstructed images by MS allow us to identify sucrose in all the conditions tested.

Sucrose ions were more abundant in the infected leaf discs, comparing to control discs. These results are in accordance with previous studies, which describe a variation of accumulation of sucrose in infected *P. viticola* plants. Up to our knowledge, our results are the first visual evidence of the localisation of sucrose translocation in grapevine leaves linked to the development of *P. viticola* infection structures.

Data availability statement

The original contributions presented in the study are included in the article/Supplementary Material. Further inquiries can be directed to the corresponding authors.

Author contributions

MM, AM, EP, AF and MSS conceived the study and performed the experimental design. MM, JC and JE-D collected the plant material. JC and JE-D characterized the *V. vinifera* 'Trincadeira' genotype. MM and AM performed the MALDI MSI analysis. MM, AM and CM performed the microscopy analysis. MM, AM, AF and MSS wrote the manuscript. All authors contributed to the article and approved the submitted version.

Funding

The authors acknowledge the support from Fundação para a Ciência e a Tecnologia (Portugal) though the projects PTDC/BAA-MOL/28675/2017, UID/MULTI/04046/2019, UIDB/04292/2020, Investigator FCT programs IF 00819/2015 to Andreia Figueiredo and CEECIND/02246/2017 to Marta Sousa Silva and the PhD grant SFRH/BD/116900/2016 to Marisa Maia. Andréa McCann thank the Excellence of Science Program of the FNRS F.R.S (Rhizoclip EOS2018000802) for financial support. Cedric Malherbe acknowledge support from the F.R.S.-FNRS as Research Associate fellowship. The authors also acknowledge the support from the Portuguese Mass Spectrometry Network (LISBOA-01-0145-FEDER-022125) and the Project EU_FT-ICR_MS, funded by the Europe and Union's Horizon 2020 research and innovation program under grant agreement nr.731077 (under a staff exchange program). The MALDI FT-ICR SolariX XR instrument was funded by FEDER BIOMED HUB Technology Support (number 2.2.1/996) and the SunChrom sprayer was founded by the European Union's Horizon 2020 program [EURLipids Interreg Eurogio Meuse-Rhine project supported by the European Regional Development Fund (FEDER)].

Acknowledgments

The authors acknowledge Gonçalo Laureano for the help in image editing and Prof. Dr. Cristina Figueiredo for the help to operate the lyophilizer.

Conflict of interest

The authors declare that the research was conducted in the absence of any commercial or financial relationships that could be construed as a potential conflict of interest.

Publisher's note

Supplementary material

The Supplementary Material for this article can be found online at: https://www.frontiersin.org/articles/10.3389/fpls.2022.1012636/full#supplementary-material

References

Adrian, M., Lucio, M., Roullier-Gall, C., Héloir, M.-C., Trouvelot, S., Daire, X., et al. (2017). Metabolic fingerprint of PS3-induced resistance of grapevine leaves against plasmopara viticola revealed differences in elicitor-triggered defenses. *Front. Plant Sci.* 8. doi: 10.3389/fpls.2017.00101

Aked, J., and Hall, J. L. (1993). The uptake of glucose, fructose and sucrose into the lower epidermis of leaf discs of pea (Pisum sativum l. cv. argenteum). *New Phytol.* 123, 271–276. doi: 10.1111/j.1469-8137.1993.tb03735.x

Alcantara, H. J. P., Jativa, F., Doronila, A. I., Anderson, C. W. N., Siegele, R., Spassov, T. G., et al. (2020a). Localization of mercury and gold in cassava (Manihot esculenta crantz). *Environ. Sci. pollut. Res. Int.* 27, 18498–18509. doi: 10.1007/s11356-020-08285-3

Ali, K., Maltese, F., Figueiredo, A., Rex, M., Fortes, A. M., Zyprian, E., et al. (2012). Alterations in grapevine leaf metabolism upon inoculation with plasmopara viticola in different time-points. *Plant Sci.* 191–192, 100–107. doi: 10.1016/j.plantsci.2012.04.014

Batovska, D. I., Todorova, I. T., Nedelcheva, D. V., Parushev, S. P., Atanassov, A. I., Hvarleva, T. D., et al. (2008). Preliminary study on biomarkers for the fungal resistance in vitis vinifera leaves. *J. Plant Physiol.* 165, 791–795. doi: 10.1016/j.jplph.2007.09.005

Batovska, D. I., Todorova, I. T., Parushev, S. P., Nedelcheva, D. V., Bankova, V. S., Popov, S. S., et al. (2009). Biomarkers for the prediction of the resistance and susceptibility of grapevine leaves to downy mildew. *J. Plant Physiol.* 166, 781–785. doi: 10.1016/j.jplph.2008.08.008

Becker, L., Bellow, S., Carré, V., Latouche, G., Poutaraud, A., Merdinoglu, D., et al. (2017). Correlative analysis of fluorescent phytoalexins by mass spectrometry imaging and fluorescence microscopy in grapevine leaves. *Anal. Chem.* 89, 7099–7106. doi: 10.1021/acs.analchem.7b01002

Becker, L., Carré, V., Poutaraud, A., Merdinoglu, D., and Chaimbault, P. (2014). MALDI mass spectrometry imaging for the simultaneous location of resveratrol, pterostilbene and viniferins on grapevine leaves. *Molecules* 19, 10587–10600. doi: 10.3390/molecules190710587

Becker, L., Poutaraud, A., Hamm, G., Muller, J.-F., Merdinoglu, D., Carré, V., et al. (2013). Metabolic study of grapevine leaves infected by downy mildew using negative ion electrospray – Fourier transform ion cyclotron resonance mass spectrometry. *Analytica Chimica. Acta* 795, 44–51. doi: 10.1016/j.aca.2013.07.068

Bezrutczyk, M., Yang, J., Eom, J.-S., Prior, M., Sosso, D., Hartwig, T., et al. (2018). Sugar flux and signaling in plant–microbe interactions. *Plant J.* 93, 675–685. doi: 10.1111/tpj.13775

Bjarnholt, N., Li, B., D'Alvise, J., and Janfelt, C. (2014). Mass spectrometry imaging of plant metabolites–principles and possibilities. *Nat. Prod. Rep.* 31, 818–837. doi: 10.1039/c3np70100j

Boughton, B. A., Thinagaran, D., Sarabia, D., Bacic, A., and Roessner, U. (2016). Mass spectrometry imaging for plant biology: A review. *Phytochem. Rev.* 15, 445–488. doi: 10.1007/s11101-015-9440-2

Bunch, J., Clench, M. R., and Richards, D. S. (2004). Determination of pharmaceutical compounds in skin by imaging matrix-assisted laser desorption/ionisation mass spectrometry. *Rapid Commun. Mass. Spectrom.* 18, 3051–3060. doi: 10.1002/rcm.1725

Burrell, M., Earnshaw, C., and Clench, M. (2007). Imaging matrix assisted laser desorption ionization mass spectrometry: A technique to map plant metabolites within tissues at high spatial resolution. *J. Exp. Bot.* 58, 757–763. doi: 10.1093/jxb/erl139

Calvano, C. D., Monopoli, A., Cataldi, T. R. I., and Palmisano, F. (2018). MALDI matrices for low molecular weight compounds: An endless story? *Anal. Bioanal. Chem.* 410, 4015–4038. doi: 10.1007/s00216-018-1014-x

Caprioli, R. M., Farmer, T. B., and Gile, J. (1997). Molecular imaging of biological samples: Localization of peptides and proteins using MALDI-TOF MS. *Anal. Chem.* 69, 4751–4760. doi: 10.1021/ac970888i

Carter, C. L., McLeod, C. W., and Bunch, J. (2011). Imaging of phospholipids in formalin fixed rat brain sections by matrix assisted laser desorption/ionization mass spectrometry. *J. Am. Soc. Mass. Spectrom.* 22, 1991–1998. doi: 10.1007/s13361-011-0227-4

Chen, Y., Gao, D., Bai, H., Liu, H., Lin, S., and Jiang, Y. (2016). Carbon dots and 9AA as a binary matrix for the detection of small molecules by matrix-assisted laser Desorption/Ionization mass spectrometry. *J. Am. Soc Mass. Spectrom.* 27, 1227–1235. doi: 10.1007/s13361-016-1396-y

Chitarrini, G., Riccadonna, S., Zulini, L., Vecchione, A., Stefanini, M., Larger, S., et al. (2020). Two-omics data revealed commonalities and differences between Rpv12- and Rpv3-mediated resistance in grapevine. *Sci. Rep.* 10, 12193. doi: 10.1038/s41598-020-69051-6

Costa, M. A., Marques, J. V., Dalisay, D. S., Herman, B., Bedgar, D. L., Davin, L. B., et al. (2013). Transgenic hybrid poplar for sustainable and scalable production of the Commodity/Specialty chemical, 2-phenylethanol. *PLos One* 8, e83169. doi: 10.1371/journal.pone.0083169

Dong, Y., Li, B., Malitsky, S., Rogachev, I., Aharoni, A., Kaftan, F., et al. (2016). Sample preparation for mass spectrometry imaging of plant tissues: A review. *Front. Plant Sci.* 7. doi: 10.3389/fpls.2016.00060

Francese, S., Dani, F. R., Traldi, P., Mastrobuoni, G., Pieraccini, G., and Moneti, G. (2009). MALDI mass spectrometry imaging, from its origins up to today: The state of the art. *Comb. Chem. High Throughput Screen* 12, 156–174. doi: 10.2174/138620709787315454

Fröbel, S., and Zyprian, E. (2019). Colonization of different grapevine tissues by plasmopara viticola–a histological study. *Front. Plant Sci.* 10. doi: 10.3389/fpls.2019.00951

Gamm, M., Héloir, M.-C., Bligny, R., Vaillant-Gaveau, N., Trouvelot, S., Alcaraz, G., et al. (2011). Changes in carbohydrate metabolism in plasmopara viticola-infected grapevine leaves. *Mol. Plant Microbe Interact.* 24, 1061–1073. doi: 10.1094/MPMI-02-11-0040

Gebauer, P., Korn, M., Engelsdorf, T., Sonnewald, U., Koch, C., and Voll, L. M. (2017). Sugar accumulation in leaves of arabidopsis sweet11/sweet12 double mutants enhances priming of the salicylic acid-mediated defense response. *Front. Plant Sci.* 8. doi: 10.3389/fpls.2017.01378

Gessler, C., Pertot, I., and Perazzolli, M. (2011). Plasmopara viticola: A review of knowledge on downy mildew of grapevine and effective disease management. *Phytopathol. Mediterr.* 50, 3–44. doi: 10.14601/Phytopathol_Mediterr-9360

Goodwin, R. J. A., Mackay, C. L., Nilsson, A., Harrison, D. J., Farde, L., Andren, P. E., et al. (2011a). Qualitative and quantitative MALDI imaging of the positron emission tomography ligands raclopride (a D2 dopamine antagonist) and SCH 23390 (a D1 dopamine antagonist) in rat brain tissue sections using a solvent-free dry matrix application method. *Anal. Chem.* 83, 9694–9701. doi: 10.1021/ac202630t

Goodwin, R. J. A., Pitt, A. R., Harrison, D., Weidt, S. K., Langridge-Smith, P. R. R., Barrett, M. P., et al. (2011b). Matrix-free mass spectrometric imaging using laser desorption ionisation Fourier transform ion cyclotron resonance mass spectrometry. *Rapid Commun. Mass. Spectrom.* 25, 969–972. doi: 10.1002/rcm.4939

Goodwin, R. J. A., Scullion, P., MacIntyre, L., Watson, D. G., and Pitt, A. R. (2010). Use of a solvent-free dry matrix coating for quantitative matrix-assisted laser desorption ionization imaging of 4-Bromophenyl-1,4-diazabicyclo(3.2.2)nonane-4-carboxylate in rat brain and quantitative analysis of the drug from laser microdissected tissue regions. *Anal. Chem.* 82, 3868–3873. doi: 10.1021/ac100398y

Gorzolka, K., Bednarz, H., and Niehaus, K. (2014a). Detection and localization of novel hordatine-like compounds and glycosylated derivates of hordatines by imaging mass spectrometry of barley seeds. *Planta* 239, 1321–1335. doi: 10.1007/s00425-014-2061-y

Goto-Inoue, N., Setou, M., and Zaima, N. (2010). Visualization of spatial distribution of γ-aminobutyric acid in eggplant (Solanum melongena) by matrix-assisted laser Desorption/Ionization imaging mass spectrometry. *Anal. Sci.* 26, 821–825. doi: 10.2116/analsci.26.821

Grassl, J., Taylor, N. L., and Millar, A. H. (2011). Matrix-assisted laser desorption/ionisation mass spectrometry imaging and its development for plant protein imaging. *Plant Methods* 7, 21. doi: 10.1186/1746-4811-7-21

Hamm, G., Carré, V., Poutaraud, A., Maunit, B., Frache, G., Merdinoglu, D., et al. (2010). Determination and imaging of metabolites from *Vitis vinifera* leaves by laser desorption/ionisation time-of-flight mass spectrometry: Imaging of metabolites from *Vitis vinifera* leaves. *Rapid Commun. Mass. Spectrom.* 24, 335–342. doi: 10.1002/rcm.4395

Hren, M., Nikolić, P., Rotter, A., Blejec, A., Terrier, N., Ravnikar, M., et al. (2009). "Bois noir" phytoplasma induces significant reprogramming of the leaf transcriptome in the field grown grapevine. *BMC Genomics* 10, 460. doi: 10.1186/1471-2164-10-460

Huchelmann, A., Boutry, M., and Hachez, C. (2017). Plant glandular trichomes: Natural cell factories of high biotechnological interest. *Plant Physiol.* 175, 6–22. doi: 10.1104/pp.17.00727

Kaspar, S., Peukert, M., Svatos, A., Matros, A., and Mock, H.-P. (2011). MALDI-imaging mass spectrometry - an emerging technique in plant biology. *Proteomics* 11, 1840–1850. doi: 10.1002/pmic.201000756

Konlechner, C., and Sauer, U. (2016). Ultrastructural leaf features of grapevine cultivars (Vitis vinifera l. ssp. vinifera). *OENO One* 50(4). doi: 10.20870/oeno-one.2016.50.4.51

Kortekamp, A., Welter, L., Vogt, S., Knoll, A., Schwander, F., Töpfer, R., et al. (2008). Identification, isolation and characterization of a CC-NBS-LRR candidate disease resistance gene family in grapevine. *Mol. Breed.* 22, 421–432. doi: 10.1007/s11032-008-9186-2

Laugesen, S., and Roepstorff, P. (2003a). Combination of two matrices results in improved performance of MALDI MS for peptide mass mapping and protein analysis. *J. Am. Soc Mass. Spectrom.* 14, 992–1002. doi: 10.1016/S1044-0305(03)00262-9

Leopold, J., Popkova, Y., Engel, K., and Schiller, J. (2018). Recent developments of useful MALDI matrices for the mass spectrometric characterization of lipids. *Biomolecules* 8, 173. doi: 10.3390/biom8040173

Li, Y., Shrestha, B., and Vertes, A. (2008). Atmospheric pressure infrared MALDI imaging mass spectrometry for plant metabolomics. *Anal. Chem.* 80, 407–420. doi: 10.1021/ac701703f

Liu, Y.-H., Song, Y.-H., and Ruan, Y.-L. (2022). Sugar conundrum in plant–pathogen interactions: Roles of invertase and sugar transporters depend on pathosystems. *J. Exp. Bot.* 73, 1910–1925. doi: 10.1093/jxb/erab562

Maia, M., Ferreira, A. E. N., Nascimento, R., Monteiro, F., Traquete, F., Marques, A. P., et al. (2020). Integrating metabolomics and targeted gene expression to uncover potential biomarkers of fungal/oomycetes-associated disease susceptibility in grapevine. *Sci. Rep.* 10, 15688. doi: 10.1038/s41598-020-72781-2

Morkunas, I., and Ratajczak, L. (2014). The role of sugar signaling in plant defense responses against fungal pathogens. *Acta Physiol. Plant* 36, 1607–1619. doi: 10.1007/s11738-014-1559-z

Nascimento, R., Maia, M., Ferreira, A. E. N., Silva, A. B., Freire, A. P., Cordeiro, C., et al. (2019). Early stage metabolic events associated with the establishment of vitis vinifera – plasmopara viticola compatible interaction. *Plant Physiol. Biochem.* 137, 1–13. doi: 10.1016/j.plaphy.2019.01.026

Ng, K.-M., Liang, Z., Lu, W., Tang, H.-W., Zhao, Z., Che, C.-M., et al. (2007). *In vivo* analysis and spatial profiling of phytochemicals in herbal tissue by matrix-assisted laser Desorption/Ionization mass spectrometry. *Anal. Chem.* 79, 2745–2755. doi: 10.1021/ac062129i

Organisation of Vine and Wine (2009). *2nd edition of the OIV descriptor list for grape varieties and vitis species.* France: International Organisation of Vine and Wine

Perry, W. J., Patterson, N. H., Prentice, B. M., Neumann, E. K., Caprioli, R. M., and Spraggins, J. M. (2020). Uncovering matrix effects on lipid analyses in MALDI imaging mass spectrometry experiments. *J. Mass. Spectrometry* 55, e4491. doi: 10.1002/jms.4491

Prezelj, N., Covington, E., Roitsch, T., Gruden, K., Fragner, L., Weckwerth, W., et al. (2016). Metabolic consequences of infection of grapevine (Vitis vinifera l.) cv. "Modra frankinja" with flavescence dorée phytoplasma. *Front. Plant Sci.* 7. doi: 10.3389/fpls.2016.00711

Puolitaival, S. M., Burnum, K. E., Cornett, D. S., and Caprioli, R. M. (2008). Solvent-free matrix dry-coating for MALDI imaging of phospholipids. *J. Am. Soc. Mass. Spectrom.* 19, 882–886. doi: 10.1016/j.jasms.2008.02.013

Rubakhin, S. S., and Sweedler, J. V. (2010a). A mass spectrometry primer for mass spectrometry imaging. In: S. Rubakhin and J. Sweedler (eds) *Mass Spectrometry Imaging. Methods in Molecular Biology* Humana Press, Totowa, NJ. 656. doi: 10.1007/978-1-60761-746-4_2

Rubakhin, S. S., and Sweedler, J. V. eds. (2010b). *Mass spectrometry imaging: Principles and protocols* (Humana Press). doi: 10.1007/978-1-60761-746-4

Sarabia, L. D., Boughton, B. A., Rupasinghe, T., van de Meene, A. M. L., Callahan, D. L., Hill, C. B., et al. (2018a). High-mass-resolution MALDI mass spectrometry imaging reveals detailed spatial distribution of metabolites and lipids in roots of barley seedlings in response to salinity stress. *Metabolomics* 14, 63. doi: 10.1007/s11306-018-1359-3

Sarabia, L. D., Boughton, B. A., Rupasinghe, T., van de Meene, A. M. L., Callahan, D. L., Hill, C. B., et al. (2018b). High-mass-resolution MALDI mass spectrometry imaging reveals detailed spatial distribution of metabolites and lipids in roots of barley seedlings in response to salinity stress. *Metabolomics* 14, 63. doi: 10.1007/s11306-018-1359-3

Schulz, S., Becker, M., Groseclose, M. R., Schadt, S., and Hopf, C. (2019). Advanced MALDI mass spectrometry imaging in pharmaceutical research and drug development. *Curr. Opin. Biotechnol.* 55, 51–59. doi: 10.1016/j.copbio.2018.08.003

Schwartz, S. A., Reyzer, M. L., and Caprioli, R. M. (2003). Direct tissue analysis using matrix-assisted laser desorption/ionization mass spectrometry: Practical aspects of sample preparation. *J. Mass. Spectrom.* 38, 699–708. doi: 10.1002/jms.505

Seaman, C., Flinders, B., Eijkel, G., Heeren, R. M. A., Bricklebank, N., and Clench, M. R. (2014). "Afterlife experiment": Use of MALDI-MS and SIMS imaging for the study of the nitrogen cycle within plants. *Anal. Chem.* 86, 10071–10077. doi: 10.1021/ac501191w

Shroff, R., Schramm, K., Jeschke, V., Nemes, P., Vertes, A., Gershenzon, J., et al. (2015). Quantification of plant surface metabolites by matrix-assisted laser desorption-ionization mass spectrometry imaging: glucosinolates on *Arabidopsis thaliana* leaves. *Plant J.* 81, 961–972. doi: 10.1111/tpj.12760

Shroff, R., Vergara, F., Muck, A., Svatos, A., and Gershenzon, J. (2008a). Nonuniform distribution of glucosinolates in arabidopsis thaliana leaves has important consequences for plant defense. *Proc. Natl. Acad. Sci.* 105, 6196–6201. doi: 10.1073/pnas.0711730105

Soares, M. S., da Silva, D. F., Forim, M. R., da Silva, M. F., das, G. F., Fernandes, J. B., et al. (2015). Quantification and localization of hesperidin and rutin in citrus sinensis grafted on c. limonia after xylella fastidiosa infection by HPLC-UV and MALDI imaging mass spectrometry. *Phytochemistry* 115, 161–170. doi: 10.1016/j.phytochem.2015.02.011

Solon, E. G., Schweitzer, A., Stoeckli, M., and Prideaux, B. (2010). Autoradiography, MALDI-MS, and SIMS-MS imaging in pharmaceutical discovery and development. *AAPS J.* 12, 11–26. doi: 10.1208/s12248-009-9158-4

Spengler, B., Hubert, M., and Kaufmann, R. (1994). MALDI ion imaging and biological ion imaging with a new scanning UV-laser microprobe *Proceedings, 42nd ASMS Conference on Mass Spectrometry and Allied Topics*, Chicago, Illinois, 1041.

Suhre, K., and Schmitt-Kopplin, P. (2008). MassTRIX: mass translator into pathways. *Nucl. Acids Res.* 36, W481–W484. doi: 10.1093/nar/gkn194

Sutton, P. N., Henry, M. J., and Hall, J. L. (1999). Glucose, and not sucrose, is transported from wheat to wheat powdery mildew. *Planta* 208, 426–430. doi: 10.1007/s004250050578

Takahashi, K., Kozuka, T., Anegawa, A., Nagatani, A., and Mimura, T. (2015). Development and application of a high-resolution imaging mass spectrometer for the study of plant tissues. *Plant Cell Physiol.* 56, 1329–1338. doi: 10.1093/pcp/pcv083

Taylor, M. J., Mattson, S., Liyu, A., Stopka, S. A., Ibrahim, Y. M., Vertes, A., et al. (2021). Optical microscopy-guided laser ablation electrospray ionization ion mobility mass spectrometry: Ambient single cell metabolomics with increased confidence in molecular identification. *Metabolites* 11(4):200. doi: 10.3390/metabo11040200

Veličković, D., Ropartz, D., Guillon, F., Saulnier, L., and Rogniaux, H. (2014). New insights into the structural and spatial variability of cell-wall polysaccharides during wheat grain development, as revealed through MALDI mass spectrometry imaging. *J. Exp. Bot.* 65, 2079–2091. doi: 10.1093/jxb/eru065

Walker, R. P., Bonghi, C., Varotto, S., Battistelli, A., Burbidge, C. A., Castellarin, S. D., et al. (2021). Sucrose metabolism and transport in grapevines, with emphasis on berries and leaves, and insights gained from a cross-species comparison. *Int. J. Mol. Sci.* 22, 7794. doi: 10.3390/ijms22157794

Yin, X., Liu, R.-Q., Su, H., Su, L., Guo, Y.-R., Wang, Z.-J., et al. (2017). Pathogen development and host responses to plasmopara viticola in resistant and susceptible grapevines: an ultrastructural study. *Horticulture Res.* 4, 17033. doi: 10.1038/hortres.2017.33

frontiers | Frontiers in Plant Science

TYPE Original Research
PUBLISHED 18 November 2022
DOI 10.3389/fpls.2022.1051756

OPEN ACCESS

EDITED BY
Xiaodong Wang,
Minzu University of China, China

REVIEWED BY
Yinglang Wan,
Hainan University, China
Dejun Hu,
China Pharmaceutical University, China

*CORRESPONDENCE
Lang-Tao Xiao
ltxiao@hunau.edu.cn
Yi Su
yisu@hunau.edu.cn

SPECIALTY SECTION
This article was submitted to Technical Advances in Plant Science, a section of the journal Frontiers in Plant Science

RECEIVED 23 September 2022
ACCEPTED 01 November 2022
PUBLISHED 18 November 2022

CITATION
Wu Z-H, Wang R-Z, Sun Z-L, Su Y and Xiao L-T (2022) A mass spectrometry imaging approach on spatiotemporal distribution of multiple alkaloids in *Gelsemium elegans*. *Front. Plant Sci.* 13:1051756. doi: 10.3389/fpls.2022.1051756

A mass spectrometry imaging approach on spatiotemporal distribution of multiple alkaloids in *Gelsemium elegans*

Zi-Han Wu[1], Ruo-Zhong Wang[1], Zhi-Liang Sun[2], Yi Su[1]* and Lang-Tao Xiao[1]*

[1]College of Bioscience and Biotechnology, Hunan Agricultural University, Changsha, China, [2]College of Veterinary Medicine, Hunan Agricultural University, Changsha, China

Gelsemium elegans contains multiple alkaloids with pharmacological effects, thus researchers focus on the identification and application of alkaloids extracted from *G. elegans*. Regretfully, the spatiotemporal distribution of alkaloids in *G. elegans* is still unclear. In this study, the desorption electrospray ionization mass spectrometry imaging (DESI-MSI) was applied to simultaneously analyze the distribution of pharmacologically important alkaloids in different organ/tissue sections of *G. elegans* at different growth stages. Finally, 23 alkaloids were visualized in roots, stems and leaves at seedling stage and 19 alkaloids were observed at mature stage. In mature *G. elegans*, 16 alkaloids were distributed in vascular bundle region of mature roots, 15 alkaloids were mainly located in the pith region of mature stems and 2 alkaloids were enriched in epidermis region of mature stems. A total of 16 alkaloids were detected in leaf veins of mature leaves and 17 alkaloids were detected in shoots. Interestingly, diffusion and transfer of multiple alkaloids in tissues have been observed along with the development and maturation. This study comprehensively characterized the spatial metabolomics of *G. elegans* alkaloids, and the spatiotemporal distribution of alkaloid synthesis. In addition, the results also have reference value for the development and application of *Gelsemium elegans* and other medicinal plants.

KEYWORDS

mass spectrometry imaging, alkaloid, *Gelsemium elegans*, spatio-temporal distribution, DESI-MSI

Introduction

Mass spectrometry imaging (MSI) emerges as an effective biological imaging technique within the last 20 years because of its versatility, high sensitivity, and label-free advantage (Dilillo et al., 2017). Being an important technique to understand the locations of molecular entities inside biochemical and biological systems (Jeckel et al., 2020), it can also capture

snapshots for the spatial distribution of metabolites in complex samples, providing an additional dimension of information for metabolic researches. Sample preparation for MSI does not require whole-tissue homogenate, furthermore, within-tissue spatial distribution profiles of metabolites in plants can be acquired through MSI (Bong et al., 2016). Recently, MSI has been employed to visualize certain target molecules in various plant organs, such as *Hypericum perfortum* roots (Tocci et al., 2018), *Ginkgo biloba* leaves (Li et al., 2018), *Vitex agnus-castus* fruits/leaves (Heskes et al., 2018) and strawberry fruits (Enomoto et al., 2018). Meanwhile, it has been used to visualize the spatial distribution of some important medicinal compositions in medicinal plants *Catharanthus roseusm* (Dutkiewicz et al., 2021) and *Camellia sinensis* (Liao et al., 2019).

Alkaloids are naturally occurring cyclic nitrogen containing compounds with low molecular-weight and alkali-like properties, mostly derived from amino acids (Cordell, 2013). As secondary metabolites found in approximately 20% of plant species, alkaloids are reported to play defensive roles against herbivores and pathogens (Lee et al., 2013). In addition, the applications of alkaloids also have pharmacological, veterinary and medical importance (Ziegler and Facchini, 2008). Owing to their diverse effects, many of the approximately 12,000 known alkaloids have been exploited as pharmaceuticals, stimulants, narcotics, and poisons (Facchini, 2001). For example, vinblastine can be used for the treatment of cancer (Souza et al., 2017), and ajmaline can be used for antiarrythmic heart disorders (Ozkartal et al., 2019).

Gelsemium elegans (*G. elegans*) is a genus of flowering plants in the *Gelsemicaeae* family being mainly distributed in North America and Southeast Asia (Jin et al., 2014). Previous studies showed that *G. elagans* has a variety of pharmacological effects including anti-tumor, anti-inflammation, skin ulcers relief, immune function, and analgesia (Liu et al., 2011; Ye et al., 2019). In fact, the basic pharmaceutically active compounds in *G. elagans* are alkaloids. According to the chemical structures, *G. elagans* alkaloids are divided into 6 types of gelsedine-, gelsemine-, humantenine-, koumine-, sarpagine- and the yohimbane-type (Jin et al., 2014). Structures of multiple alkaloids in *G. elagans* were characterized by high-performance liquid chromatography coupled with quadruopole time-of-flight mass spectrometry (LC-QTOF/MS) (Liu et al., 2017a) and nuclear magnetic resonance (NMR) (Wang et al., 2017). Meanwhile, the relative quantification is usually carried out through liquid chromatography coupled with mass spectrometry (LC-MS) (Liu et al., 2017b). Furthermore, an offline preparative three-dimensional HPLC (3D-HPLC) method was developed to perform the systematic purification of 24 indole alkaloids in *G. elegans* (Liu et al., 2021). Based on the two-dimension LC-UV-MS plus online heart-cutting method, a total of 256 alkaloids were grouped and tentatively identified in *G. elegans* (Liu et al., 2022).

As one of MSI-based technologies, DESI has firstly been applied in identification and visualization of plant target compounds, such as flavones and alkaloids. Recently, high-performance thin layer chromatography coupled with desorption electrospray ionization multistage mass spectrometry (HPTLC-DESI-MS^n) analysis was used to identify 13 aporphine and 4 benzylisoquinoline-type alkaloids in *Ocotea spixiana* (Conceicao et al., 2020). The seven *Uncaria* alkaloids were quantitatively imaged in rat brains by using DESI-MSI (Gao et al., 2022). Visualizing the distribution of a metabolite is an important approach to explore its translocation and the possible pathways of biosynthesis (Ifa et al., 2011; Kumara et al., 2019). High-throughput determination of alkaloids is necessary for the research of plant spatial metabolomics. Although DESI-MSI has been applied in the quantification of plant alkaloids, the application in high-throughput determination is rare. In our previous study, we employed DESI-MSI to visualize the distributions of several alkaloids in *G. elegans* (Wu et al., 2022b). Regretfully, the spatiotemporal distribution of more alkaloids in *G. elagans* is still unclear. For better exaction and application, it is essential to determine the detailed tissue localization and putative mobility of alkaloids in *G. elagans*. In this study, we simultaneously analyzed the spatiotemporal distributions of multiple alkaloids in organs/tissues of *G. elegans* at different growth stages by using the desorption electrospray ionization mass spectrometry imaging (DESI-MSI). The results also showed reference value for the development and application of *G. elegans* and other medicinal plants.

Materials and methods

Reagents and chemicals

Methanol was obtained from Merck Chemicals Co., Ltd. (Darmstadt, Germany). Saccharose was purchased from the Sinopharm Chemical Reagent Co., Ltd. (Shanghai, China). Glass slides were obtained from Wuhan Servicebio Technology Co., Ltd. (Wuhan, China). Optimum Cutting Polymer (O.C.T.) was purchased from Sakura (USA). Ultrapure water (resistivity ≥ 18.25 MΩ/cm) obtained from WaterPro water system (ULUPURE, China). All the reagents and chemicals employed in the experiments were of superior analytical grade (least 98% purity).

Plant culture conditions

The seeds of *G. elegans* were collected from Longyan (N24° 43′12″, E116°43′48″), Fujian Province, China. The seeds were washed with sterile distilled water, and vernalization at 4 °C was carried out for 48 h. The seeds were germinated and transplanted

into sand pots. The potted seedlings were grown in greenhouse with a photoperiod of 16/8 h light/darkness, 70% humidity, and a temperature of 24/20 °C day/night. For DESI-MSI analysis, the seedlings (30 d, 60 d and 90 d after planting) and the mature plants (180 d after planting) of *G. elegans* were collected.

Alkaloid analysis by LC-MS/MS

The sample preparation method and analytical method for LC-MS/MS was analyzed as previously reported (Wu et al., 2022b). Fresh tissues of *G. elegans* were ground with liquid nitrogen and 100 mg aliquot of the homogenate was immediately collected in microcentrifuge tube. Each tissue has three replicates. The homogenate was extracted twice by ultrasonic bath (Shumei KQ-250DE, Jiangsu, China) in 2.5 mL of 80% ethanol (1:25) for 0.5 h at 60 °C. The extraction solution was combined for filtration, and 1 mL of the filtered solution was evaporated by nitrogen. The sample was prepared by dissolving it in 1 mL of acetonitrile-ammonium acetate (1:4, volume percent) and filtering through a 0.22-μm membrane filter, 10 μL of which was used to LC-MS/MS analysis.

The UPLC-MS/MS was equipped with an Agilent 1290 series liquid chromatography (Agilent Technologies, USA) and Agilent 6460 triple quadruple mass spectrometer (Agilent Technologies, USA). The sample extraction solutions were separated on a Waters C18 column (3.5 μm, 4.6 μm×150 mm, Waters, USA). The separation conditions were as follows: the column oven temperature was kept at 40 °C, and the flow rate of the mobile phase was 0.3 mL/min. Auto MS/MS analysis was performed in both scan mode and multiple reaction monitoring (MRM) mode. Nitrogen gas was used as the drying and collision gas. The ionization source conditions were set as follows: flow rate of the nebulizer gas, 12 L/min; source temperature of the mass spectrometer, 350 °C; nebulizer pressure, 40 psi; capillary voltage, 3.50 kV; scan range, *m/z* 50-1000. The data acquisition was used by Agilent MassHunter workstation software (version B.07.00).

Plant sample preparation for DESI-MSI

Frozen sections of *G. elegans* organ/tissue were made for DESI-MSI. Fresh organ/tissue samples (root, stem, leaf and shoot) were immediately wrapped in aluminum foils and were frozen in liquid nitrogen. Three replicates of organ/tissue samples were made into frozen sections. The frozen samples were then transferred to a freezer (Haier DW-86L388J, Qingdao, China) for storage at -80 ℃. The frozen samples were put up on the specimen chuck, and O.C.T. embedding agent was dropped around the organ/tissue. The specimen chuck with sample was put on the quick-freezing table of the frozen section machine (Thermo CRYOSTAR NX50, San Jose, CA, USA). When O.C.T. became white and hard, the samples were sectioned with the slice thickness 8-10 μm. The roots, stems and leaves were neatly sliced along their cross sections. The shoots were longitudinally sliced. The organ/tissue sections were adhered to a glass slide and was analyzed by DESI-MSI.

DESI-MSI instrumentation

DESI-QToF-MS (Waters Xevo G2-XS, Milford, MA, USA) was employed for MSI analysis. Methanol: water=98:2 (v/v) was used as the solvent and was sprayed at an angle of 60° to surface. The flow rate was 2 μL/min. Nebulizing gas (nitrogen) pressure was 5 bar. Distance between the emitter and the mass spectrometer inlet was kept at 3 mm, the emitter was positioned 2 mm above the tissue surface, and the mass spectrometer inlet was 0.5 mm to the tissue surface. Imaging area was chosen according to the sample dimensions, the spatial resolution used was 50 μm × 50 μm, and the spatial scanning rate was 100 μm/s. Imaging acquisition interval varied between 6.0 and 6.5 hours in 1 cm × 1 cm area of tissue sample. Data were acquired in positive ion mode with a spray voltage of 4.5 kV. Signals were recorded from *m/z* 50 to 1200 and the ion source temperature was 150°C. Each experiment has three replicates. Each frozen section was scanned three times by DESI-MSI.

Compounds imaging and data processing

The acquisition setup, processing, and visualization of data were performed using High Definition Imaging (HDI) 1.5 (Waters Corporation, Manchester, UK) software. Data were acquired and mined using MassLynx software version 4.1 (Waters Corporation, Manchester, UK). To identify the metabolites, each interested peak was scanned for the details of MS^2 spectrum. The ion intensity values of the organs/tissues were obtained from the mass spectrum exported from the HDI software with centroid data. The image brightness intensities were calculated according to the ion intensity of samples and were plotted as the color scale. The relative quantification of alkaloids was performed according to the image brightness intensities captured by the DESI-MSI.

Results

Alkaloids identified in *G. elegans*

G. elegans is a woody and evergreen climber which thrives in warm and humid climates (Figures 1A-C). The leaves of *G. elegans* are ovate, lanceolate and verticillate (Figure 1D). The roots are light brown, nearly smooth and wiry. The center of the

root cross section appears pink (Figure 1E). The stems are smooth and twining, containing a milky latex (Figure 1F). In this study, through LC-MS/MS we identified 26 alkaloids, including 2 gelsemine-type alkaloids, 1 koumine-type alkaloid, 12 gelsedine-type alkaloids, 2 humantenine-type alkaloids, 1 yohimbane-type alkaloid and 8 sarpagine-type alkaloids (Figures S1–3 and Table 1). According to the structural information, most of alkaloids belonged to monoterpenoid indole alkaloids, which may derive from the precursors of tryptamine and secologanin through a series of biosynthetic processes. These alkaloids were characterized with two nitrogen atoms, and showed higher pharmacodynamics, such as analgesia, anti-tumor and anti-inflammation.

DESI based imaging pipeline for alkaloids in *G. elegans*

Among MSI-based technologies, matrix-assisted laser desorption ionization (MALDI) and DESI have been widely applied in recent years (Muller et al., 2011). MALDI-MSI requires a sample embedded in a typical matrix that can absorb laser energy and help the transfer of analytes into the gas and ionic phases. High laser precision guarantees high spatial resolution, up to 1 μm/pixel (Bjarnholt et al., 2014). However, the high matrix background noise makes MALDI-MSI unsuitable for the analysis of *m/z* less than 1000 molecules (Buscher et al., 2009). DESI-MSI has the advantages of minimal sample preparation, detection under atmospheric pressure, and small-molecule applicability (Campbell et al., 2012). Cryosectioning is a commonly used method to prepare plant tissue slices, in which freezing well quenches metabolic processes (Boughton et al., 2016). The glass slide bearing a tissue sample was placed on the mobile platform and directly analyzed by DESI-MSI. Its sample preparation is convenient, and the consumption of sample metabolites is minimal.

In this study, we were interested in simultaneously analyzing the spatiotemporal distributions of multiple alkaloids in organs/tissues of *G. elegans*. The molecular weight of alkaloids is generally not higher than 1000 and the structures of alkaloids are relatively stable. Due to the requirement of simultaneously analyzing multiple alkaloids in multiple organs/tissues, DESI-MSI seems to be the best choice. Therefore, DESI-MSI was employed to visualize the spatiotemporal localization of multiple alkaloids in *G. elegans* (Figure 2). Frozen sections of four organ/tissue sections (roots, stems, leaves, and shoots) of *G. elegans* were prepared (Figure 2A). The glass slide bearing a tissue sample was placed on the mobile platform. To obtain a higher image resolution, methanol in water (98:2, v/v) was used as the solvent (Manicke et al., 2008). As a key component in the DESI, the DESI sprayer consists of a solvent emitter surrounded by a second capillary that delivers a nebulizing gas flow (Wu et al., 2022a). The surface of frozen section is divided into a series of 50 μm × 50 μm lattice with a certain coordinate (X, Y). The DESI directs charged droplets to the lattice *via* a spray capillary, the ESI (electrospray ionization) stream impacts the extracting and

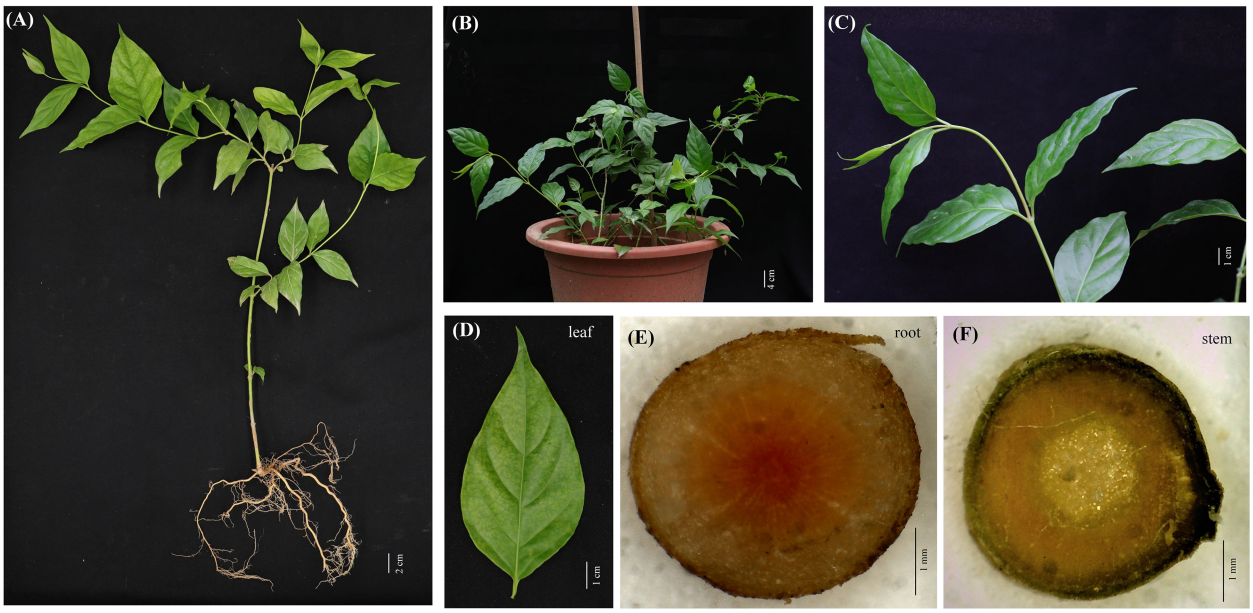

FIGURE 1
G. elegans plants cultured in pot. **(A–C)** The mature stage of *G. elegans*. **(D)** The leaf of *G. elegans*. **(E)** The root cross-sections. **(F)** The stem cross-section.

10.3389/fpls.2022.1051756

TABLE 1 Identified alkaloids in *Gelsemiume legans*.

	Alkaloid	Chemical formula	Ion pair ($[M+H]^+$)	Category
1	19-(*R*)-hydroxydihydrogelsemine	$C_{20}H_{24}N_2O_3$	341→311	gelsemine-type
2	gelsevirine	$C_{21}H_{24}N_2O_3$	353→322	gelsemine-type
3	kouminol	$C_{20}H_{24}N_2O_2$	325→136	koumine-type
4	Nb-methylgelsedilam	$C_{18}H_{20}N_2O_4$	329→109	gelsedine-type
5	14-hydroxygelsenicine	$C_{19}H_{22}N_2O_4$	343→108	gelsedine-type
6	4,20-dehydrogelsemicine	$C_{20}H_{24}N_2O_4$	357→326	gelsedine-type
7	11,14-dihydroxygelsenicine	$C_{19}H_{22}N_2O_5$	359→108	gelsedine-type
8	gelsemicine	$C_{20}H_{26}N_2O_4$	359→311	gelsedine-type
9	11-hydroxygelsemicine	$C_{20}H_{24}N_2O_5$	373→342	gelsedine-type
10	hydroxylation of gelsemicine	$C_{20}H_{26}N_2O_5$	375→313	gelsedine-type
11	14-acetoxygelsenicine	$C_{21}H_{24}N_2O_5$	385→339	gelsedine-type
12	11-methoxydihydrogelesemine	$C_{21}H_{28}N_2O_5$	389→281	gelsedine-type
13	14-acetoxy-15-hydroxygelsenicine	$C_{21}H_{24}N_2O_6$	401→343	gelsedine-type
14	11-methoxy-19-hydroxygelselegine	$C_{21}H_{28}N_2O_6$	405→343	gelsedine-type
15	gelseoxazolidinine	$C_{23}H_{28}N_2O_6$	429→339	gelsedine-type
16	humantenine	$C_{21}H_{26}N_2O_3$	355→163	humantenine-type
17	11-hydroxyhumantenine	$C_{21}H_{26}N_2O_4$	371→325	humantenine-type
18	sempervirine	$C_{19}H_{16}N_2$	273→245	yohimbane-type
19	dehydrokoumidine	$C_{19}H_{20}N_{20}$	293→204	sarpagine-type
20	koumidine	$C_{19}H_{22}N_2O$	295→138	sarpagine-type
21	19-(*Z*)-anhydrovobasinediol	$C_{20}H_{24}N_2O$	309→222	sarpagine-type
22	3-hydroxykoumidine	$C_{19}H_{22}N_2O_2$	311→267	sarpagine-type
23	gelsemine N-oxide	$C_{20}H_{22}N_2O_3$	339→279	sarpagine-type
24	Na-methoxy-19-(*Z*)-anhydrovobasinediol	$C_{21}H_{26}N_2O_2$	339→179	sarpagine-type
25	19*E*-16-*epi*-voacarpine	$C_{21}H_{24}N_2O_4$	369→166	sarpagine-type
26	gelsempervine A	$C_{22}H_{26}N_2O_4$	383→279	sarpagine-type

ionizing analytes. The ions are desorbed into the gas phase and then transferred *via* an atmospheric ion transfer line into the mass spectrometer, thus enabling measurement of ions (Figure 2B). In the last step, the recorded mass spectra were converted into two-dimensional ion images on the certain lattice according to the coordinate (X, Y). For each spatial coordinate, the amounts of ionizable molecules present as a function of their *m/z*. The resulting mass spectra for each coordinate (X, Y) was computationally reconstructed to form a complete dataset. The resultant reconstructed ion image represented the spatial distribution of the corresponding molecules. The mass spectra were processed with Masslynx software version 4.1 and images were viewed using HDImaging version 1.4 (Figure 2C).

Visualizing alkaloids locations in plant organs/tissues

To visulize the spatial distribution of alkaloids in *G. elegans*, the plant organ/tissue sections were detected by DESI-MSI in positive ionization mode. The typical DESI-MSI spectrums of alkaloids in plant organ/tissue sections were acquired (Figure S4). A large number of alkaloids related signals were detected in the ranges of *m/z* 100-1200. These alkaloids were confirmed by comparing the *m/z* values and MS/MS spectra with the results obtained by LC-QTOF/MS (Table 1).

In situ distributions of alkaloids in the sections of mature roots, stems, leaves and shoots were imaged (Figures 3–5). The microscopic pictures of frozen sections in tissues were shown in Figure S5. The results showed that 19 alkaloids were detected and imaged *via* DESI-MSI (Figures 3–5). 16 alkaloids were detected in the roots, all of which were located in the vascular bundle region and decreased gradually from pith to epidermis. In mature stems, 17 alkaloids were detected but their spatial distributions were not consistent. Two sarpagine-type alkaloids, gelsemine N-oxide (*m/z* 339) and 19*E*-16-*epi*-voacarpine (*m/z* 369) were mainly enriched in epidermis region, and the others displayed a similar localization pattern in roots, i.e., the 15 alkaloids were mainly located in the stem pith region and were significantly decreased in the epidermis. 16 alkaloids were detected in leaves and 17 in shoots. 16 alkaloids in leaves were mainly located in leaf veins. In shoots, most of alkaloids

10.3389/fpls.2022.1051756

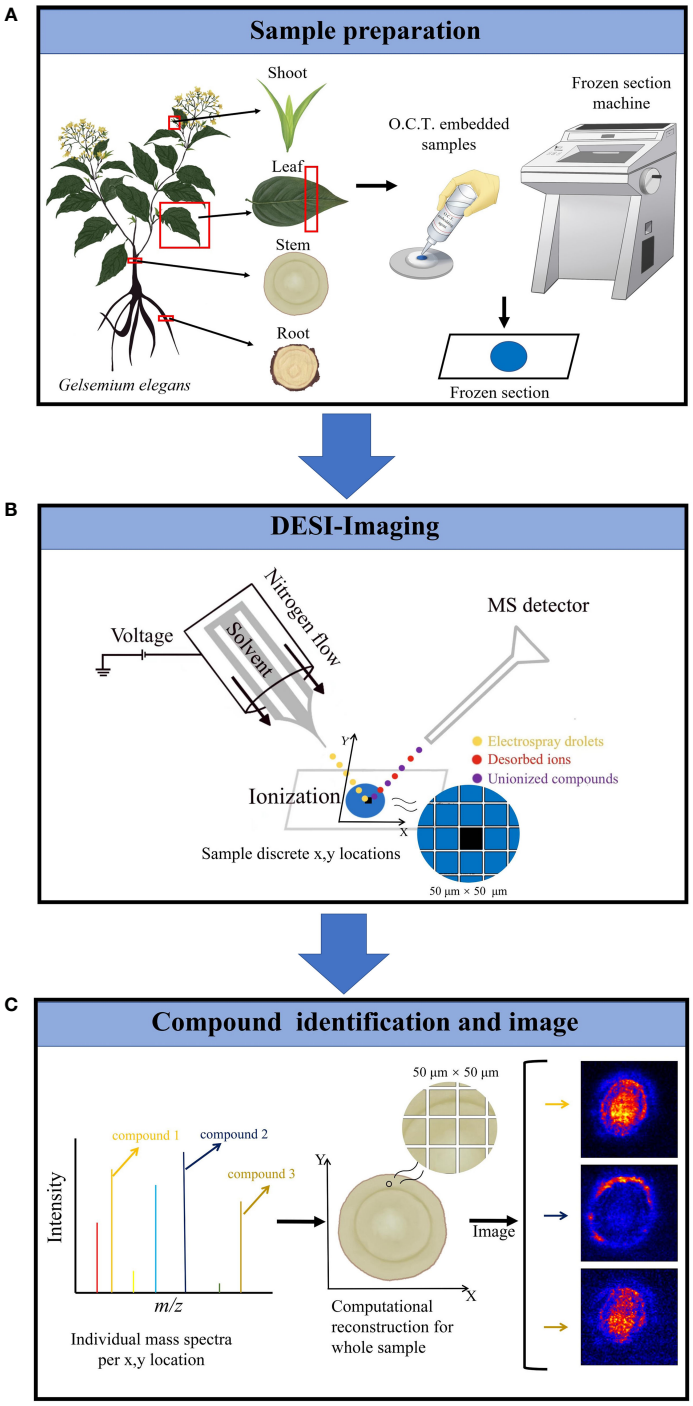

FIGURE 2
DESI-MS imaging experiment workflow. **(A)** The plant sample preparation for DESI-MSI. Frozen sections of four organ/tissue sections (roots, stems, leaves, and shoots) of *G elegans* were prepared. O.C.T. was used as the embedded agent. **(B)** The frozen sections were placed on the mobile platform of DESI-MSI. The DESI sprayer consists of a solvent emitter surrounded by a second capillary that delivers a nebulizing gas flow. Methanol in water (98:2, v/v) was used as the solvent. The DESI directs charged droplets to 50 μm × 50 μm lattice with a certain coordinate (X, Y) *via* a spray capillary, the ESI (electrospray ionization) stream impacts the extracting and ionizing analytes. Finally, the mixed droplets were ejected into the mass spectrometer. Imaging area was determined according to the lattice dimensions. **(C)** Target molecules identification and imaging. The resulting mass spectra for each coordinate (X, Y) was computationally reconstructed to form a complete dataset. The resultant reconstructed ion image represents the spatial distribution of the corresponding molecules. The acquisition setup, processing, and visualization of data were performed using HDI 1.5.

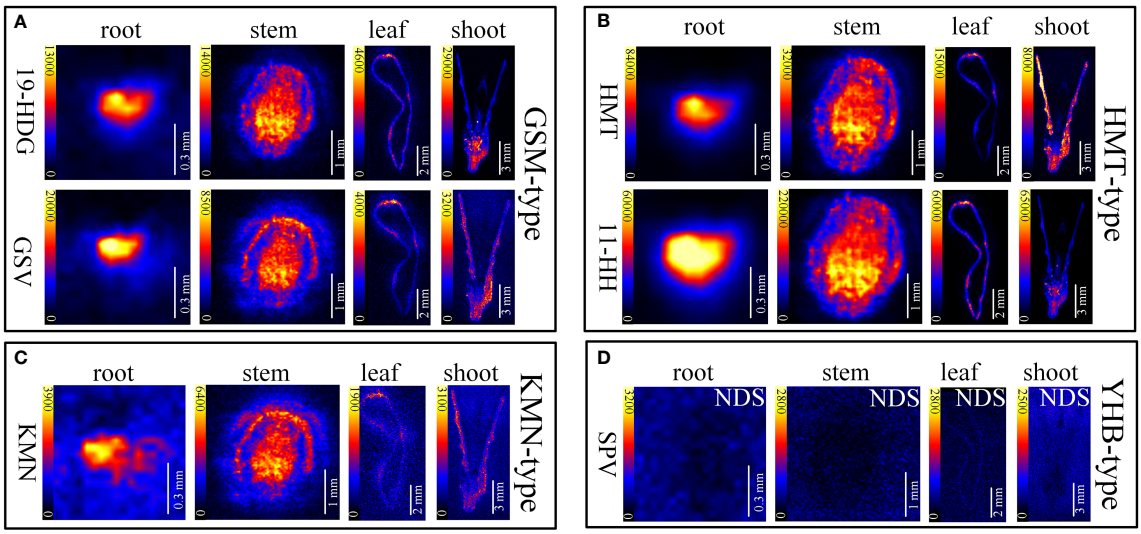

FIGURE 3
In situ visualization of alkaloids in sections of mature roots, stems, leaves and shoots. The color scale from dark to yellow indicates the regions of minimum (absence) and maximum relative quantification of multiple alkaloids in different organ/tissue. The relative quantifications of alkaloids were performed according to the image brightness intensities captured by the DESI-MSI. The names of the alkaloids are abbreviated. **(A)** Gelsmine-type (GSM-type) alkaloids. 19-HDG, 19-(*R*)-hydroxydihydrogelsemine (*m/z* 341.1865); GSV, gelsevirine (*m/z* 353.1865). **(B)** Humantenine-type (HMT-type) alkaloids. HMT, humantenine (*m/z* 355.2022); 11-HH, 11-hydroxyhumantenine (*m/z* 371.1971). **(C)** Koumine-type (KMN-type) alkaloids. KMN, kouminol (*m/z* 325.1916). **(D)** Yohimbane-type (YHB-type) alkaloids; SPV, sempervirine (*m/z* 273.1370). NDS means no detectable signal. Each organs/tissues had three replicates and analyzed by DESI-MSI.

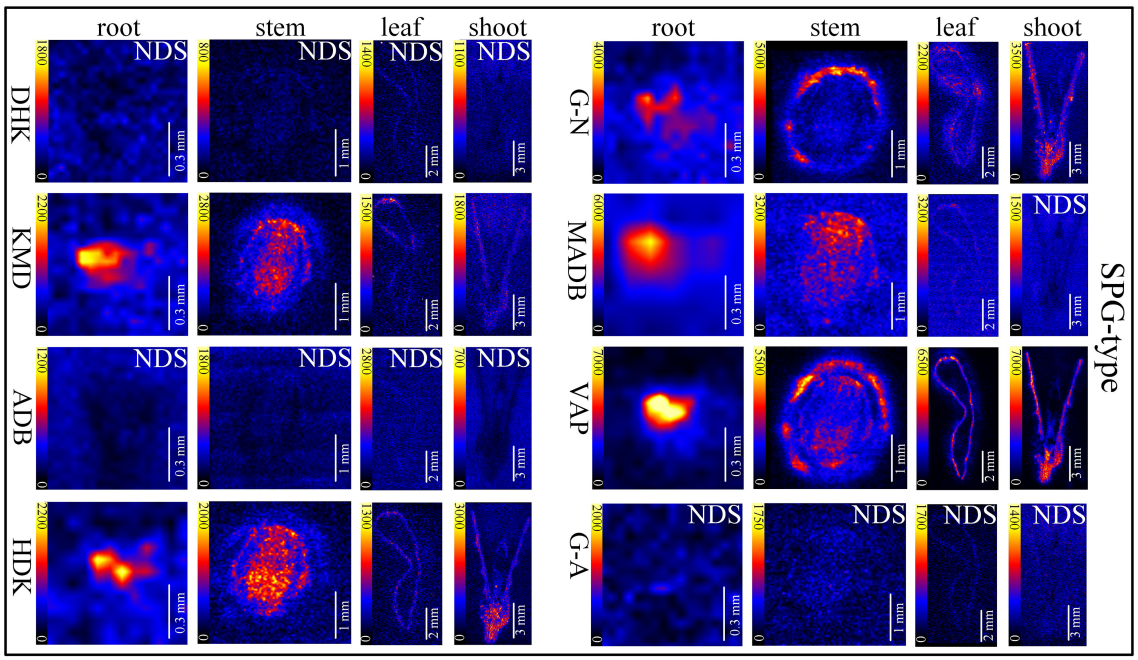

FIGURE 4
In situ visualization of sarpagine-type (SPG-type) alkaloids in different organ/tissue sections. NDS means no detectable signal. The names of the alkaloids are abbreviated. DHK, dehydrokoumidine (*m/z* 293.1644); KMD, koumidine (*m/z* 295.1810); ADB, 19-(*Z*)-anhydrovobasinediol (*m/z* 309.1881); HDK, 3-hydroxykoumidine (*m/z* 311.1760); G-N, gelsemine N-oxide (*m/z* 339.1709); MADB, Na-methoxy-19(*Z*)anhydrovobasinediol (*m/z* 339.2071); VAP, 19*E*-16-*epi*-voacarpine (*m/z* 369.1814); G-A, gelsempervine A (*m/z* 383.1978).

10.3389/fpls.2022.1051756

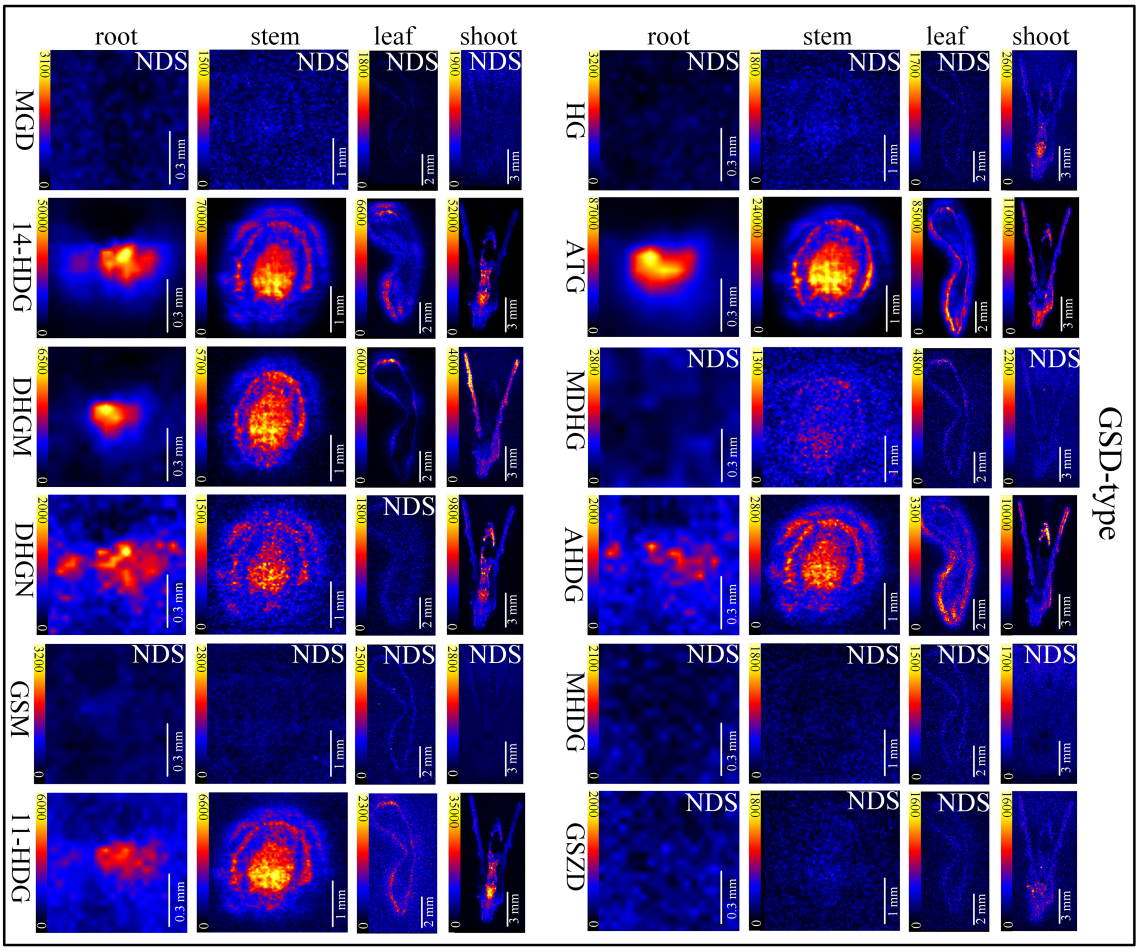

FIGURE 5
In situ visualization of gelsedine-type (GSD-type) alkaloids in different organ/tissue sections. NDS means no detectable signal. The names of the alkaloids are abbreviated. MGD, Nb-methylgelsedilam (*m/z* 329.1271); 14-HDG, 14-hydroxygelsenicine (*m/z* 343.1658); DHGM, 4,20-dehydrogelsemicine (*m/z* 357.1814); DHGN, 11,14-dihydroxygelsenicine (*m/z* 359.1607); GSM, gelsemicine (*m/z* 359.1951); 11-HDG:11-hydroxygelsemicine (*m/z* 373.1763); HG, hydroxylation of gelsemicine (*m/z* 375.1924); ATG, 14-acetoxygelsenicine (*m/z* 385.1763); MDHG, 11-methoxydihydrogelesemine (*m/z* 389.2085); AHDG, 14-acetoxy-15-hydroxygelsenicine (*m/z* 401.1713); MHDG, 11-methoxy-19-hydroxygelselegine (*m/z* 405.2009); GSZD, gelseoxazolidinine (*m/z* 429.2030).

were distributed in young leaves and bud primordium. However, 14-hydroxygelsenicine (*m/z* 343), 11-hydroxygelsemicine (*m/z* 373) and 11,14-dihydroxygelsenicine (*m/z* 359) were distributed in bud axis which further developed into stem. Dehydrokoumidine (*m/z* 293), 19-(*Z*)-anhydrovobasinediol (*m/z* 309), gelsempervine A (*m/z* 383), sempervirine (*m/z* 273), Nb-methylgelsedilam (*m/z* 329), gelsemicine (*m/z* 359) and 11-methoxy-19-hydroxygelselegine (*m/z* 405) were not detected. In addition, some non-alkaloid constituents were also visualized by DESI-MSI, *e.g.* ferulic acid (*m/z* 195) and GEIR-1 (*m/z* 213) were detected in stems, leaves and shoots, gelsemiol (*m/z* 201) and semperoside (*m/z* 361) were detected in shoots (Figure S6).

Alkaloids distributions in root at different seedling stages

The accumulation of alkaloids is both spatially and temporally. In this study, DESI-MSI was used to visualize multiple alkaloids in seedling roots of *G. elegans* respectively at 30, 60 and 90 d-age. The typical DESI-MSI spectrums of alkaloids in seeding roots were acquired (Figure S7). The maps captured by DESI-MSI revealed the spatial distribution of multiple alkaloids (Figure S8) and the image brightness intensities represented their relative contents in tissues. By using the HDI 1.5 software, the relative quantification range of alkaloids in main location was shown (Table 2). Accordingly, 20

10.3389/fpls.2022.1051756

TABLE 2 Distribution of alkaloids in seedling roots.

Category	Alkaloids	*m/z*	30 d		60 d		90 d	
			Main location	Brightness intensity	Main location	Brightness intensity	Main location	Brightness intensity
gelsemine-type alkaloids	19-(*R*)-hydroxydihydrogelsemine	341.1865	pith	7023-13812	pith	6552-9501	pith	13218-22893
	gelsevirine	353.1865	pith	1702-2922	pith	3530-5529	pith	2581-5677
koumine-type alkaloid	kouminol	325.1916	pith	1489-2219	pith	1421-3205	pith	1132-2620
gelsedine-type alkaloids	Nb-methylgelsedilam	329.1271	NDS		epidermis	439-1902	NDS	
	14-hydroxygelsenicine	343.1658	pith	601-791	pith	1480-2239	pith	4092-7726
	4,20-dehydrogelsemicine	357.1814	pith	458-859	pith	2082-2656	pith	1205-2683
	11,14-dihydroxygelsenicine	359.1607*	NDS		NDS		NDS	
	gelsemicine	359.1951*	NDS		NDS		NDS	
	11-hydroxygelsemicine	373.1763	pith	202-551	pith	1763-2678	pith	711-2982
	hydroxylation of gelsemicine	375.1924	pith	898-1341	NDS		NDS	
	14-acetoxygelsenicine	385.1763	NDS		pith	518-892	pith	2092-3890
	11-methoxydihydrogelesemine	389.2085	NDS		NDS		NDS	
	14-acetoxy-15-hydroxygelsenicine	401.1713	NDS		NDS		NDS	
	11-methoxy-19-hydroxygelselegine	405.2009	NDS		NDS		NDS	
	gelseoxazolidinine	429.2030	NDS		NDS		NDS	
humantenine-type alkaloids	humantenine	355.2022	pith	6073-12192	pith	9167-13538	pith	35577-48563
	11-hydroxyhumantenine	371.1971	pith	9569-15522	pith	13192-18574	pith	45829-81294
yohimbane-type alkaloid	sempervirine	273.1370	pith	1929-4077	epidermis	4275-21647	epidermis	1029-13829
sarpagine-type alkaloids	dehydrokoumidine	293.1644	pith	526-1131	pith	409-1083	NDS	
	koumidine	295.1810	pith	2388-4146	pith	1039-1736	pith	552-1285
	19-(*Z*)-anhydrovobasinediol	309.1881	pith	1228-2032	pith	310-1773	pith	513-2029
	3-hydroxykoumidine	311.1760	pith	2074-3817	pith	1120-1329	pith	902-1511
	gelsemine N-oxide	339.1709*	NDS		NDS		pith	285-1185
	Na-methoxy-19(*Z*) anhydrovobasinediol	339.2071*	pith	709-914	pith	519-793	pith	23-1004
	19*E*-16-*epi*-voacarpine	369.1814	pith	954-1229	pith	811-1113	pith	688-1683
	gelsempervine A	383.1978	pith	1107-1208	pith	2539-4478	epidermis	298-1438

Note: NDS means no detectable signal. * means the alkaloids with very similar m/z, the ion pairs, chemical structure formulas and ion mass spectrums of these alkaloids are shown in Table 1 and Figures S1, 2. The table showed the main location of mutiple alkaloids in seedling roots. The brightness intensity range indicate relative quantification range of alkaloids in main location. The image brightness intensities were captured by DESI-MSI. performed according to the image brightness intensities captured by DESI-MSI.

alkaloids were detected in *G. elegans* root at seedling stage. Along with the root development, more alkaloids were detected. For example, 14-acetoxygelsenicine (*m/z* 385) was detected in 60 d-age seedling and gelsemine N-oxide (*m/z* 339) had significant signal response in 90 d-age seedlings. In seedling roots, most of alkaloids were accumulated in the vascular bundle region. However, Nb-methylgelsedilam (*m/z* 329) were only detected in the epidermis of 60 d-age roots. Sempervirine (*m/z* 273) was enriched in the vascular bundle of 30 d-age roots, and was concentrated in the epidermis at 60 d and 90 d. Additionally, the alkaloids detected in seedling roots were not the same compared with that detected in mature roots (Figure 3). 14-acetoxy-15-hydroxygelsenicine (*m/z* 401) and 11,14-dihydroxygelsenicine (*m/z* 359) were detected in mature roots, but not detected in seedling roots. 19-(*Z*)-anhydrovobasinediol (*m/z* 309), gelsempervine A (*m/z* 383) and sempervirine (*m/z* 273) were only found in seedling roots.

Alkaloids distributions in stem at different seedling stages

The typical DESI-MSI spectrums of alkaloids in seeding stems were acquired (Figure S9). 21 alkaloids were visualized in the seedling stems through DESI-MSI, and more than half of the alkaloids were detected at the later stage of seedling

(Figure S10 and Table 3). 10 alkaloids were detected in 30 d-age seedling, 13 alkaloids had signal response in 60 d-age seedlings, but 21 alkaloids were imaged in 90 d-age seedlings. Interestingly, the alkaloids detected in seedling stems was more than alkaloids in mature stems. A surprising discovery was that *in situ* distribution of alkaloids showed the phenomenon of transfer and diffusion along with the development and maturity of stems. In mature stems, 19*E*-16-*epi*-voacarpine (*m/z* 369) was mainly located in epidermis region (Figure 3), but in pith region at seedling stage. It indicated that 19*E*-16-*epi*-voacarpine gradually diffused from the inside to the outside during the growth process, and finally accumulated in epidermis region. 14-acetoxygelsenicine (*m/z* 385) and Na-methoxy-19(*Z*) anhydrovobasinediol (*m/z* 339) were enriched in pith region in 30 and 60 d-age seedlings, but diffused from pith to epidermis in 90 d-age seedlings. In addition, gelsemicine (*m/z* 359), 19-(*Z*)-anhydrovobasinediol (*m/z* 309) and gelsempervine A (*m/z* 383) were only detected in 90 d-age stems.

Alkaloids distributions in leaf at different seedling stages

The typical DESI-MSI spectrums of alkaloids in seeding leaves were acquired (Figure S11). In seedling leaves, many alkaloids showed different distribution patterns (Figure S12

TABLE 3 Distribution of alkaloids in seedling stems.

Category	Alkaloids	*m/z*	30 d		60 d		90 d	
			Main location	Brightness intensity	Main location	Brightness intensity	Main location	Brightness intensity
gelsemine-type alkaloids	19-(*R*)-hydroxydihydrogelsemine	341.1865	pith	1091-2247	pith	3102-9495	pith	3016-19385
	gelsevirine	353.1865	NDS		pith	929-2394	pith	2103-15928
koumine-type alkaloid	kouminol	325.1916	NDS		pith	1211-2384	pith	1980-10920
gelsedine-type alkaloids	Nb-methylgelsedilam	329.1271	NDS		NDS		NDS	
	14-hydroxygelsenicine	343.1658	pith	311-856	pith	301-1093	pith	9988-38293
	4,20-dehydrogelsemicine	357.1814	NDS		pith	3093-4847	pith	1982-13790
	11,14-dihydroxygelsenicine	359.1607*	NDS		NDS		NDS	
	gelsemicine	359.1951*	NDS		NDS		pith	522-2847
	11-hydroxygelsemicine	373.1763	pith	233-702	pith	422-873	pith	1106-9483
	hydroxylation of gelsemicine	375.1924	pith	294-763	NDS		pith	1101-1211
	14-acetoxygelsenicine	385.1763	pith	7092-16384	pith	2122-3357	epidermis	2009-16101
	11-methoxydihydrogelesemine	389.2085	NDS		NDS		pith	272-1893
	14-acetoxy-15-hydroxygelsenicine	401.1713	NDS		NDS		epidermis	1013-38112
	11-methoxy-19-hydroxygelselegine	405.2009	NDS		NDS		NDS	
	gelseoxazolidinine	429.2030	NDS		NDS		NDS	
humantenine-type alkaloids	humantenine	355.2022	pith	1409-3745	pith	11038-17428	pith	15294-120294
	11-hydroxyhumantenine	371.1971	pith	6029-17032	pith	10294-20394	pith	8049-49338
yohimbane-type alkaloid	sempervirine	273.1370	NDS		NDS		NDS	
sarpagine-type alkaloids	dehydrokoumidine	293.1644	NDS		NDS		pith	85-1755
	koumidine	295.1810	NDS		pith	179-998	pith	982-7973
	19-(*Z*)-anhydrovobasinediol	309.1881	NDS		NDS		pith	504-4982
	3-hydroxykoumidine	311.1760	pith	2520-5921	pith	1579-3912	pith	492-5522
	gelsemine N-oxide	339.1709*	NDS		NDS		epidermis	97-1410
	Na-methoxy-19(*Z*) anhydrovobasinediol	339.2071*	pith	1262-3320	pith	412-1167	epidermis	488-4439
	19*E*-16-*epi*-voacarpine	369.1814	pith	57-782	pith	378-1259	pith	503-4928
	gelsempervine A	383.1978	NDS		NDS		pith	78-14388

Note: NDS means no detectable signal. * means the alkaloids with very similar m/z, the ion pairs, chemical structure formulas and ion mass spectrums of these alkaloids are shown in Table 1 and Figures S1, 2. The table showed the main location of mutiple alkaloids in seedling stems. The brightness intensity range indicate relative quantification range of alkaloids in main location. The image brightness intensities were captured by DESI-MSI.

10.3389/fpls.2022.1051756

TABLE 4 Distribution of alkaloids in seedling leaves.

Category	Alkaloids	*m/z*	30 d		60 d		90 d	
			Main location	Brightness intensity	Main location	Brightness intensity	Main location	Brightness intensity
gelsemine-type alkaloids	19-(*R*)-hydroxydihydrogelsemine	341.1865	mesophyll	767-4648	mesophyll	438-1711	vein	1039-8924
	gelsevirine	353.1865	mesophyll	211-1455	mesophyll	393-1503	vein	514-2948
koumine-type alkaloid	kouminol	325.1916	mesophyll	83-1575	NDS		vein	286-2855
gelsedine-type alkaloids	Nb-methylgelsedilam	329.1271	NDS		NDS		NDS	
	14-hydroxygelsenicine	343.1658	mesophyll	29-692	mesophyll	93-877	vein	449-2983
	4,20-dehydrogelsemicine	357.1814	mesophyll	332-1439	mesophyll	474-9469	vein	2103-13957
	11,14-dihydroxygelsenicine	359.1607*	NDS		NDS		NDS	
	gelsemicine	359.1951*	NDS		NDS		NDS	
	11-hydroxygelsemicine	373.1763	mesophyll	83-1019	mesophyll	309-893	vein	77-1059
	hydroxylation of gelsemicine	375.1924	NDS		NDS		NDS	
	14-acetoxygelsenicine	385.1763	mesophyll	1032-7093	mesophyll	694-2355	vein	1112-11948
	11-methoxydihydrogelesemine	389.2085	NDS		NDS		NDS	
	14-acetoxy-15-hyd roxygelsenicine	401.1713	NDS		mesophyll	94-683	mesophyll	182-1055
	11-methoxy-19-hydroxygelselegine	405.2009	NDS		NDS		NDS	
	gelseoxazolidinine	429.2030	NDS		NDS		NDS	
humantenine-type alkaloids	humantenine	355.2022	mesophyll	1232-14429	mesophyll	3193-9523	vein	5016-69301
	11-hydroxyhumantenine	371.1971	mesophyll	4034-11074	mesophyll	3815-11093	vein	4022-18192
yohimbane-type alkaloid	sempervirine	273.1370	NDS		NDS		NDS	
sarpagine-type alkaloids	dehydrokoumidine	293.1644	NDS		NDS		NDS	
	koumidine	295.1810	NDS		NDS		vein	419-1672
	19-(*Z*)-anhydrovobasinediol	309.1881	mesophyll	84-1410	NDS		vein	526-1611
	3-hydroxykoumidine	311.1760	mesophyll	1432-4783	NDS		vein	392-1492
	gelsemine N-oxide	339.1709*	mesophyll	133-691	NDS		vein	189-1782
	Na-methoxy-19(*Z*) anhydrovobasinediol	339.2071*	NDS		NDS		vein	312-2188
	19*E*-16-*epi*-voacarpine	369.1814	mesophyll	392-1321	mesophyll	343-1511	vein	179-2801
	gelsempervine A	383.1978	NDS		NDS		NDS	

Note: NDS means no detectable signal. * means the alkaloids with very similar m/z, the ion pairs, chemical structure formulas and ion mass spectrums of these alkaloids are shown in Table 1 and Figures S1, 2. The table showed the main location of mutiple alkaloids in seedling leaves. The brightness intensity range indicate relative quantification range of alkaloids in main location. The image brightness intensities were captured by DESI-MSI.

and Table 4). 16 alkaloids were detected in seedling leaves (Figure 3). 14-acetoxy-15-hydroxygelsenicine (*m/z* 401) and Na-methoxy-19(*Z*) anhydrovobasinediol (*m/z* 339) were respectively detected in leaf of 60 and 90 d-age seedling. As results, alkaloids were mainly concentrated in mesophyll at the early stage of seedling leaves, but they gradually enriched in leaf veins along with the development and eventually accumulates in large quantities at the later stage of seedling leaves. However, 14-acetoxy-15-hydroxygelsenicine (*m/z* 401) distribution was scattered in the leaves of 90 d-age seedling. 4 alkaloids were imaged in 30 d-age seedling, and no signal response in 60 d-age seedling, but they were surprisingly detected again in the leaves of 90 d-age seedling.

Discussion

Capabilities and applications of MSI in metabolomics

MSI has been developed to understand the spatial distribution of small organic molecules in organisms, and has been successfully applied to a variety of plants, including *Hypericum perfortum* roots (Tocci et al., 2018), *Ginkgo biloba* leaves (Li et al., 2018), *Vitex agnus-castus* fruits and leaves (Heskes et al., 2018) and strawberry fruits (Enomoto et al., 2018). MSI analysis enables spatial acquisition of targeted or untargeted metabolism data. MSI permits the determination of

exactly where the target metabolites accumulate because of its higher resolution and accuracy. Recently, spatial metabolomics was developed based on MSI, which has greatly accelerated the development of biomedicine (Yen et al., 2014). This method was performed to study the distribution of key flavonoids involved in various synthesis pathways in mint leaves (Freitas et al., 2019). Through spatial metabolomics based on MSI, the localization of asparaptine A was identified in *Asparagus officinalis* (Nakabayashi et al., 2021). Spatial metabolomics was employed to simultaneously determine the spatial localization and distribution patterns of endogenous molecules in plant tissues and provide a theoretical basis for understanding the synthesis and interactions of multiple components (Palla et al., 2022).

DESI-MSI for visualizing spatiotemporal distribution of multiple alkaloids in *Gelsemium elegans*

Since the relationship between metabolites and their spatial distribution in plants attracts research interests (Moreno-Pedraza et al., 2019), DESI was successfully applied to the detection of alkaloids. In recent years, HPTLC-DESI-MS^n was used to identify 13 aporphine and 4 benzylisoquinoline-type alkaloids in *Ocotea spixiana* (Conceicao et al., 2020). The quantitative imaging of 7 *Uncaria* alkaloids in rat brains using DESI-MSI was also performed (Gao et al., 2022). DESI-MSI was also used to visualize the spatial distribution of 63 metabolites in *Salvia miltiorrhiza*, and the complementary data obtained from the metabolomics coupled with mass spectrometry imaging enabled the identification of key reactions involved in flavonoid biosynthesis (Tong et al., 2022). Therefore, DESI-MSI is an useful tool to analyze the relationship between the spatial distribution and relative content of a specific compound. The authors' group has previously applied DESI-MSI and visualized the spatial distribution of three alkaloids (gelsemine, koumine, and gelsenicine) in *G. elegans* (Wu et al., 2022b). In this study, *in situ* distribution of multiple alkaloids in organ/tissue sections of *G. elegans* at different growth stages were simultaneously visualized by DESI-MSI. 26 alkaloids in *G. elegans* were analyzed by LC-MS/MS, and the precursor ions, product ions and chemical formulas of these alkaloids were presented (Table 1). Among a total of 23 alkaloids detected in roots, stems, leaves and shoots of *G. elegans* by DESI-MSI, 19 alkaloids were found to exhibit specific spatiotemporal distribution *in planta* (Figure 3).

In mature roots, 16 alkaloids were located in vascular bundle region, and were decreased gradually from pith to epidermis. However, research on *Rauvolfia tetraphylla* showed that the spatial distribution of three alkaloids in roots mainly accumulated in epidermis (Kumara et al., 2019), indicating the *in-situ* distribution of alkaloids in roots of different medical plants is tissue specific. In mature stems, 17 alkaloids were detected and most of them were distributed in the pith region. However, sarpagine-type alkaloids such as gelsemine N-oxide and 19*E*-16-*epi*-voacarpine were mainly enriched in epidermis region. Sarpagine-type alkaloids serve as the precursors for the more complex ajmaline- and koumine- type indole alkaloids, and exhibit antimalarial activity (Chen et al., 2022). The accumulation of alkaloids is both spatially and temporally. Multiple alkaloids in roots, stems and leaves at different seedling stages of *G. elegans* were visualized by DESI-MSI (Figures S7–12; Tables 2–4). Moreover, the relative quantification (RQ) of alkaloids were performed according to the image brightness intensities captured by the DESI-MSI. The relative content of most alkaloids increased along with the growth of *G. elegans*. As many as 20, 21 and 16 alkaloids were respectively detected in seedling roots, stems and leaves. In seedling roots, 14-acetoxygelsenicine and gelsemine N-oxide showed spatial distribution from 60 d and 90 d, respectively. In seedling leaves, 14-acetoxy-15-hydroxygelsenicine and Na-methoxy-19-(*Z*)-anhydrovobasinediol were detected from 60 d and 90 d. In seedling stems, the accumulation time points of alkaloids were found to be inconsistent, 10 and 13 alkaloids had signal response respectively at 30 d, 60 d, and the later stage of seedling. Several secondary metabolites have been reported to accumulate in developing seeds, presumably confer resistance against abiotic and biotic stress during seed dispersal and germination (Patrick and Offler, 2001; Dyer et al., 2001; Alves et al., 2007). Secondary metabolites are either synthesized *de novo* in the seed from available precursors or are transported from elsewhere in the plant. In the present study, although it is hard to tell whether the alkaloids detected in seedlings at 30 d are synthesized locally or not, it is sure that the alkaloids detected at the later stage was produced by a series of enzymatic reactions during plant development. In either case, it will be interesting to examine their spatial and temporal pattern of accumulation. Another surprising finding was the spatial distribution of multiple alkaloids changed significantly along with the stem development, 14-acetoxygelsenicine and Na-methoxy-19-(*Z*)-anhydrovobasinediol were enriched in vascular bundle region at the early stage of seedling and then diffused to epidermis at 90 d. 19*E*-16-*epi*-voacarpine was mainly located in vascular bundle region of seedling stems, and then diffused to epidermis region of mature stems. Since the biosynthesis and storage of plant metabolites are highly regulated, it is possible that these alkaloids localized in stems at the early stage will play roles in stress resistance at different growth stages or the alkaloids transportation to the epidermis from other parts are involved. Thus the spatial-temporal distribution of these alkaloids would be precisely regulated in stress responses.

The spatial metabolomics is a developing sub-branch of metabolomics rarely employed in medical plant studies, especially the plant alkaloids research. Only a few studies in plants have been previously reported including the spatial metabolome (monoterpene and paeonol glycosides, tannins,

flavonoids, saccharides and lipids) of *Paeonia suffruticosa* and *Paeonia lactiflora* roots by MALDI-MSI (Li et al., 2021), the spatial metabolome (flavonoids, ginkgolic acids, cardanols, saccharides, phospholipids and chlorophylls) of *Ginkgo biloba* by MALDI and LDI-MSI (Li et al., 2018). Using DESI-MSI method, we successfully visualized the spatial distribution for as more as 26 alkaloids in different *G. elegans* tissues at different growth stages, and analyzed the spatial transport of specific alkaloid. In addition to the visualization of spatial distribution of alkaloids in plant tissues, this study also provides robust data for further constructing spatial omics frameworks for multiple alkaloids in *G. elegans*, which will greatly promote DESI-MSI application in plants.

Conclusion

The DESI-MSI technique provides an efficient approach to directly visualize the target molecules *in situ* in plants without the extra extraction and processing. In this study, 23 alkaloids were visualized in roots, stems and leaves at seedling stage and 19 alkaloids were observed at mature stage by using DESI-MSI. Among them, 16 alkaloids were distributed in vascular bundle region of mature roots, 15 alkaloids were mainly located in the pith region of mature stems and 2 alkaloids were enriched in epidermis region of mature stems. In addition, 17 alkaloids were detected in shoots and 16 alkaloids were detected in mature leaf veins. Interestingly, along with the development process of *G. elegans*, *in situ* distribution showed that multiple alkaloids in tissues may undergo diffusion and transfer. Overall, our work indicated DESI-MSI is a promising spatial omics technique for visualizing the spatiotemporal distribution of alkaloids in plants.

Data availability statement

The original contributions presented in the study are included in the article/Supplementary Material. Further inquiries can be directed to the corresponding authors.

Author contributions

Z-HW and R-ZW developed the sample preparation and MSI method, and compiled the manuscript. YS interpreted the results and drafted the manuscript. Z-LS supported the method development and the data analysis. L-TX acquired funding, supervised the project and revised the manuscript. All authors contributed to the article and approved the submitted version.

Funding

This study was supported by the financial support from the National Natural Science Foundation of China (grant number: 91317312 and 31871714), and Provincial Natural Science Foundation of Hunan (grant number: 2022JJ30294).

Acknowledgments

We are very grateful to Zhihong Gong (Waters Corporation, Shanghai) for his technical support during DESI experiments, Zhaoying Liu (Hunan Agricultural University, Changsha) for providing seeds of *Gelsemium elegans*, and Yaqi Liu (University of the Arts London, London) for image processing assistance.

Conflict of interest

The authors declare that the research was conducted in the absence of any commercial or financial relationships that could be construed as a potential conflict of interest.

Publisher's note

Supplementary material

The Supplementary Material for this article can be found online at: https://www.frontiersin.org/articles/10.3389/fpls.2022.1051756/full#supplementary-material

References

Alves, M. N., Sartoratto, A., and Trigo, ,. J. R. (2007). Scopolamine in brugmansia suaveolens (Solanaceae): defense, allocation, costs, and induced response. *J. Chem. Ecol.* 33, 297–309. doi: 10.1007/s10886-006-9214-9

Bjarnholt, N., Li, B., D'Alvise, J., and Janfelt, C. (2014). Mass spectrometry imaging of plant metabolites - principles and possibilities. *Nat. Prod. Rep.* 31, 818–837. doi: 10.1039/c3np70100j

Bong, Y., Li, B., Malitsky, S., Rogachev, L., Aharoni, A., Kaftan, F., et al. (2016). Sample preparation for mass spectrometry imaging of plant tissues: A review. *Front. Plant Sci.* 7. doi: 10.3389/fpls.2016.00060

Boughton, B. A., Thinagaran, D., Sarabia, D., Bacic, A., and Roessner, U. (2016). Mass spectrometry imaging for plant biology: A review. *Phytochem. Rev.* 15, 445–488. doi: 10.1007/s11101-015-9440-2

Buscher, J. M., Czernik, D., Ewald, J. C., Sauer, U., and Zamboni, N. (2009). Cross-platform comparison of methods for quantitative metabolomics of primary metabolism. *Anal. Chem.* 81, 2135–2143. doi: 10.1021/ac8022857

Campbell, D. I., Ferreira, C. R., Eberlin, L. S., and Cooks, ,. R. G. (2012). Improved spatial resolution in the imaging of biological tissue using desorption electrospray ionization. *Anal. Bioanal. Chem.* 404, 389–398. doi: 10.1007/s00216-012-6173-6

Chen, W., Ma, Y., He, W., Wu, Y., Huang, Y., Zhang, Y., et al. (2022). Structure units oriented approach towards collective synthesis of sarpagine-ajmaline-koumine type alkaloids. *Nat. Commun.* 13, 908. doi: 10.1038/s41467-022-28535-x

Conceicao, R. S., Reis, I. M. A., Cerqueira, A. P. M., Perez, C. J., Junior, M., Branco, A., et al. (2020). Rapid structural characterisation of benzylisoquinoline and aporphine alkaloids from *Ocotea spixiana* acaricide extract by HPTLC-DESI-MS^n. *Phytochem. Anal.* 31, 711–721. doi: 10.1002/pca.2935

Cordell, G. A. (2013). Fifty years of alkaloid biosynthesis in phytochemistry. *Phytochemistry.* 91, 29–51. doi: 10.1016/j.phytochem.2012.05.012

Dilillo, M., Ait-Belkacem, R., Esteve, C., Pellegrini, D., Nicolardi, S., Costa, M., et al. (2017). Ultra-high mass resolution MALDI imaging mass spectrometry of proteins and metabolites in a mouse model of glioblastoma. *Sci. Rep.* 7, 603. doi: 10.1038/s41598-017-00703-w

Dutkiewicz, E. P., Su, C.-H., Lee, H.-J., Hsu, C.-C., and Yang, Y.-L. (2021). Visualizing vinca alkaloids in the petal of *Catharanthus roseus* using functionalized titanium oxide nanowire substrate for surface-assisted laser desorption/ionization imaging mass spectrometry. *Plant J.* 105, 1123–1133. doi: 10.1111/tpj.15092

Dyer, L. A., Dodson, C. D., Beihoffer, J., and Letourneau, ,. D. K. (2001). Trade-offs in antiherbivore defenses in piper cenocladum: ant mutualists versus plant secondary metabolites. *J. Chem. Ecol.* 27, 581–592. doi: 10.1023/a:1010345123670

Enomoto, H., Sato, K., Miyamoto, K., Ohtsuka, A., and Yamane, H. (2018). Distribution analysis of anthocyanins, sugars, and organic acids in strawberry fruits using matrix-assisted laser desorption/ionization-imaging mass spectrometry. *J. Agr. Food Chem.* 66, 4958–4965. doi: 10.1021/acs.jafc.8b00853

Facchini, P. J. (2001). Alkaloid biosynthesis in plants: biochemistry, cell biology, molecular regulation, and metabolic engineering applications. *Annu. Rev. Plant Physiol. Plant Mol. Biol.* 52, 29–66. doi: 10.1146/annurev.arplant.52.1.29

Freitas, J. R. L. E., Vendramini, P. H., Melo, J. O. F., Eberlin, M. N., and Augusti, R. (2019). Assessing the spatial distribution of key flavonoids in *Mentha* × *piperita* leaves: an application of desorption electrospray lonization mass spectrometry imaging (DESI-MSI). *J. Brazil. Chem. Soc* 30, 1437–1446. doi: 10.21577/0103-5053.20190039

Gao, L., Zhang, Z., Wu, W., Deng, Y., Zhi, H., Long, H., et al. (2022). Quantitative imaging of natural products in fine brain regions using desorption electrospray ionization mass spectrometry imaging (DESI-MSI): *Uncaria* alkaloids as a case study. *Anal. Bioanal. Chem.* 414, 4999–5007. doi: 10.1007/s00216-022-04130-3

Heskes, A. M., Sundram, T. C. M., Boughton, B. A., Jensen, N. B., Hansen, N. L., Crocoll, C., et al. (2018). Biosynthesis of bioactive diterpenoids in the medicinal plant *Vitex agnus-castus*. *Plant J.* 93, 943–958. doi: 10.1111/tpj.13822

Ifa, D. R., Srimany, A., Eberlin, L. S., Naik, H. R., Bhat, V., Cooks, R. G., et al. (2011). Tissue imprint imaging by desorption electrospray ionization mass spectrometry. *Anal. Methods* 3, 1910–1912. doi: 10.1039/c1ay05295k

Jeckel, A. M., Matsumura, K., Nishikawa, K., Morimoto, Y., Saporito, R. A., Grant, T., et al. (2020). Use of whole-body cryosectioning and desorption electrospray ionization mass spectrometry imaging to visualize alkaloid distribution in poison frogs. *J. Mass. Spectrom.* 55, 4520. doi: 10.1002/jms.4520

Jin, G. L., Su, Y. P., Liu, M., Xu, Y., Yang, J., Liao, K. J., et al. (2014). Medicinal plants of the genus *Gelsemium* (Gelsemiaceae, gentianales)-a review of their phytochemistry, pharmacology, toxicology and traditional use. *J. Ethnopharmacol.* 152, 33–52. doi: 10.1016/j.jep.2014.01.003

Kumara, P. M., Shaanker, R. U., and Pradeep, T. (2019). UPLC and ESI-MS analysis of metabolites of *Rauvolfia tetraphylla* l. and their spatial localization using desorption electrospray ionization (DESI) mass spectrometric imaging. *Phytochemistry.* 159, 20–29. doi: 10.1016/j.phytochem.2018.11.009

Lee, E. J., Hagel, J. M., and Facchini, ,. P. J. (2013). Role of the phloem in the biochemistry and ecophysiology of benzylisoquinoline alkaloid metabolism. *Front. Plant Sci.* 4. doi: 10.3389/fpls.2013.00182

Liao, Y., Fu, X., Zhou, H., Rao, W., Zeng, L., and Yang, Z. (2019). Visualized analysis of within-tissue spatial distribution of specialized metabolites in tea (*Camellia sinensis*) using desorption electrospray ionization imaging mass spectrometry. *Food Chem.* 292, 204–210. doi: 10.1016/j.foodchem.2019.04.055

Li, B., Ge, J. Y., Liu, W., Hu, D. J., and Ping, L. (2021). Unveiling spatial metabolome of *Paeonia suffruticosa* and *Paeonia lactiflora* roots using MALDI MS imaging. *New Phyto.* 231, 892–902. doi: 10.1111/NPH.17393

Li, B., Neumann, E. K., Ge, J. Y., Gao, W., Yang, H., Li, P., et al. (2018). Interrogation of spatial metabolome of *Ginkgo biloba* with high-resolution matrix-assisted laser desorption/ionization and laser desorption/ionization mass spectrometry imaging. *Plant Cell Environ.* 41, 2693–2703. doi: 10.1111/pce.13395

Liu, D., Han, Y., Zhou, H., Jin, H., Kang, H., Huang, F., et al. (2021). Offline preparative three-dimensional HPLC for systematic and efficient purification of alkaloids from *Gelsemium elegans* benth. *J. Chromatogr. A.* 1640, 461935. doi: 10.1016/j.chroma.2021.461935

Liu, Y. C., Lin, L., Cheng, P., Sun, Z. L., Wu, Y., and Liu, Z. Y. (2017a). Fingerprint analysis of gelsemium elegans by HPLC followed by the targeted identification of chemical constituents using HPLC coupled with quadrupole-time-of-flight mass spectrometry. *Fitoterapia.* 121, 94–105. doi: 10.1016/j.fitote.2017.07.002

Liu, D., Liu, Y., Shen, A., Li, X., Yu, L., Wang, C., et al. (2022). Analysis of alkaloids in *Gelsemium elegans* benth using an online heart-cutting + comprehensive RPLCxRPLC system tandem mass spectrometry. *Talanta.* 239, 123069. doi: 10.1016/j.talanta.2021.123069

Liu, M., Shen, J., Liu, H., Xu, Y., Su, Y. P., Yang, J., et al. (2011). Gelsenicine from *Gelsemium elegans* attenuates neuropathic and inflammatory pain in mice. *Biol. Pharm. Bull.* 34, 1877–1880. doi: 10.1248/bpb.34.1877

Liu, Y. C., Xiao, S., Yang, K., Ling, L., Sun, Z. L., and Liu, Z. Y. (2017b). Comprehensive identification and structural characterization of target components from gelsemium elegans by high-performance liquid chromatography coupled with quadrupole time-of-flight mass spectrometry based on accurate mass databases combined with MS/MS spectra. *J. Mass. Spectrom.* 52, 378–396. doi: 10.1002/jms.3937

Manicke, N. E., Wiseman, J. M., Ifa, D. R., and Cooks, R. G. (2008). Desorption electrospray ionization (DESI) mass spectrometry and tandem mass spectrometry (MS/MS) of phospholipids and sphingolipids: ionization, adduct formation, and fragmentation. *J. Am. Soc. Mass. Spectr.* 19, 531–543. doi: 10.1016/j.jasms.2007.12.003

Moreno-Pedraza, A., Rosas-Roman, I., Garcia-Rojas, N. S., Guillen-Alonso, H., Ovando-Vazquez, C., Diaz-Ramirez, D., et al. (2019). Elucidating the distribution of plant metabolites from native tissues with laser desorption low-temperature plasma mass spectrometry imaging. *Anal. Chem.* 91, 2734–2743. doi: 10.1021/acs.analchem.8b04406

Muller, T., Oradu, S., Ifa, D. R., Cooks, R. G., and Krautler, B. (2011). Direct plant tissue analysis and imprint imaging by desorption electrospray ionization mass spectrometry. *Anal. Chem.* 83, 5754–5761. doi: 10.1021/ac201123t

Nakabayashi, R., Hashimoto, K., Mori, T., Toyooka, K., Sudo, H., and Saito, K. (2021). Spatial metabolomics using imaging mass spectrometry to identify the localization of asparaptine a in *Asparagus officinalis*. *Plant Biotechnol. (Tokyo).* 38, 311–315. doi: 10.5511/plantbiotechnology.21.0504b

Ozkartal, T., Auricchio, A., and Conte, G. (2019). Ajmaline infusion during automated screening in brugada syndrome and spontaneous type 1 electrocardiogram unmasks non-suitability for subcutaneous implantable cardioverter-defibrillator. *Eur. Heart J.* 40, 1888–1889. doi: 10.1093/eurheartj/ehz049

Palla, G., Spitzer, H., Klein, M., Fischer, D., Schaar, A. C., Kuemmerle, L. B., et al. (2022). Squidpy: a scalable framework for spatial omics analysis. *Nat. Methods* 19, 171–178. doi: 10.1038/s41592-021-01358-2

Patrick, J. W., and Offler, C. E. (2001). Compartmentation of transport and transfer events in developing seeds. *J. Exp. Bot.* 52, 551–564. doi: 10.1093/jxb/52.356.551

Souza, J., Lourenco, H. M., and Mendes, G. (2017). Low-dose chemotherapy with methotrexate and vinblastine for desmoid tumors: a single institution experience. *Ann. Onco.* 28, 3528. doi: 10.1093/annonc/mdx387.022

Tocci, N., Gaid, M., Kaftan, F., Belkheir, A. K., Belhadj, I., Liu, B. Y., et al. (2018). Exodermis and endodermis are the sites of xanthone biosynthesis in *Hypericum perforatum* roots. *New Phytol.* 217, 1099–1112. doi: 10.1111/nph.14929

Tong, Q., Zhang, C., Tu, Y., Chen, J., Li, Q., Zeng, Z., et al. (2022). Biosynthesis-based spatial metabolome of *Salvia miltiorrhiza bunge* by combining metabolomics approaches with mass spectrometry-imaging. *Talanta.* 238, 123045. doi: 10.1016/j.talanta.2021.123045

Wang, L., Wang, J. F., Mao, X., Jiao, L., and Wang, X. J. (2017). Gelsedine-type oxindole alkaloids from *Gelsemium elegans* and the evaluation of their cytotoxic activity. *Fitoterapia.* 120, 131–135. doi: 10.1016/j.fitote.2017.06.005

Wu, V., Tillner, J., Jones, E., McKenzie, J. S., Gurung, D., Mroz, A., et al. (2022a). High resolution ambient MS imaging of biological samples by desorption electro-flow focussing ionization. *Anal. Chem.* 94, 10035–10044. doi: 10.1021/acs.analchem.2c00345

Wu, Z. H., Su, Y., Luo, Z. F., Sun, Z. L., Gong, Z. H., and Xiao, ,. L. T. (2022b). In situ visual distribution of gelsemine, koumine, and gelsenicine by MSI in *Gelsemium elegans* at different growth stages. *Molecules.* 27, 1810. doi: 10.3390/molecules27061810

Ye, Q., Feng, Y., Wang, Z., Zhou, A., Xie, S., Fan, L., et al. (2019). Effects of dietary *Gelsemium elegans* alkaloids on intestinal morphology, antioxidant status, immune responses and microbiota of *Megalobrama amblycephala*. *Fish. Shellfish. Immun.* 94, 464–478. doi: 10.1016/j.fsi.2019.09.048

Yen, T. C., Visvikis, D., Pan, T., and Fang, ,. Y. H. (2014). Biomedical imaging: role and opportunities of medical imaging in the "omics" era. *BioMed. Res. Int.* 2014, 930213. doi: 10.1155/2014/930213

Ziegler, J., and Facchini, ,. P. J. (2008). Alkaloid biosynthesis: metabolism and trafficking. *Annu. Rev. Plant Biol.* 59, 735–769. doi: 10.1146/annurev.arplant.59.032607.092730

frontiers | Frontiers in Plant Science

TYPE Original Research
PUBLISHED 16 December 2022
DOI 10.3389/fpls.2022.1083901

OPEN ACCESS

EDITED BY
Xiaodong Wang,
Minzu University of China, China

REVIEWED BY
Zongwei Cai,
Hong Kong Baptist University, Hong Kong SAR, China
Zhili Li,
Institute of Basic Medical Sciences, Chinese Academy of Medical Sciences and Peking Union Medical College, China

*CORRESPONDENCE
Song He
hes1224@163.com
Lei Guo
guolei@bmi.ac.cn

†These authors have contributed equally to this work

SPECIALTY SECTION
This article was submitted to Technical Advances in Plant Science, a section of the journal Frontiers in Plant Science

RECEIVED 29 October 2022
ACCEPTED 29 November 2022
PUBLISHED 16 December 2022

CITATION
Qin L, Han J, Wang C, Xu B, Tan D, He S, Guo L, Bo X and Xie J (2022) Key defatting tissue pretreatment protocol for enhanced MALDI MS Imaging of peptide biomarkers visualization in the castor beans and their attribution applications. *Front. Plant Sci.* 13:1083901. doi: 10.3389/fpls.2022.1083901

Key defatting tissue pretreatment protocol for enhanced MALDI MS Imaging of peptide biomarkers visualization in the castor beans and their attribution applications

Luyuan Qin[1†], Junshan Han[2†], Chuang Wang[1,3], Bin Xu[1], Deyun Tan[4], Song He[2*], Lei Guo[1*], Xiaochen Bo[2] and Jianwei Xie[1]

[1]State Key Laboratory of Toxicology and Medical Countermeasures, Institute of Pharmacology and Toxicology, Academy of Military Medical Sciences, Beijing, China, [2]Department of Bioinformatics, Institute of Health Service and Transfusion Medicine, Beijing, China, [3]Ministry of Education Key Laboratory of Ethnic Medicine, College of Pharmacy, Minzu University of China, Beijing, China, [4]Institute of Cash Crop Research, Zibo Academy of Agricultural Sciences, Zibo, China

Introduction: Castor bean or ricin-induced intoxication or terror events have threatened public security and social safety. Potential resources or materials include beans, raw extraction products, crude toxins, and purified ricin. The traceability of the origins of castor beans is thus essential for forensic and anti-terror investigations. As a new imaging technique with label-free, rapid, and high throughput features, matrix-assisted laser desorption ionization mass spectrometry imaging (MALDI-MSI) has been gradually stressed in plant research. However, sample preparation approaches for plant tissues still face severe challenges, especially for some lipid-rich, water-rich, or fragile tissues. Proper tissue washing procedures would be pivotal, but little information is known until now.

Methods: For castor beans containing plenty of lipids that were fragile when handled, we developed a comprehensive tissue pretreatment protocol. Eight washing procedures aimed at removing lipids were discussed in detail. We then constructed a robust MALDI-MSI method to enhance the detection sensitivity of RCBs in castor beans.

Results and Discussion: A modified six-step washing procedure was chosen as the most critical parameter regarding the MSI visualization of peptides. The method was further applied to visualize and quantify the defense peptides, Ricinus communis biomarkers (RCBs) in castor bean tissue sections from nine different geographic sources from China, Pakistan, and Ethiopia. Multivariate statistical models, including deep learning network, revealed a valuable classification clue concerning nationality and altitude.

KEYWORDS

castor beans, MALDI-MSI, tissue washing, peptide attribution markers, geographical origin

1 Introduction

As one of the top ten oil crops in the world, the castor oil plant, *Ricinus communis*, is originated in Africa and currently widely distributed in tropical, subtropical, and temperate regions worldwide (Polito et al., 2019). It has reached an industrial scale in more than 30 countries because of its high economic value. At least one million tons of castor beans are harvested and processed annually to prepare castor oil, a widely used raw material in mechanical and chemical industries, cosmetics, and pharmaceutical industries. However, castor bean contains a relatively high abundance of water-soluble toxic protein, ricin, which is easily extracted into aqueous solutions during castor oil production.

Due to easy preparation, strong concealment, vast source, and no specific antidote, ricin has had military, criminal and terrorist uses in history. It is one of the typical "culprits" in terror events or toxication incidents. A notorious case of intoxication was the death of Georgi Markov in 1978, and ricin was identified as the agent used for his assassination (Darby et al., 2001). In 2002, castor beans and the method for preparing ricin were discovered during a raid on terrorists in London. Since then, a series of ricin terror incidents have occurred. From 2012 to 2018, ricin letters were intermittently sent to the White House, causing great panic in the international community. Accidental oral ingestion or intentional poisoning *via* castor beans or defatted press cake fertilizer has occurred from time to time, either for human beings or livestock (Worbs et al., 2011; Aggarwal et al., 2017).

Castor beans, raw extraction products, crude toxins and purified ricin are all potential resources or materials in the intoxication or bioterror events left for forensic and anti-terrorism investigation. In response to the national security, public security, and clinical toxication caused by castor beans originating from varied resources and locations worldwide, the traceability of castor beans from different cultivars and geographic locations is a critical issue addressed.

How could we quickly obtain the proof of origin or accomplished cultivar identification when we deal with castor beans as one of the main pieces of evidence in forensic science? Peptide mass fingerprinting information of digested *Ricinus communis* extracts, or ricin, ricin agglutinin provided by MALDI-MS (Duriez et al., 2008) was a helpful approach. In addition to ricin itself, other characteristic components in castor beans are expected to provide an alternative way. For example, Darby et al. identified the alkaloid ricinine in castor beans as a co-existed substance with ricin based on liquid chromatography-mass spectrometry (LC-MS) and matrix-assisted laser desorption/ionization-time of flight mass spectrometry (MALDI-TOF MS) (Darby et al., 2001). Pigott et al. focused on analyzing the metabolome of castor beans for cultivar and provenance determination by ^{1}H-Nuclear magnetic resonance spectroscopy (Pigott et al., 2011). Therefore, the direct detection of low molecular weight biomarkers in castor beans may be a faster, more effective, and more reliable alternative method, which can aid in the cultivar and geographic source determination of castor beans (Vuckovic et al., 2016).

Besides ricin, ricinine, and the metabolomes, Ovenden (Ovenden et al., 2009) et al. identified three low molecular weight peptides in six different cultivars of castor beans by LC-MS and MALDI-MS, known as *Ricinus communis* biomarkers or RCBs, designated as RCB-1, -2, and -3, respectively. RCB-1 and RCB-2 were commonly found in varying amounts in six different cultivars, while RCB-3 was found only in the "*Carmencita*" cultivar. After that, Ovenden et al. identified RCB-4 and RCB-5 in the castor beans of the "*impala*" cultivar (Ovenden et al., 2014). Moreover, Fredriksson et al. (Fredriksson et al., 2018) developed a method for chemical analysis of forensic attribution markers related to the purification of ricin based on a complex set of biomarkers including carbohydrates, fatty acids, RCBs, ricin, etc. (Fredriksson et al., 2018). Compared with the toxic protein, peptides have better sensitivity and easier pretreatment due to their more straightforward structure. This previous research revealed the potential of RCBs as attribution biomarkers compounds in distinguishing the cultivars of castor beans. It inspires our interest in unveiling the inherent information of this series of peptides with more advanced and fully informative techniques.

Mass spectrometry imaging (MSI) is a label-free molecular imaging technique with simple sample preparation, which can identify molecular compositions in biological samples and visualize the spatial distribution of compounds *in situ* in tissue section and is a powerful non-targeted analysis tool. The most widely used ionization method in MSI is MALDI, a soft ionization mass spectrometry technique with less fragmentation, high spatial resolution, sensitivity, and imaging speed (Greco et al., 2018; Neagu et al., 2019). With the prosperous and continuous development, MALDI-MSI has been gradually applied in the field of plant research in recent years, such as revealing the spatial distribution of metabolites in *Clausena lansium* tissue sections (Tang et al., 2021) and *in situ* characterizing peptides in *Medicago truncatula* root nodules (Keller et al., 2020) as well as proteins in tomato (Bencivenni et al., 2014), etc. Recently, Sturtevant et al. revealed heterogeneous tissue distribution of mono-, di- and tri-hydroxy-triacylglycerols in the embryo and endosperm tissues of castor beans to understand better the regulation of triacylglycerol accumulation in oilseeds by MALDI-MSI (Sturtevant et al., 2019).

Many endogenous plant peptides can be served as significant markers of plant growth and development, defense responses, and symbiotic relationships with other species. It is hence increasingly necessary to reveal the role of endogenous peptides at the molecular level. Gemperline (Gemperline et al., 2016) et al. uncovered the spatial distribution of hundreds of endogenous peptides in different growth stages of legume

Medicago truncatula by MALDI-MSI. They speculated the transfer of endogenous peptides through the distribution differences in seedlings, mature roots, and nodules. It thus revealed the potential of MALDI-MSI towards endogenous plant peptide markers.

In MALDI-MSI, the optimization of sample preparation is the most crucial step to ensure high sensitivity, high spatial resolution, high-quality signal, and intensity. However, compared to animal tissues, sample preparation approaches are more challenging for plant tissues due to the inherent features of plants, especially for some lipid-rich, water-rich, or fragile plant tissues. Therefore, developing a specific optimized sample preparation protocol is essential for MALDI-MSI detection of peptides in plants, such as obtaining a uniform matrix spray effect and optimizing washing steps. Several works have confirmed that the action of washing sections with organic solvents, such as ethanol, isopropanol, toluene, xylene, and chloroform, etc., prior to matrix application and MALDI-MSI is effective to remove plenty of the lipids and salts, thereby increasing the intensity of peptides and proteins (Goodwin et al., 2008; Thomas et al., 2013; Buchberger et al., 2020; Vu et al., 2021). But most of them focused on animal tissue sections, and no reports on lipid removal from lipid-rich plant tissue sections can be found. Therefore, the washing protocol for lipid removal should be thoroughly investigated for this type of sample.

In this paper, we proposed a systematic sample preparation protocol for castor beans containing plenty of lipids, and their tissue sections were fragile when handled. The washing protocols of lipid removal were focused on, with the aid of staining and MSI visualization of peptides. A modified six-step washing procedure was finally chosen among all eight measures to remove lipids as much as possible. We then constructed a MALDI-MSI method to enhance the detection sensitivity of defense peptides, RCB-1, RCB-2, and RCB-3, in castor beans. We further established a stable isotope internal standard (IS) quantitative method of MALDI-MSI to determine the content of RCBs in castor beans. Moreover, regarding the distribution of different geographic sources revealed by the defatted MSI signals in castor beans, we employed several statistical and classification tools to unravel their characteristics. We hope this work will provide a new research perspective for the traceability of castor bean relevant events of castor bean intoxication.

2 Materials and methods

2.1 Reagents and materials

2,5-dihydroxybenzoic acid (DHB) and α-Cyano-4-hydroxycinnamic Acid (CHCA) were purchased from Brucker Daltonik GmbH (Bremen, Germany). Sodium salt of carboxy methyl cellulose (CMC-Na) was purchased from Sigma-Aldrich Co. (USA). Acetonitrile (ACN), methanol, ethanol, isopropanol, methylbenzene, dimethylbenzene, and trifluoroacetic acid (TFA) were obtained from Merck (Melbourne, Australia). Peptide calibration standard II (pep II), designed for calibration in a low mass range between 700 and 3200 Da, was purchased from Brucker Daltonik GmbH (Bremen, Germany). Standard peptides of RCB-1, RCB-2, and RCB-3 were synthesized by Sangon Biotech with a HPLC purity of 98.9% (Shanghai, China). Stable-isotopically labeled internal standard (SILIS) of RCB-2 was synthesized by Synpeptide Co. (Nanjing, China), the carbon and nitrogen atoms in the twelfth phenylalanine in the amino acid sequence were labeled ($^{13}C_9{}^{15}N_1$-RCB-2). All reagents and solvents used in this work were of analytical grade or higher. Ultrapure water was generated by a Milli-Q A10 water purification system (Millipore, MA, USA).

Resistance conductive indium tin oxide (ITO)-coated microscope glass was purchased from Brucker Daltonik GmbH (Bremen, Germany). Oil Red O Staining Kit was purchased from Beyotime (Shanghai, China). The castor beans (*Ricinus communis*) originated from Beijing, Xinjiang Uygur Autonomous Region, Hebei, Shanxi, Inner Mongolia Autonomous Region, and Sichuan provinces in China were purchased from the local medicine markets. The castor beans originated from Shandong (commercial brand Zibi No. 9), Ethiopia in Africa, and Pakistan in Asia were kindly provided by Zibo Academy of Agricultural Sciences. The species of castor beans were identified by Prof. Deyun Tan.

2.2 Instruments

Autoflex III MALDI TOF/TOF MS instrument (Bruker Daltonik, Germany), in which a Smartbeam 3D Nd: YAG (355 nm) at a frequency of 200 Hz was mounted, FlexControl 3.4 software for acquisition, and FlexImaging 4.1 for MSI data collection (Bruker Daltonik, Germany). Cryostat sectioning was performed in a CM 1950 cryostat (Leica, Germany), and optical scanning was finished with a Perfection V370 scanner (EPSON, Japan). The matrix spraying or coating was performed in a GET-Sprayer (Beijing Huayi Innovation &Biotechnology Co., Beijing, China).

2.3 Sample preparation

A sample preparation optimization procedure was carried out, including matrix solution composition, tissue washing and matrix coating. The sample was visually evaluated after each step of sample preparation with the CCD camera inside the Autoflex III MALDI-MS during MSI measurements.

2.3.1 Tissue sectioning

The castor beans were peeled to remove the outer seed coat and then embedded in the prepared 4% CMC-Na solution. The CMC-Na-embedded seeds were frozen at -20°C for five days

before sectioning. Seeds were cryo-sectioned at -30°C into 20 µm thickness and immediately thaw-mounted on the conductive sides of ITO-coated microscope glass slides. The slides were dried under a vacuum for 20 minutes and stored at -80°C.

2.3.2 Washing protocol

Before matrix coating, tissue sections were submerged into 20 mL of freshly prepared washing solvents for the time indicated in the specific protocol to remove lipids. Altogether, eight washing protocols were evaluated, and a "no wash" procedure was used as a negative control.

2.3.3 Optimization of matrix solution composition

The concentration of CHCA, ACN, and TFA were the variables selected to be optimized for the matrix solution composition. The appropriate range of the three variables was determined based on the results of the single factor experiment. The box-Behnken design combined with response surface methodology (RSM) was performed to optimize the optimal CHCA matrix solutions for RCBs. Experimental design and result analysis were finished using Design-Expert 13.0.1.0 (Stat-Ease, Inc., Minneapolis, MN, USA).

2.3.4 Matrix coating and optimization

Tissue section slices were evenly sprayed with CHCA matrix solutions using a GET-Sprayer. In the GET-Sprayer device, a high-voltage power source was added between the matrix solution sprayer system and the tissue section to form a strong formation between the spray needle and the conductive glass slide to obtain a uniformly distributed matrix coating effect. An orthogonal experimental design method was performed to establish the optimized matrix spraying conditions, in which the factors included air pressure, spraying flow rate, and spraying time.

2.4 MALDI-MSI analysis

Before MALDI-MSI, the instrument was calibrated by spotting the pep II calibration standard onto the matrix-coated ITO glass slide. All the mass spectra were automatically acquired over a mass range of m/z 1000 to 4000 in the positive reflection mode. Laser shots of 400 times were accumulated at one raster position and a raster step size of 100 µm.

2.5 Quantification of RCBs

For quantitative determination, a series of concentrations of RCB-1 to RCB-3 peptide standard mixture, including 100, 200, 500, 1000, and 5000 µg/L, were prepared in 50% ACN. Before matrix application, 1 µL of each of these solutions were deposited onto the blank area of the ITO slide around the tissue and air-dried. Aliquots of 500 µg/L SILIS of RCB-2 were uniformly mixed with CHCA matrix and then sprayed on the tissue sections and ITO slide. Calibration curves were generated by plotting the average intensity ratio of the major $[M+H]^+$ ion of RCB-1 (m/z 2066.95), RCB-2 (m/z 1979.92), RCB-3 (m/z 1961.96) to the intensity of major $[M+H]^+$ ion of $^{13}C_9{}^{15}N_1$-RCB-2 (m/z 1989.92) versus the concentration of RCB-1 to 3 applied to the ITO slide (3 microspots for each concentration). Finally, the concentrations of RCBs in tissue sections from different origins were calculated by calibration curves.

2.6 Data reprocessing and multivariate statistical analysis

Phenotypes of five important agronomic traits of castor beans of nine geographical origins, including hundred-grain weight (one hundred random seeds for weighing were randomly selected), seed length (five seeds with the same size were randomly selected, the total length of five seeds head to tail were measured and the average value was taken), seed width (five seeds with the same size were randomly selected, the total length of five seeds from left to right were measured and the average value was taken), seed size (the seed length times the seed width was calculated as an index represented the overall size of the seed), and seed plumpness (the grain weight divided by the size, an index represented the character of the heaviness of seed endosperm) were statistically analyzed by GraphPad Prism 9.0.0. The violin plot was drawn to visually compare the phenotype and regional features of castor beans from different geographical sources. The dimension reduction of five agronomic traits data of castor bean samples from nine geographical origins was analyzed using the principal component analysis (PCA) model in OriginPro 2021 (OriginPro Co., USA).

The MSI data was visualized using FlexImaging v.4.1. Afterwards, the data were reprocessed and analyzed by SCiLS Lab version 2016b (Bruker, Germany), in which the normalization was performed based on the total ion count, and the PCA was applied for unsupervised analysis. The number of principal components was the minimum, with a cumulative contribution rate greater than 90%.

All MSI data were further analyzed by deep neural network (DNN, Spyder-python 3.9), in which the dual-channel DNN model was used to train the MSI data from nine different geographical sources for supervised analyses, including two types of characteristics, peak intensity and pixel position on tissue sections. The total sample data were obtained by summarizing the MSI data from nine different geographical sources and aligning the mass spectra peaks. All data were split into training, validation, and test sets at the ratio of 8:1:1,

and the accuracy rate was used as the performance evaluation index. In the dual-channel DNN model, the total dimension of all features was 2065, the number of neurons in hidden layers of the sub-network where the peak intensity features were located was 512 and 256, and the number of neurons in output layer was 128. The number of neurons in hidden layers of the sub-network where the pixel features were located was 256 and 64, and the number of neurons in output layer was 1. After concatenating the outputs of the two sub-networks a 129-dimensional vector, which was then fed into a two-layer fully connected network (the third sub-networks) was obtained, and the number of neurons in the output layer was 9. The activation function was the ReLU function. Dropout and BatchNorm2d regularization were used to help prevent overfitting of the training. The loss function was the cross-entropy loss function, and the batch size was 10. Finally, the Shapley Additive explanations (SHAP) were used to interpret the classification results of the dual-channel DNN model. The core idea of SHAP was to calculate the marginal contribution of features to the model output. Distributed stochastic neighbor embedding (t-SNE) model was used to reduce the dimension of the output of the first layer of the fully connected network (the third sub-networks).

3 Results and discussion

3.1 Sample preparation

3.1.1 Tissue sectioning

Note that the successful preparation of tissue sections is the first step but the most key parameter in imaging analysis. However, cryosection of fragile and high lipid plant tissues is quite challenging, and we should take care to avoid a critical loss of morphological features and delocalization (Li et al., 2018). The investigated objects in this work are the castor beans, which are presented as plant seeds with high lipid content, it is prone to curling and adhesion during the preparation of frozen tissue sections. Therefore, according to experience, 4% CMC-Na was used as embedding media to give adequate sample support and maintain tissue section morphology during cryo-sectioning. In addition, we found that for these lipid-rich plant seeds, entirely freezing the sample before slicing facilitated the preparation of topographically intact slices while keeping the blade temperature at -30 °C or lower. Finally, we prepared the castor bean sections with a thickness of 20 μm and intact tissue morphology.

3.1.2 Effect of matrix solution composition on MSI

We firstly compared two most common matrices, DHB and CHCA for peptide measurement in MALDI and MALDI-MSI (Blutke et al., 2020) in the preliminary experiments. We chose CHCA as the matrix instead of DHB because had shown that CHCA was better than DHB in the detection of RCBs for providing stronger intensity and uniform crystallization (data not shown). Considering that the optimization of CHCA matrix solution composition for RCBs is necessary for good profiling and imaging data acquisition, we adopted RSM, the most relevant multivariate technique, for this analytical optimization. It describes the behavior of data sets to make accurate statistical previsions (Bezerra et al., 2008). Hereby we designed three experimental variables, including the concentration of CHCA, ACN, and TFA, respectively, to determine the optimized condition *via* RSM. According to the appropriate range of CHCA, ACN, and TFA concentration determined as 3~10 mg/mL, 50%~90%, and 0.1%~0.5%, respectively, by single factor experiment (Supplemental Figure S1A), the levels and actual values of parameters were settled (Table S1).

Experimental and predicted results of 17 randomized runs for selected responses obtained under different experimental conditions were presented in Table S2. It is shown that the predicted intensity values of RCB-1 to RCB-3 well matched the experimental results. Analysis of variance (ANOVA) for the response surface quadratic model of RCB-2 was adopted to assess the statistical significance of model coefficients. The significant model ($p<0.05$) and the non-significant lack of fit ($p>0.05$) validated the adequacy of the model that can be used for the optimization of the matrix solution composition (Table S3). ANOVA for the response surface quadratic model of RCB-1 and RCB-3 was also performed, and the influence of parameters was almost similar. The three-dimensional response plots and contour plots of RCB-1 to RCB-3 showed the interactive effect of investigated three variables (Supplemental Figures S1B–D). The optimized combination was finally set as 9 mg/mL CHCA dissolved in 90% aqueous ACN containing 0.1% TFA.

3.1.3 Effect of matrix coating on MSI

In addition to matrix solution optimization, matrix coating for homogeneous matrix crystals is critical to obtain high-quality MALDI-MSI results. Among all matrix coating methods such as spray gun, sublimation, vibration spray, and electrospray ways, electrospray can offer a good atomization effect with excellent fine particle sizes. Wang et al. developed a matrix coating approach assisted by an electric field, which significantly improved the intensity of lipids, peptides, and proteins compared with vibration spray and sprayer gun and obtained good imaging spectra (Wang et al., 2015; Wang et al., 2016; Wang et al., 2017). Guo et al. developed an electric field-assisted scanning-spraying (EFASS) matrix coating system to deposit matrix on tissue with crystal sizes of less than 10 μm (Guo et al., 2015). Compared with airbrush and sublimation, the EFASS system could effectively enhance detection sensitivity and allow for uncovering more analytes in the tissue section.

We employed EFASS to ensure a uniform matrix spraying effect in this work. Three parameters, the nitrogen pressure, the spraying velocity, and the spraying time, were optimized by an

orthogonal design of three factors at three levels (Figure 1; Table S4). The primary and secondary dominants were spraying velocity and spraying time. The optimized parameters combination were the nitrogen pressure, 0.3 MPa, and the spraying velocity, 10 µL/min, and the spraying time, 15 min. Coating one tissue section of ca. 35 mm^2 × 65 mm^2 each time costs 150 µL of the matrix solution.

3.1.4 Effect of washing protocol on MSI

The most delicate sample preparation step in MSI is tissue washing, which can directly alter the quantity of analytes in the sample and thus significantly change the spatial distribution. The current washing protocols are usually needed to be specifically designed based on the characteristics of the analyte and each type of tissue in MSI (Goodwin, 2012). According to the experimental knowledge from animal tissue sections ((Lemaire et al., 2006; Thomas et al., 2013), the organic solvents commonly used for washing are ethanol and isopropanol (Goodwin et al., 2008; van Hove et al., 2011). For example, Buchberger (Buchberger et al., 2020) et al. used seven different proportions of ethanol to water to optimize the washing protocol in crustacean brain tissue sections. The results showed that using 50% ethanol to wash sections for 10 s was the best washing condition. After washing, the intensity of 34 neuropeptides has been improved. Maslov et al. (Rešetar Maslov et al., 2019) systematically optimized 17 washing protocols for the MALDI-MSI analysis of peptides in dry-cured ham samples. When isopropanol was used for gradient elution, it effectively removed salt and fat and improved the intensity of peptides. In addition, it obviously improved the "sweet spot" effect of the matrix, increased the uniformity of the matrix, and obtained better MSI data.

To our knowledge, only one work reported the effect of organic solvents washing on MALDI-MSI analysis in plant tissues. Recently, Sun et al. significantly improved the sensitivity and coverage of metabolites in *Salvia miltiorrhiza Bge* by using acetone as a simple organic washing protocol in MALDI-MSI (Sun et al., 2020). The lipid removal effect of organic solvents washing on MALDI-MSI analysis of peptides in lipid-rich plant tissue sections has not been explored yet. Herein we investigated the washing protocol for defatting in detail for castor beans for the first time as a plant tissue material containing about 60% lipids.

In this paper, we selected and thoroughly discussed eight different washing protocols based on their known efficacy for lipid removal from the literature (Seeley et al., 2008; Deutskens et al., 2011; Yang and Caprioli, 2011; Rešetar Maslov et al., 2019) or with slight modification to reduce high-abundant lipid components and increase the intensity of peptide ions. Meanwhile, we introduced the Oil Red O staining method to visualize and monitor the lipid removal efficiency after the washing step. The dye Oil Red O is highly soluble in lipids

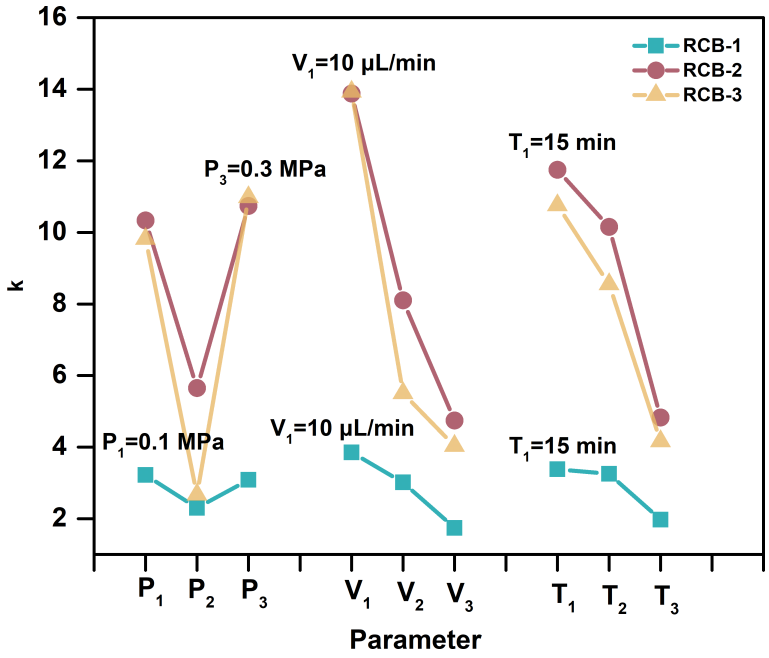

FIGURE 1
The optimization of the EFASS parameters by an orthogonal design of three factors and three levels. The Nitrogen pressure was 0.1 MPa, 0.2 MPa, and 0.3 MPa. The spraying velocity was 10 µL/min, 20 µL/min, and 30 µL/min, and the spraying time was 15 min, 30 min, and 45 min, respectively.

and can specifically mark the lipid in the tissue as red or orange-red color. This staining method has already been commonly used in pathological diagnosis to display the lipid in the tissue but has not been applied to the MALDI-MSI technique.

As shown in Figure 2, tissue sections were bright red in color for the "no wash" control (protocol A). In the average mass spectrum of MALDI-MSI, hundreds of peaks with high intensity in the range of m/z 1000~1200 were observed, while the intensity of RCBs in the range of m/z 1900~2100 was relatively low. We exported peaks in the range of m/z 1000~1200, up to 536 peaks, to LIPID MAPS database (https://lipidmaps.org) with a selection of fatty acyls, glycerolipids, glycerophospholipids, sphingolipids, sterol lipids ions ($[M+H]^+$, $[M+Na]^+$ and $[M+K]^+$) for retrieval, and preliminarily matched 183 results, of which 30 peaks with strong intensity were marked in Figure 3. All the matching results were summarized in Table S5 and the main matching results of 30 peaks were summarized in Table 1. These lipids may mainly be triacylglycerols, fatty esters, fatty acids, glycerophosphocholines, and phosphosphingolipids.

We then performed tissue washing with different organic solvents for salts and lipids removal (protocol B~I), including ethanol, isopropanol, chloroform, and xylene, in a stepwise way with a single kind or mixture form in different ratios. The commonly used organic solvent for removing salts and lipids was ethanol. For example, Yang et al. washed the tissue section first with 70% ethanol for 30 s and then with 100% ethanol for 30 s towards the rat brain tissue section (Yang and Caprioli, 2011). We evaluated this same washing protocol as protocol B. However, it did not significantly increase the intensity of RCBs while the red color was still maintained. In lieu of isopropanol in the same washing procedure provided a slight improvement in increasing the intensity of RCBs with a negligible defatting effect (protocol C).

Chloroform has a higher hydrophobility than ethanol and isopropanol, which was often used for lipid extraction. Carnoy's solution, constituted by 60% *(v/v)* ethanol, 30% *(v/v)* chloroform, and 10% *(v/v)* glacial acetic acid, has been applied to the washing procedure to remove lipids in the MALDI-MSI experiment on dry-cured ham (Rešetar Maslov et al., 2019) and rat brain tissue section (Deutskens et al., 2011), and has achieved good effect. We also introduced this Carnoy's solution to our protocol D. The tissue was firstly rinsed with 70% ethanol followed by 100% ethanol to fix the section, which is a standard step used in classical histology, then applied with Carnoy's solution to remove most of the lipids from the section, followed by washing with 100% ethanol to remove the remaining chloroform from Carnoy's solution. Next, 0.1% TFA aqueous solution removed salts, and a final step of 100% ethanol removed excess water. This washing protocol significantly increased the intensity of RCBs with a greatly reduced red color in a tissue section stained with Oil Red O. Besides, we found that Carnoy's solution has a positive effect on maintaining the intact morphology of the fragile plant tissue sections in the process of tissue washing.

Similarly, ethanol was replaced with isopropanol in protocol E, which offered the most significant result in significantly reduced red color under Oil Red O staining. A high-quality RCBs distribution profile was shown in the images of MSI based on the average mass spectrum of strong RCBs signals. It indicated that, unlike animal tissue sections, isopropanol might be more conducive to lipid removal and peptide intensity enhancement in plant tissues than ethanol.

It was critical to strictly control the washing time in the process of tissue washing (Buchberger et al., 2020), and we further investigated the effect of washing duration on increasing the intensity of peptide in castor bean tissue sections based on the protocol E. When each washing step was lengthened to 60 s in protocol F, we found no significant difference in comparison with 30 s-interval (protocol E) but with a potential risk of delocalization of analytes. While each washing step only lasted 15 s (protocol G), the lipid removal was insufficient, as shown in darkening MSI images and decreased average intensity.

It has been reported that the alternative use of ethanol and xylene mixture achieved good dehydration and defatting effects in treating fat-rich tissues in pathology (Ding et al., 2019). Here we designed and tested another two protocols containing this kind of mixed reagents. Firstly, we consequentially applied 70% ethanol and 50% ethanol-50% xylene mixture to dehydrate the tissue sections of the castor bean. Because xylene is insoluble in water, it was used after dehydration treatment to dissolve the fat rapidly. Afterward, we added a single step of 100% ethanol (in protocol H) or further followed by Carnoy's solution (in protocol I) to simultaneously amend the effect of dehydration and defatting, but neither protocol worked well. It suggested the introduction of xylene to defat the plant tissue section was not so ready and ideal. Finally, we determined that protocol E (Successively washing with 70% isopropanol, 100% isopropanol, Carnoy's solution, 100% isopropanol, 0.1% TFA, and 100% isopropanol for 30 s, respectively) was the optimized condition for MALDI-MSI analysis of RCBs and other peptides.

In addition, we also roughly determined the recovery of RCBs by using the single point correction method to demonstrate the efficiency of the optimized washing protocol E. A mixed standard solution of 0.5 mg/L RCB-1, -2,-3 (containing 0.5 mg/L $^{13}C_9{}^{15}N_1$-RCB-2 as IS) was prepared to calculate the concentration of all samples. Towards adjacent tissue sections from Xinjiang, in which three consecutive tissue sections in parallel on one ITO slide, the consecutive washing solutions in six steps were separately collected and concentrated to 1 mL, and then 0.5 mg/L $^{13}C_9{}^{15}N_1$-RCB-2 were added as IS for MALDI-MS determination. Considering that the single tissue section area from Xinjiang is about 50 mm^2, the thickness is 20 µm, and the density is regarded as 1 mg/mm^3, therefore, its weight is 1 mg. The recovery of RCBs should be calculated as the lost content divided by the total content of RCBs in 1 mg tissue.

For the estimation of total content of RCBs in 1 mg tissue, we treated 100 mg castor bean homogenate with 1 mL of 50%

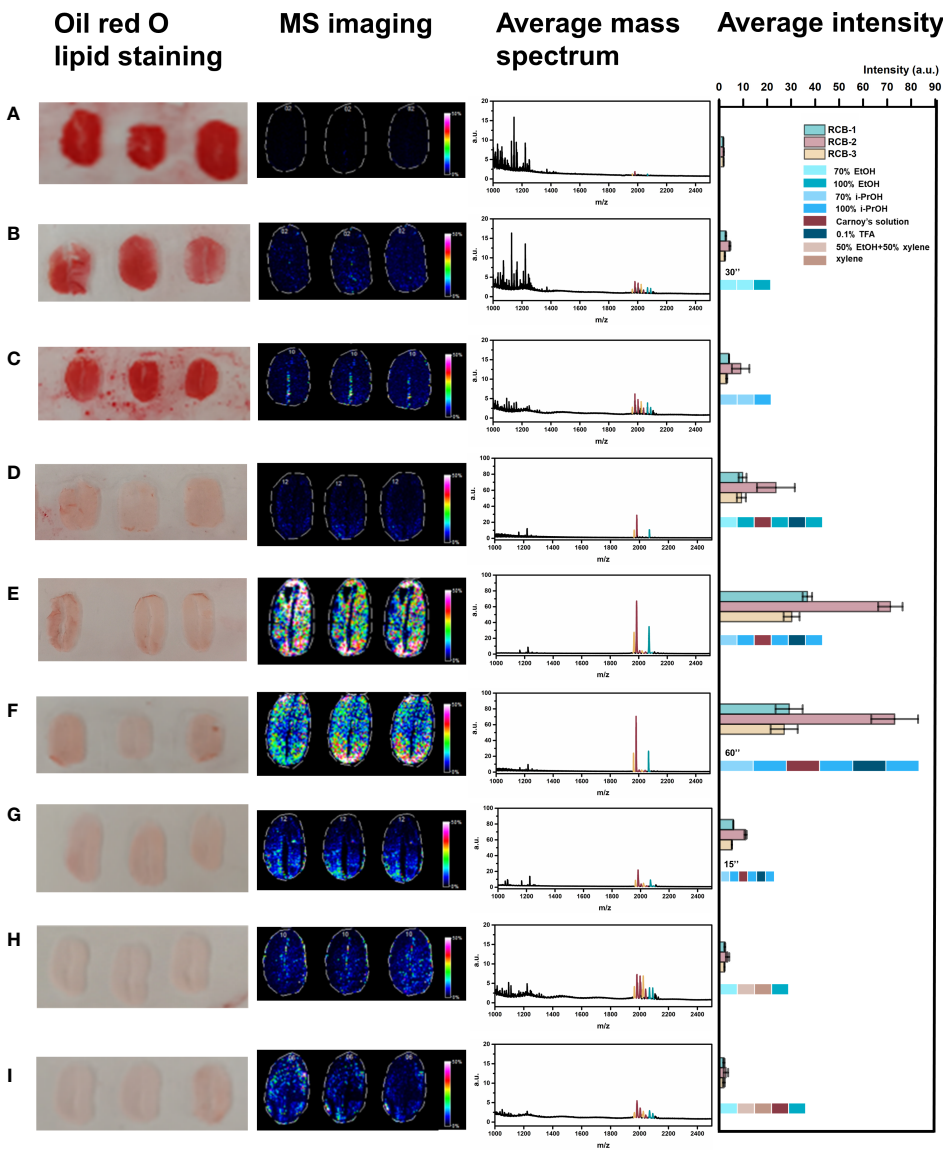

FIGURE 2
Comparison of different washing protocols. **(A)** No wash; **(B)** Wash with 70% ethanol, 70% ethanol, 100% ethanol for 30 s, respectively; **(C)** Wash with 70% isopropanol, 70% isopropanol, 100% isopropanol for 30 s, respectively; **(D)** Wash with 70% ethanol, 100% ethanol, Carnoy's solution,* 100% ethanol, 0.1%TFA, 100% ethanol for 30 s, respectively; **(E)** Wash with 70% isopropanol, 100% isopropanol, Carnoy's solution, 100% isopropanol, 0.1%TFA, 100% isopropanol for 30 s, respectively; **(F)** Wash with 70% isopropanol, 100% isopropanol, Carnoy's solution, 100% isopropanol, 0.1%TFA, 100% isopropanol for 60 s, respectively; **(G)** Wash with 70% isopropanol, 100% isopropanol, Carnoy's solution, 100% isopropanol, 0.1%TFA, 100% isopropanol for 15 s, respectively; **(H)** Wash with 70% ethanol, 1:1(v/v) mixture of ethanol and xylene, xylene, 100% ethanol for 30 s, respectively; **(I)** Wash with 70% ethanol, 1:1(v/v) mixture of ethanol and xylene, xylene, Carnoy's solution, 100% ethanol for 30 s, respectively. *(*Carnoy's solution= 60% (v/v) ethanol, 30% (v/v) chloroform, 10% (v/v) glacial acetic acid).*

ACN:0.1% TFA aqueous solution to avoid content derivation from a single tissue section and would adopt an average value in the calculation (detailed in Supplementary experimental). The results showed that RCBs were only slightly lost in step five (0.1% TFA washing) and step six (100% isopropanol washing). The recoveries of RCB-1 to 3 were 95.9%, 88.2%, and 90.3%, respectively (Figure S2). It indicated that the current optimized washing protocol E can maintain and expose the largest amount of target RCB peptides toward castor bean tissues.

Meanwhile, since that it is hard to observe RCBs without tissue washing, we can not directly judge the components drift by comparing the distribution before and after washing. We regard that this tissue washing protocol may not cause components drift, or the range of drift is very small. First,

10.3389/fpls.2022.1083901

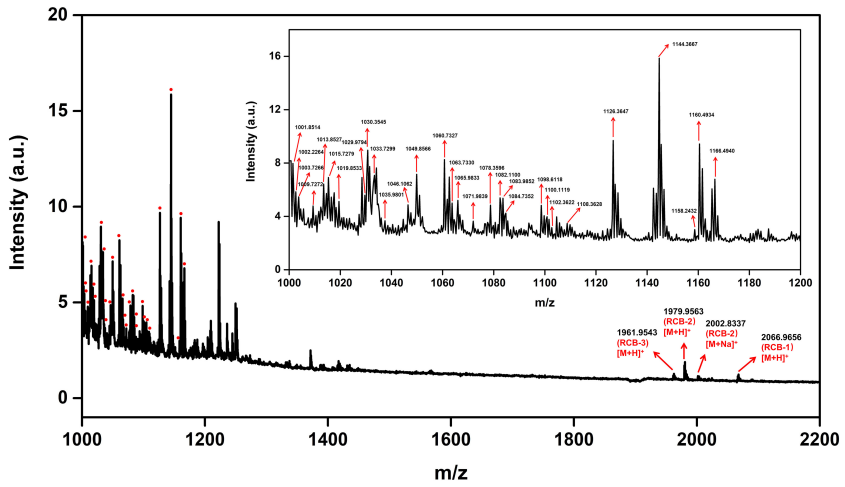

FIGURE 3
Average mass spectrum of tissue sections "no wash." The red dot indicates the annotated lipid.

TABLE 1 LIPID MAPS database matching results.

Input Mass	Matched Mass	Delta	Name	Formula	Ion
1001.8514	1001.8532	0.0018	TG 63:8	$C_{66}H_{112}O_6$	$[M+H]^+$
1001.8514	1001.8508	0.0006	TG 61:5	$C_{64}H_{114}O_6Na$	$[M+Na]^+$
1002.2264	1002.2093	0.0171	CoA 11:2; O3	$C_{32}H_{52}N_7O_{20}P_3SNa$	$[M+Na]^+$
1002.2264	1002.2247	0.0017	CoA 12:1; O	$C_{33}H_{56}N_7O_{18}P_3SK$	$[M+K]^+$
1002.2264	1002.2611	0.0347	CoA 13:0	$C_{34}H_{60}N_7O_{17}P_3SK$	$[M+K]^+$
1003.7266	1003.7749	0.0483	TG 64:14	$C_{67}H_{102}O_6$	$[M+H]^+$
1003.7266	1003.7725	0.0459	TG 62:11	$C_{65}H_{104}O_6Na$	$[M+Na]^+$
1003.7266	1003.7151	0.0115	TG 61:12	$C_{64}H_{100}O_6K$	$[M+K]^+$
1009.7272	1009.7621	0.0349	TG 61:9	$C_{64}H_{106}O_6K$	$[M+K]^+$
1013.8527	1013.8532	0.0005	TG 64:9	$C_{67}H_{112}O_6$	$[M+H]^+$
1013.8527	1013.8508	0.0019	TG 62:6	$C_{65}H_{114}O_6Na$	$[M+Na]^+$
1013.8527	1013.8873	0.0346	TG 60:0	$C_{63}H_{122}O_6K$	$[M+K]^+$
1015.7279	1015.7725	0.0446	TG 63:12	$C_{66}H_{104}O_6Na$	$[M+Na]^+$
1015.7279	1015.7151	0.0128	TG 62:13	$C_{65}H_{100}O_6K$	$[M+K]^+$
1019.8533	1019.9001	0.0468	TG 64:6	$C_{67}H_{118}O_6$	$[M+H]^+$
1019.8533	1019.8977	0.0444	TG 62:3	$C_{65}H_{120}O_6Na$	$[M+Na]^+$
1019.8533	1019.8038	0.0495	TG 63:10	$C_{66}H_{108}O_6Na$	$[M+Na]^+$
1019.8533	1019.8403	0.0130	TG 61:4	$C_{64}H_{116}O_6K$	$[M+K]^+$
1029.9794	1029.9784	0.0010	TG 64:1	$C_{67}H_{128}O_6$	$[M+H]^+$
1030.3545	1030.3522	0.0023	CoA 18:2	$C_{39}H_{66}N_7O_{17}P_3S$	$[M+H]^+$
1030.3545	1030.3134	0.0411	CoA 15:0; O	$C_{36}H_{64}N_7O_{18}P_3SNa$	$[M+Na]^+$
1033.7299	1033.7621	0.0322	TG 63:11	$C_{66}H_{106}O_6K$	$[M+K]^+$
1035.9801	1035.9314	0.0487	TG 65:5	$C_{68}H_{122}O_6$	$[M+H]^+$
1046.1062	1046.0824	0.0238	FA 70:0; O2	$C_{70}H_{140}O_4$	$[M+H]^+$
1049.8566	1049.8508	0.0058	TG 65:9	$C_{68}H_{114}O_6Na$	$[M+Na]^+$
1049.8566	1049.8873	0.0307	TG 63:3	$C_{66}H_{122}O_6K$	$[M+K]^+$
1060.7327	1060.6907	0.0420	MIPC 40:0; O4	$C_{52}H_{102}NO_{18}P$	$[M+H]^+$
1063.7330	1063.7151	0.0179	TG 66:17	$C_{69}H_{100}O_6K$	$[M+K]^+$

(Continued)

TABLE 1 Continued

Input Mass	Matched Mass	Delta	Name	Formula	Ion
1065.9833	1065.9760	0.0073	TG 65:1	$C_{68}H_{130}O_6Na$	$[M+Na]^+$
1071.9839	1072.0042	0.0203	CE 46:3; O2	$C_{73}H_{130}O_4$	$[M+H]^+$
1078.3596	1078.3522	0.0074	CoA 22:6	$C_{43}H_{66}N_7O_{17}P_3S$	$[M+H]^+$
1078.3596	1078.3497	0.0099	CoA 20:3	$C_{41}H_{68}N_7O_{17}P_3SNa$	$[M+Na]^+$
1078.7346	1078.7141	0.0205	MIPC 42:0; O2	$C_{54}H_{106}NO_{16}PNa$	$[M+Na]^+$
1082.1100	1082.0800	0.0300	FA 71:0; O2	$C_{71}H_{142}O_4Na$	$[M+Na]^+$
1083.9852	1083.9655	0.0197	TG 65:0	$C_{68}H_{132}O_6K$	$[M+K]^+$
1084.7352	1084.7635	0.0283	MIPC 44:0; O2	$C_{56}H_{110}NO_{16}P$	$[M+H]^+$
1084.7352	1084.7131	0.0221	PC 56:12	$C_{64}H_{104}NO_8PK$	$[M+K]^+$
1098.6118	1098.6466	0.0348	MIPC 40:0; O4	$C_{52}H_{102}NO_{18}PK$	$[M+K]^+$
1100.1119	1100.1294	0.0175	FA 74:1; O2	$C_{74}H_{146}O_4$	$[M+H]^+$
1102.3622	1102.4097	0.0475	CoA 22:2; O	$C_{43}H_{74}N_7O_{18}P_3S$	$[M+H]^+$
1102.3622	1102.3497	0.0125	CoA 22:5	$C_{43}H_{68}N_7O_{17}P_3SNa$	$[M+Na]^+$
1102.3622	1102.3499	0.0123	CoA 19:0; O	$C_{40}H_{72}N_7O_{18}P_3SK$	$[M+K]^+$
1108.3628	1108.3991	0.0363	CoA 24:5	$C_{45}H_{72}N_7O_{17}P_3S$	$[M+H]^+$
1108.3628	1108.3967	0.0339	CoA 22:2	$C_{43}H_{74}N_7O_{17}P_3SNa$	$[M+Na]^+$
1126.3647	1126.4073	0.0426	CoA 22:1; O	$C_{43}H_{76}N_7O_{18}P_3SNa$	$[M+Na]^+$
1126.3647	1126.3497	0.0150	CoA 24:7	$C_{45}H_{68}N_7O_{17}P_3SNa$	$[M+Na]^+$
1126.3647	1126.3863	0.0216	CoA 22:1	$C_{43}H_{76}N_7O_{17}P_3SK$	$[M+K]^+$
1144.3667	1144.3603	0.0064	CoA 24:6; O	$C_{45}H_{70}N_7O_{18}P_3SNa$	$[M+Na]^+$
1144.3667	1144.3969	0.0302	CoA 22:0; O	$C_{43}H_{78}N_7O_{18}P_3SK$	$[M+K]^+$
1144.3667	1144.3393	0.0274	CoA 24:6	$C_{45}H_{70}N_7O_{17}P_3SK$	$[M+K]^+$
1144.7417	1144.7846	0.0429	MIPC 46:0; O4	$C_{58}H_{114}NO_{18}P$	$[M+H]^+$
1158.2432	1158.2076	0.0356	FA 78:0; O2	$C_{78}H_{156}O_4$	$[M+H]^+$
1160.4934	1160.4879	0.0055	CoA 26:1; O	$C_{47}H_{84}N_7O_{18}P_3S$	$[M+H]^+$
1166.4940	1166.4749	0.0191	CoA 26:1	$C_{47}H_{84}N_7O_{17}P_3SNa$	$[M+Na]^+$

according to the reports in the literature, all three RCBs contain two pairs of disulfide bonds, the structure made them stable in the surrounding microenvironment. Second, we did not detect RCBs on ITO slides around the cleaned tissue sections. Third, we have carried out a preliminary *in situ* digestion experiment of proteins on castor beans tissue sections, and found that after tissue section washing by protocol E, enzymatic incubation, matrix coating and other steps, high abundance of RCBs can still be detected in the tissue section, which also indicated that RCBs can stably exist in the tissue.

3.2 Distribution of RCBs in castor beans

In previous work, we have performed *de novo* sequencing to verify the sequences of high disulfide bonds abundant RCBs by MALDI-MS/MS (Supplementary Data; Figure S3) (He et al., 2021). The sequence characteristics of RCBs are very similar to that of a class of plant peptides called "plant defensins" reported in the literature (Thevissen et al., 2007). Therefore, RCBs may be related to their own detoxification. In addition, in the identification and detection view, peptides are better candidates offering better sensitivity and easier pretreatment due to their simpler structures than ricin.

Figures 4A, B showed the optical image and Saffron O-fast histological staining image of medial longitudinal castor bean sections with arrows indicating endosperm, the embryo (embryonic axis and cotyledons), and testa tissues. To investigate the distribution of RCBs in castor beans, we performed MALDI-MSI analysis and obtained MS images with a spatial resolution of 100 μm. Figure 4C was MS imaging on castor beans from night geographical locations. RCB-1 to -3 were generally distributed in the whole endosperm but not uniform and mainly enriched in testa and embryo tissue in some geographical locations, especially in Ethiopia and Pakistan. Our results show that RCB-1 to 3 were compartmentalized differently among the embryo and testa tissues from different countries (Ethiopia, Pakistan, and China). For all castor bean sections from nine geographic origins, we did not find either RCB-4 or RCB- as Ovenden et al. reported towards the *"impala"* cultivar from Tanzania (Ovenden et al., 2014).

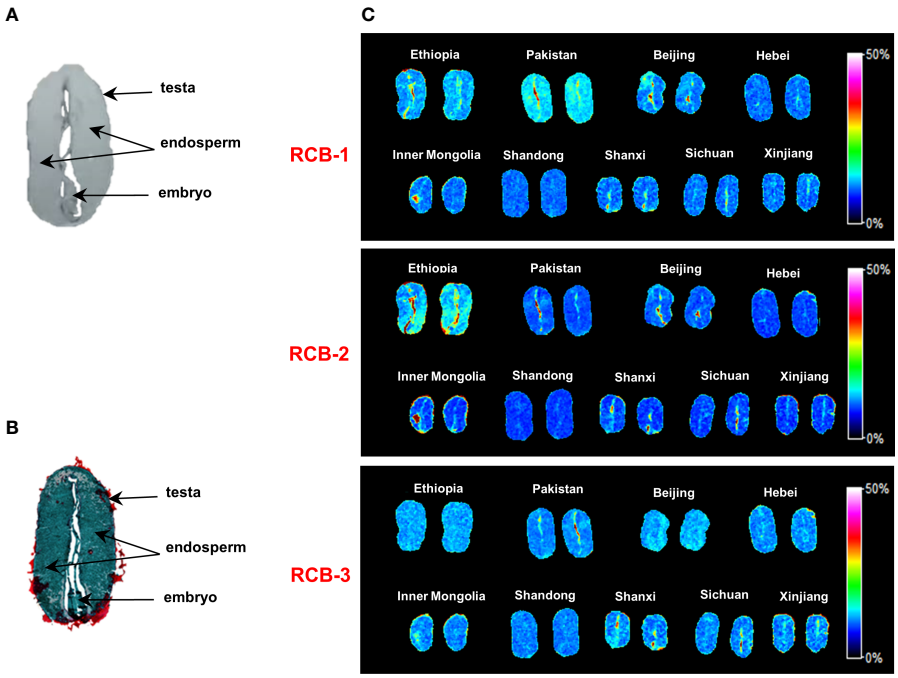

FIGURE 4
MALDI-MSI analysis of RCBs in positive ion mode in castor bean sections. **(A)** Optical imaging of the castor bean structure; **(B)** Saffron O-fast green plant tissue staining; **(C)** Distribution of RCB-1, -2 and -3 in castor beans from geographical sources. Color scales encode arbitrary ion relative strength.

3.3 Quantitative determination of RCBs in castor beans from different geographical origins

Due to the tissue heterogeneity, matrix coating heterogeneity, poor analyte extraction, and ionization suppression effects, the quantitative analysis of MALDI-MSI is still challenging. Currently, SILIS has been reported to calibrate the variability of ion suppression to maximize quantitative reproducibility, and it is the most pervasive method in MSI (Pirman et al., 2013; Havlikova et al., 2019). Herein, we also used SILIS to establish the standard curve and calculate the content of RCBs in tissue sections. The calibration curves generated by plotting the average intensity ratio of RCB-1, RCB-2, and RCB-3 to the $^{13}C_9{}^{15}N_1$-RCB-2 versus the concentration of RCB-1 to -3 applied to the ITO slide were shown in Figure 5A. RCB-1, RCB-2, and RCB-3 all had good linearity (R^2 = 0.99). The standard peptide solution was directly spotted on the ITO slide to generate standard curves, which did not consider the matrix effect of the tissue itself.

The average intensity ratio (RCB-1,2,3/$^{13}C_9{}^{15}N_1$-RCB-2) of castor bean tissue sections was introduced to the standard curve equation to calculate the content of RCBs in tissue sections. To obtain the quantitative concentration in gram per gram of tissue, the density of castor bean tissue is assumed to be 1 mg/mm^3. The volume in mm^3 was obtained by multiplying the area value of the tissue section by the thickness of the section. The final concentration of RCBs in g/g of tissue was obtained by comparing the calculated weight of RCBs with the total weight of the tissue. The quantitative data are summarized in Fiugre 5. Three RCB peptides were present in varying amounts in nine different geographic sources, the content of RCB-2 was the highest, followed by RCB-1, and the content of RCB-3 was the lowest in any source. It was similar to the content of RCB-1 to -3 in other cultivars of castor beans reported in the literature, that is, RCB-1 and RCB-2 existed in higher amounts in all cultivars, while RCB-3 was present only in some cultivars (Ovenden et al., 2009). Although the distribution of tissue sections was different, the content of RCBs in nine geographical sources was roughly the same.

It should be noted that the direct measured RCB content in the tissue section *via* this SILIS way was order of magnitude lower than the determined value towards averaged castor bean homogenate. Possible reason lies in that, the standard curve made on ITO slide surface is quite different from which on the tissue, and the endogenous components in the tissue section hinder the ionization of target RCBs and IS peptides. Hereby we introduced the tissue extinction coefficient (TEC) to amend the ion suppression of RCBs in the tissue section and resolve the discrepancy problem. The TEC of the tissue section was *ca.* 0.01

10.3389/fpls.2022.1083901

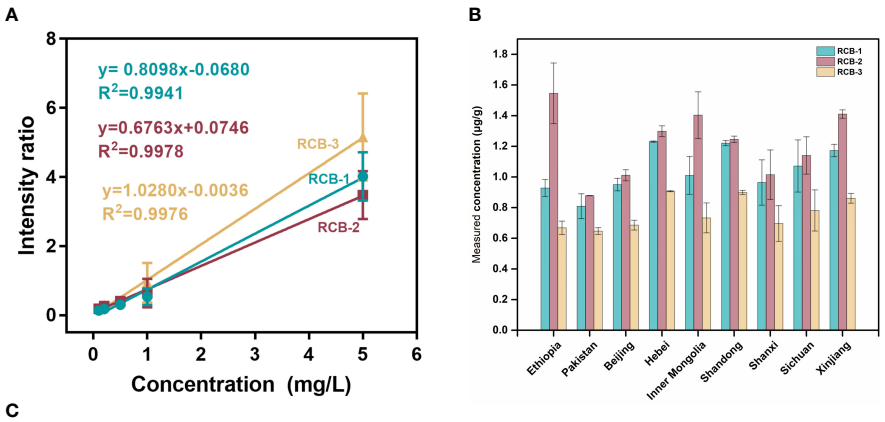

C

Regions	Adjusted concentration by TEC factor (μg/g)		
	RCB-1	RCB-2	RCB-3
Ethiopia	92.8±5.6	154.6±19.8	66.8±4.4
Pakistan	80.9±8.1	87.8±0.1	64.7±2.2
Beijing	90.5±4.1	101.1±3.6	68.6±3.2
Hebei	123.1±0.4	129.8±3.5	90.7±0.3
Inner Mongolia	101.0±12.4	140.3±15.2	73.3±9.7
Shandong	122.1±1.7	124.6±2.0	89.9±1.3
Shanxi	96.4±14.8	101.5±16.1	69.7±11.6
Sichuan	107.2±17.0	114.1±12.2	71.8±13.4
Xinjiang	117.3±4.1	141.1±2.7	86.1±3.2

FIGURE 5
Quantitation of RCB-1,-2 and -3 in castor bean tissues from nine geographical sources by MALDI-MSI. **(A)** Calibration curves of RCB-1, -2, and -3, the error bars in the graph represented the standard deviation of three microspots for each calibration solution; **(B)** The measured concentrations, and **(C)** the adjusted concentrations by TEC factor of RCB-1, -2, and -3 in castor bean tissues from nine geographical sources.

(detailed in Supplementary experimental; Table S6), so the adjusted RCB content was calculated from the direct measured RCB content divided by the TEC factor, and it can approach the measured value in homogenates, indicating an effective elimination of tissue matrix effect.

3.4 Multivariate statistical analysis of castor beans from different geographical origins

Regarding the castor beans from nine different geographical sources with five important phenotype traits, we found no significant difference except for castor beans from Ethiopia, which had relatively large sizes and weights with a distinctive appearance (Figure 6A). Considering that PCA recombines the original variables into a group of new comprehensive variables that are independent of each other, ideally, samples with similar compound types and amounts will cluster together in the scores plot of the PCA model, PCA with five traits as characteristic values was used to explore whether it is possible to distinguish castor beans of nine different sources only from their appearance (Figure 6). From the score plot of the principal component (PC1) and PC2, PC1 explained 89.1%, and PC2 explained 9.3% of the total data variation and the high values of R^2 and Q^2 manifest the outstanding prediction capability of the PCA models and well explain the cumulative variation of the PCs of the data (R^2 = 0.983, Q^2 = 0.914). The geographical origins of castor beans from Ethiopia were clustered into one category, and others (seven China sources and Pakistan) were clustered into another category. It indicated that the five phenotype traits of castor beans from other eight geographical sources were similar except for Ethiopia, therefore, castor beans can hardly be distinguished from each other only in terms of their appearance traits. From the loading plot, no significant difference in the contribution of the five characters to the PC1, indicating that hundred-grain weight, length, width, size and plumpness made almost no difference a considerable contribution to the classification of Ethiopia and other eight sources. We hope to explore further the original traceability of the castor beans at the molecular level *via* the MSI technique.

Hence, we employed PCA as an unsupervised analysis model to perform the dimension reduction of MSI data of castor bean

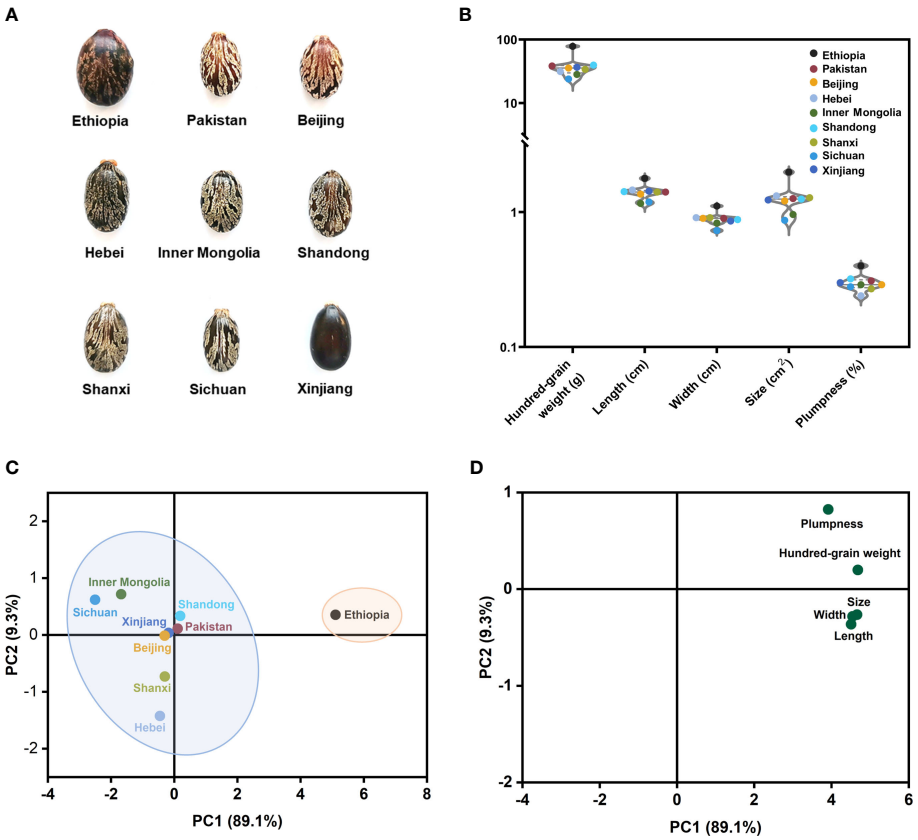

FIGURE 6
Phenotype description and PCA analysis of castor beans from nine different sources. **(A)** Appearance and morphology of castor beans; **(B)** Violin plot of five phenotypic traits of castor beans. Score plot **(C)** and loading plot **(D)** of the PCA analysis model based on five features of castor beans from different geographical sources.

samples from nine geographical regions, including data sets of all peaks and data sets containing only RCBs, using protocol E in the sample pretreatment. Data sets of all peaks were generated automatically with the TIC normalization by "Find peaks" tool and data sets containing only RCBs was generated by manual m/z selection on SCiLS Lab 2016b. The Peak Alignment tool was then used to align all peaks. Figure 7 shows the scores plot of the two PCs for the regional distribution of castor beans. For the data sets of all peaks, the score plot from PC1 (93.9%) and PC2 (2.8%) accounted for 96.7% of the total variance observed across the groups. Despite some overlapping profiles in nine groups, there was a separate trend among the different countries (Ethiopia, Pakistan and China), indicating the major distinct feature existed among different countries. Provinces and autonomous regions in China were almost clustered into one category, indicating that the type and content of chemical components in China were somewhat common. Similar results could also be obtained from PCA analysis of data sets containing mere RCBs (Figure 7B). The score plot from PC1 (80.0%) and PC2 (13.1%) accounted for 93.1% of the total variance. It suggested that the RCBs as an index have some unique region attribution value.

MSI experiment obtained a three-dimensional data cube with spatial coordinates (x and y) and an m/z axis containing the spectrum information. However, the available spatial information was lost and abandoned in most data analysis of MSI. The advent of deep learning, a class of models and associated learning methods based on artificial neural networks, has greatly facilitated such spatial analysis and may offer a promising strategy for classifying MSI data as it has been successfully applied to image classification. For example, Behrmann et al. proposed an adapted architecture based on deep convolutional networks to classify two lung tumor subtypes (Behrmann et al., 2018). DNN is a robust neural network, in its composition of multiple network layers, the input layer(s), hidden layer(s), and output layer(s) are set in different positions. Each layer is fully connected, and the output from each layer is an input to the next. The unique characteristic of DNN is, after feature mapping layer by layer, DNN maps the features of the existing spatial samples to another space to learn

10.3389/fpls.2022.1083901

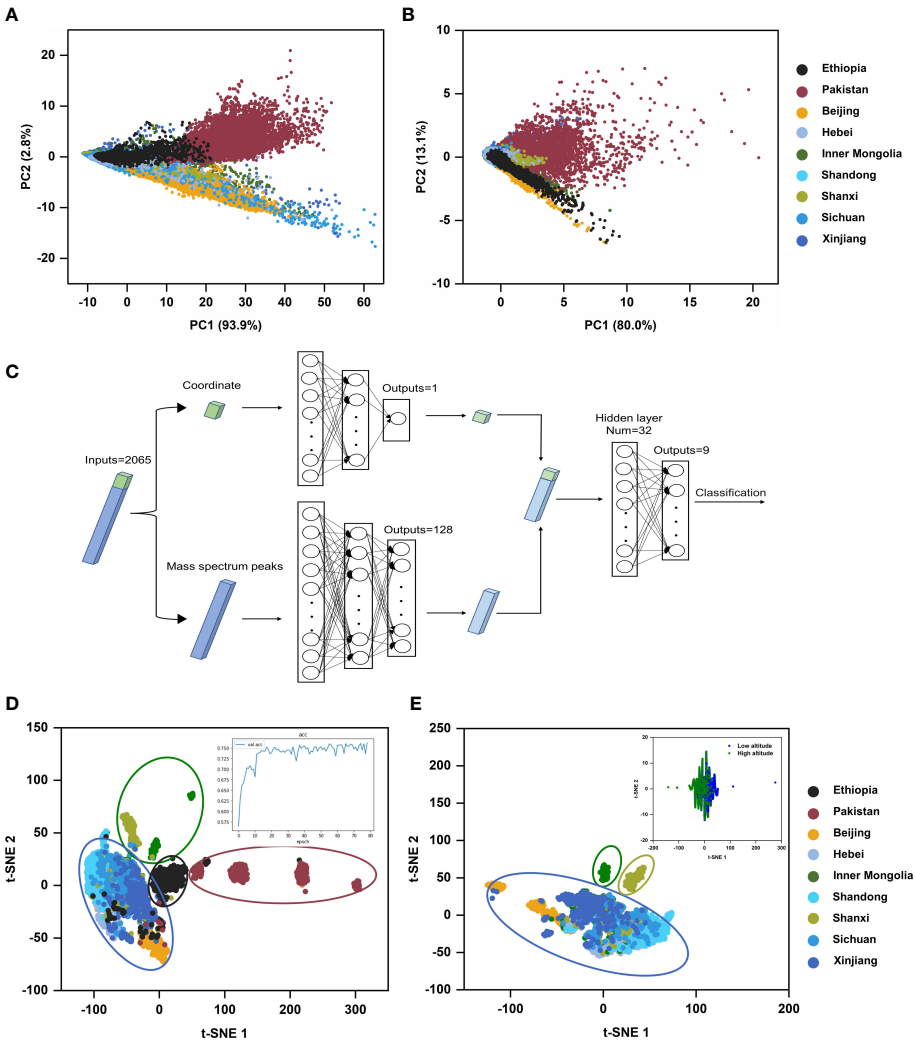

FIGURE 7
Multivariate statistical analysis results of castor beans from different geographical sources. **(A)** Score plot of the MSI dataset of all mass spectra peaks in PCA model; **(B)** Score plot of the MSI dataset of the mass spectra peaks of RCBs in PCA model; **(C)** Schematic diagram of DNN model; **(D)** t-SNE visual scatter plot of DNN model based on MSI dataset from nine geographical sources, the inset was the accuracy rate curve of neural network; **(E)** t-SNE plot of DNN model based on MSI dataset from seven geographical sources in China, the inset was a t-SNE plot of DNN model based on MSI dataset from different altitudes.

better feature expression for the current input. Here we firstly examined the classification potential of the dual-channel DNN. This DNN was designed according to the fabrication feature of MSI data, *i.e.*, each sample data was defined by two types of characteristics, the position of the sample point (the coordinate) and mass spectra information in this point (Figure 7C).

For both channels, two types of different features of the sample data were separately input into two sub-networks and then simultaneously trained. The features extracted from the two sub-networks were concatenated and inputted into the third sub-network with two fully connected layers for classification. After five repeated experiments, the average classification accuracy of the dual-channel DNN model for nine samples from different geographical sources was beyond 76%. Afterward, we used t-SNE to reduce the 32-dimensional features extracted from the first layer in the third sub-networks into a two-dimensional scatter plot, which distinctly displayed the distribution characteristics of samples from different geographical sources.

DNN provided more insights in comparison with PCA analysis. (i) It indicated a distinct trend among three countries, Ethiopia, Pakistan, and China. (ii) Inner Mongolia, Shanxi, and the other five provinces or autonomous regions were clustered into three groups among all seven regions of China (Figures 7D, E), disclosing a new clue from the viewpoint of altitude difference. Inner Mongolia and Shanxi are located on the

Mongolian plateau, and the other five provinces or autonomous regions are located in flat or basin areas on China mainland. We also inputted the dichotomous sample data composed of different altitudes into the dual-channel DNN model for training, and the accuracy of the test set reached 85%. (iii) Furthermore, the feature importance analysis using SHAP for nine respective sources (Figure S4) revealed that among the top 20 features with SHAP values among the 2065-dimensional features, the position (x, y) in the tissue section always has the prior rank no matter which geographic origin. It indicated the importance of analyzing the integrated MSI data as a whole set since the peak intensity values of mass spectra of sample points in the same tissue section from different geographical sources differed.

4 Conclusions

In this work, we developed a comprehensive tissue pretreatment protocol for MALDI-MSI analysis of endogenous peptide molecules in the castor bean containing plenty of lipids. In particular, we discovered a modified six-step organic solvents washing protocol containing alternative rinses of isopropanol and Carnoy's solution to provide a good lipid removal effect as well aa s significant improvement on the sensitivity of endogenous peptide biomarkers, RCBs, in castor bean tissues. It is the first report to depict good images of peptides inside lipid-rich plant tissue. With the other optimized crucial steps in sample preparation, we ensured the construction of a robust MALDI-MSI method to enhance the detection sensitivity of RCBs in castor beans. We then clearly mapped the spatial distribution and quantified RCBs in castor bean tissue sections, as well as from nine different geographic sources from seven regions of China and two regions from Ethiopia and Pakistan. Employed with multivariate statistical models of PCA, DNN, and t-SNE, the interpretation of the generated MSI data revealed valuable classification clues from nationality and altitude, in which RCBs contribute specific values as geographic attribution biomarkers. It put forward a task of further examination work on more geographical origins of castor bean plants. This method provides a new research perspective for the traceability of castor bean-relevant intoxication events.

Data availability statement

The original contributions presented in the study are included in the article/Supplementary Material. Further inquiries can be directed to the corresponding authors.

Author contributions

LQ conducted the experiments, analyzed data, and interpreted the results. LQ wrote the primary manuscript with support from BX. JH assisted in the multivariate statistical analysis of the DNN and wrote the relevant content with support from SH. CW assisted in this experiment. DT provided castor beans from Ethiopia, Pakistan, and Shandong province and a full discussion of the relevant investigation. LG supervised the experiment, revised the manuscript, and provided financial support, XB and JX reviewed the manuscript and approved it for the final release. All authors provided critical feedback, helped shape the research, and authorized the final manuscript.

Funding

This research received financial support from the National Natural Science Foundation of China (No. 21974152) and Major science and technology project (Major key techniques) in Shandong Province, China (2015ZDJSD3003).

Conflict of interest

The authors declare that the research was conducted in the absence of any commercial or financial relationships that could be construed as a potential conflict of interest.

The handling editor XW declared a shared affiliation with the author CW at the time of review.

Publisher's note

Supplementary material

The Supplementary Material for this article can be found online at: https://www.frontiersin.org/articles/10.3389/fpls.2022.1083901/full#supplementary-material

References

Aggarwal, R., Aggarwal, H., and Chugh, P. (2017). Medical management of ricin poisoning. *J. Med. Allied. Sci.* 7, 82. doi: 10.5455/jmas.259532

Behrmann, J., Etmann, C., Boskamp, T., Casadonte, R., Kriegsmann, J., and Maass, P. (2018). Deep learning for tumor classification in imaging mass spectrometry. *Bioinformatics* 34, 1215–1223. doi: 10.1093/bioinformatics/btx724

Bencivenni, M., Faccini, A., Zecchi, R., Boscaro, F., Moneti, G., Dossena, A., et al. (2014). Electrospray MS and MALDI imaging show that non-specific lipid-transfer proteins (LTPs) in tomato are present as several isoforms and are concentrated in seeds. *J. Mass Spectrom.* 49, 1264–1271. doi: 10.1002/jms.3454

Bezerra, M. A., Santelli, R. E., Oliveira, E. P., Villar, L. S., and Escaleira, L. A. (2008). Response surface methodology (RSM) as a tool for optimization in analytical chemistry. *Talanta* 76, 965–977. doi: 10.1016/j.talanta.2008.05.019

Blutke, A., Sun, N., Xu, Z. H., Buck, A., Harrison, L., Schriever, S. C., et al. (2020). Light sheet fluorescence microscopy guided MALDI-imaging mass spectrometry of cleared tissue samples. *Sci. Rep.* 10, 13. doi: 10.1038/s41598-020-71465-1

Buchberger, A. R., Vu, N. Q., Johnson, J., Delaney, K., and Li, L. (2020). A simple and effective sample preparation strategy for MALDI-MS imaging of neuropeptide changes in the crustacean brain due to hypoxia and hypercapnia stress. *J. Am. Soc Mass Spectrom.* 31, 1058–1065. doi: 10.1021/jasms.9b00107

Darby, S. M., Miller, M. L., and Allen, R. O. (2001). Forensic determination of ricin and the alkaloid marker ricinine from castor bean extracts. *J. Forensic Sci.* 46, 1033–1042. doi: 10.1520/JFS15097J

Deutskens, F., Yang, J., and Caprioli, R. M. (2011). High spatial resolution imaging mass spectrometry and classical histology on a single tissue section. *J. Mass Spectrom.* 46, 568–571. doi: 10.1002/jms.1926

Ding, W., Zhou, L., Tang, W., Ying, L., and Yao, H. (2019). Introduction of a method for removing fat during tissue dehydration. *Chin. J. Pathol.* 48, 248–250. doi: 10.3760/cma.j.issn.0529-5807.2019.03.017

Duriez, E., Fenaille, F., Tabet, J. C., Lamourette, P., Hilaire, D., Becher, F., et al. (2008). Detection of ricin in complex samples by immunocapture and matrix-assisted laser desorption/ionization time-of-flight mass spectrometry. *J. Proteome Res.* 7, 4154–4163. doi: 10.1021/pr8003437

Fredriksson, S., Wunschel, D. S., Lindström, S. W., Nilsson, C., Wahl, K., and Åstot, C. (2018). A ricin forensic profiling approach based on a complex set of biomarkers. *Talanta* 168, 628–635. doi: 10.1016/j.talanta.2018.03.070

Gemperline, E., Keller, C., Jayaraman, D., Maeda, J., Sussman, M. R., Ané, J. M., et al. (2016). Examination of endogenous peptides in medicago truncatula using mass spectrometry imaging. *J. Proteome Res.* 15, 4403–4411. doi: 10.1021/acs.jproteome.6b00471

Goodwin, R. J. A. (2012). Sample preparation for mass spectrometry imaging: small mistakes can lead to big consequences. *J. Proteomics* 75, 4893–4911. doi: 10.1016/j.jprot.2012.04.012

Goodwin, R. J., Pennington, S. R., and Pitt, A. R. (2008). Protein and peptides in pictures: imaging with MALDI mass spectrometry. *Proteomics* 8, 3785–3800. doi: 10.1002/pmic.200800320

Greco, V., Piras, C., Pieroni, L., Ronci, M., Putignani, L., Roncada, P., et al. (2018). Applications of MALDI-TOF mass spectrometry in clinical proteomics. *Expert Rev. Proteomics* 15, 683–696. doi: 10.1080/14789450.2018.1505510

Guo, S., Wang, Y., Zhou, D., and Li, Z. (2015). Electric field-assisted matrix coating method enhances the detection of small molecule metabolites for mass spectrometry imaging. *Anal. Chem.* 87, 5860–5865. doi: 10.1021/ac504761t

Havlikova, J., Randall, E. C., Griffiths, R. L., Swales, J. G., Goodwin, R. J. A., Bunch, J., et al. (2019). Quantitative imaging of proteins in tissue by stable isotope labeled mimetic liquid extraction surface analysis mass spectrometry. *Anal. Chem.* 91, 14198–14202. doi: 10.1021/acs.analchem.9b04148

He, W., Wang, C., Yang, J., Xu, B., Guo, L., and Xie, J. (2021). Tracing origins of castor beans through potential defensin peptides unraveled by MALDI mass spectrometry imaging. *FENXI CESHI XUEBAO (J. Instrum. Anal.)* 40, 543–550. doi: 10.3969/j.issn.1004-4957.2021.04.015

Keller, C., Gemperline, E., and Li, L. (2020). MALDI mass spectrometry imaging of peptides in medicago truncatula root nodules. *Methods Mol. Biol.* 2139, 341–351. doi: 10.1007/978-1-0716-0528-8_25

Lemaire, R., Wisztorski, M., Desmons, A., Tabet, J. C., Day, R., Salzet, M., et al. (2006). MALDI-MS direct tissue analysis of proteins: Improving signal sensitivity using organic treatments. *Anal. Chem.* 78, 7145–7153. doi: 10.1021/ac060565z

Li, B., Zhang, Y., Ge, J., Liu, K., and Li, P. (2018). Sample preparation for mass spectrometry imaging of leaf tissues: a case study on analyte delocalization. *Anal. Bioanal. Chem.* 410, 7449–7456. doi: 10.1007/s00216-018-1355-5

Neagu, A. N. (2019). Proteome Imaging: From Classic to Modern Mass Spectrometry-Based Molecular Histology. *Adv. Exp. Med. Biol.* 1140, 55–98. doi: 10.1007/978-3-030-15950-4_4

Ovenden, S. P. B., Fredriksson, S. A., Bagas, C. K., Bergström, T., Thomson, S. A., Nilsson, C., et al. (2009). *De novo* sequencing of RCB-1 to -3: peptide biomarkers from the castor bean plant ricinus communis. *Anal. Chem.* 81, 3986–3996. doi: 10.1021/ac900371y

Ovenden, S. P., Pigott, E. J., Rochfort, S., and Bourne, D. J. (2014). Liquid chromatography-mass spectrometry and chemometric analysis of ricinus communis extracts for cultivar identification. *Phytochem. Anal.* 25, 476–484. doi: 10.1002/pca.2519

Pigott, E. J., Roberts, W., Ovenden, S. P. B., Rochfort, S., and Bourne, D. J. (2011). Metabolomic investigations of ricinus communis for cultivar and provenance determination. *Metabolomics* 8, 634–642. doi: 10.1007/s11306-011-0355-7

Pirman, D. A., Reich, R. F., Kiss, A., Heeren, R. M., and Yost, R. A. (2013). Quantitative MALDI tandem mass spectrometric imaging of cocaine from brain tissue with a deuterated internal standard. *Anal. Chem.* 85, 1081–1089. doi: 10.1021/ac302960j

Polito, L., Bortolotti, M., Battelli, M. G., Calafato, G., and Bolognesi, A. (2019). Ricin: an ancient story for a timeless plant toxin. *Toxins (Basel)* 11, 324. doi: 10.3390/toxins11060324

Rešetar Maslov, D., Svirkova, A., Allmaier, G., Marchetti-Deschamann, M., and Kraljević Pavelić, S. (2019). Optimization of MALDI-TOF mass spectrometry imaging for the visualization and comparison of peptide distributions in dry-cured ham muscle fibers. *Food Chem.* 283, 275–286. doi: 10.1016/j.foodchem.2018.12.126

Seeley, E. H., Oppenheimer, S. R., Mi, D., Chaurand, P., and Caprioli, R. M. (2008). Enhancement of protein sensitivity for MALDI imaging mass spectrometry after chemical treatment of tissue sections. *J. Am. Soc Mass Spectrom.* 19, 1069–1077. doi: 10.1016/j.jasms.2008.03.016

Sturtevant, D., Romsdahl, T. B., Yu, X. H., Burks, D. J., Azad, R. K., Shanklin, J., et al. (2019). Tissue-specific differences in metabolites and transcripts contribute to the heterogeneity of ricinoleic acid accumulation in Ricinus communis L. (castor) seeds. *Metabolomics* 15, 6. doi: 10.1007/s11306-018-1464-3

Sun, C., Liu, W., Ma, S., Zhang, M., Geng, Y., and Wang, X. (2020). Development of a high-coverage matrix-assisted laser desorption/ionization mass spectrometry imaging method for visualizing the spatial dynamics of functional metabolites in salvia miltiorrhiza bge. *J. Chromatogr. A* 1614, 460704. doi: 10.1016/j.chroma.2019.460704

Tang, X., Zhao, M., Chen, Z., Huang, J., Chen, Y., Wang, F., et al. (2021). Visualizing the spatial distribution of metabolites in clausena lansium (Lour.) skeels using matrix-assisted laser desorption/ionization mass spectrometry imaging. *Phytochemistry* 192, 112930. doi: 10.1016/j.phytochem.2021.112930

Thevissen, K., Kristensen, H. H., Thomma, B. P., Cammue, B. P., and François, I. E. (2007). Therapeutic potential of antifungal plant and insect defensins. *Drug Discovery Today* 12, 966–971. doi: 10.1016/j.drudis.2007.07.016

Thomas, A., Patterson, N. H., Laveaux Charbonneau, J., and Chaurand, P. (2013). Orthogonal organic and aqueous-based washes of tissue sections to enhance protein sensitivity by MALDI imaging mass spectrometry. *J. Mass. Spectrom.* 48, 42–48. doi: 10.1002/jms.3114

Van Hove, E. R., Smith, D. F., Fornai, L., Glunde, K., and Heeren, R. M. (2011). An alternative paper based tissue washing method for mass spectrometry imaging: localized washing and fragile tissue analysis. *J. Am. Soc Mass. Spectrom.* 22, 1885–1890. doi: 10.1007/s13361-011-0203-z

Vu, N. Q., Buchberger, A. R., Johnson, J., and Li, L. (2021). Complementary neuropeptide detection in crustacean brain by mass spectrometry imaging using formalin and alternative aqueous tissue washes. *Anal. Bioanal. Chem.* 413, 2665–2673. doi: 10.1007/s00216-020-03073-x

Vuckovic, I., Rapinoja, M. L., Vaismaa, M., Vanninen, P., and Koskela, H. (2016). Application of comprehensive NMR-based analysis strategy in annotation, isolation and structure elucidation of low molecular weight metabolites of ricinus communis seeds. *Phytochem. Anal.* 27, 64–72. doi: 10.1002/pca.2600

Wang, X., Han, J., Hardie, D. B., Yang, J., and Borchers, C. H. (2016). The use of matrix coating assisted by an electric field (MCAEF) to enhance mass spectrometric imaging of human prostate cancer biomarkers. *J. Mass. Spectrom.* 51, 86–95. doi: 10.1002/jms.3728

Wang, X., Han, J., Hardie, D. B., Yang, J., Pan, J., and Borchers, C. H. (2017). Metabolomic profiling of prostate cancer by matrix assisted laser desorption/

ionization-fourier transform ion cyclotron resonance mass spectrometry imaging using matrix coating assisted by an electric field (MCAEF). *Biochim. Biophys. Acta Proteins Proteomics* 1865, 755–767. doi: 10.1016/j.bbapap.2016.12.012

Wang, X., Han, J., Yang, J., Pan, J., and Borchers, C. H. (2015). Matrix coating assisted by an electric field (MCAEF) for enhanced tissue imaging by MALDI-MS. *Chem. Sci.* 6, 729–738. doi: 10.1039/c4sc01850h

Worbs, S., Köhler, K., Pauly, D., Avondet, M. A., Schaer, M., Dorner, M. B., et al. (2011). Ricinus communis intoxications in human and veterinary medicine-a summary of real cases. *Toxins (Basel)* 3, 1332–1372. doi: 10.3390/toxins3101332

Yang, J., and Caprioli, R. M. (2011). Matrix sublimation/recrystallization for imaging proteins by mass spectrometry at high spatial resolution. *Anal. Chem.* 83, 5728–5734. doi: 10.1021/ac200998a

frontiers | Frontiers in Plant Science

TYPE Original Research
PUBLISHED 12 January 2023
DOI 10.3389/fpls.2022.1125872

OPEN ACCESS

EDITED BY
Xiaodong Wang,
Minzu University of China, China

REVIEWED BY
Tao Yi,
Hong Kong Baptist University,
Hong Kong SAR, China
Gui-Hua Tang,
Sun Yat-sen University, China

*CORRESPONDENCE
Ronghui Gu
rhgu@gzu.edu.cn

†These authors have contributed equally to this work

SPECIALTY SECTION
This article was submitted to Technical Advances in Plant Science, a section of the journal Frontiers in Plant Science

RECEIVED 16 December 2022
ACCEPTED 28 December 2022
PUBLISHED 12 January 2023

CITATION
Liu Q, Huang Y, Linghu C, Xiao J and Gu R (2023) Metabolic profiling, *in-situ* spatial distribution, and biosynthetic pathway of functional metabolites in *Dendrobium nobile* stem revealed by combining UPLC-QTOF-MS with MALDI-TOF-MSI. *Front. Plant Sci.* 13:1125872. doi: 10.3389/fpls.2022.1125872

Metabolic profiling, *in-situ* spatial distribution, and biosynthetic pathway of functional metabolites in *Dendrobium nobile* stem revealed by combining UPLC-QTOF-MS with MALDI-TOF-MSI

Qingling Liu[1,2†], Yuan Huang[3†], Chu Linghu[4,5], Jianfen Xiao[1,2] and Ronghui Gu[1,4,5*]

[1]Key Laboratory of Plant Resource Conservation and Germplasm Innovation in Mountainous Region (Ministry of Education), Guizhou University, Guiyang, China, [2]College of Life Sciences, Guizhou University, Guiyang, China, [3]College of Pharmacy, Guizhou University of Traditional Chinese Medicine, Guiyang, China, [4]School of Liquor and Food Engineering, Guizhou University, Guiyang, China, [5]National & Local Joint Engineering Research Center for the Exploitation of Homology Resources of Medicine and Food, Guizhou University, Guiyang, China

The stem of *Dendrobium nobile* Lindl. (Orchidaceae), called "*Shihu*" in traditional Chinese medicine, is a well-known medicinal and edible plant material in China. It is used as an antipyretic, analgesic, and tonic to nourish the stomach and *Yin* (i.e., to improve the production of body fluids). These therapeutic properties are attributed to its alkaloids, sesquiterpenoids, bibenzyls, fluorenones, and phenanthrenes. However, a comprehensive understanding of these metabolites and their spatial distribution in stems is lacking. In this study, ultra-performance liquid chromatography/quadrupole time-of-flight mass spectrometry (UPLC-QTOF-MS) was performed to obtain detailed metabolites information about *D. nobile* stems. Then, the spatial distributions of diverse metabolites, including alkaloids and sesquiterpenoids, were characterized and visualized by matrix-assisted laser desorption/ionization time-of-flight mass spectrometry imaging (MALDI-TOF-MSI). Based on the spatial and metabolic profiling data, sesquiterpene alkaloid dendrobine was chosen for the exhaustive study of a biosynthetic pathway in *D. nobile*. This is the first report on mass spectrometry imaging for *Dendrobium* species. As a result, critical bioactive metabolites such as 11 alkaloids, 10 sesquiterpenes, and 13 other metabolites were putatively identified and relatively quantified. The identified alkaloids were distributed in the parenchyma or vascular bundle, and sesquiterpenes were present in all regions of the stem with higher abundance in the vascular bundle and cuticle, or in the cuticle and epidermis. The biosynthetic pathway and accumulation pattern of dendrobine in *D. nobile* stem were also proposed. Our findings not only provided a critical methodology for the thorough understanding of physiological changes in metabolites and precise utilization of *D. nobile* stem, but also displayed an effective strategy for insight into the biosynthesis of bioactive metabolites in plants.

KEYWORDS

***Dendrobium nobile*, spatial imaging, UPLC-QTOF-MS, MALDI-MSI, dendrobine, sesquiterpenes, biosynthetic pathway**

1 Introduction

Dendrobium nobile Lindl. is a prized medicinal, ornamental, and edible plant species from the genus *Dendrobium* in Orchidaceae family. The stems of *D. nobile*, *D. chrysotoxum*, *D. fimbriatum*, or *D. huoshanense* are called *Shihu* (石斛) in the *Chinese Pharmacopoeia* for nourishing *Yin* (*Yin* refers to body fluids. Nourishing *Yin*, an important term in traditional Chinese medicine (TCM), refers to improve the production of body fluids), nourishing the lung and stomach, strengthening the body, brightening the eyes, relieving coughs, and clearing heat (Nie et al., 2020). The medicinal utilization of *Shihu* in China can trace back to 2000 years ago following the records in Shennong's Classic of Material Medica (*Shen Nong Ben Cao Jing*). The detailed document of *Shihu* was found in Compendium of Materia Medica (*Ben Cao Gang Mu*) (1590 AD) (Mou et al., 2021). Among these above-mentioned species, *D. nobile* is regarded as the base fundamental species of *Shihu*, which annual production nowadays exceeds 4.5 million kg in China (Teoh, 2019).

Due to the crucial medicinal values of *D. nobile* stem in TCM, its phytochemistry and modern pharmacology have attracted increasing attention. Some review papers have summarized that the main bioactive constituents of *D. nobile* stem were alkaloids, sesquiterpenes, dibenzyls, phenanthrenes, and polysaccharides, and the important pharmacological effects include anti-tumor, anti-oxidation, anti-aging, anti-inflammation, improving immunity, anti-fatigue, neuroprotection, and protecting the liver and kidney (He et al., 2020; Nie et al., 2020; Linghu et al., 2021; Wang et al., 2022). Among these constituents, alkaloids have caught researcher's special concerns because it was the earliest identified classification of bioactive compounds in *Dendrobium* and responsible for numerous pharmacological effects (Chen and Chen, 1935). More importantly, dendrobine, the first active alkaloid isolated from *D. nobile* and a major ingredient in its stem, has drawn attention due to its wide applications for health benefits, such as analgesic, antipyretic, antiviral, and antihyperlipidaemic effects (Li R, et al., 2017; Gong et al., 2021). In addition, sesquiterpenes from *D. nobile* stem not only showed relatively high content but also acted as vital pharmacological activity, especially providing the most of precursors for the biosynthesis of dendrobine-type alkaloid in *D. nobile* stem (Gong et al., 2021; Mou et al., 2021). However, the comprehensive qualitative and spatial distribution of alkaloids and sesquiterpenes in mature *D. nobile* stem are still lacking.

Analyzing the metabolic profiling and spatial distribution of important metabolites in mature *D. nobile* stem is critical for the thoroughly understanding of its physiological changes and precise utilization of the prized plant resource. Recently, metabolomics has developed rapidly and applied widely to profile plant metabolites and study plant physiology (Šimura et al., 2018). In particular, the application of UPLC-QTOF-MS improved the resolution, sensitivity, and throughput for metabolites detection (Gu et al., 2019), which made the metabolomics studies possible to probe greater amounts of metabolic information for complex biological mixtures and discover previously unidentified metabolites (Tong et al., 2022). For the studies on metabolite spatial distribution, mass spectrometry imaging (MSI) has been developed as a powerful *in-situ* analysis technique to visualize the spatial distribution of metabolites in complex biological mixtures (He et al., 2019). Among MSI technologies, the matrix-assisted laser desorption/ionization mass spectrometry imaging (MALDI-MSI) is the most frequently used because of the suitable spatial resolution of imaging (3-100 μm) and the wide measurable mass range with soft ionization type (Qin et al., 2018). MALDI-MSI has been proven successfully in the visualization of metabolites in plant tissues. For instance, it has been carried out to analyze the cyanogenic glucoside in sorghum (Montini et al., 2020), lipids in cottonseeds (Liu et al., 2021), and alkaloids in areca nut (Wu et al., 2022).

In this study, we focused on the metabolic profiles and their relative content in mature *D. nobile* stem, especially the spatial distribution of alkaloids and sesquiterpenes. Moreover, the accumulation pattern and biosynthesis of sesquiterpene alkaloid dendrobine in mature *D. nobile* stem were also proposed. This work reported the use of MALDI-MSI to demonstrate the distribution of metabolites in mature *D. nobile* stem for the first time, particularly in alkaloids and sesquiterpenes. The findings showed that the combination of UPLC-QTOF-MS and MALDI-MSI was a superior methodology with both sensitive and visualizable, providing a deep insight into the metabolic profiling and *in situ* spatial distribution of some special and crucial bioactive metabolites in medicinal and edible plants.

2 Material and methods

2.1 Plant material

Dendrobium nobile was grown on the imitation wild cultivation base at Wanglong in Chishui City, Guizhou province. Based on the growth cycle of *D. nobile*, the suitable harvest time of *D. nobile* stem was between September and October in Guizhou. Three-year-old mature stems of *D. nobile* were collected in October 2020. Immediately after harvesting, the samples were put in dry ice for transportation, and stored in a freezer at -80°C until used.

2.2 Chemicals

The solvents, including LC/MS-grade water, acetonitrile, methanol, formic acid, acetic acid, and trifluoroacetic acid, were

Abbreviations: UPLC-QTOF-MS, ultra-performance liquid chromatography/quadrupole time-of-flight mass spectrometry; MALDI-MSI, matrix-assisted laser desorption/ionization mass spectrometry imaging; 2-MBT, 2-mercaptobenzothiazole; DHB, 2,5-dihydroxybenzoic acid; CHCA, α-cyano-4-hydroxycinnamic acid; ITO, indium tin oxide; DDB, dendrobine; DNO, dendrobine-*N*-oxide; DDM, dendramine; NMD, *N*-methyl-dendrobinium; MBB, mubironine B; DDX, dendroxine; NID, *N*-isopentenyl-dendroxinium; NBN, nobilonine; NHD, *N*-isopentenyl-6-hydroxydendroxinium; 4/6HD, 4/6-hydroxy-dendroxine; FLN, findlayanin; DTC, dendroterpene C; NBM, nobilomethylene; DSG, dendroside G; DSF, dendroside F; DBF, dendronobilin F; NIA, niranthin; STS, stigmasterol; MVA, mevalonate, FPP, farnesyl diphosphate; FPPS, farnesyl diphosphate synthase; CYP450, cytochrome P450 oxidase; SES, sesquiterpene synthase; HMGS, 3-hydroxy-3-methylglutaryl-CoA synthase; HMGR, 3-hydroxy- 3-methylglutaryl-CoA reductase; MVD, mevalonate diphosphate decarboxylase.

bought from Sigma-Aldrich (Saint Louis, MO, USA). 2,5-dihydroxybenzoic acid (DHB), α-cyano-4-hydroxycinnamic acid (CHCA), and 2-mercaptobenzothiazole (2-MBT) were purchased from J&K Scientific (Beijing, China). Dendrobine standard was purchased from Yuanye Shengwu (Shanghai, China).

2.3 Sample preparation for UPLC-QTOF-MS analysis

The fresh stem was crushed manually on ice. The crushed sample (1g) was extracted with 10 mL of 80% methanol (v/v) followed by an ultrasonic bath for 30 min at room temperature and then centrifugation (6000 r/min) for 15 min using a Cence H1850 centrifuge (Changsha, China). The supernatant was transferred, and the extraction was repeated twice. The combined supernatant was evaporated under nitrogen flow at room temperature to obtain extracts and kept at -20 °C. Prior to UPLC-QTOF-MS analysis, the extract was dissolved in 80% methanol (v/v) to a concentration of 1 mg/mL and then subjected to centrifugation (15000 r/min). The supernatant (100 μL) was added to the sample vial with a 250 μL insert pipe for analysis.

2.4 Sample preparation for MALDI-MSI analysis

The preparation of *D. nobile* stems sections were based on previously reported methods (He et al., 2019) with few modification. Briefly, fresh stems were stored at -80 °C until use; the stems were cryo-sectioned into 20-μm-thick slices at -20 °C on a freezing microtome (Leica CM1860, Germany) and then were immediately adhered to indium tin oxide (ITO) glass microscope slides. A matrix solution containing 2-MBT (12 mg/mL) in acetonitrile/ddH_2O/TFA (80:20:0.2, v/v/v) was prepared and sprayed to the surfaces of stem sections by air-brush sprayer *via* five cycles (5 s spraying, 60 s drying). After air-drying in a fume hood, an extra matrix spray was conducted on the same stem sections for 40 cycles. The optical images of the stem section were obtained using a Photo Scanner (Epson Perfection V550). The standard histological optical images were gained by Hematoxylin and eosin (H&E) staining following a previous procedure (Casadonte and Caprioli, 2011).

2.5 UPLC-QTOF-MS and MALDI-MSI analysis

The UPLC-QTOF-MS analysis was executed with an ACQUITY UPLC coupled to Xevo G2 QTOF mass spectrometer system (Waters, Milford, MA, USA). The UPLC system was equipped with ACQUITY UPLC BEH C18 column (2.1×50 mm, I.D. 1.7 μm), autosampler, binary pump, and column compartment. The mobile phase consisted of water containing 0.1% formic acid (A) and acetonitrile containing 0.1% formic acid (B). The gradient elution procedure was as follows: 0-1.0 min, 3-13% B; 1.0-2.5 min, 13-25% B; 2.5-4.0 min, 25-40% B; 4.0-8.0 min, 40-60% B; 8.0-8.5 min, 60-97% B; 8.5-11.0 min, 97% B; 11.0-13.5 min, 97-3% B, 13.5-15.0 min, 3% B. The column temperature was 40°C, the flow rate was 0.5 mL/min, and the injection volume was 1 μL.

Mass spectrometry was obtained from both positive and negative ionization modes with scan time (1 s) and scan mass range (50-1500 Da). The capillary voltages were 3.0 kV (positive mode) and 2.5 kV (negative mode), and the sample cone voltage was 30 V. The desolvation temperature and ion source temperature were 400°C and 110°C, respectively. Nitrogen was used as the carrier gas with an 800 L/h flow rate for desolvation gas and a 50 L/h flow rate for sample cone gas. The low collision energy was 6 eV, and the high collision energy was changed repeatedly from 20 eV to 60 eV. Leucine-enkephalin (1 μg/mL) was used as Lock-Mass solution during data collection. The UPLC-QTOF-MS system was controlled by MassLynx 4.2 software (Waters, Milford, MA, USA).

MALDI-MSI was carried out on Bruker AutoFlex Speed MALDI TOF mass spectrometer (Bruker Daltonics, Germany) equipped with a 2000 Hz solid-state Smartbeam Nd: YAG UV laser (355 nm, Azura Laser AG). The detected mass ranges from 120 Da to 500 Da in positive-ion mode. Profiling data of MALDI-MS were obtained from 5000 laser shots accumulation, and each scan accumulated 500 laser shots. The images were acquired using Bruker's *FlexImaging* v. 4.1. Moreover, serine ($[M + H]^+$, m/z 106.0498), L-glutamic ($[M + H]^+$, m/z 148.0604), and proline ($[M + H]^+$, m/z 116.0706) were used for external mass calibration. 2-MBT ($[M + H]^+$, m/z 167.994) was used for internal mass calibration. The calibration was performed with cubic enhanced mode.

2.6 Processing of LC-MS data

The raw mass spectrum data with *.raw* format obtained in centroid mode were converted by *Reifycs* ABF converter software (https://www.reifycs.com/AbfConverter/) to get.*abf* format files, and furtherly imported into MS-DIAL software (Ver.4.7) for peak alignment, peak picking, normalization, deconvolution, and compound identification (Tsugawa et al., 2019). The main parameter settings were as follows: retention time range, 0-15 min; MS1 tolerance, 0.015 Da; MS2 tolerance, 0.02 Da; mass range, 50-1500 Da; smoothing level, 3 scans; minimum peak width, 5 scans; retention time tolerance, 0.05 min; identification score cut off, 80%. Adduct types as $[M+H]^+$, $[M+Na]^+$, $[M+H-H_2O]^+$, $[2M+H]^+$, and $[2M+Na]^+$ in positive-ion mode, and $[M-H]^-$, $[M-H-H_2O]^-$, $[M+FA-H]^-$, $[2M-H]^-$, and $[2M+FA-H]^-$ in negative-ion mode. Identification was performed by comparing MS, MS/MS, and retention index with MS/MS-Public-Pos/Neg database in MS-DIAL. The metabolites were regarded as potential identifications when the matching degree with the spectrum database was higher than 80%. The *.txt* file results, including sample name, metabolites, peak area, retention time, and quantitative quality, were exported after MS-DAIL process. The fragment ions of exported compounds were further confirmed by its original MS and MSe data in MassLynx with mass error<10 ppm and compared with mass data reported in related databases (SciFinder, PubMed, Mzcloud) and literatures.

2.7 Statistical analysis

Heatmap analysis were carried out using HeatMap illustrator tool in TBtool v1.01 software. The ion maps of detected compounds were

reconstructed using Bruker *FlexImaging* 4.1 software. The general histogram analysis was performed using GraphPad Prism software (GraphPad Software, Inc., La Jolla, CA, USA) and was calculated on the base of the peak intensity of identified compounds. The data were presented as mean ± standard deviation (SD).

3 Results and discussion

3.1 Metabolic profiling of *D. nobile* stems

Based on the established UPLC-QTOF-MS methods, the prepared extracts of *D. nobile* stems were analyzed and acquired the mass spectral data in both positive and negative ionization modes. The MS-DAIL platform and MassLynx software were used to identify and characterize the metabolites. By comparing the multi-level ion fragment information, mass spectrometry database, and related literature data, a total of 34 compounds were tentatively identified, including 11 alkaloids, 10 sesquiterpenes, 5 amino acids, 1 lignan, 1 steroid, and 6 others. Detailed information on the identifications, including compound type, name, formula, and fragments were performed in Table S1. The results showed alkaloids and sesquiterpenes were the main constituents in the mature *D. nobile* stem, which was accordant to the previous report that alkaloids and sesquiterpenes were the primary active constituents in the stems of *D. nobile*, especially alkaloids were representatives of the earliest identified classification of compounds from *Dendrobium* species (Xu et al., 2013; Mou et al., 2021). Based on the structural features of identified alkaloids and sesquiterpenes, we classified alkaloids as dendrobine-type alkaloids (dendrobine, dendrobine-*N*-oxide, dendramine, mubironine B, *N*-methyl-dendrobinium, and *N*-isopentenyl-dendrobinium) (Figure 1A), and dendroxine-type alkaloids (dendroxine, 4-hydroxy-dendroxine/6-hydroxy-dendroxine, *N*-isopentenyl-6-hydroxydendroxinium, *N*-isopentenyl-dendroxinium, and nobilonine) (Figure 1B). Moreover, the identified sesquiterpenes were also classified into two types, the one was dendrobine-type sesquiterpenes (findlayanin, endroterpene C, nobilomethylene, dendroside G, dendroside F, and dendronobilin F) (Figure 1C), and the remaining were listed as other-type (Figure 1D).

The alkaloids from *D. nobile* shown numerous significant pharmacological effects, including neuroprotection, hepatic lipid regulation, anti-tumor, anti-diabetes, anti-inflammatory, and anti-virus (Linghu et al., 2021). Meanwhile, the sesquiterpenes from *D. nobile* also exhibited multiple bioactivities such as anti-microbial, anti-malarial, anti-inflammatory, anti-tumor, and immunomodulatory (Gong et al., 2021).

3.2 Relative quantification of the identified compounds

Heatmap and boxplot analysis were applied to compare the relative content of the identified different metabolites in the

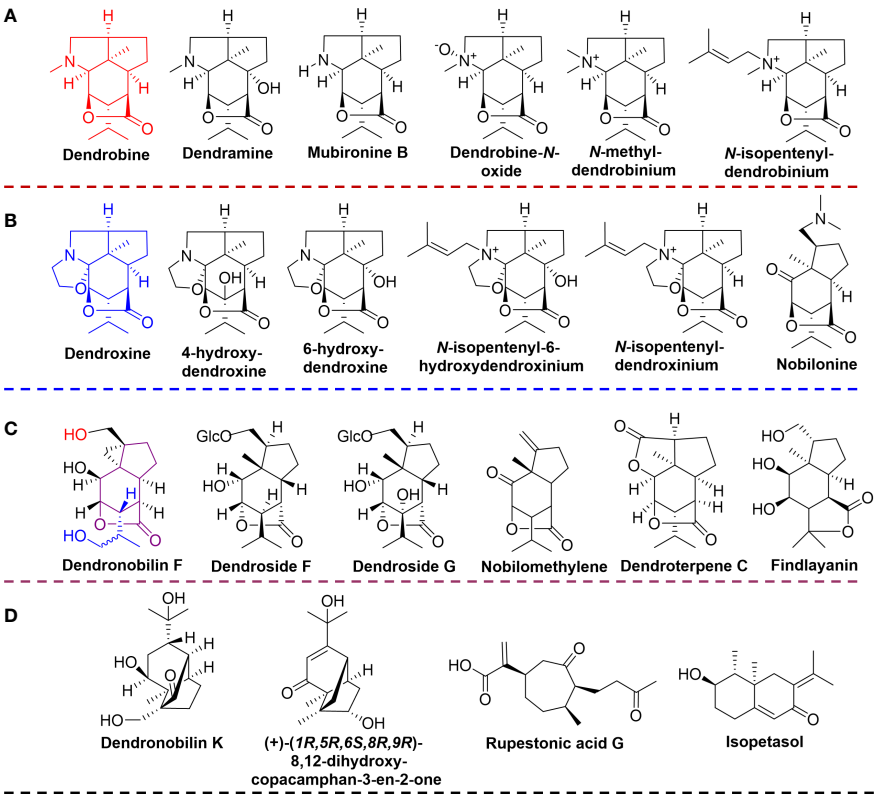

FIGURE 1
The structures of identified alkaloids and sesquiterpenes. **(A)** dendrobine-type alkaloids; **(B)** dendroxine-type alkaloids; **(C)** dendrobine-type sesquiterpenes; **(D)** other type sesquiterpenes.

matured stems of *D. nobile*. As shown in Figure 2A, alkaloids were the most abundant metabolites in stems, especially dendrobine-type alkaloids. Sesquiterpenes presented a certain abundance, but different metabolites in sesquiterpenes were varied in relative content. Most of amino acids showed lower content in mature stems. The identified lignan (niranthin, NIA) and steroid (stigmasterol, STS) displayed higher content than most of the identified amino acids. Furtherly, the boxplot demonstrated the relative content of each identified metabolites distinctly (Figures 2B-G). Notably, dendrobine-type alkaloids (Figure 2B) had higher content than dendroxine-type alkaloids (Figure 2C), revealing that the alkaloid biosynthesis and accumulation were main dendrobine-type and few dendroxine-type alkaloids during the development of *D. nobile* stem. Dendrobine (DDB) has the highest accumulation than other dendrobine-type alkaloids, particularly the relative content higher than dendrobine-*N*-oxide (DNO) and dendramine (DDM) have (Figure 2B). Dendrobine was the characteristic and first found alkaloid from *D. nobile*, which has considered as the evaluation indicator (mass content>0.4%) for the quality control of this species by *Chinese Pharmacopoeia* (2020 edition) (Mou et al., 2021). The low accumulations of DDM, DNO, *N*-methyl-dendrobinium (NMD), and mubironine B (MBB) were gradually reduced, indicating these compounds may have little biosynthesis or may provide intermediates for the biosynthesis of DDB. The relative content of dendroxine-type alkaloids decreased in the trends following dendroxine (DDX), *N*-isopentenyl-dendroxinium (NID), nobilonine (NBN), *N*-isopentenyl-6-hydroxydendroxinium (NHD), and 4/6-hydroxy-dendroxine (4/6HD) (Figure 2C), revealing that NID, NBN, NHD, and 4/6HD may have little biosynthesis or decompose at mature *D. nobile* stems.

The different sesquiterpenes were also varied in the relative content of mature *D. nobile* stem (Figures 2D-E). For the accumulation of dendrobine-type sesquiterpenes, findlayanin (FLN) showed the highest content, followed by dendroterpene C (DTC), nobilomethylene (NBM), dendroside G (DSG), dendroside F (DSF), and dendronobilin F (DBF) (Figure 2D), indicating that DBF may provide the basic skeleton; and both of DSF and DSG with glycosyl group may support energy for the biosynthesis of the sesquiterpene with more complex structure (such as NBM, DTC, and FLN) during the *D. nobile* stem mature. Most dendrobine-type sesquiterpenes have been reported as intermediates for the biosynthesis of dendrobine (Gong et al., 2021). Besides, the different accumulated levels of the identified amino acid and others, including lignin (NIA) and steroid (STS), were presented in Figures 2F, G, respectively.

3.3 Visualization and spatial distribution of diverse metabolites in *D. nobile* stem

Many studies previously focused on the qualitative and quantitative of *D. nobile* metabolites, particularly in alkaloids and sesquiterpenes. However, the spatial distributions of these critical compounds in stem are still lacking, which has severely hampered the thorough understanding of *D. nobile* physiological activities and the biosynthesis of the crucial metabolites. Thus, we herein analyzed the spatial distribution of alkaloids and sesquiterpenes in *D. nobile* stem for the first time to understand the biosynthesis of metabolites.

3.3.1 Optimization of sample preparation and MALDI matrix

In general, the frozen section of the samples from human and animal tissues can be prepared easily for MALDI-MSI analysis. While plant tissues difficult to prepare the frozen section due to the varied textures, waxy, and other physical characteristics. For the sample preparation of *D. nobile* stem (Figures 3A–D), we have investigated preparation methods, including sucrose phosphate buffer protection, chloroform washes, and slice thickness. The frozen section can present a complete cross-view without notch under the slice thickness at 20, 22, and 24 μm, but the better peak intensity performance of the mass spectrum was shown on the 20-μm-thick slices (Figures 3B-D, F).

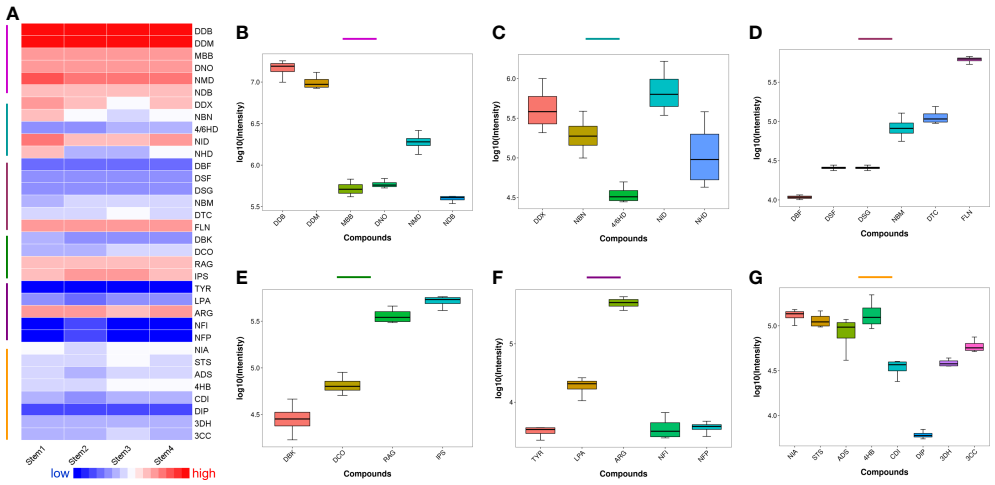

FIGURE 2
Relative content of the identified metabolites, including alkaloids and sesquiterpenes, from the mature stems of *Dendrobium nobile*. **(A)** heatmap for full view; **(B)** dendrobine-type alkaloids; **(C)** dendroxine-type alkaloids; **(D)** dendrobine-type sesquiterpenes; **(E)** other types sesquiterpenes; **(F)**: amino acid; **(G)**: other metabolites; All the full names of identified metabolites could be found in Table S1.

Matrix was considered as a vital role in the detection of metabolites for MALDI-MSI analysis (Liu et al., 2018). 2,5-dihydroxybenzoic acid (DHB), α-cyano-4-hydroxycinnamic acid (CHCA), and 2-mercaptobenzothiazole (2-MBT) have been widely used as MALDI matrices for the detection of low-molecular-weight metabolites (He et al., 2019). To obtain more abundant alkaloids and sesquiterpenes information, we selected DHB, CHCA, and 2-MBT as matrix to compare the performance of MALDI-MSI analysis on *D. nobile* stem. Under the same optimized conditions, 2-MBT was found with the best signal intensity distributed on the sample and the better performance of alkaloids and sesquiterpenes (Figures 3G-I). Thus, 2-MBT was proposed as the suitable matrix for MSI analysis in this study.

3.3.2 Distribution of alkaloids in *D. nobile* mature stems

As shown in Figure 4, the spatial distribution of dendrobine-type alkaloids was varied in the mature stem. Most of these alkaloids were distributed in the parenchyma or vascular bundle, while *N*-methyl-dendrobinium was obviously distributed in the cuticle (Figure 3E and Figure 4). As the most important bioactive metabolite in *D. nobile*, dendrobine was extremely abundant in the epidermis but also prominent in vascular bundle and little exist in parenchyma, indicating that the biosynthesis of dendrobine may occur in vascular bundle and parenchyma but transfer to epidermis for accumulation during stem maturation. The distribution of dendramine and dendrobine-*N*-oxide was found in all stem tissues, while the stronger signals were detected in vascular bundle for dendramine and in epidermis for dendrobine-*N*-oxide. However, the abundance of *N*-isopentenyl-dendrobinium and mubironine B were concentrated in vascular bundle and parenchyma and were absent in most part of cuticle.

The spatial distribution of identified dendroxine-type alkaloids in mature stems was almost identical, and the metabolites were obviously concentered in epidermis (Figure 3E and Figure 5). The lower signals of these metabolites indicated the low accumulation in mature *D. nobile* stem, which was consistent with their relative content detected by UPLC-QTOF-MS and speculation that dendroxine-type alkaloids may little biosynthesize. Particularly necessary to point out that 4/6-hydroxy-dendroxine was a pair of isomers, which was hard to distinguish by MALDI-MSI; thereby, the same MS image was used to show their distribution. [*N*-isopentenyl-6-hydroxydendroxinium+Na]$^+$ and [*N*-isopentenyl-dendroxinium +K]$^+$ also shared the same MS image for their quite similar ion mass (m/z 399.238 and 399.217) (Figure 5). Moreover, nobilonine could be a precursor or intermediate for biosynthesis of dendroxine-

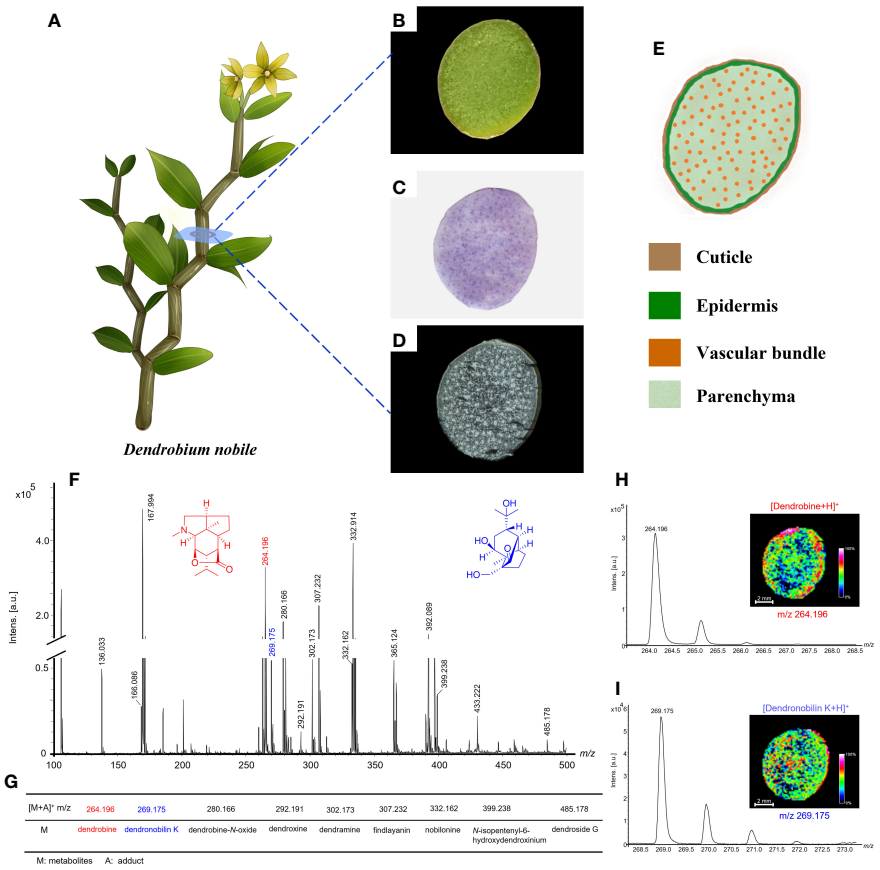

FIGURE 3
Morphology of *Dendrobium nobile* and MALDI-MS results based on optimized conditions. **(A)** Morphology of the plant; **(B)** Cross-section image of *D nobile* stem; **(C)** H&E stain image; **(D)** Frozen section; **(E)** The schematic image of cross-sections of *D nobile* stem showed the location of different tissues; **(F)** MALDI-MS results from the optimized frozen section of *D nobile* stem in positive-ion mode using 2-MBT as a matrix; **(G)** Table display of part of detected alkaloids and sesquiterpenes; **(H)** Dendrobine was used to show the optimized conditions suitable for alkaloids detection; **(I)** Dendronobilin K was used to show the optimized conditions suitable for sesquiterpenes detection.

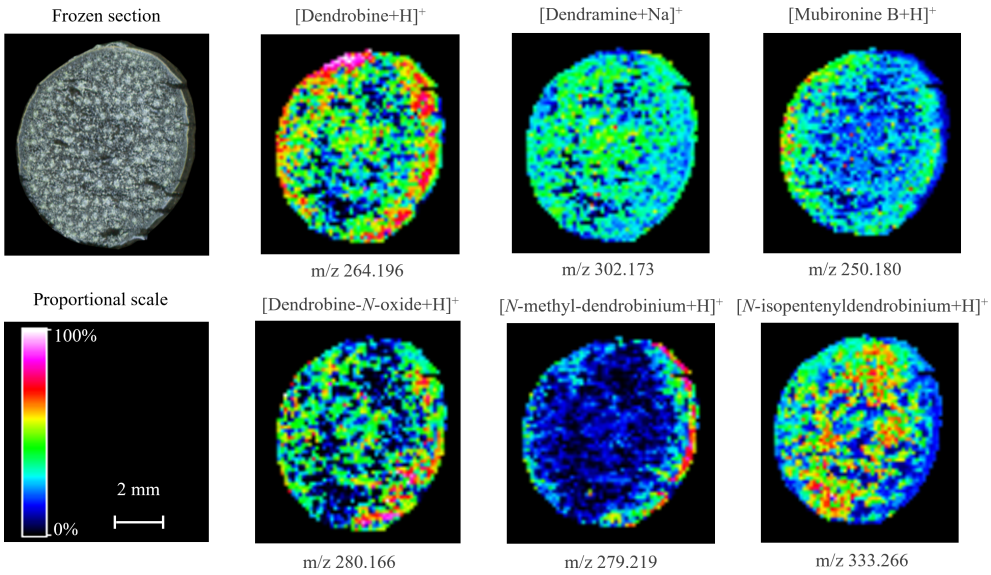

FIGURE 4
Distribution of dendrobine-type alkaloids in mature *Dendrobium nobile* stem imaged by MALDI-MSI. Heat maps were applied to present the relative distributions and contents.

and dendrobine-type alkaloids, which was verified by its shallow signal in MS image of mature *D. nobile* stem.

3.3.3 Distribution of sesquiterpenes in *D. nobile* mature stem

We also visualized the distribution of sesquiterpenes, another kind of important medicinal substance in *D. nobile* stem, by MALDI-MSI (Figure 6). The cross-section imaging of mature stem showed that dendronobilin F, dendroside G, dendroterpene C, and findlayanin were concentrated in the area of the cuticle and epidermis. The distribution of nobilomethylene, dendronobilin K, rupestonic acid G, and isopetasol were present in all regions of stem with higher abundance in the vascular bundle and cuticle. Dendroside F showed a low signal in all areas of stem imaging with a relatively stronger signal in the vascular bundle. These findings revealed that most of sesquiterpene precursors were still widely distributed in the mature stem, *e.g.*, nobilomethylene, dendronobilin K, rupestonic acid G, and isopetasol, while the sesquiterpene showed low abundance,

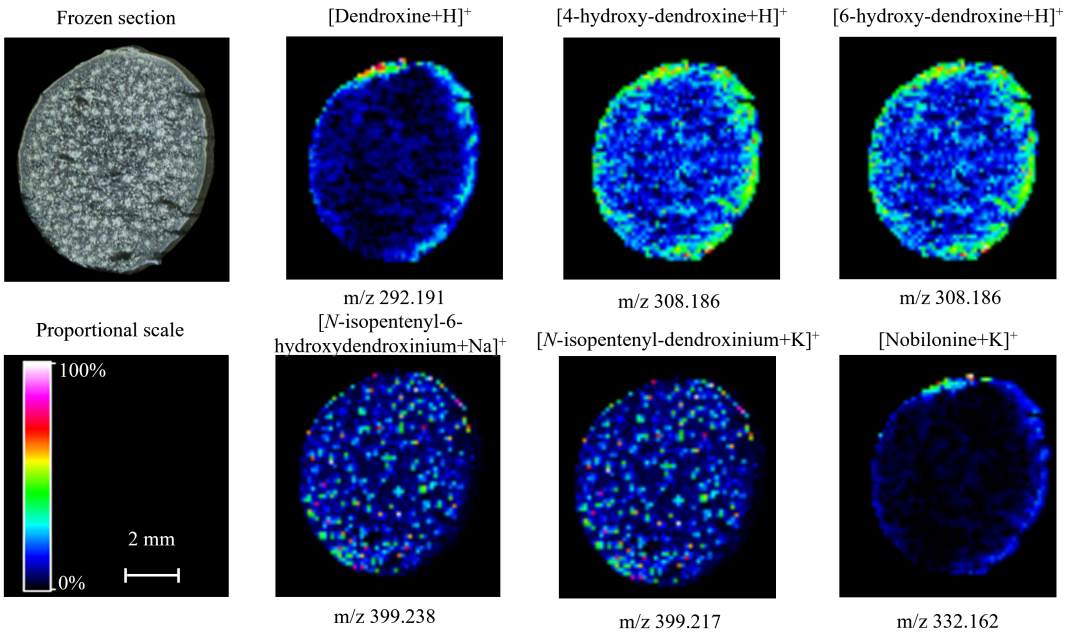

FIGURE 5
Distribution of dendroxine-type alkaloids in mature *Dendrobium nobile* stem imaged by MALDI-MSI. Heat maps were applied to present the relative distributions and contents.

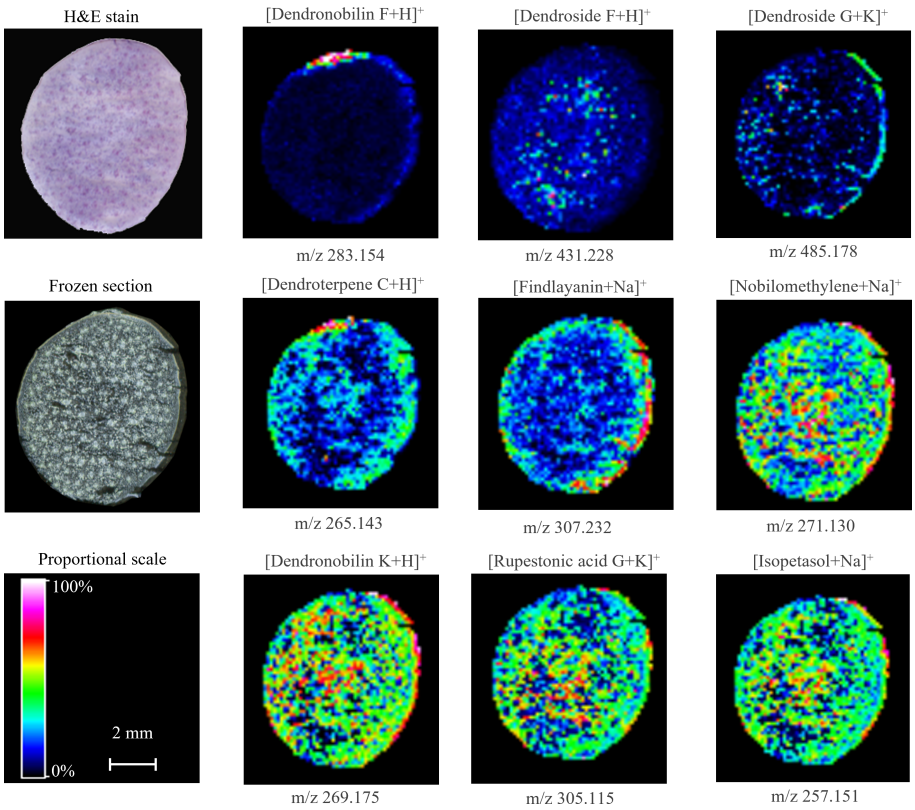

FIGURE 6
Distribution of sesquiterpenes in mature *Dendrobium nobile* stem imaged by MALDI-MSI. Heat maps were applied to present the relative distributions and contents.

e.g., dendronobilin F, dendroside F, dendroside G, and dendroterpene C. The spital distribution and low abundance of these metabolites demonstrated that sesquiterpenes were consumed to biosynthesize alkaloids during the maturation of *D. nobile* stem, particularly in dendrobine biosynthesis.

The spatial distribution of identified alkaloids and sesquiterpenes varied in the mature stem of *D. nobile*. The abundance of these metabolites was consistent in their relative content measured by UPLC-QTOF-MS, that is dendrobine-type alkaloids> dendroxine-type alkaloids> sesquiterpenes. Based on the accorded results from UPLC-QTOF-MS and MALDI-MSI analysis, we made a careful conclusion that sesquiterpenes were the precursors or intermediates contributing to the biosynthesis of dendrobine-type alkaloids and dendroxine-type alkaloids, which mainly accumulated in cuticle and epidermis regions, and traditional collection season of *D. nobile* (mature stem) in Guizhou was benefited for obtaining alkaloid but not for sesquiterpenes.

3.4 Metabolic pathway for the biosynthesis of dendrobine in *D. nobile* stem

Dendrobine, belonging to sesquiterpene alkaloids, accounted for 92.6% of *D. nobile* alkaloids (Xu et al., 2017). Moreover, dendrobine was also the first isolated bioactive alkaloid from *D. nobile* (Chen and Chen, 1935), and has been considered as the indicator ingredient for the quality evaluation of *D. nobile* stem attributing to its many important pharmacological effects (Li R et al., 2017; Song et al., 2019). Given this, the synthesis of dendrobine has attracted lots of researchers' interest. So far, total chemical synthesis of dendrobine has been available, but the yield and purity of dendrobine still meet the challenge (Gong et al., 2021). Therefore, biosynthesis of dendrobine was prospect and primary investigation, which promoted some enzymes and genes of the biosynthetic pathway of dendrobine have been found, such as cytochrome P450 oxidase (CYP450), farnesyl diphosphate synthase (FPPS), sesquiterpene synthase (SES), 3-hydroxy-3-methylglutaryl-CoA synthase (*HMGS*), 3-hydroxy- 3-methylglutaryl-CoA reductase (*HMGR*), and mevalonate diphosphate decarboxylase (*MVD*) (Li Q et al., 2017; Gong et al., 2021; Gong et al., 2022). However, due to the enormous genome of *D. nobile* and the complex structure of dendrobine, the biosynthesis of dendrobine was still unclear.

This study combined the superiority of both UPLC-QTOF-MS and MALDI-MSI, high accuracy and visualizable information, to analyze the biosynthesis and accumulation of dendrobine in *D. nobile* stem. Dendrobine was a sesquiterpene alkaloid, thus, the sesquiterpenes were proposed as precursors and intermediates in dendrobine biosynthesis, which pathway was also like that of sesquiterpene due to the sesquiterpene skeleton of dendrobine. Our metabolic profiling by UPLC-QTOF-MS has revealed that, a wide variety of sesquiterpene metabolites were identified in *D. nobile* stem, whereas the abundance was low. This result corresponded to the fact

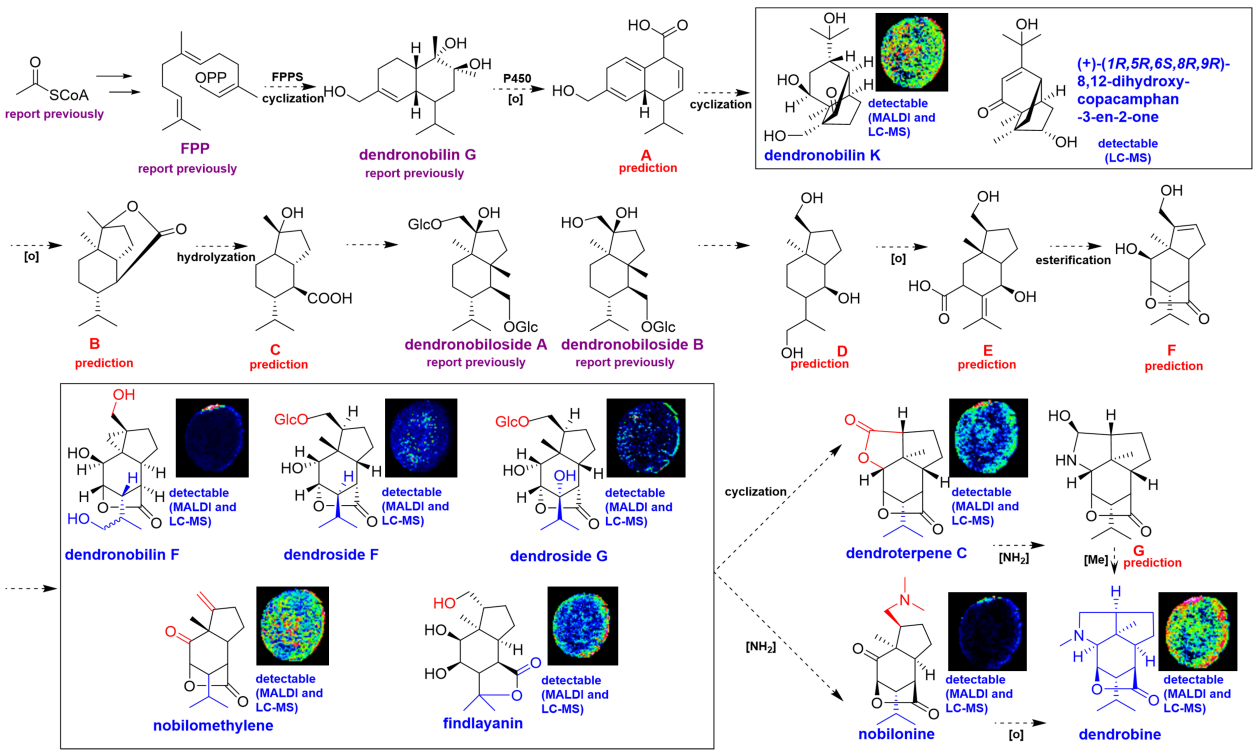

FIGURE 7
Proposed metabolic pathway for the biosynthesis of dendrobine in mature *Dendrobium nobile* stem based on the integrating analysis from UPLC-QTOF-MS and MALDI-MSI. **(A-G)** are the predicted skeleton of proposed intermediates.

that sesquiterpene was consumed for dendrobine biosynthesis during the maturation of *D. nobile* stem. Figure 7 displayed information referring to the main compounds of the proposed dendrobine biosynthesis pathway in stems of *D. nobile* based on the data of UPLC-QTOF-MS and MALDI-MS, and previous speculation (Gong et al., 2021).

As shown in Figure 7, farnesyl diphosphate (FPP) was first obtained from acetyl-CoA in the mevalonate (MVA) pathway, that is, the proposed biosynthetic pathway of dendrobine was started by the catalysis of FPPS. Then FPP can form dendronobilin G through intramolecular cyclization under the action of FPPS. Dendronobilin G putatively produces intermediate A under the effects of P450 oxidoreductase. Subsequently, the intermediate A undergoes molecule rearrangement, cyclization, and Michael addition to form dendronobilin K and (+)-(1R,5R,6S,8R,9R)-8,12-dihydroxy-copacamphan-3-en-2-one. These compounds were oxidized to produce B skeleton with opened-ring and hydrolyzation, and produce C- and D-type compounds, like dendronobiloside A and dendronobiloside B. D-type intermediates undergo redox reactions furtherly to form E, and E subjected to esterification to produce intermediate F. Thus far, the skeleton of picrotoxane-type sesquiterpene (E and F) was present through the intramolecular esterification of intermediate D. We have identified and visualized five picrotoxane-type sesquiterpenes in *D. nobile* stem. These picrotoxane-type sesquiterpenes may on the one hand form dendronobilin C by cyclization, dendronobilin C was aminated to form intermediate G, and G was finally methylated to produce dendrobine. On the other hand, the sesquiterpenes may be aminated to form nobilonine, nobilonine then transfer to dendrobine by cyclization and decarboxylation. Gong et al. (2021) have speculated a similar biosynthetic pathway of dendrobine, while our work found the most of sesquiterpenes in the pathway, including their relative contents and spatial distribution, which further confirmed the biosynthetic pathway of dendrobine.

4 Conclusion

This work conducted a comprehensive metabolic profiling and spatial distribution of metabolites from the stem of *D. nobile* by integrating the advantages of UPLC-QTOF-MS and MALDI-TOF-MSI in high sensitivity and *in situ* visualization, respectively. The critical bioactive metabolites, such as 11 alkaloids, 10 sesquiterpenes, and 13 other metabolites, were putatively identified and relatively quantified. For the first time, *in situ* spatial distribution of metabolites in *Dendrobium* was investigated. The results revealed that most of these alkaloids were distributed in the parenchyma or vascular bundle. Meanwhile, dendrobine was highly abundant in the epidermis but also prominent in vascular bundle and little existed in parenchyma, and the identified sesquiterpenes present in all regions of stem with higher abundance in vascular bundle and cuticle, or in cuticle and epidermis. Moreover, the biosynthetic pathway and accumulation pattern of dendrobine in *D. nobile* stem were also proposed. These findings not only provided a critical methodology for the thorough understanding of physiological changes in chemical and precise utilization of *D. nobile* stem, but

also displayed an effective strategy for insight into the biosynthesis of biological active plant metabolites.

Data availability statement

The original contributions presented in the study are included in the article/Supplementary Material. Further inquiries can be directed to the corresponding author.

Author contributions

RG designed and supervised the study. QL, YH, CL, and RG carried out the experiments and data analysis. QL and YH wrote the draft manuscript. JX, YH, and RG revised the manuscript. All authors contributed to the article and approved the submitted version.

Funding

This work was supported by the Basic Research Program of Guizhou Province (2021ZKYB085), the Youth Talent Improving Program of Guizhou University (2019GDPY39), the Natural Science Foundation for First-class Disciplines Special Program of Guizhou University (2020GDTG03), and National Natural Science Foundation of China (32260104).

Acknowledgments

We are grateful to Mr. Liang Qin from Huayi Technology Innovation Center for the assistance with imaging data processing.

Conflict of interest

The authors declare that the research was conducted in the absence of any commercial or financial relationships that could be construed as a potential conflict of interest.

Publisher's note

All claims expressed in this article are solely those of the authors and do not necessarily represent those of their affiliated organizations, or those of the publisher, the editors and the reviewers. Any product that may be evaluated in this article, or claim that may be made by its manufacturer, is not guaranteed or endorsed by the publisher.

Supplementary material

The Supplementary Material for this article can be found online at: https://www.frontiersin.org/articles/10.3389/fpls.2022.1125872/full#supplementary-material

References

Casadonte, R., and Caprioli, R. M. (2011). Proteomic analysis of formalin-fixed paraffin-embedded tissue by MALDI imaging mass spectrometry. *Nat. Protoc.* 6 (11), 1695–1709. doi: 10.1038/nprot.2011.388

Chen, K., and Chen, A. L. (1935). The alkaloid of chin-shih-hu. *J. Biol. Chem.* 111 (3), 653–658. doi: 10.1016/S0021-9258(18)75010-2

Gong, D.-Y., Chen, X.-Y., Guo, S.-X., Wang, B.-C., and Li, B. (2021). Recent advances and new insights in biosynthesis of dendrobine and sesquiterpenes. *Appl. Microbiol. Biotechnol.* 105 (18), 6597–6606. doi: 10.1007/s00253-021-11534-1

Gong, D., Wu, B., Qin, H., Fu, D., Guo, S., Wang, B., et al. (2022). Functional characterization of a farnesyl diphosphate synthase from *Dendrobium nobile* lindl. *AMB Express* 12 (1), 129. doi: 10.1186/s13568-022-01470-2

Gu, R., Rybalov, L., Negrin, A., Morcol, T., Long, W., Myers, A. K., et al. (2019). Metabolic profiling of different parts of *Acer truncatum* from the Mongolian plateau using UPLC-QTOF-MS with comparative bioactivity assays. *J. Agric. Food Chem.* 67 (5), 1585–1597. doi: 10.1021/acs.jafc.8b04035

He, H., Qin, L., Zhang, Y., Han, M., Li, J., Liu, Y., et al. (2019). 3, 4-dimethoxycinnamic acid as a novel matrix for enhanced *in situ* detection and imaging of low-molecular-weight compounds in biological tissues by MALDI-MSI. *Anal. Chem.* 91 (4), 2634–2643. doi: 10.1021/acs.analchem.8b03522

He, L., Su, Q., Bai, L., Li, M., Liu, J., Liu, X., et al. (2020). Recent research progress on natural small molecule bibenzyls and its derivatives in *Dendrobium* species. *Eur. J. Med. Chem.* 204, 112530. doi: 10.1016/j.ejmech.2020.112530

Li, Q., Ding, G., Li, B., and Guo, S.-X. (2017). Transcriptome analysis of genes involved in dendrobine biosynthesis in *Dendrobium nobile* lindl. infected with mycorrhizal fungus MF23 (*Mycena* sp.). *Sci. Rep.* 7 (1), 1–16. doi: 10.1038/s41598-017-00445-9

Li, R., Liu, T., Liu, M., Chen, F., Liu, S., and Yang, J. (2017). Anti-influenza a virus activity of dendrobine and its mechanism of action. *J. Agric. Food Chem.* 65 (18), 3665–3674. doi: 10.1021/acs.jafc.7b00276

Linghu, C., Gu, R.-H., and Qin, L.-K. (2021). Research progress on chemical constituents and pharmacological effects of *Dendrobium nobile*. *Chin. Tradit. Herb. Drugs* 52 (24), 1–16. doi: 10.7501/j.issn.0253-2670.2021.24.032

Liu, B., Meng, X., Li, K., Guo, J., and Cai, Z. (2021). Visualization of lipids in cottonseeds by matrix-assisted laser desorption/ionization mass spectrometry imaging. *Talanta* 221, 121614. doi: 10.1016/j.talanta.2020.121614

Liu, H., Zhou, Y., Wang, J., Xiong, C., Xue, J., Zhan, L., et al. (2018). *N*-Phenyl-2-naphthylamine as a novel MALDI matrix for analysis and *in situ* imaging of small molecules. *Anal. Chem.* 90 (1), 729–736. doi: 10.1021/acs.analchem.7b02710

Montini, L., Crocoll, C., Gleadow, R. M., Motawia, M. S., Janfelt, C., and Bjarnholt, N. (2020). Matrix-assisted laser desorption/ionization-mass spectrometry imaging of metabolites during sorghum germination. *Plant Physiol.* 183 (3), 925–942. doi: 10.1104/pp.19.01357

Mou, Z., Zhao, Y., Ye, F., Shi, Y., and Zhao, D. (2021). Identification, biological activities and biosynthetic pathway of *Dendrobium* alkaloids. *Front. Pharmacol.* 12. doi: 10.3389/fphar.2021.605994

Nie, X., Chen, Y., Li, W., and Lu, Y. (2020). Anti-aging properties of *Dendrobium nobile* lindl.: From molecular mechanisms to potential treatments. *J. Ethnopharmacol.* 257, 112839. doi: 10.1016/j.jep.2020.112839

Qin, L., Zhang, Y., Liu, Y., He, H., Han, M., Li, Y., et al. (2018). Recent advances in matrix-assisted laser desorption/ionisation mass spectrometry imaging (MALDI-MSI) for *in situ* analysis of endogenous molecules in plants. *Phytochem. Anal.* 29 (4), 351–364. doi: 10.1002/pca.2759

Šimura, J., Antoniadi, I., Široká, J., Tarkowská, D. E., Strnad, M., Ljung, K., et al. (2018). Plant hormonomics: Multiple phytohormone profiling by targeted metabolomics. *Plant Physiol.* 177 (2), 476–489. doi: 10.1104/pp.18.00293

Song, T.-H., Chen, X.-X., Lee, C. K.-F., Sze, S. C.-W., Feng, Y.-B., Yang, Z.-J., et al. (2019). Dendrobine targeting JNK stress signaling to sensitize chemotoxicity of cisplatin against non-small cell lung cancer cells *in vitro* and *in vivo*. *Phytomedicine* 53, 18–27. doi: 10.1016/j.phymed.2018.06.018

Teoh, E. S. (2019). *Orchids as aphrodisiac, medicine or food* Vol. 79 (Singapore: Springer).

Tong, Q., Zhang, C., Tu, Y., Chen, J., Li, Q., Zeng, Z., et al. (2022). Biosynthesis-based spatial metabolome of *Salvia miltiorrhiza* bunge by combining metabolomics approaches with mass spectrometry-imaging. *Talanta* 238, 123045. doi: 10.1016/j.talanta.2021.123045

Tsugawa, H., Nakabayashi, R., Mori, T., Yamada, Y., Takahashi, M., and Rai, A. (2019). A cheminformatics approach to characterize metabolomes in stable-isotope-labeled organisms. *Nat. Methods* 16 (4), 295–298. doi: 10.1038/s41592-019-0358-2

Wang, G., Wang, J., Deng, Y., Qin, L., He, Y., and Tan, D. (2022). Chemical constituents and nutritional health functions of *Dendrobium nobile*: a review. *Food Sci. Technol.* 42, 1–19. doi: 10.1590/fst.84522

Wu, J., Cui, C., Zhao, H., Zhou, G., Qin, L., Li, X., et al. (2022). *In situ* detection and imaging of *Areca catechu* fruit alkaloids by MALDI-MSI. *Ind. Crops Prod.* 188, 115533. doi: 10.1016/j.indcrop.2022.115533

Xu, J., Han, Q.-B., Li, S.-L., Chen, X.-J., Wang, X.-N., Zhao, Z.-Z., et al. (2013). Chemistry, bioactivity and quality control of *Dendrobium*, a commonly used tonic herb in traditional Chinese medicine. *Phytochem. Rev.* 12 (2), 341–367. doi: 10.1007/s11101-013-9310-8

Xu, Y.-Y., Xu, Y.-S., Wang, Y., Wu, Q., Lu, Y.-F., Liu, J., et al. (2017). *Dendrobium nobile* lindl. alkaloids regulate metabolism gene expression in livers of mice. *J. Pharm. Pharmacol.* 69 (10), 1409–1417. doi: 10.1111/jphp.12778

frontiers | Frontiers in Plant Science

TYPE Original Research
PUBLISHED 18 January 2023
DOI 10.3389/fpls.2023.1105374

OPEN ACCESS

EDITED BY
Xiaodong Wang,
Minzu University of China, China

REVIEWED BY
Jun Han,
University of Victoria, Canada
Ping Cheng,
Shanghai University, China

*CORRESPONDENCE
Xu Xu
xuxu@sit.edu.cn

SPECIALTY SECTION
This article was submitted to Technical Advances in Plant Science, a section of the journal Frontiers in Plant Science

RECEIVED 22 November 2022
ACCEPTED 02 January 2023
PUBLISHED 18 January 2023

CITATION
Shen Y-L, Zhuang S-J, Yang F, Gong C and Xu X (2023) Prefabricated platinum nanomaterial matrix for MALDI-MS imaging of oligosaccharides and lipids in plant tissues.
Front. Plant Sci. 14:1105374.
doi: 10.3389/fpls.2023.1105374

Prefabricated platinum nanomaterial matrix for MALDI-MS imaging of oligosaccharides and lipids in plant tissues

Yu-Lin Shen, Si-Jia Zhuang, Fan Yang, Can Gong and Xu Xu*

School of Chemical and Environmental Engineering, Shanghai Institute of Technology, Shanghai, China

Matrix-assisted laser desorption ionization mass spectrometry imaging (MALDI-MSI) can visualize the spatial distribution characteristics of molecules in tissues in situ, in which the matrix plays a key role. In this paper, we propose a platinum nanomaterial pre-coated matrix, which can be prepared in bulk by sputtering platinum nanoparticles onto slides using an ion sputterer and then used for MALDI-MS analysis by placing tissue sections on the matrix. We used this matrix for MALDI-MS imaging analysis of corn kernels and germinated wheat sections, and the results show that triacylglycerides were mainly distributed in the embryo of corn kernels and germinated wheat, and sugars were mainly distributed in the endosperm, with the highest content of disaccharides.It provides a simple and reliable experimental condition for analyzing the distribution of oligosaccharide and lipid components in plant tissues.

KEYWORDS

matrix-assisted laser desorption ionization mass spectrometry imaging, matrix, platinum nanomaterials, plant tissue, oligosaccharide, lipid

Introduction

MALDI MSI is an efficient technique for plant metabolomics research (Susniak et al., 2020). It can be used to characterize the spatial distribution of metabolites in plants (Li et al., 2018) and reveal the spatial and temporal metabolic patterns of plant secondary metabolite production, transport, and storage (Sun et al., 2020). Conventional organic matrixes such as α-cyano-4-hydroxycinnamic acid (CHCA) and 2,5-dihydroxybenzoic acid (DHB) have the propensity to produce non-uniform crystals with analytes, maybe resulting in poor repeatability and misinterpretation of MS images (Mueller et al., 2021).

As alternatives to traditional matrixes, researchers have proposed metal/metal oxide-based (Sakurai et al., 2018; Sagandykova et al., 2022), carbon-based (Xu et al., 2021), and silicon-based (Dou et al., 2022) matrixes. Metal particles with nanoscale diameters are of interest due to their unique plasmon absorption in the visible region, in which gold nanoparticles (Au NP) and silver nanoparticles (Ag NP) are the often utilized metal

matrixes. However, they are susceptible to gold and silver cluster ion. Studies have shown platinum nanoparticles (Pt NP) have softer surfaces than Au and AgNPs (Picca et al., 2017). Pt is very stable and does not oxidize quickly under ambient atmospheric conditions. Black Pt nanoparticles are effective MALDI-MS matrix for the whole UV-Vis region at laser wavelengths. Due to its extremely high melting temperature (2045 K), high crystallinity, and relatively low thermal conductivity (71.6 W $m^{-1}K^{-1}$ at 300 K), Pt can reduce fragmentation of metal nanoparticles such as clusters and is a good candidate matrix for MALDI-MS (Kawasaki et al., 2007).

In this study, we present an imaging method using platinum nanomaterials as a pre-coated matrix for visualizing and analyzing the spatial distribution of metabolites in plant tissues. This pre-coated matrix can be prepared in bulk using an ion sputterer. Tissue sections can be placed directly on the pre-coated matrix layer to conduct MALDI MSI studies, which reduces sample component diffusion, improves reproducibility, and simplifies experimental steps. The pre-coated matrix was successfully used for imaging oligosaccharide and lipid components in germinating wheat and corn sections.

Materials and methods

Materials

Gelatin, L-phenylalanine (99%), L-tyrosine (99%), and naringin (98%) were purchased from Adamas-beta(Shanghai,China).Palmitic acid (>97%), stearic acid (>98%), linoleic acid (>97%), and D-(+)-raffinose(>98%) were purchased from TCI Chemical Industries (Shanghai, China).Abscisic acid (ABA, 98%) were purchased from Sigma-Aldrich(St. Louis, USA).Dipalmitoyl phosphatidylcholine (DPPC) was purchased from Avanti Polar Lipids (Alabama, USA). Indolebutyric acid (99%)and α-cyclodextrin (≥98%) were purchased from Yuanye Biotechnology (Shanghai, China).Glycerol trioleate (99%) and 2,5-dihydroxybenzoic acid (DHB, 99%)were purchased from J&K Scientific (Beijing, China).Paeoniflorin (98%), sucrose (AR), and L-glutamic acid (≥99%) were purchased from Titan Technology (Shanghai, China).Ethanol (absolute, AR grade) was purchased from Sinopharm (Beijing, China).Methanol (HPLC grade) and dichloromethane (AR grade) were purchased from Boer Chemical Reagent (Shanghai, China), deionized water was obtained from Milli-Q Water Purification System (Millipore, Billerica, MA, USA).

Tissue-Tek OCT compound was purchased from Sakura Finetek (CA, USA). Microscope cover glasses (22mm × 22mm) were purchased from Citotest Scientific (Nanjing, China).We purchased fresh sweet corn from a local supermarket. Wheat seeds (Jimai 22) were from Crop Research Institute, Shandong Academy of Agricultural Sciences.

Preparation of platinum pre-coated matrix

The matrix was prepared using commercial magnetron sputtering equipment (Hitachi E-1010, Tokyo, Japan) with high-purity platinum targets (>99.9%). The distance between the platinum target and the sample was approximately 3.5 cm during sputtering. The platinum was deposited on a glass coverslip with a 20 mA discharge current under reduced pressure (15 Pa).

Preparation of authentic compound solutions

Water-soluble authentic compounds, including L-phenylalanine, L-tyrosine, L-glutamic acid, sucrose, raffinose, and α-cyclodextrin, were prepared in water. Water-insoluble authentic compounds, including palmitic acid, stearic acid, linoleic acid, naringin, paeoniflorin, abscisic acid, Indolebutyric acid, and glycerol trioleate, were prepared in anhydrous ethanol. DPPC was prepared in dichloromethane. All of the authentic compounds concentrations were 1 mg/ml. 2 μL solution of each authentic compound was spotted on a pre-coated platinum matrix pre-heated to 70°C to ensure uniform deposition. For comparison of platinum nanomaterials and organic matrix, 10 mg/ml of DHB was prepared in methanol-water solution (1:1, V/V) for positive ion mode analysis. 2 μl DHB was spotted on a glass coverslip to dry, followed by 2 μl of authentic compound solution.

Preparation of soybean extract: 10g of soybean were mashed and sieved, then 1 g of the sieved soybean powder was added to 50 mL of methanol and sonicated for two hours. The precipitate was centrifuged to extract the supernatant.

MALDI MSI sample preparation

Conditions for germination: The wheat seeds were rinsed five times with deionized water. They were soaked in a beaker with water for 2 hours, then transferred to a tray lined with wet paper towels, covered with wet gauze, placed at room temperature, and shielded from light to facilitate germination. The seeds were kept moist by regular application of water to the surface.

Sample preparation: Fresh samples (corn kernels, germinated wheat) were embedded in gelatin solution (10%, W/V) and then frozen in a -80°C refrigerator. For cryosectioning, frozen samples were fixed directly on sample holders with optimal cutting temperature (OCT) compounds, and 12 μm-thick tissue sections were obtained using a slicer at -20°C and thaw-mounted on slides pre-coated with platinum matrix. To prevent condensation, tissue sections were dehydrated for 30 minutes in a vacuum desiccator at room temperature.

MALDI MSI

MALDI MSI measurements were performed using a 7.0 T SolariX FTICR mass spectrometer (Bruker Daltonics, USA) equipped with dual ion sources (ESI and MALDI) and a Smartbeam II 355 nm laser. The m/z range obtained in positive ion mode was 53-1000. The single scan spectrum consisted of 25 cumulative 600 Hz laser shots with "Minimum" laser focus. The laser power in the positive ion mode was 70%. The spatial resolution of MALDI images of germinating wheat tissue sections was 100 μm, while the spatial resolution of MALDI

images of sweet corn tissue sections was 150 µm. MALDI MS data processing was performed with Bruker DataAnalysis 4.0.HyStar software (Version 3.4) was used to capture imaging data, and Bruker FlexAnalysis software was used to handle the imaging data.

Results and discussion

Selection of experimental conditions for pre-coated matrix

In order to optimize the sputtering time of Pt nanomaterials, we analyzed L-phenylalanine, palmitic acid, naringin, abscisic acid, raffinose, glycerol trioleate, and DPPC in positive ion mode, and repeated them 3 times respectively. We compared the variations in their peak intensities at 0.5, 1, 2, 3, and 4 min sputtering times (Figures 1, Figure S1). With the increase in sputtering time, the peak intensities first increased and then leveled off or decreased. Figure 1 shows the mass spectra of raffinose detected at different sputtering times; it has the highest signal intensity and less background signal when sputtering for 1 min. All following experiments utilized 1 min sputtering time.

Evaluation of repeatability of platinum nano pre-coated matrix

Palmitic acid, raffinose, abscisic acid, and glycerol trioleate were selected to examine the intra- and inter-spot reproducibility of the platinum pre-coated matrix. MALDI MS analysis was performed on nine sample spots on one pre-coated matrix layer and nine positions on one sample spot. As shown in Figure S2, the intra-spot repeatability was <5%, and inter-spot repeatability was <6%, indicating that the sputtering coated Pt matrix was homogenous and provided the high repeatability for MALDI-MS of the compounds.

Pt pre-coated matrixes for the detection of various small molecules

The detection coverage capability of the platinum pre-coated matrix was further explored in MALDI MS analysis of various plant-associated small molecules. Figure S3 and Table S1 show the 15 small molecule compounds detected by DHB and platinum pre-coated matrix. The amino acids detected were mainly $[M+Na]^+$ and $[M+2Na-H]^+$ peaks, whereas the other chemicals were mainly $[M+Na]^+$ and $[M+K]^+$ peaks. At the same laser intensity, glutamic acid was not detected by DHB, and significant background noise was present. In contrast, all 15 compounds present in the plant were detected by the Pt nano pre-coated matrix with a significantly higher S/N. Thus, platinum has a wider detection range and better selectivity.

Soybean extracts were examined and contrasted with DHB to confirm the use of Pt nano matrix. Figure 2 shows the mass spectra, which revealed that the identified compounds were mainly oligosaccharides and lipids. As indicated in Supplementary Table 2, the preliminary qualitative identification was based on the accurate molecular weight, isotopic distribution of the high-resolution mass spectra, and reference to relevant literature (Zhang et al., 2018). The platinum pre-coated matrix significantly increased the signal strength under the same mass spectral circumstances, allowing the detection of lipids, while DHB failed to exhibit a triacylglyceride peak. Using sputtered platinum pre-coated matrix, the triacylglyceride signal peak was found at 40% laser intensity, as a comparison, DHB could detect the triacylglyceride peak only at more than 60% laser intensity (Figure S4). Thus, our prepared platinum pre-coated matrix requires less laser energy than conventional organic matrixes while detecting more mass spectral peaks.

MALDI MSI analysis of oligosaccharides and lipids in germinated wheat and corn kernels

For the wheat seeds to germinate naturally, they were kept at ambient temperature and shielded from light. Wheat seeds undergo several developmental stages after absorbing water, including embryonic enlargement, skin splitting, whitening, bud breaking through the seed coat, rooting, and leaf growth. Following 12 days of germination, when the wheat seeds had developed roots, sprouted leaves, and softened (Figure S5), we collected them for MALDI MSI analysis. Monosaccharides (m/z 203.0526), disaccharides (m/z 365.1054), trisaccharides (m/z 527.1582), tetrasaccharides (m/z689.2110), pentasaccharides (m/z851.2639) and triacylglycerides were mainly detected in germinated wheat seeds. We identified oligosaccharides based on the reference pure chemicals and tandem mass spectrometry (see Figure S6).The MS data revealed a fairly

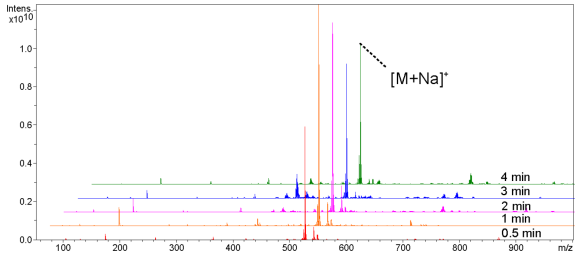

FIGURE 1
Comparison of ion signal intensities of Raffinose at 0.5, 1, 2, 3, and 4 min sputtering times.

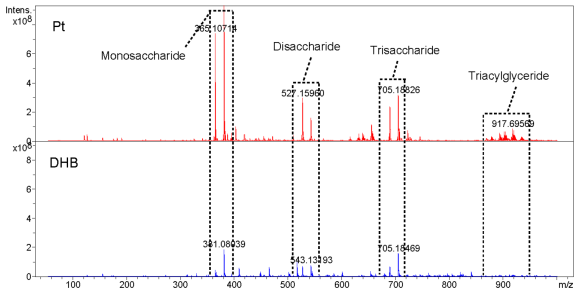

FIGURE 2
Metabolite detection of soybean extracts by MALDI-FTICR MS using pre-coated Pt and DHB as the matrix, respectively(At 50% laser intensity).

regular peak pattern, which matched to fragmented oligosaccharides with an interval (m/z = 162) caused by glycosidic cleavages. In the MS/MS of selected precursors, mass differences of hexose residues (162.05 Da) were annotated. Based on the comparison of the reference pure chemicals, MS/MS and highly regular MS peak patterns, these peaks were considered as oligosaccharides with lengths from 2 to 5 hexose residues, known as disaccharides, trisaccharides, tetrasaccharides and pentasaccharides. Figure 3A demonstrated the spatial distribution features of the components in the seeds. Oligosaccharides were predominantly present uniformly in the endosperm, with the highest content of disaccharides, whose $[M+Na]^+$ peaks were uniformly distributed throughout the endosperm, and the $[M+K]^+$ peaks were predominantly present in the outer endosperm and growing shoots, with a higher concentration in the shoots. In addition to disaccharides, the shoots contained fewer oligosaccharides than the endosperm. The embryo was primarily composed of triacylglycerides with m/z values of 877.7295, 879.7412, 901.7255, and 903.7412. During seed germination, amylase converts the starch in the endosperm into glucose and maltose, which supply energy to the embryo and stimulate it's rooting and germination.

The imaging diagram reveals that the embryo and endosperm are dissimilar and looks perform diverse physiological roles during germination, which is represented in the significant metabolic gap between their separate groups. The great majority of the endosperm in wheat seeds is consisted of starch, which is digested by amylase during germination to form oligosaccharides and then further degraded to produce glucose and maltose (disaccharides). Thus, the high disaccharide content is found in the plant tissue following seed germination. The result is well illustrated by the imaging map, which depicts the high disaccharides concentration in the endosperm.

Fresh sweet corn kernels were fetched for imaging analysis. The results showed that disaccharides and triacylglycerides were mainly present in sweet corn. The primary triacylglycerides were PLL (m/z 877.7295), POL/PLO (m/z 879.7412), POO/PLS (m/z 881.7568), LLL (m/z 901.7255), OLL (m/z 903.7412), OOL (m/z 905.7568), OOO (m/z907.7725) and SOO (m/z 909.7881), in which P is palmitic acid, L is linoleic acid, O is oleic acid and S means stearic acid. Figure 3B demonstrated that the distribution of various triacylglycerides differed between the endosperm and embryo of corn, with the embryo containing the majority of triacylglycerides. The disaccharides were mainly distributed in the endosperm, and no other oligosaccharides were detected in the kernels.

Conclusion

In this study, we proposed a platinum nanomaterial pre-coated matrix as an effective material for various small molecule detection and imaging by MALDI-FTICR MS. The preparation method is simple and can be prepared in batches, which simplifies the experimental steps; high-quality spectra were obtained by optimizing the sputtering time, with good repeatability, greater S/N,

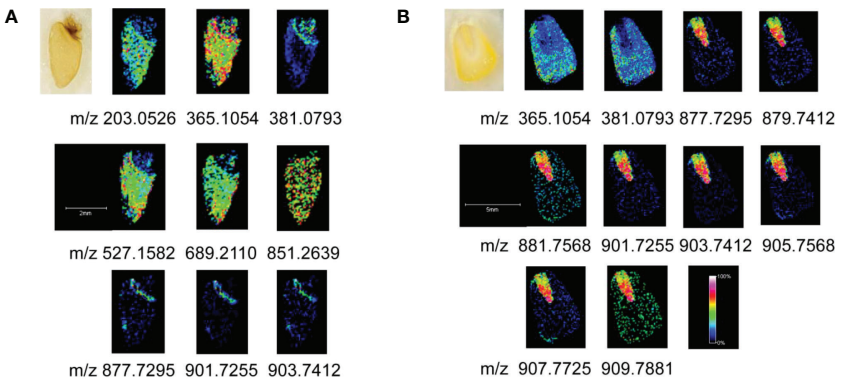

FIGURE 3
MALDI MSI of oligosaccharides and lipids. **(A)** Germinated wheat; **(B)** corn kernels.

and a broader detection range compared to conventional organic matrixes. Using this pre-coated matrix in conjunction with the MALDI MSI technology, high-resolution imaging maps of oligosaccharides and lipids in germinated wheat seeds and fresh corn kernels were acquired. The method also provides basic technical support to study the distribution of oligosaccharides and lipids in plant tissues and will be further utilized to study other plant metabolites in the future.

Data availability statement

The original contributions presented in the study are included in the article/Supplementary Material. Further inquiries can be directed to the corresponding author.

Author contributions

Y-LS: Writing - original draft, participated in the design of the project, methodology, preliminary research and manuscript revision. S-JZ: Participated in the preliminary research. FY: Participated in preparation of platinum pre-coated matrix. CG: Participated in preliminary research. XX: Writing - original draft, participated in the design of the project, methodology, preliminary research and manuscript revision. All authors contributed to the article and approved the submitted version.

Funding

The study is financial funded by the National Natural Science Foundation of China (31671928 and 82074055).

Conflict of interest

The authors declare that the research was conducted in the absence of any commercial or financial relationships that could be construed as a potential conflict of interest.

Publisher's note

Supplementary material

The Supplementary Material for this article can be found online at: https://www.frontiersin.org/articles/10.3389/fpls.2023.1105374/full#supplementary-material

References

Dou, S. Z., Wang, Z. S., Chen, Q. Y., and Lu, N. (2022). One-step fabrication of high-density Si nanotips as SALDI-MS substrate for highly sensitive detection. *Sensors Actuators B: Chemical.* 359, 131578–131587. doi: 10.1016/j.snb.2022.131578

Kawasaki, H., Yonezawa, T., Watanabe, T., and Arakawa, R. (2007). Platinum nanoflowers for surface-assisted laser Desorption/Ionization mass spectrometry of biomolecules. *J. Phys. Chem. C.* 111 (44), 16278–16283. doi: 10.1021/jp075159d

Li, B., Neumann, E. K., Ge, J. Y., Gao, W., Yang, H., Li, P., et al. (2018). Interrogation of spatial metabolome of ginkgo biloba with high-resolution matrix-assisted laser desorption/ionization and laser desorption/ionization mass spectrometry imaging. *Plant Cell Environment.* 41 (11), 2693–2703. doi: 10.1111/pce.13395

Mueller, M. A., Bhandari, D. R., and Spengler, B. (2021). Matrix-free high-resolution atmospheric-pressure SALDI mass spectrometry imaging of biological samples using nanostructured DIUTHAME membranes. *Metabolites.* 11 (9), 624. doi: 10.3390/metabo11090624

Picca, R. A., Calvano, C. D., Cioffi, N., and Palmisano, F. (2017). Mechanisms of nanophase-induced desorption in LDI-MS. a short review. *Nanomaterials* 7 (4), 75/1–75/19. doi: 10.3390/nano7040075

Sagandykova, G., Pryshchepa, O., Rafinska, K., Mametov, R., Madajski, P., and Pomastowski, P. (2022). LDI-MS performance of gold nanostars as an inorganic matrix for low molecular weight analytes. *Int. J. Mass Spectrometry.* 478, 116872–116882. doi: 10.1016/j.ijms.2022.116872

Sakurai, M., Yang, M. R., Xu, J. W., Nguyen, M. T., Yonezawa, T., Hashimoto, K., et al. (2018). Copper ion production using zeolite and application to MALDI MS of small molecules. *Int. J. Mass Spectrom.* 434, 179–184. doi: 10.1016/j.ijms.2018.09.028

Sun, C. L., Zhang, M. M., Dong, H. J., Liu, W., Guo, L. P., and Wang, X. (2020). A spatially-resolved approach to visualize the distribution and biosynthesis of flavones in scutellariabaicalensis georgi. *J. Pharm. Biomed. Analysis.* 179, 113014. doi: 10.1016/j.jpba.2019.113014

Susniak, K., Krysa, M., Gieroba, B., Komaniecka, I., and Sroka-Bartnicka, A. (2020). Recent developments in MALDI MSI application in plant tissues analysis. *Acta Biochim. Polonica.* 67 (3), 277–281. doi: 10.18388/abp.2020_5394

Xu, Y., Deng, Y. Z., Ye, R. R., Gong, C., Liu, Z. X., Zhao, Y. Z., et al. (2021). MALDI-MS imaging of lipids and small molecules in rat brain tissue based on graphene oxide film pre-coated matrix. *Int. J. Mass Spectrometry.* 464, 116573–116580. doi: 10.1016/j.ijms.2021.116573

Zhang, S. D., Gong, C., Lu, Y., and Xu, X. (2018). Separation of triacylglycerols from edible oil using a liquid chromatography-mass spectrometry system with a porous graphitic carbon column and a toluene-isopropanol gradient mobile phase. *J. Am. Oil Chem. Soc* 95 (10), 1253–1266. doi: 10.1002/aocs.12107

frontiers | Frontiers in Plant Science

TYPE Original Research
PUBLISHED 14 February 2023
DOI 10.3389/fpls.2023.1133848

OPEN ACCESS

EDITED BY
Xiaodong Wang,
Minzu University of China, China

REVIEWED BY
Qiang Li,
Huazhong Agricultural University, China
Guo Ziwu,
Chinese Academy of Forestry, China

*CORRESPONDENCE
Wei Fan
fanwei@caf.ac.cn
Yuejin Fu
bj-fyj@163.com
Yun Lu
y.lu@caf.ac.cn

SPECIALTY SECTION
This article was submitted to Technical Advances in Plant Science, a section of the journal Frontiers in Plant Science

RECEIVED 29 December 2022
ACCEPTED 26 January 2023
PUBLISHED 14 February 2023

CITATION
Liu B, Chen Q, Tang L, Zhu L, Zou X, Li B, Fan W, Fu Y and Lu Y (2023) Screening of potential chemical marker with interspecific differences in *Pterocarpus* wood and a spatially-resolved approach to visualize the distribution of the characteristic markers.
Front. Plant Sci. 14:1133848.
doi: 10.3389/fpls.2023.1133848

Screening of potential chemical marker with interspecific differences in *Pterocarpus* wood and a spatially-resolved approach to visualize the distribution of the characteristic markers

Bo Liu[1], Qian Chen[1], Lina Tang[1], Liming Zhu[1], Xianwu Zou[1], Botao Li[1], Wei Fan[2*], Yuejin Fu[1*] and Yun Lu[1*]

[1]Research Institute of Wood Industry, Chinese Academy of Forestry, Beijing, China, [2]State Key Laboratory of Tree Genetics and Breeding, Chinese Academy of Forestry, Beijing, China

Profiling the spatial distributions and tissue changes of characteristic compounds with interspecific differences is critical to elucidate the complex species identification during tree species traceability, wood anti-counterfeiting verification and timber trade control. In this research, in order to visualize the spatial position of characteristic compounds in two species with similar morphology (*Pterocarpus santalinus* and *Pterocarpus tinctorius*), a high coverage MALDI-TOF-MS imaging method was used to found the mass spectra fingerprints of different wood species. 2-Mercaptobenzothiazole matrix was used to spray wood tissue section to enhance the detection effect of metabolic molecules, and the mass spectrometry imaging data were obtained. Based on this technology, the spatial location of fifteen potential chemical markers with remarkable interspecific differences in 2 *Pterocarpus* timber species were successfully obtained. Distinct chemical signatures obtained from this method can promote rapid identification at the wood species level. Thus, matrix-assisted laser desorption/time-of-flight/ionization mass spectrometry imaging (MALDI-TOF-MSI) provides a spatial-resolved way for traditional wood morphological classification and breaking through the limitations of traditional wood identification technology.

KEYWORDS

***Pterocarpus santalinus* and *Pterocarpus tinctorius*, MALDI-TOF-MSI, chemical fingerprint, species-level timber identification, wood anatomy**

Introduction

The strong demand for wood products in the market has led to the rapid growth of the global timber trade volume year on year. After a decline in the early 2000s, the trade volume of illegally harvested timber rose again (Tacconi, 2012). In recent years, tropical timber trade control represented by the species listed in the Convention on International Trade in Endangered Species of Wild Fauna and Flora (CITES) Appendix has been a hot and sensitive issue of global concern. Interpol estimates that 15% - 30% of the global timber trade violates the laws or international treaties of the host country (Irwin, 2019). At present, there were more than 500 wood species belonging to 20 families, 31 genera, have been listed in the CITES Appendix (CITES, 2022), and gradually extended its control scope to various tropical wood species. CITES strives to strengthen coordination and cooperation with other relevant international organizations to further strengthen the management of international timber trade (Belton et al., 1998).

Pterocarpus santalinus (*P. santalinus*) and *Pterocarpus tinctorius* (*P. tinctorius*) have been listed in CITES Appendix II for control and protection. Their logs, wood chips, powders and extracts were prohibited from import, export and trade without an export license or reexport certificate (The World Conservation Union (IUCN), 2022). The macrostructural and microstructural differences between *P. santalinus* and *P. tinctorius* were not obvious (Figure 1). Therefore, it is difficult to distinguish the species differences between them by using the traditional identification of wood anatomy based on structural characteristics of wood. These two species were misidentified frequently both in customs inspections and market consumption. But they were quite different in terms of value and trade restrictions. The traditional timber genus identification based on wood anatomical features has been widely used in botany. However, it is still very difficult to distinguish wood at the species level according to its morphology alone, which has certain limitations (Ng et al., 2016; Liu et al., 2018; Jiao et al., 2019).

In view of the fact that wood morphological methods can only distinguish wood, with the development of analytical instruments and technology, molecular biological analysis and chemical metabolite analysis have been developed for wood identification (Jiao et al., 2018a). Although wood DNA barcode technology can identify 'species', it is expensive, DNA extraction is difficult, usually involves complex procedures, and the technology is not popular. Moreover, for the wood species identification, it still lacks the optimization and determination of universal DNA barcode (Yu et al., 2017; Jiao et al., 2018b). Stable isotope technology can realize the identification of 'species', and can also track the origin of wood. However, this method requires high sample sources and has low resolution (generally greater than 250km). In the field of plant classification and recognition, a general standard database has not been formed yet (Jiao et al., 2014). Some macroscopic features of wood, such as wood color and texture, come from the chemical composition inside the wood (Irwin, 2019). Therefore, the difference of wood histochemical characteristics is also the external manifestation of genomic differences among different species. Each species can leave specific metabolomic evidence under different growth conditions such as different development stages, environment, soil and climate and so on (Gudi et al., 2015). Therefore, wood species identification by using wood metabonomic characteristics combined with various mass spectrometry has become one of the efforts of wood researchers in recent years.

As for chemical analysis, because of its high sensitivity and selectivity, GC-MS (Gas chromatography - mass spectrometry) and LC-MS (Liquid chromatography - mass spectrometry) have been widely employed in life analysis, plant metabolomics, environmental detection, food evaluation and other research fields (Ashton and Rabi, 2016). The mobile phase of GC-MS is gas (such as helium), which is very suitable for analyzing low-grade and low-boiling metabolites that are easy to vaporize, and for samples of thermally stable molecules. The mobile phase of LC-MS is liquid, which is not affected by sample volatility and thermal stability. However, sample treatment is required before determination, such as uniform grinding or cutting, and extraction of samples. Compared with GC-MS, LC-MS has more longer sample pretreatment and higher cost of organic solvent consumption. In addition, although the sample preparation process of DART-MS (Direct analysis in real time mass spectrometry) technology is simple (Zhang et al., 2019a), but like the other two technologies, the location and spatial concentration information of the target in the tissue cannot be obtained, which is very useful for studying the correlation between wood chemical composition and wood macro- and micro-structural characteristics in wood identification.

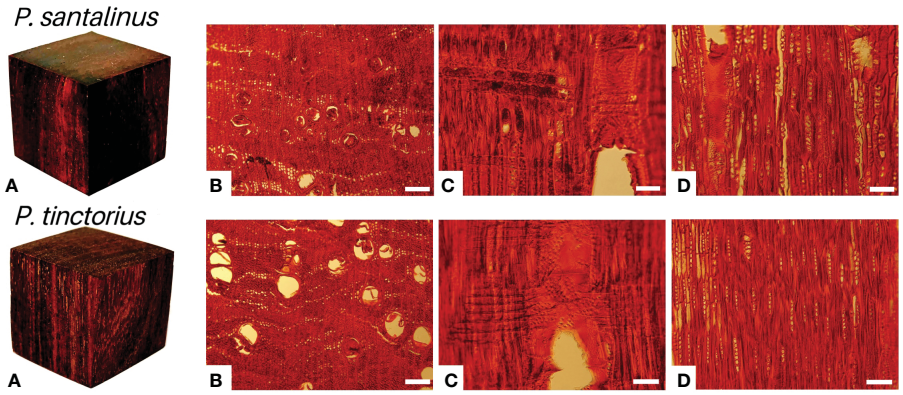

FIGURE 1
Macroscopic **(A)** and microscopic photographs **(B–D)** of *P. santalinus* and *P. tinctorius*. **(B–D)**-Transverse, radial and tangential sections of *P. santalinus* and *P. tinctorius*, respectively. Scale bars, 200 μm **(B)** and 100 μm **(C, D)**.

MALDI-TOF-MSI (Matrix-assisted laser desorption/ionization time-of-flight mass spectrometry imaging) is and effective technique to characterize tissue molecule profiles, which has the advantages of accuracy, rapidity and high throughput, especially in the aspect of molecular specificity (Lu et al., 2017). As a label free detection technology, it can analyze various types of compounds, such as metabolite of small molecules, lipids, peptides, glycans, proteins and drug molecules, and can be used to find disease markers, explore differences between different groups, or determine the spatial distribution of target molecules. Compared with traditional methods, such as GC-MS and LC-MS, MALDI-TOF-MSI does not require complex sample pretreatment, labeling and chromatographic separation, thus can reduce the change and loss of active components, which is more suitable for the analysis of complex samples (Cornett et al., 2007). MALDI-TOF-MSI allows the spatially resolved detection of thousands of compounds in a single tissue section, and has been widely used in many biological systems of plants (Debois et al., 2014; Shroff et al., 2015) For instance, MALDI-TOF-MSI was used for the analysis of the functional metabolite of ginseng, the active ingredient of aloe, the development regulation of *Arabidopsis thaliana*, the ingredients of ginkgo leaves, and the flavonoids in Huangceng, etc. (Kuo et al., 2019; Sun et al., 2019; Liu et al., 2019a; Li et al., 2020; Sun et al., 2021). The localization of metabolites in roots, leaves and tender stems was visualized by MALDI-TOF-MSI for the study of the classification of ginsenosides and the distribution of flavonoids and other metabolites. Therefore, MALDI-TOF-MSI has great potential in visualizing the structural components of wood tissue. In this study, the MALDI-TOF-MSI approach was applied for the rapid identification of two precious *Pterocarpus* species controlled by CITES, and the spatial location of the characteristic compounds with interspecific differences in the two species was imaged for the first time.

Materials and methods

Materials and reagents

Wood specimens of *P. santalinus* and *P. tinctorius* heartwood were supplied from Wood Collections of Chinese Academy of Forestry (WOODPEDIA). Indium-tin oxide (ITO) coated glass slides and double-sided conductive tape were purchased from China's Sinopharm. ACN in chromatographic grade were purchased from Merck (Darmstadt, Germany). TFA were purchased from Sigma-Aldrich (Taufkirchen, Germany). ddH_2O was purified by filtration system (Sartorius arium-comfort II, Germany). 2-MBT were supplied by Bruker Beijing laboratory (Bruker, Germany).

Matrix coating

Matrix coating was carried out with an ImagePrep electronic matrix sprayer (Bruker Daltonics, Germany). The spray of matrix was performed according to the spray method provided by the instrument. The MALDI matrix for each wood section detection was 6 mL 2-MBT, which was prepared by ACN (12mg/mL), TFA and double distilled water (80:0.2:19.8, v/v/v). In previous researches, 2-MBT, DMCA, 2,5-dihydroxybenzoic acid, α- cyano-4-hydroxycnmic acid, graphene oxide, and silver nanoparticles have been used as matrices. It was found that 2-MBT had better ionization efficiency, more effective signal peaks and better signal intensity for wood slices (He et al., 2019; Liu et al., 2019b).

Sample preparation

Small wood blocks of about 1 cm^3 were cut from each specimen, without any chemical or boiling treatment. Transverse sections of 20 μm in thickness were cut with a sliding microtome (Leica SM2010R, Germany). All sections were held flatly by slides for optical imaging and matrix coating. Before entering the mass spectrometer, the wood slices were sticked on indium-tin oxide (ITO) coated glass slides with double-sided conductive tape by using clean tweezers. 6 mL of 2-MBT matrix solution was uniformly sprayed onto the surface of the wood tissue by ImagePrep electronic matrix sprayer in two times (3 mL each time). After 2-3 seconds of spray each time, the slices were then slightly dried for 60-120 seconds. This process was repeated 50 times. The whole spraying process took about 40 minutes. After being sprayed, the wood slices were put into a vacuum tank for 10 minutes drying. During spraying, be sure to keep the spraying environment wet enough. The coated glass slides were installed on the imaging target plate, and then put it into the mass spectrometer.

MALDI-TOF-MSI

All of the profiling and imaging experiments were carried out using a Bruker Autoflex Speed MALDI-time-of-flight (TOF)/TOF mass spectrometer (Bruker Daltonics, Germany), equipped with a 2000 Hz solid-state, Smartbeam Nd: YAG laser (355 nm). Sample was analyzed in the positive-ion and reflection mode with broadband detection. A mass range of m/z 400 to 1300 were performed. 50 μm laser raster step-sizes was used for the *in situ* detection of low-molecular weight compounds in wood tissue sections. When collecting profiling data, evenly print 30 points each time, 100 shots for each point (if the ideal peak cannot be found, then evenly print 30 points each time, 200 shots for each point). A total of 3000 shots are stacked as one time, and each wood slice was printed 3 times, and 3 profiling data were saved respectively. All wood samples were tested under the same conditions (including laser energy, detector gain, number of shots, etc.).

Data analysis

For data collected from MALDI-TOF-MSI, the Bruker's FlexAnalysis 3.4 software was performed for the analysis of the preliminary mass spectra. According to the botanical structure characteristics of National standard of the People's Republic of China: Hongmu (General Administration of Quality Supervision, Inspection and Quarantine of the People's Republic of China, 2017), the fiber, vessel, axial parenchyma, wood ray and other tissues in the measurement area of each sample were defined. In each sample, these four tissue regions of wood structure were also

areas of interest for the distribution analysis of metabolic compounds. The Bruker FlexImaging 4.1 software was used for the reconstruction of the ion map of low molecular weight compounds.

Results and discussion

MALDI-TOF-MS analysis of *P. santalinus* and *P. tinctorius*

The representative heartwood samples were selected from the herbarium, and the chemical fingerprints of two species have been obtained through the detection of MALDI-FOF-MS. The flow chart of analytical methods was shown in Figure S1. The overall average mass spectra of *P. santalinus* and *P. tinctorius* gained by MALDI-TOF-MSI under positive ionization mode were showed in Figure 2. In the range of 400-1300 m/z, chemical signals were detected in the mass spectra of *P. santalinus* and *P. tinctorius*, and the *P. santalinus* samples showed more high abundant ions than *P. tinctorius*. However, when the wood chip samples of *P. santalinus* and *P. tinctorius* detected by DART-FTICR-MS, the peak range was 200-800 m/z (Zhang et al., 2019a). There was a significant difference between the number of peaks detected in the mass spectra of *P. santalinus* and *P. tinctorius* (Figure S2). 202 peaks were detected in *P. santalinus* and 123 peaks were detected in *P. tinctorius* (Table S1). The *P. santalinus* sample has about 64% more peaks than *P. tinctorius*. The wavelength and shape of peaks in the spectra of *P. santalinus* and *P. tinctorius* were very similar. There were 96 common peaks, such as 421.66, 465.62, 497.58, 582.76, 596.77, 747.66 and 886.04 m/z, but the abundance of ions were more or less different. Several significantly different peaks can be observed from the spectra, such as 465.54, 529.47, 885.97 and 1202.48 m/z, which hardly existed in the spectra of *P. tinctorius*, and 497.49 and 1052.91 m/z, which could be found in the spectra of *P. santalinus*. These peaks with significant differences are benefit the differentiation of the two wood species.

MALDI-TOF-MSI analysis of *P. santalinus* and *P. tinctorius*

Figure 3 showed the tissue heterogeneity distribution of some representative molecules. Ion images directly showed the existence of significantly different metabolites in the two kinds of wood slices. Such as m/z 504.7, 529.5, 616.7, 879.6, 895.6, 111.6, 1216.5, 1218.5, 1230.5, 1236.4 (Figure 3B5, B15, B20, B21, B24, B29, B31, B32, B33), among these peaks, the ion abundance of *P. tinctorius* was very small or absent, while at the m/z 458.6, 534.8, 582.7, 854.7, 926.6, 1052.9, 1140.6, 1272.9 (Figure 3A3, A6, A11, A19, A22, A23, A25, A34) etc., the ion abundance of *P. santalinus* was very small or absent. This result is consistent with the specific peaks obtained from the mass spectrum, showed in Table S1. Ion image showed that some metabolites with low relative content (in blue) can also be observed and detected by MALDI-TOF-MSI. Common LC-MS will homogenize plant tissue, and metabolites with low content cannot be detected, but MALDI-TOF-MS can detect metabolites with low content at a specific location. MALDI-TOF-MS imaging makes it easy to intuitively lock the category of differential compounds of two wood species, and facilitate further exploration through data analysis. As showed in Figure 4, volcano plot displayed two important indicators (Fold change/p-Value). With more than 1.5 times of change and $P<0.05$ as the screening condition, the differential metabolites that can serve as marker compounds between the two wood species can be screened intuitively and reasonably. The differential metabolites screened from the volcano plot include all the significant differential metabolites shown in the ion image. It fully shows that mass spectrometry imaging has the ability to screen differential expression factors among samples, and is more intuitive than the results of mathematical statistics.

The ion images showed the heterogeneous distribution and relative abundance of different metabolites in wood xylem tissues, which were obviously related to the botanical structure of *P. santalinus* and *P. tinctorius*. It mainly involves four types of tissues, namely fiber, axial parenchyma cell, wood ray and vessel (Figure 3A1, B1). The location of metabolites in wood tissue structure can be preliminarily determined by corresponding optical images of tissue section. The anatomical characteristics of the parenchyma cells of *P. santalinus and P. tinctorius* are tangential banded, aliform or confluent, with obvious structural characteristics, so it is better to locate and compare the distribution of metabolites in the ion images. Some metabolites are obviously distributed in parenchyma cells, such as m/z 566.7, 596.7, 610.7, 747.6 and 749.6, the relative content of metabolites in the parenchyma cells of *P. santalinus* was about 50-75%. While in the parenchyma cells of *P. tinctorius*, the relative

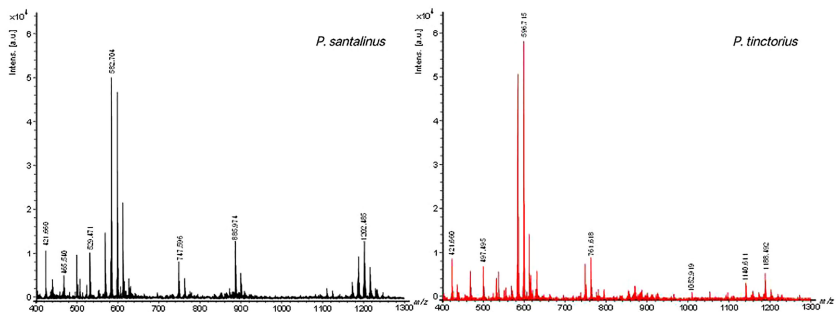

FIGURE 2
MALDI-TOF mass spectra of wood slices of *P. santalinus* (black) and *P. tinctorius* (red).

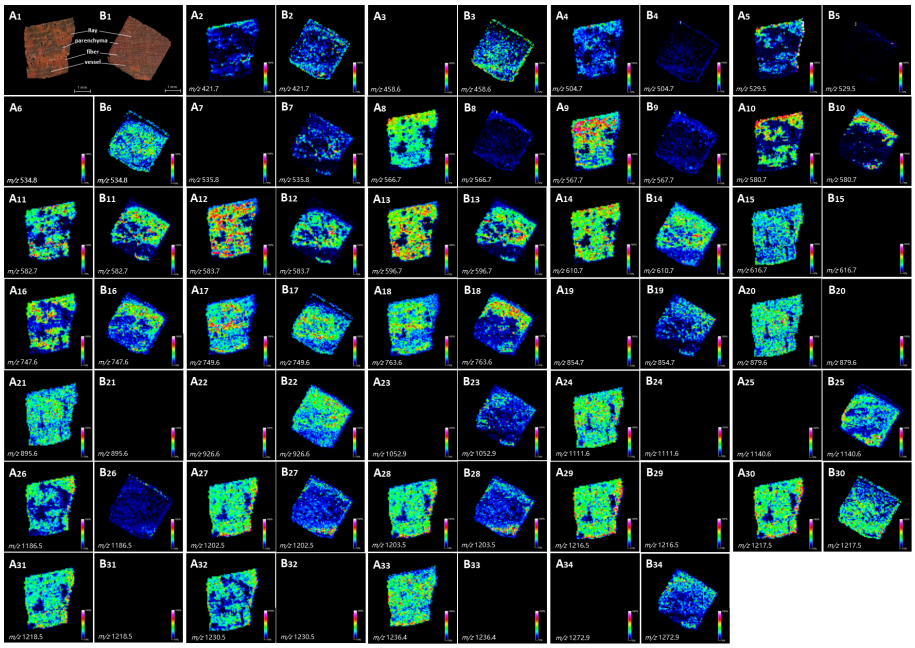

FIGURE 3
Optical images of tissue sections and localization modes of metabolite ions in wood slices of *P. santalinus* and *P. tinctorius* with significant differences. **(A1, B1)**, optical images of tissue section of *P. santalinus* and *P. tinctorius*, respectively, including four main types of tissue cells. **(A2–A34, B2–B34)**, localization modes of metabolite ions in wood slices of *P. santalinus* and *P. tinctorius*, respectively.

content of metabolites m/z 610.7, 747.6 and 749.6 can also reach about 50%. Wood fiber is the cell type with the largest tissue proportion in the *Pterocarpus* species. The high abundant metabolites are distributed in the wood fiber cells of the two species, with the widest relative content range. In *P. santalinus*, m/z 567.7, 583.7, 596.7, 610.7, 763.6, 879.6, 1111.6, 1202.5, 1203.5, 1217.5 and 1236.4 etc. were involved, and m/z 596.7, 763.6, 854.7 and 926.6 etc. were involved in *P. tinctorius*. There were also many metabolites with high content in the wood ray cells. Because both *P. santalinus* and *P. tinctorius* are all rays storied, and the rays are thin and densely arranged, the ion image on the wood transverse section showed a clear distribution.

The distribution quantity of metabolites in *P. santalinus* is obviously more than that in *P. tinctorius* (Figure 5). The ion image showed that there were few high abundance metabolites in the vessel, which may also be related to the fine wood structure of the two species, namely, the vessel diameter was small, the vessel arranged not too tightly (vessels exclusively solitary or few in radial multiples of 2-3 cells, scattered in 2-5 cells/mm^2) and the distribution density was also small, so the vessel tissue structure was not fully displayed. In general, there were more metabolites in fibers, parenchyma cells and rays, and less metabolites in vessel were observed by ion imaging, which has a certain relationship with tissue ratio and resolution of ion imaging. The localization of all metabolites revealed by ion imaging combined

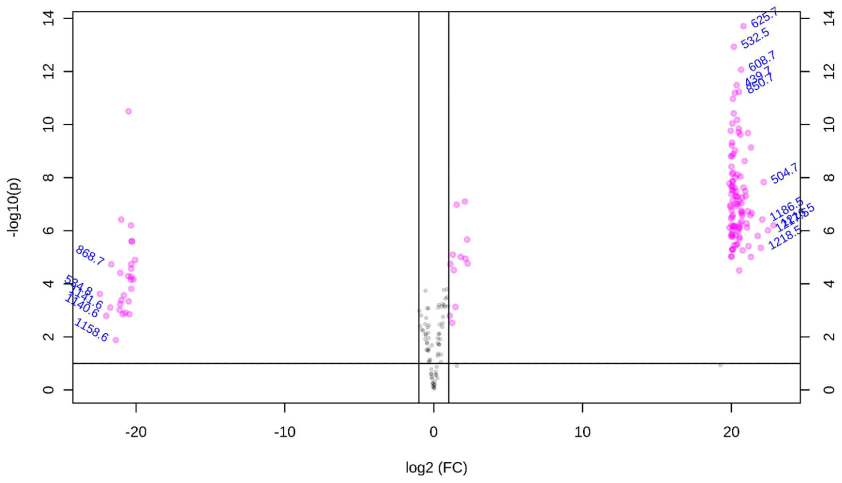

FIGURE 4
Volcano plot results of *P. santalinus* and *P. tinctorius*.

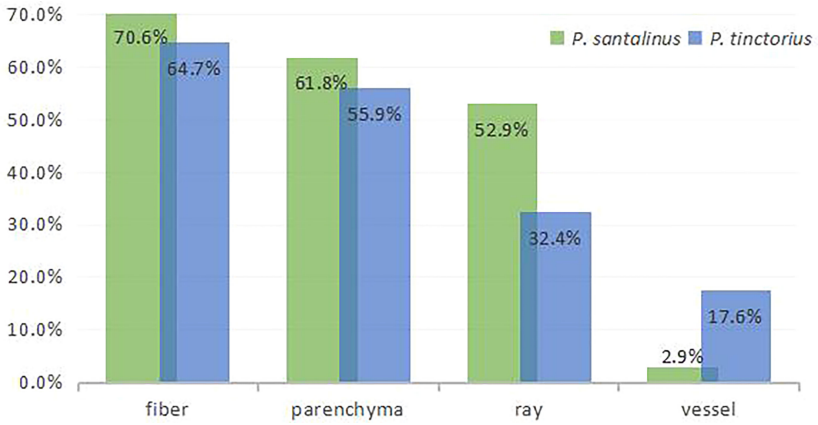

FIGURE 5
Histogram of tissue distribution of metabolites detected by MALDI-TOF-MSI.

the chemical information and histological characteristics of plants, which is helpful to understand the coevolution and provenance relationship between two species of *Pterocarpus* wood. MALDI-TOF-MSI analysis made up the gap between morphology and chemistry in complex biological samples.

Markers for the identification of *P. santalinus* and *P. tinctorius*

PCA (Principal Component Analysis) is a commonly used multivariate statistical method to investigate the correlation between multiple variables. Through linear dimensionality reduction of data, it can generate features that are easy to be found and more easily understood by humans (Rasmus and Age 2014; Hur et al., 2010). The PCA score plot of the MALDI-TOF-MS spectra of *P. santalinus* and *P. tinctorius* were shown in Figure S3. The results showed clustering behavior related to the wood species. All samples were divided into two independent groups. The separation trend between the two groups was good, and there was no abnormal point. PCA can effectively process high-dimensional data, but is not sensitive to variables with small correlation. PLS-DA (Partial least squares Discriminant Analysis) integrates multiple linear regression analysis, canonical correlation analysis and principal factor analysis, which can avoid potential problems such as data non normal distribution, factor indeterminacy and model failure to identify. Variable importance on projection (VIP) is the variable weight value of the PLS-DA model variable, which is used to measure the influence intensity and interpretation ability of the accumulation difference of various metabolites on the classification and discrimination of each group of samples. VIP value larger than 1 is a common screening standard for different metabolites (Ahn et al., 2020). The variables are sorted by combining the VIP value and the p value in the t-test, and the selected highly correlated variables can be considered as candidate variables for species differences (Rajalahti et al., 2009). Due to the high dimensional and massive characteristics of mass spectrometry data, the principle of VIP value larger than 1.5 and P value less than 0.05 was used to screen potential markers of interspecific differences by combining single-dimensional and multi-dimensional statistical analysis methods. Using this screening principle, fifteen variables were considered as markers (Figure S4 and Table 1). The fifteen variables were all in the significant screening results of interspecific differences in ion images obtained by MALDI-TOF-MSI (Figure 3). Each variable has high VIP value and strong species difference expression. The results of heat map (Figure S5) and correlation analysis (FigureS6) also confirm this result. It is indicated that the fifteen variables can be used as chemical markers for samples classification of *P. santalinus* and *P. tinctorius*, which can effectively reduce the time and workload of locating compounds and massive data evaluation.

For dry wood, especially the identification of chemical components of wood specimens that have been dried and preserved for many years or even decades, it has always been a difficult point in the field of wood identification, whether it is the use of DNA extraction technology, or the use of chemical component chromatography/mass spectrometry technology for species level identification (Jiao et al., 2018b; Zhang et al., 2019b). Compared with fresh plant materials, such as leaves, roots, stems, or xylem of fresh wood, secondary mass spectrometry can be obtained to identify compounds by MALDI-TOF-MS/MS (Wang et al., 2016; Kuo et al., 2019; Li et al., 2020; Shen et al., 2022). However, for dry wood, compared with fresh tissue, it is difficult to ionize. We have not succeeded in obtaining secondary mass spectrometry using MALDI-TOF-MS/MS in this study. If the secondary mass spectrometry of dried wood samples can be obtained, combined with the ion image of MALDI-TOF-MSI, it can improve the understanding of the unique functions of individual species and their biological functions in plant growth and development, as well as the impact on the macro and micro properties of wood.

MALDI-TOF-MSI is a powerful, cost-effective, fast and robust species classification technology, which has been successfully applied to the classification and identification of microorganisms, herbal active substances and proteins. However, the wood MALDI-TOF-MSI database is not yet available, which does not meet the needs of wood identification and classification. In order to further distinguish species that are closely related and difficult to classify, it is increasingly important to establish, categorize and expand databases.

TABLE 1 Potential chemical markers for the interspecific differentiation of *P. santalinus* and *P. tinctorius*.

Mass measured	PLS-DA VIP scores	Relative peak intensity		Localization	
		P. santalinus	*P. tinctorius*	*P. santalinus*	*P. tinctorius*
566.7	5.00	30%	5.8%	fiber, pyrenchyma cell	fiber, pyrenchyma cell
1202.5	4.50	26.3%	4.3%	fiber, pyrenchyma cell, ray	fiber, pyrenchyma cell
610.7	3.75	43.7%	25.6%	fiber, pyrenchyma cell, ray	fiber, pyrenchyma cell, ray
1216.5	3.25	14.7%	0	fiber, pyrenchyma cell, ray	—
1203.5	2.75	16.5%	3.4%	fiber, pyrenchyma cell, ray	fiber, pyrenchyma cell
1217.5	2.55	11.5%	0	fiber, pyrenchyma cell, ray	—
529.5	2.50	21.2%	0	fiber	—
534.8	2.45	0	11.2%	—	fiber, vessel
504.7	2.10	9.4%	0	fiber	—
582.7	2.05	100%	87.2%	—	fiber, pyrenchyma cell, ray
1186.5	1.95	8.7%	1.2%	fiber	fiber
567.7	1.80	11.8%	3.1%	fiber, ray	fiber
1140.6	1.75	0	10.7%	—	fiber, pyrenchyma cell
1218.5	1.70	8.4%	0	fiber, pyrenchyma cell, ray	—
580.7	1.65	17.2%	8.6%	fiber, pyrenchyma cell, ray	fiber, pyrenchyma cell

Conclusion

Through accurate, rapid and high-throughput MALDI-TOF-MSI analysis of dried wood tissue sections, fifteen potential chemical markers were determined to identify two species of *Pterocarpus*. The results clearly demonstrate that MALDI-TOF-MSI combining multivariate statistical analysis is suitable for the rapid and effective species-level identification of *P. santalinus* and *P. tinctorius*. MALDI Imaging is a powerful tool for visualizing the wood metabolites of *P. santalinus* and *P. tinctorius* for the first time. Some substances with very low content can be detected. Results verified not only the feasibility of using MALDI-TOF-MSI method to identify wood, but also the possibility of using dry wood instead of leaves or fresh tissue as the detection objective, when wood is the plant material to be identified. We hope that in the future, we can carry out chemical fingerprinting research based on MALDI-TOF-MSI for more wood species with similar anatomical characteristics and difficult to distinguish, build a database, and provide technical support for curbing illegal timber logging activities and for protecting endangered and valuable wood species. The compatibility between different mass spectra and the in-depth mining analysis of chemical markers will also be the future research direction of the application of chromatography-mass spectrometry technology in the analysis of different compounds.

Data availability statement

The raw data supporting the conclusions of this article will be made available by the authors, without undue reservation.

Author contributions

BLiu, YL and YF contributed to the conception and design of the study, QC, LT and LZ performed the experiment, XZ and BLi performed data analyses, and BLiu and WF wrote the manuscript. All authors contributed to the article and approved the submitted version.

Funding

This work was supported financially by the National Natural Science Foundation of China (Grant No. 31870539 and 31870535), the Fundamental Research Funds of the Chinese Academy of Forestry (Grant No. CAFYBB2022ZC002).

Acknowledgments

We would like to express our gratitude to Dr. Liang Qin of Centre for Imaging and Systems Biology, Minzu University of China for experimental guidance and technical support, and the xylarium (wood collection) of the Chinese Academy of Forestry (WOODPEDIA) for its help in providing wood samples.

Conflict of interest

The authors declare that the research was conducted in the absence of any commercial or financial relationships that could be construed as a potential conflict of interest.

The reviewer GZ declared a shared affiliation with the authors to the handling editor at the time of review.

Publisher's note

All claims expressed in this article are solely those of the authors and do not necessarily represent those of their affiliated organizations, or those of the publisher, the editors and the reviewers. Any product that may be evaluated in this article, or claim that may be made by its manufacturer, is not guaranteed or endorsed by the publisher.

Supplementary material

The Supplementary Material for this article can be found online at: https://www.frontiersin.org/articles/10.3389/fpls.2023.1133848/full#supplementary-material

References

Ahn, H. S., Yeom, J., Yu, J., Kwon,, Y. I., Kim, J. H., Kim, K., et al. (2020). Convergence of plasma metabolomics and proteomics analysis to discover signatures of high-grade serous ovarian cancer. *Cancers* 12 (11), 3447. doi: 10.3390/cancers12113447

Ashton, D. L., and Rabi, A. M. (2016). Rapid high-throughput species identification of botanical material using direct analysis in real time high resolution mass spectrometry. *J. Visualized Experiments* 116, 1–11. doi: 10.3791/54197

Belton, P. S., Colquhoun, I. J., Kemsley, E. K., Delgadillo, I., et al. (1998). Application of chemometrics to the 1H NMR spectra of apple juices: Discrimination between apple varieties. *Food Chem.* 61 (1), 207–213. doi: 10.1016/s0308-8146(97)00103-9

Cornett, D. S., Reyzer, M. L., Chaurand, P., and Caprioli, R. M. (2007). MALDI imaging mass spectrometry: Molecular snapshots of biochemical systems. *Nat. Methods* 4, 828–833. doi: 10.1038/nmeth1094

Debois, D., Jourdan, E., Smargiasso, N., Thonart, P., De Pauw, E., and Ongena, M. (2014). Spatiotemporal monitoring of the antibiome secreted by bacillus biofilms on plant roots using MALDI mass spectrometry imaging. *Anal. Chem.* 864431–4438. doi: 10.1021/ac500290s

Dormontt, E. E., Boner, M., Braun, B., Breulmann, G., Degen, B., Espinoza, E., et al. (2015). Forensic timber identification: It's time to integrate disciplines to combat illegal logging. *Biol. Conserv.* 191, 790–798. doi: 10.1016/j.biocon.2015.06.038

Gudi, G., Krahmer, A., Kruger, H., and Schulz, H. (2015). Attenuated total reflectancefourier transform infrared spectroscopy on intact dried leaves of sage (*Salvia officinalis* l.): Accelerated chemotaxonomic discrimination and analysis of essential oil composition. *J. Agric. Food Chem.* 63, 8743–8750. doi: 10.1021/acs.jafc.5b03852

He, H., Qin, L., Zhang, Y., Han, M., Li, J., Liu, Y., et al. (2019). 3,4-dimethoxycinnamic acid as a novel matrix for enhanced *In situ* detection and imaging of low-Molecular-Weight compounds in biological tissues by MALDI-MSI. *Anal. Chem.* 91, 2634–2643. doi: 10.1021/acs.analchem.8b03522

Hur, M., Yeo, I., Park, E., Kim, Y. H., Yoo, J., Kim, E., et al. (2010). Combination of statistical methods and Fourier transform ion cyclotron resonance mass spectrometry for more comprehensive, molecular-level interpretations of petroleum samples. *Anal. Chem.* 82, 211–218. doi: 10.1021/ac901748c

Ida, H., Mihaly, C., Erik, D. K., Lene, R. N., and Ida, T. (2015). The use of DNA barcoding in identification and conservation of rosewood (*Dalbergia* spp.). *PloS One* 179, 113014. doi: 10.1371/journal.pone.0138231

Irwin, A. (2019). Tree sleuths are using DNA tests and machine vision to crack timber crimes. *Nature* 73 (2), 19–21. doi: 10.1038/d41586-019-01035-7

Jiao, L., He, T., Eleanor, E. D., Zhang, Y., Andrew, J. L., and Yin, Y. (2018a). Applicability of chloroplast DNA barcodes for wood identification between *Santalum album* and its adulterants. *Holzforschung*. doi: 10.1515/hf-2018-0047

Jiao, L., Lu, Y., He, T., Li, J., and Yin, Y. (2019). A strategy for developing high-resolution DNA barcodes for species discrimination of wood specimens using the complete chloroplast genome of three pterocarpus species. *Planta* 250, 95–104. doi: 10.1007/s00425-019-03150-1

Jiao, L., Yin, Y., Cheng, Y., and Jiang, X. (2014). DNA Barcoding for identification of the endangered species aquilaria sinensis: Comparison of data from heated or aged wood samples. *Holzforschung* 68 (4), 487–494. doi: 10.1515/hf-2013-0129

Jiao, L., Yu, M., Alex, C. W., He, T., Li, J., Liu, B., et al. (2018b). DNA Barcode authentication and library development for the wood of six commercial *Pterocarpus* species: The critical role of xylarium specimens. *Sci. Rep.* 8:1945, 1–10. doi: 10.1038/s41598-018-20381-6

Kuo, T. H., Huang, H. C., and Hsu, C. C. (2019). Mass spectrometry imaging guided molecular networking to expedite discovery and structural analysis of agarwood natural products. *Analytica Chimica Acta* 1080, 95–103. doi: 10.1016/j.aca.2019.05.070

Liu, Y., Chen, L., Qin, L., Han, M., Li, J., Luo, F., et al. (2019b). Enhanced *in situ* detection and imaging of lipids in biological tissues by using 2,3-dicyanohydroquinone as a novel matrix for positive-ion MALDI-MS imaging. *Chem. Commun.* 55, 12559. doi: 10.1039/c9cc06961e

Liu, H., Guo, S., Lu, M., Zhang, Y., Li, J., Wang, W., et al. (2019a). Biosynthesis of DHGA12 and its roles in arabidopsis seedling establishment. *Nat. Commun.* 10, 1768. doi: 10.1038/s41467-019-09467-5

Liu, Y., Xiang, L., Zhang, Y., Lai, X., Xiong, C., Li, J., et al. (2018). DNA Barcoding based identification of *Hippophae* species and authentication of commercial products by high resolution melting analysis. *Food Chem.* 242, 62–67. doi: 10.1016/j.foodchem.2017.09.040

Li, S., Zhu, N., Tang, C., Duan, H., Wang, Y., Zhao, G., et al. (2020). Differential distribution of characteristic constituents in root, stem and leaf tissues of *Salvia miltiorrhiza* using MALDI mass spectrometry imaging (Pre-proof). *Fitoterapia* 146, 104679. doi: 10.1016/j.fitote.2020.104679

Lu, M., Yang, X., Yang, Y., Qin, P., Wu, X., and Cai, Z. (2017). Nanomaterials as assisted matrix of laser Desorption/Ionization time-of-Flight mass spectrometry for the analysis of small molecules. *Nanomaterials* 7 (4), 87. doi: 10.3390/nano7040087

General Administration of Quality Supervision, Inspection and Quarantine of the People's Republic of China. (2017). *National standard of the People's republic of China: Hongmu (GB/T 18107-2017)*.

Ng, K. K., Lee, S. L., Tnah, L. H., Nurulfarhanah, Z., Ng, C. H., Lee, C. T., et al. (2016). Forensic timber identification: A case study of a cites listed species, *Gonystylus bancanus* (Thymelaeaceae). *Forensic Sci. Int. Genet.* 23, 197–209. doi: 10.1016/j.fsigen.2016.05.002

Rajalahti, T., Arneberg, R., Berven, F. S., Myhr, K. M., Ulvik, R. J., and Kvalheim, O. M. (2009). Biomarker discovery in mass spectral profiles by means of selectivity ratio plot. *Chemom. Intell. Lab. Syst.* 95, 35–48. doi: 10.1016/j.chemolab.2008.08.004

Rasmus, B., and Age, K. S. (2014). Principal component analysis. *Anal.* 6, 2812–2831. doi: 10.1039/C3AY41907J

Shen, B., Yang, X., Sarah, E. N., Yang, X., Liu, Y., Jia, S., et al. (2022). Cell-based ambient venturi autosampling and matrix-assisted laser desorption ionization mass spectrometric imaging of secretory products. *Anal. Chem.* 94, 3456–3466. doi: 10.1021/acs.analchem.1c03625

Shroff, R., Schramm, K., Jeschke, V., Nemes, P., Vertes, A., Gershenzon, J., et al. (2015). Quantification of plant surface metabolites by MALDI mass spectrometry imaging: glucosinolates on arabidopsis thaliana leaves. *Plant J.* 81961–972. doi: 10.1111/tpj.12760

Sun, C., Ma, S., Li, L., Wang, D., Liu, W., Liu, F., et al. (2021). Visualizing the distributions and spatiotemporal changes of metabolites in panax notoginseng by MALDI mass spectrometry imaging. *J. Ginseng Res.* doi: 10.1016/j.jgr.2021.04.001

Sun, C., Zhang, M., Dong, H., Liu, W., Guo, L., and Wang, X. (2019). A spatially-resolved approach to visualize the distribution and biosynthesis of flavones in *Scutellaria baicalensis* georgi. *J. Pharm. Biomed. Anal.* doi: 10.1016/j.jpba.2019.113014

Tacconi, L. (2012). *Illegal logging: "Law enforcement, livelihoods and the timber trade"* (Routledge: Earthscan).

The World Conservation Union (IUCN). (2022). Convention on international trade in endangered species of wild fauna and flora appendices I, II and III. *CoP19*.

Tsumura, Y., Kado, T., Yoshida, K., Abe, H., Ohtani, M., Taguchi, Y., et al. (2011). Molecular database for classifying shorea species (*Dipterocarpaceae*) and techniques for checking the legitimacy of timber and wood products. *J. Plant Res.* 124, 35–48. doi: 10.1007/s10265-010-0348-z

Wang, S., Bai, H., Cai, Z., Gao, D., Jiang, Y., Liu, J., et al. (2016). MALDI imaging for the localization of saponins in root tissues and rapid differentiation of three *Panax* herbs. *Electrophoresis* 37, 1956–1966. doi: 10.1002/elps.201600027

Yu, M., Jiao, L., Guo, J., Alex, C. W., He, T., Jiang, X., et al. (2017). DNA Barcoding of vouchered xylarium wood specimens of nine endangered *Dalbergia* species. *Planta* 246, 1165–1176. doi: 10.1007/s00425-017-2758-9

Zhang, M., Zhao, G., Guo, J., Alex, C. W., Charles, C. L., and Yin, Y. (2019a). Timber species identification from chemical fingerprints using direct analysis in real time (DART) coupled to Fourier transform ion cyclotron resonance mass spectrometry (FTICR-MS): comparison of wood samples subjected to different treatments. *Holzforschung* 73 (11), 975–985. doi: 10.1515/hf-2018-0304

Zhang, M., Zhao, G., Liu, B., He, T., Guo, J., Jiang, X., et al. (2019b). Wood discrimination analyses of *Pterocarpus tinctorius* and endangered *Pterocarpus santalinus* using DART-FTICR-MS coupled with multivariate statistics. *IAWA J.* 40 (1), 58–74. doi: 10.1163/22941932-40190224

frontiers | Frontiers in Plant Science

TYPE Original Research
PUBLISHED 24 February 2023
DOI 10.3389/fpls.2023.1144449

OPEN ACCESS

EDITED BY
Xiaodong Wang,
Minzu University of China, China

REVIEWED BY
Haiqiang Liu,
Minzu University of China, China
Ronghui Gu,
Guizhou University, China

*CORRESPONDENCE
Fang Ju
291838679@qq.com

†These authors have contributed equally to this work

SPECIALTY SECTION
This article was submitted to Technical Advances in Plant Science, a section of the journal Frontiers in Plant Science

RECEIVED 14 January 2023
ACCEPTED 13 February 2023
PUBLISHED 24 February 2023

CITATION
Liu Y, Nie X, Wang J, Zhao Z, Wang Z and Ju F (2023) Visualizing the distribution of flavonoids in litchi (*Litchi chinenis*) seeds through matrix-assisted laser desorption/ionization mass spectrometry imaging. *Front. Plant Sci.* 14:1144449. doi: 10.3389/fpls.2023.1144449

Visualizing the distribution of flavonoids in litchi (*Litchi chinenis*) seeds through matrix-assisted laser desorption/ionization mass spectrometry imaging

Yukun Liu[1†], Xiaofei Nie[2†], Jilong Wang[3], Zhenqi Zhao[4], Zhimei Wang[5] and Fang Ju[2*]

[1]Department of Breast Surgery, Breast Disease Center, Affiliated Qingdao Central Hospital, Qingdao University, Qingdao, China, [2]Department of Oncology, Affiliated Qingdao Central Hospital, Qingdao University, Qingdao, China, [3]Department of Acupuncture and Moxibustion, Affiliated Qingdao Central Hospital, Qingdao University, Qingdao, China, [4]Department of Radiology, Affiliated Qingdao Central Hospital, Qingdao University, Qingdao, China, [5]Department of Gynecological Neoplasms, Affiliated Qingdao Central Hospital, Qingdao University, Qingdao, China

Flavonoids are one of the most important bioactive components in litchi (*Litchi chinensis* Sonn.) seeds and have broad-spectrum antiviral and antitumor activities. Litchi seeds have been shown to inhibit the proliferation of cancer cells and induce apoptosis, particularly effective against breast and liver cancers. Elucidating the distribution of flavonoids is important for understanding their physiological and biochemical functions and facilitating their efficient extraction and utilization. However, the spatial distribution patterns and expression states of flavonoids in litchi seeds remain unclear. Herein, matrix-assisted laser desorption/ionization mass spectrometry imaging (MALDI-MSI) was used for *in situ* detection and imaging of the distribution of flavonoids in litchi seed tissue sections for the first time. Fifteen flavonoid ion signals, including liquiritigenin, apigenin, naringenin, luteolin, dihydrokaempferol, daidzein, quercetin, taxifolin, kaempferol, isorhamnetin, myricetin, catechin, quercetin 3-β-D-glucoside, baicalin, and rutin, were successfully detected and imaged *in situ* through MALDI-MSI in the positive ion mode using 2-mercaptobenzothiazole as a matrix. The results clearly showed the heterogeneous distribution of flavonoids, indicating the potential of litchi seeds for flavonoid compound extraction. MALDI-MS-based multi-imaging enhanced the visualization of spatial distribution and expression states of flavonoids. Thus, apart from improving our understanding of the spatial distribution of flavonoids in litchi seeds, our findings also facilitate the development of MALDI-MSI-based metabolomics as a novel effective molecular imaging tool for evaluating the spatial distribution of endogenous compounds.

KEYWORDS

litchi seed, flavonoid, matrix-assisted laser desorption/ionization, mass spectrometry imaging, spatial distribution

Introduction

Litchi (*Litchi chinensis* Sonn.; order Sapindales, family Sapindaceae), also known as Lizhi, Danli, and Liguo, is a subtropical fruit tree with a cultivation history in China of more than 2,300 years (Hu et al., 2021). It is the only species of *Litchi* (Yao et al., 2021). Litchi is an important fruit crop in southern China and is planted on more than 550,000 ha with an annual output of more than 2.2 million tons (Hu et al., 2021). The cultivation area and output of litchi in China account for more than 60% of global production (Li et al., 2020). Litchi seeds are a major product, but only a small portion is processed for biological utilization, and many litchi seeds are discarded as waste. The abandonment of fruit seed residues is not only a considerable problem for the environment but also a waste of global resources. Litchi seeds are rich in various bioactive compounds, such as flavonoids, saponins, volatile oils, polyols, alkaloids, steroids, coumarins, fatty acids, amino acids, and sugars (Dong et al., 2019; Punia and Kumar, 2021), resulting in a variety of biological functions, including antiviral and anti-oxidation activities, reducing the degree of liver damage and lowering blood glucose levels (Choi et al., 2017; Dong et al., 2019; Punia and Kumar, 2021). Accumulating evidence has confirmed the antitumor/anticancer effects of litchi seed extracts (Emanuele et al., 2017; Tang et al., 2018; Zhao et al., 2020).

Flavonoids are polyphenolic compounds and endogenous bioactive components, which act as secondary metabolites with extensive pharmacological activities. Flavonoids exert important pharmacological properties, including cardioprotective, anticancer, anti-inflammatory, and anti-allergic activities (Maleki et al., 2019; Ciumărnean et al., 2020; Liskova et al., 2021; Rakha et al., 2022). Regarding anticancer activity, many preclinical studies indicated the antiproliferative effects of flavonoids on lung (Berk et al., 2022), prostate (Vue et al., 2016), colorectal (Park et al., 2012; Li et al., 2018b), and breast (Pan et al., 2012) cancers. Furthermore, flavonoids have anticancer effects on breast tumors through multiple mechanisms (Martinez-Perez et al., 2014; Magne Nde et al., 2015; Zhang et al., 2018; Sudhakaran et al., 2019). Flavonoids can inhibit procarcinogen bioactivation and estrogen-producing and estrogen-metabolizing enzymes (Surichan et al., 2012; Miron et al., 2017), as well as breast cancer resistance protein (BCRP) (Fan et al., 2019). Administering flavonoids could inhibit inflammation, proliferation, tumor growth, and metastasis (Peluso et al., 2013; Khan et al., 2021; Guo et al., 2022). Although many studies have shown the pharmacological effects of flavonoids widely distributed in litchi seeds, almost all such studies were based on the extraction, enrichment, and separation of bioactive components, and few have focused on the spatial distribution and expression states of flavonoids. In fact, the precise reveal of the distribution of these flavonoids in litchi seeds is important for understanding the physiological and biochemical functions of these compounds and facilitating their extraction and utilization.

Matrix-assisted laser desorption/ionization mass spectrometry imaging (MALDI-MSI) has emerged as a molecular-imaging tool for simultaneously detecting and characterizing the spatial distribution and relative abundance of endogenous and exogenous compounds, such as lipids, proteins, metabolites, peptides, and drugs (Van De Plas et al., 2015; Qin et al., 2018; Piehowski et al., 2020). Although MALDI-MSI has been used in plant science with endogenous molecular profiling to determine the spatial distribution of small molecules in plant tissues (Zaima et al., 2010; Taira et al., 2015; Huang et al., 2016; Li et al., 2018a), to the best of our knowledge, no previous study has utilized MALDI-MSI to characterize the spatial distribution of flavonoids in litchi seeds.

This study is the first to use MALDI-MSI for the *in situ* detection and imaging of flavonoids in litchi seed tissues. The results clearly showed the heterogeneous distribution of flavonoids in litchi seeds, indicating the potential of litchi seeds as a source for flavonoid extraction. MALDI-MS-based multi-imaging enhanced the visualization of spatial distribution and expression states of flavonoids. Our findings provide insights into the spatial distribution of flavonoids in litchi seeds and support the development of MALDI-MSI-based metabolomics as an appealing and credible molecular imaging technique for evaluating the spatial distribution of endogenous compounds.

Materials and methods

Materials and reagents

Fresh litchi fruit was collected from the Yongfuda litchi orchard (Haikou, Hainan, China) in June 2022. Haikou is located on Hainan Island in China. It has a typical tropical marine climate and annual sunshine duration of over 2,000 h. The climate is humid, the temperature rises fast, and the average annual precipitation is approximately 260 mm. The Yongfuda litchi orchard is located in a volcanic rock soil planting area. Once harvested, the peel and flesh of the litchi were immediately removed, and the litchi seeds were flash-frozen with liquid nitrogen by slow immersion to prevent seed shattering and endogenous compound changes. The commonly used MALDI matrix, 2-mercaptobenzothiazole (2-MBT), was obtained from Sigma-Aldrich (St. Louis, MO, USA). Amino acid and oligopeptide standards, including His, Gly-Gly-Leu (tripeptide), Ala-His-Lys (tripeptide), Leu-Leu-Tyr (tripeptide), and Arg-Gly-Asp-dTyr-Lys (pentapeptide), were purchased from Bankpeptide Biological Technology Co., Ltd. (Hefei, Anhui, China). Trifluoroacetic acid (TFA) and liquid chromatography–mass spectrometry (LC-MS)-grade methanol and ethanol were obtained from Merck & Co., Inc. (Darmstadt, Germany). Ultrapure water in the whole process of the experiments was prepared using a Millipore Milli-Q system (Bedford, MA, USA). All other reagents and chemicals were purchased from Merck, unless otherwise noted.

Tissue sectioning

For tissue sectioning, a Leica CM1860 cryostat (Leica Microsystems Inc., Wetzlar, Germany) was used. The frozen litchi seeds were cryo-sectioned into 12-μm-thick slices at a temperature

of −20°C, and then the cryo-sectioned samples were thaw-mounted instantly on the conductive indium tin oxide films of microscope glass slides purchased from Bruker Daltonics (Bremen, Germany) (Figures 1A, B).

Matrix coating

After being air-dried, the serial litchi seed tissue sections were used for MALDI matrix coating (Figure 1C). A 2-MBT matrix solution was prepared at an optimal concentration of 15 mg/ml and dissolved in methanol/water/TFA (80:20:0.2, v/v/v). Air-dried tissue sections were coated with the 2-MBT matrix solution by a GET-Sprayer (III) (HIT Co., Ltd, Beijing, China). Briefly, the 2-MBT matrix solution 15 cycles (5 s spray, 10 s incubation, and 20 s drying time) was sprayed on the surface of the tissue sections to pre-seed a thin layer of the 2-MBT matrix. After the tissue sections were completely air-dried in a vented fume hood, the matrix solution was evenly sprayed for 50 more of the same cycles.

Histological staining

In order to obtain the histological images of litchi seed tissue sections, a slightly modified hematoxylin and eosin staining method was carried out based on an established procedure (Casadonte and Caprioli, 2011). Briefly, the tissue sections were washed in a series of ethanol solutions (100%, 95%, 80%, and 70% aqueous ethanol; 15 s/wash). After 10-s ultrapure water washing, tissue sections were stained with hematoxylin solution for 2 min and then washed with ultrapure water and 70% and 95% aqueous ethanol for 30 s each. The eosin solution was applied for another 1 min. Then, all tissue sections were washed with 95% and 100% ethanol and xylene for 30-s dehydration.

Optimal image acquisition

Optical images of the tissue sections were acquired using an Epson Perfection V550 photo scanner (Seiko Epson Corp, Suwa, Japan) according to previous studies (Wu et al., 2021; Shi et al., 2022).

MALDI-MS

An Autoflex Speed MALDI time-of-fight (TOF)/TOF mass spectrometer (Bruker Daltonics) with a MALDI source equipped with a 2,000-Hz solid-state Smartbeam Nd : YAG UV laser (355 nm, Azura Laser AG, Berlin, Germany) was used for profiling and imaging (Figure 1D).

To acquire *in situ* (+) MS profiling data of flavonoids from the tissue sections, all mass spectra were obtained over the *m/z* range of 100 to 700, each mass spectrum included an accumulation of 50 laser scans, and each scan was amassed from 500 laser shots. Three biological replicates of the sample and three technical replicates of

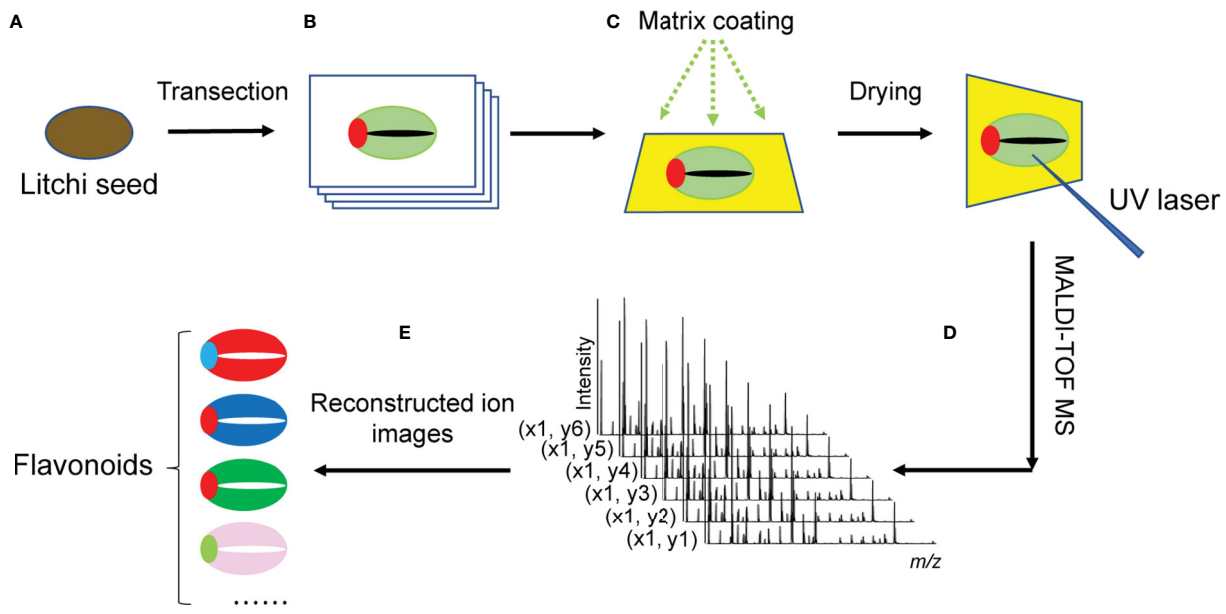

FIGURE 1
Schematic diagram of MALDI-MSI procedure for imaging flavonoids in litchi seeds. **(A)** Whole litchi seeds were used for transection into 12-μm-thick slices in a cryostat microtome. **(B)** Serial tissue sections were immediately thaw-mounted on the conductive sides of indium tin oxide (ITO)-coated microscope glass slides. Optical images of the litchi seed section were obtained using a scanner. **(C)** To assist ionization, the sections were coated with the organic matrix. **(D)** MALDI-TOF-MS was used to detect analytes *in situ* on the surface of litchi seed tissue sections. The mass spectra of ionized analytes were acquired at each detected pixel point. **(E)** MS images of analytes were reconstructed from the MS spectra obtained at each laser spot using specific imaging reconstruction software. MALDI-MSI, matrix-assisted laser desorption/ionization mass spectrometry imaging; TOF, time of fight; MS, mass spectrometry.

each biological replicate were performed for MALDI-MS data acquisition (n = 3 × 3). To acquire the images of flavonoids, a 250-μm laser raster step-size was utilized for flavonoid *in situ* detection in tissues, and each pixel (scan spot) included 300 laser shots. With the use of *FlexImaging* 4.1 (Bruker Daltonics), the three "teaching points" for the correct positioning of the solid-state UV laser (Smartbeam Nd : YAG) for spectral acquisition were marked around a tissue section using a white ink correction pen. The *m/z* values of the compound ions that can be used for external mass calibration were listed as follows: His ($[M+H]^+$, *m/z* 156.0768), Gly-Gly-Leu (tripeptide, $[M+H]^+$, *m/z* 246.1448), Ala-His-Lys (tripeptide, $[M+H]^+$, *m/z* 355.2088), Leu-Leu-Tyr (tripeptide, $[M+H]^+$, *m/z* 408.2493), and Arg-Gly-Asp-dTyr-Lys (pentapeptide, $[M+H]^+$, *m/z* 620.3151). Gly-Gly-Leu (tripeptide, $[M+H]^+$, *m/z* 246.1448) and Arg-Gly-Asp-dTyr-Lys (pentapeptide, $[M+H]^+$, *m/z* 620.3151) ions were selected in combination with the matrix ion of 2-MBT($[M+H]^+$, *m/z* 167.9942) for internal mass calibration in the cubic enhanced mode. For the MALDI-TOF-MS analysis, MS/MS spectra were acquired in collision-induced dissociation (CID) mode, and argon was used as the collision gas. The flavonoid fragment ions were acquired under the following condition: ion source 1, 19.0 kV; ion source 2, 17.4 kV; lens, 8.8 kV; reflector 1, 21.0 kV; reflector 2, 9.8 kV; and accelerating voltage, 20.0 kV. The UV laser power ranged from 65% to 90%. MS/MS spectra were recorded based on no less than 5,000 laser shots over the *m/z* range of 0 to 100 with a sampling rate of 2.00 G/s, a detector gain of 9.5×, and an electronic gain of 100 mV.

Data analysis

For the MS profiling and MS/MS data analysis, Bruker *FlexAnalysis* 3.4 (Bruker Daltonics) was used for the preliminary viewing and processing of the mass spectra. Once the monoisotopic peak list was generated and exported, two metabolome databases (METLIN and HMDB) (Tautenhahn et al., 2012; Wishart et al., 2022) were used for the search of the detected *m/z* values of precursor ions and CID fragment ions against potential metabolite identities within an acceptable mass error of ±5 ppm. Three ion adduct forms (i.e., $[M + H]^+$, $[M + Na]^+$, and $[M + K]^+$) were considered for the database search. For MALDI tissue imaging, Bruker *FlexImaging* 4.1 software was used for the reconstitution of the ion maps of the detected flavonoids (Figure 1E). For the generation of the ion images using *FlexImaging*, the mass filter width was set at 5 ppm.

Flavonoid extraction and identification by LC-MS/MS

Flavonoids were extracted from the seeds of litchi for LC-MS/MS analysis. The details of the extraction of the flavonoids from litchi seeds and the procedure of LC-MS/MS analysis for the identification and structural confirmation of the flavonoids can be found in the Supplementary Material.

Results and discussion

Morphological characteristics of litchi seeds

As shown in Figures 2A, B, under a light microscope, the litchi seed showed the following structures: testa, micropyle, embryo, cotyledon, and cotyledon gap. Among these structures, the testa was dark coffee-colored, the embryo was brown, and the cotyledon was oyster white. In addition, a gap was observed in the middle of the cotyledon. After hematoxylin and eosin staining, litchi seeds were observed again under a light microscope (Figure 2C). The anatomical structure of the litchi seeds is illustrated in Figure 2D.

Flavonoids detected *in situ* by MALDI-TOF-MS

As shown in Figure 3, many flavonoid-related signals were detected in the *m/z* range of 100–700. These compounds were confirmed by comparing the *m/z* values and MS/MS spectra with those obtained by LC-MS/MS (Table 1). According to collision-induced dissociation, 15 flavonoids compounds were identified through MALDI-TOF-MS: liquiritigenin (*m/z* 257.081, $[M+H]^+$), apigenin (*m/z* 271.060, $[M+H]^+$), naringenin (*m/z* 273.076, $[M+H]^+$), daidzein (*m/z* 293.020, $[M+Na]^+$), luteolin (*m/z* 287.056, $[M+H]^+$), dihydrokaempferol (*m/z* 289.071, $[M+H]^+$), catechin (*m/z* 329.043, $[M+H]^+$), quercetin (*m/z* 303.051, $[M+H]^+$), kaempferol (*m/z* 309.036, $[M+Na]^+$), isorhamnetin (*m/z* 317.066, $[M+H]^+$), myricetin (*m/z* 319.046, $[M+H]^+$), quercetin 3-β-D-glucoside (*m/z* 465.102, $[M+H]^+$), baicalin (*m/z* 469.073, $[M+Na]^+$), rutin (*m/z* 649.118, $[M+K]^+$), and taxifolin (*m/z* 305.065, $[M+H]^+$).

MALDI-MS imaging of flavonoids

MALDI-MSI can provide a snapshot of the distribution of molecules at a specific location on a tissue surface. We present the mass spectrometry images of all 15 flavonoids and performed our classification analysis in Figure 4.

Ion images of the 15 flavonoids indicated that they can be broadly classified into four types. Four compounds were distributed mainly in the embryo: liquiritigenin (*m/z* 257.081, $[M+H]^+$), luteolin (*m/z* 287.056, $[M+H]^+$), dihydrokaempferol (*m/z* 289.071, $[M+H]^+$), and kaempferol (*m/z* 309.036, $[M+Na]^+$). Luteolin was highly concentrated in the embryo and less concentrated in other parts, while kaempferol was distributed at low abundance in the cotyledons and more in the embryo. Myricetin (*m/z* 319.046, $[M+H]^+$), baicalin (*m/z* 469.073, $[M+Na]^+$), and rutin (*m/z* 649.118, $[M+K]^+$) were primarily distributed in the cotyledons. Baicalin and rutin were distributed at the periphery of the cotyledons, and myricetin was distributed to one side of the cotyledon gap. Most of the compounds were distributed in both cotyledons and embryos, including naringenin (*m/z* 273.076, [M

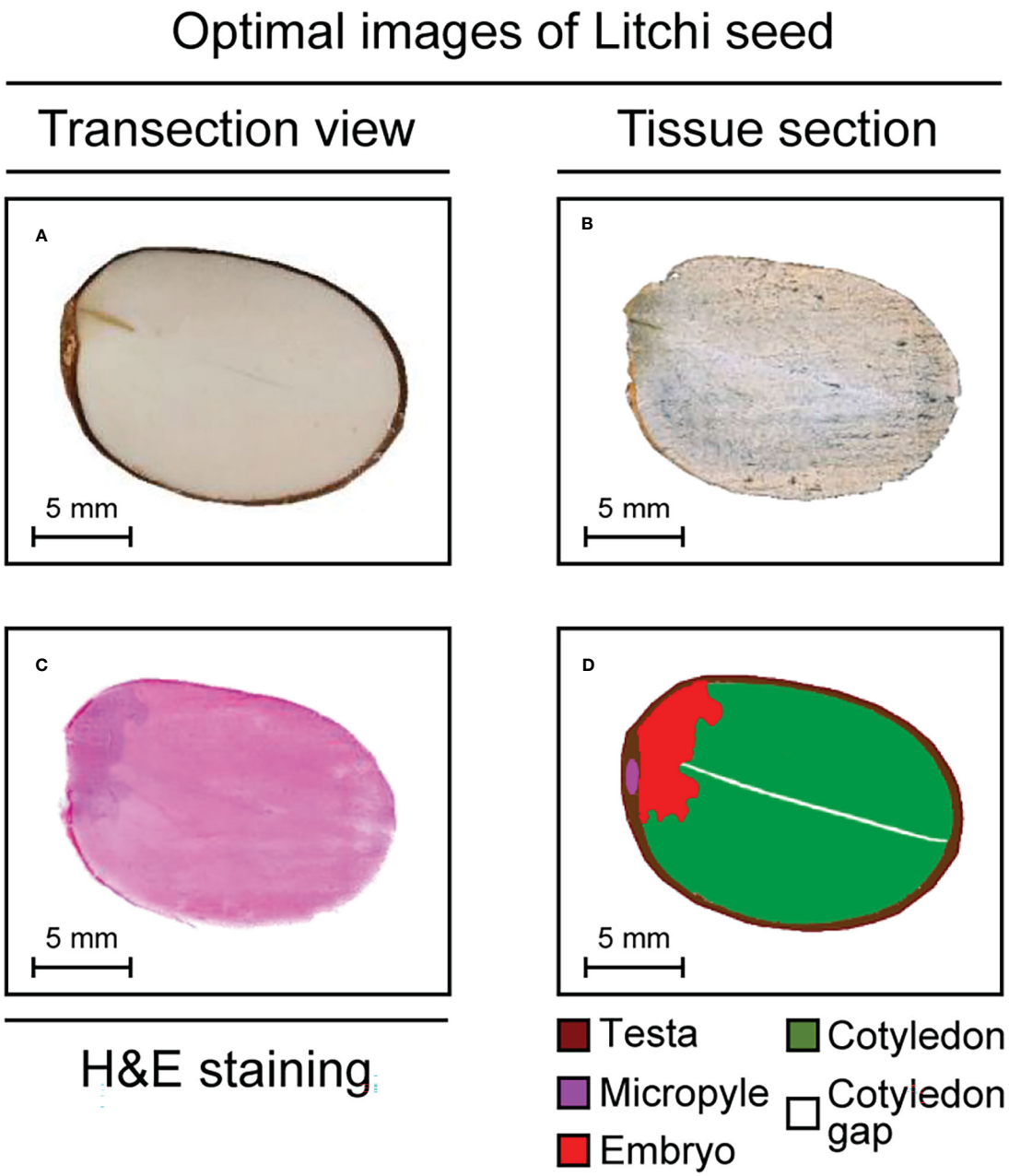

FIGURE 2
Optimal images of litchi seed tissue sections. **(A, B)** Photos of litchi seed tissue sections. **(C)** An H&E-stained litchi seed tissue section. **(D)** A cartoon of anatomical structure of litchi seed tissue section. H&E, hematoxylin and eosin.

+H]$^+$), apigenin (*m/z* 271.060, [M+H]$^+$), daidzein (*m/z* 293.020, [M+Na]$^+$), quercetin (*m/z* 303.051, [M+H]$^+$), isorhamnetin (*m/z* 317.066, [M+H]$^+$), catechin (m/z 329.043, [M+H]$^+$), and quercetin 3-β-D-glucoside (*m/z* 465.102, [M+H]$^+$). Naringenin and catechin were concentrated throughout the litchi seed, their distribution being more homogeneous and without obvious tissue specificity. Quercetin, quercetin 3-β-D-glucoside, and apigenin were distributed at the periphery of the cotyledons and in the embryo. The compound daidzein was uniformly distributed, whereas isorhamnetin was more distributed at the apical part of the cotyledons. Finally, the taxifolin (*m/z* 305.065, [M+H]$^+$) content was low and mainly distributed in the inner seed testa.

Four compounds were mainly distributed in the embryo: liquiritigenin, luteolin, dihydrokaempferol, and kaempferol. As the embryo is the most important part of the seed in plant development, these flavonoids may provide essential substances for growth and development and improve seed resistance. Luteolin was highly concentrated in the embryo and less concentrated in other parts. Luteolin, through inducing root nodulation, plays an important role in nitrogen metabolism in nitrogen-fixing plants and enhanced plant stress tolerance by promoting its nitrogen enrichment (Peters et al., 1986). Liquiritigenin was also mainly concentrated in the embryo and lesser in the cotyledons close to the embryo. Liquiritigenin increases ultraviolet irradiation, indicating

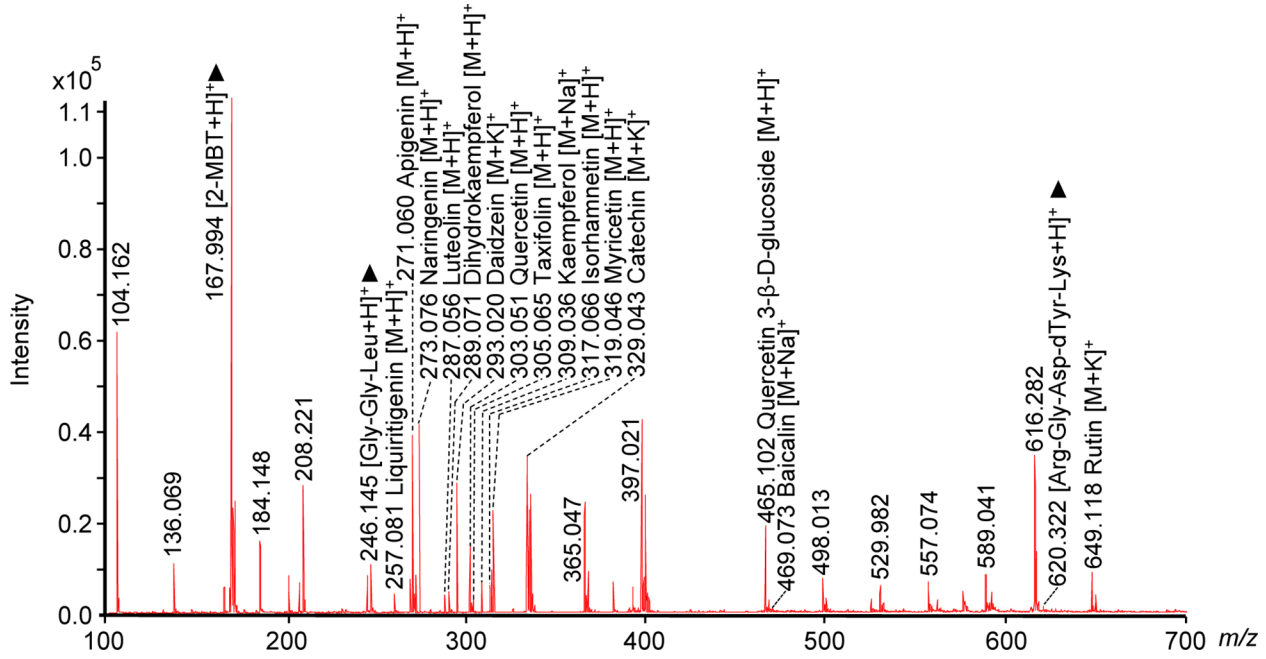

FIGURE 3
Mass spectrum of flavonoids detected *in situ* in a litchi seed tissue section using MALDI-TOF-MS and 2-MBT as the matrix in the positive ion mode. Two peptide standard ions, Gly-Gly-Leu (tripeptide, $[M+H]^+$, *m/z* 246.145) and Arg-Gly-Asp-dTyr-Lys (pentapeptide, $[M+H]^+$, *m/z* 620.322), and one matrix ion, 2-MBT ($[M+H]^+$, *m/z* 167.994), were used as the reference peaks and are labeled with black triangle "▲". Three biological repetitions and three technical repetitions were performed (n = 3 × 3). MALDI, matrix-assisted laser desorption/ionization; TOF, time-of-fight; MS, mass spectrometry; 2-MBT, 2-mercaptobenzothiazole.

its anti-radiation function (Sun et al., 2012). Dihydrokaempferol and kaempferol were interconvertible; therefore, both had similar distribution characteristics and are distributed in the cotyledons as well as the embryo. Many studies have demonstrated that kaempferol, as a precursor of ubiquitin-ketone (coenzyme Q) biosynthesis, is an atypical node between primary and specialized metabolism (Soubeyrand et al., 2018; Berger et al., 2022). Kaempferol is involved in plant defense and signaling in response to stressful conditions (Soubeyrand et al., 2018; Jan et al., 2022). Dihydrokaempferol is involved in plant growth and development. As a precursor of orange pelargonidin-type anthocyanins, dihydrokaempferol plays a role in flower coloring (Johnson et al., 2001). Liquiritigenin rapidly inactivates the PI3K/AKT/mTOR pathway. *In vivo* studies demonstrated that liquiritigenin can significantly inhibit tumor growth, increase cell autophagy, and accelerate cell apoptosis. In addition, it attenuates the malignant-like biological behaviors in triple-negative breast cancer cells through its induction of autophagy-related apoptosis *via* the PI3K/AKT/mTOR pathway (Ji et al., 2021), decreased DNMT activity, and elevated BRCA1 expression and transcriptional activity (Liang et al., 2021). Dihydrokaempferol has strong anti-inflammatory and antioxidant activities, which can improve the inflammatory performance and oxidative stress state of acute pancreatitis (Liang et al., 2020; Zhang et al., 2021). In contrast, kaempferol shows more pharmacological activities, such as anti-bacterial (Yeon et al., 2019), anti-inflammatory (Yeon et al., 2019), anti-oxidant (Chen and Chen, 2013), antitumor (Calderón-Montaño et al., 2011), and anti-diabetic activities (Yang et al., 2021b), and are cardio-protective (Chen et al., 2022b) and neuro-protective (Wang et al., 2020). Currently, kaempferol is also commonly used in cancer chemotherapy (Ren et al., 2019). The mechanisms of kaempferol's anticancer include apoptosis, cell cycle arrest at the G2/M phase, downregulation of epithelial–mesenchymal transition-related markers, and repression of overactivation of the phosphatidylinositol 3-kinase/protein kinase B signaling pathway (Imran et al., 2019; Wang et al., 2019). Luteolin sensitizes cancer cells to treatment-induced cytotoxicity *via* suppressing cell survival pathways and enhancing apoptosis pathways, including the apoptosis pathway of the tumor suppressor protein p53 (Lin et al., 2008). These compounds can be extracted from the embryo of litchi seeds, which is convenient for obtaining a higher content of target substances for pharmaceutical and mass production in the future.

Myricetin, baicalin, and rutin were mainly found in the cotyledons of litchi seeds. Myricetin was mainly concentrated on one side of the cotyledon gap, while rutin and baicalin were mainly distributed at the periphery (Figure 4). From a physiological point of view, flavonoids such as myricetin and baicalin assist in the reinforcement of plant tissues, maintenance of seed dormancy, and longevity of seeds during storage (Shirley, 1998). Rutin may participate in strengthening the plant's defense system against environmental stresses, including UV exposure, low-temperature stress, drought stress, and bacterial pathogen infection (Suzuki et al., 2015; Yang et al., 2016). Myricetin has therapeutic effects on a variety of diseases, such as inflammation, cerebral ischemia, Alzheimer's disease (AD), cancer, diabetes, pathogenic

TABLE 1 The lists of 15 detectable flavonoids in litchi seed tissue sections by MALDI-TOF-MS using 2-MBT as the matrix in the positive ion mode.

Measured *m/z*	Calculated *m/z*	Error (ppm)	Assignment			Structurally specific CID ions (*m/z*)	
			Ion form	Compound	Molecular formula	MALDI-MS/MS	LC-MS/MS
257.081	257.0808	3.1	[M+H]+	Liquiritigenin	C15H12O4	–	137.024, 147.042, 211.073, 239.068, 257.081
271.060	271.0601	0.4	[M+H]+	Apigenin	C15H10O5	119.041, 243.056, 271.060	91.051, 119.044, 153.010, 243.059, 271.060
273.076	273.0758	0.7	[M+H]+	Naringenin	C15H12O5	119.044, 147.043, 273.076	119.041, 123.038, 147.040, 153.013, 273.076
287.056	287.0550	3.5	[M+H]+	Luteolin	C15H10O6	–	135.043, 153.009, 269.044, 287.056
289.071	289.0707	1	[M+H]+	Dihydrokaempferol	C15H12O6	–	153.013, 243.062, 271.063, 289.071
293.020	293.0211	3.8	[M+K]+	Daidzein	C15H10O4	227.064, 255.062, 293.021	199.072, 227.061, 255.060, 293.020
303.051	303.0499	3.6	[M+H]+	Quercetin	C15H10O7	153.017, 201.046, 257.043, 303.050	153.014, 201.048, 229.043, 257.040, 303.051
305.065	305.0656	2	[M+H]+	Taxifolin	C15H12O7	–	123.041, 149.016, 153.012, 167.033, 231.058, 305.065
309.036	309.0370	3.2	[M+Na]+	Kaempferol	C15H10O6	–	121.022, 153.014, 165.018, 213.054, 287.051, 309.036
317.066	317.0656	1.3	[M+H]+	Isorhamnetin	C16H12O7	153.013, 229.042, 27.041, 302.027	153.012, 229.043, 274.040, 302.029, 317.066
319.046	319.0448	3.8	[M+H]+	Myricetin	C15H10O8	217.042, 245.041, 273.025, 319.045	153.011, 217.043, 245.044, 273.027, 319.046
329.043	329.0422	2.4	[M+K]+	Catechin	C15H14O6	123.043, 139.027, 165.054, 291.078	123.042, 139.026, 165.053, 291.079, 329.042
465.102	465.1028	1.7	[M+H]+	Quercetin 3-β-D-glucoside	C21H20O12	229.043, 303.042, 465.103	153.013, 229.042, 257.033, 303.044, 465.103
469.073	469.0741	2.3	[M+Na]+	Baicalin	C21H18O11	–	123.013, 271.049, 447.088, 469.07
649.118	649.1165	2.3	[M+K]+	Rutin	C27H30O16	129.053, 303.046, 465.103, 611.146, 649.118	129.054, 145.053, 147.051, 303.048, 465.102, 611.147, 649.117

Structurally specific CID ions of extracted metabolites were detected by MALDI-MS/MS or LC-MS/MS using CID. "-": the CID ions can not be detected by MALDI-MS/MS in this work. MALDI, matrix-assisted laser desorption/ionization; TOF, time of fight; MS, mass spectrometry; 2-MBT, 2-mercaptobenzothiazole; CID, collision-induced dissociation; LC-MS/MS, liquid chromatography–tandem mass spectrometry.

microorganism infection, thrombosis, and atherosclerosis (Song et al., 2021). Furthermore, myricetin has been reported to regulate the expression of STAT3, PI3K/AKT/mTOR, AChE, IκB/NF-κB, BrdU/NeuN, Hippo, eNOS/NO, ACE, MAPK, Nrf2/HO-1, TLR, and GSK-3β (Song et al., 2021). Rutin shows clear antioxidant and anticancer effects, including a strong ability to inhibit tumors in breast cancer, especially triple-negative breast cancer (Iriti et al., 2017; Liang et al., 2021). Baicalin, similar to rutin and myricetin, has inhibitory effects on lung, breast, and bladder cancers, through different signaling pathways and mechanisms (Ge et al., 2021; Kong et al., 2021; Zhao et al., 2021). Owing to their important pharmacological effects, our study of their spatial distribution provided a basis for the precise extraction of flavonoids for developing drugs.

Seven flavonoids, i.e., naringenin, apigenin, daidzein, quercetin, isorhamnetin, catechin, and quercetin-3-β-D-glucoside, were mainly found in both the cotyledon and embryo of litchi seeds. Among these compounds, catechin, naringenin, daidzein, apigenin, and quercetin-3-β-D-glucoside have homogeneous distributions with relatively high abundance. Isorhamnetin was mainly distributed in the radicle and tip of the cotyledon, while quercetin was distributed at the periphery of the cotyledon. Flavonoids are secondary metabolites in plants that play a critical role in impairing ultraviolet irradiation, regulating the oxidative stress response, and influencing the transport of plant hormones, flower coloring, and pathogen resistance (Buer et al., 2010; Chen et al., 2022a). Naringenin plays various roles in plant–microbe interactions (An et al., 2021). Lignin biosynthesis and coenzyme ligase (4CL) are involved in plant growth, and naringenin is one of the metabolites in this pathway that inhibit enzymes such as 4-CL (Deng et al., 2004). Apigenin (4′,5,7-trihydroxyflavone) is a bioactive compound that belongs to the flavone class, and it is the aglycone of many

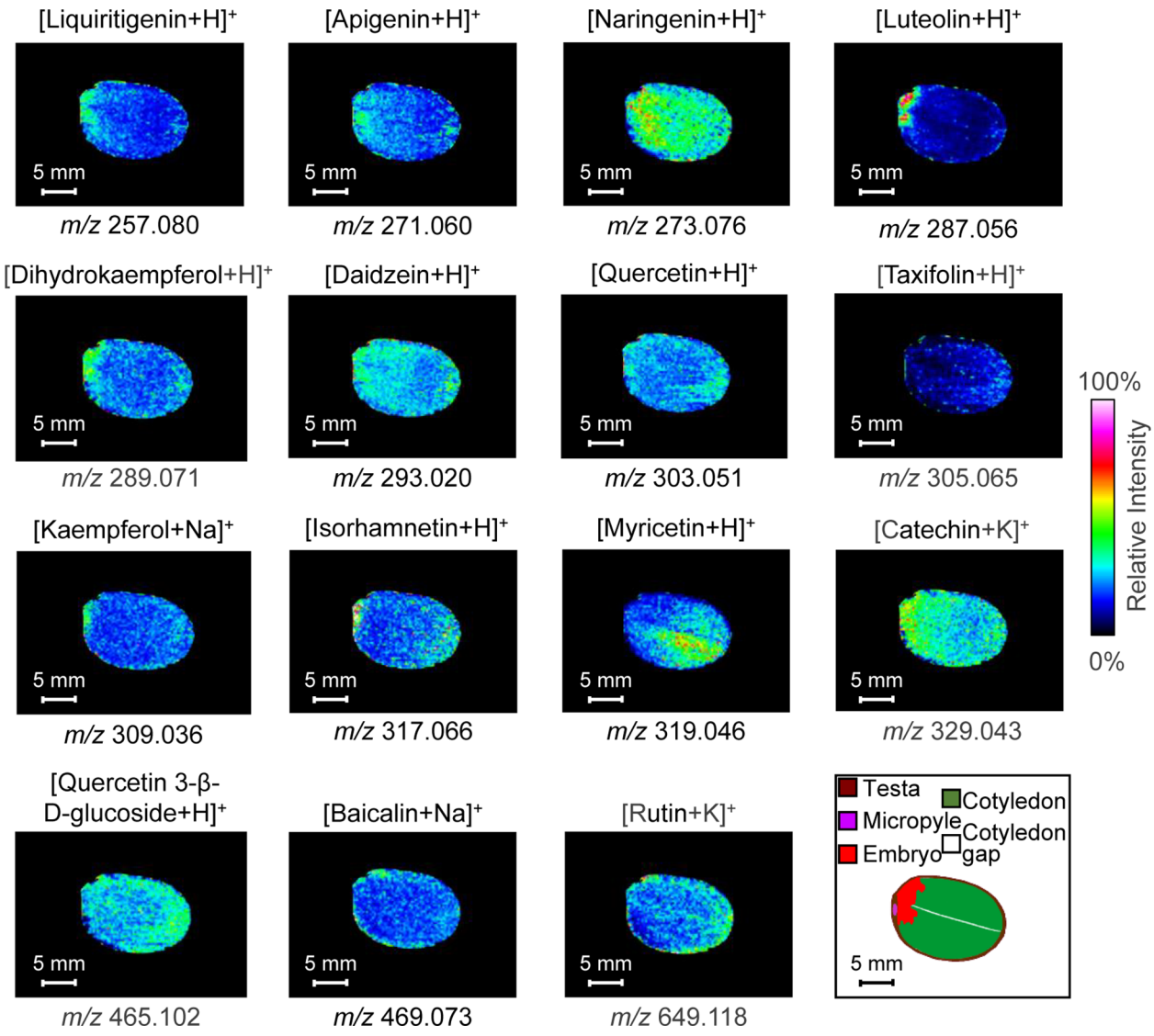

FIGURE 4
Ion images of 15 detectable flavonoids in litchi seed tissue sections from MALDI-TOF-MS using 2-MBT as the matrix in positive ion mode. MS imaging was acquired at 250-μm spatial resolution. MALDI, matrix-assisted laser desorption/ionization; TOF, time of fight; MS, mass spectrometry; 2-MBT, 2-mercaptobenzothiazole.

naturally occurring glycosides. It ameliorates the damaging effects of salinity on rice seedlings, presumably by regulating selective ion uptake by roots and translocation to shoots, thus maintaining the higher K^+/Na^+ ratio critical for normal plant growth under salinity stress (Mekawy et al., 2018). Daidzein, as an isoflavonoid, plays crucial roles in the expression of the nod genes of rhizobial bacteria. The expression of this compound in roots will increase the synthesis and secretion of nodulation factors, promoting a series of physiological changes in plant cells and initiating the formation of nodules (Bosse et al., 2021). Quercetin promotes a series of physiological and biochemical processes in plants, including seed germination, pollen growth, photosynthesis, and antioxidant machinery, thus facilitating proper plant growth and development (Singh et al., 2021). In addition, quercetin is an antioxidant that enhances plant resistance to some biotic and abiotic stresses. Quercetin-3-β-D-glucoside is a quercetin-derived compound with attached glucose instead of the 3-OH group of quercetin. Isorhamnetin is a methylated flavonoid derived from quercetin. Catechins, as a type of flavonoid, also belong to phenolic compounds. Making up more than 70% of polyphenols, catechins consist of ester and non-ester catechins. The multifunctional catechins contribute to decreased reactive oxygen species and better adaptability of plants to the environment (Jiang et al., 2020). Some of these flavonoids have been previously extracted from litchi seeds, for example, catechin and naringenin (Zhu et al., 2019). Similar to other flavonoids, most of these compounds have many pharmacological effects, including anti-inflammatory, antioxidant, and antidiabetic activities. In particular, since

the start of the COVID-19 epidemic, antiviral activity has been reported for catechin (Mishra et al., 2021) and quercetin (Bernini and Velotti, 2021). The antitumor effects of flavonoids have also been extensively studied, with the following mechanisms reported: inducing oxidative stress (Souza et al., 2017), enhancing chemotherapy drug effect (Yang et al., 2021a), and regulating signaling pathways (Amado et al., 2014). Notably, daidzein is a phytohormone similar to estrogens and thus may have a therapeutic effect on estrogen-dependent diseases (Meng et al., 2017). Therefore, flavonoid compounds are useful for developing drug-based therapies, and exploring the distribution of flavonoids will facilitate efficient extraction and utilization.

Although taxifolin was successfully detected in sections *in situ* using MALDI-MSI, the abundance of this compound was low. As shown in Figure 4, taxifolin was mainly found in the testa and peripheral part of the cotyledons, indicating that the compound can protect seed embryos from external biotic and abiotic factors, such as soil microbes (e.g., fungi and bacteria) and saline-alkali abiotic stress, thus improving seed vitality and germination rate (Ninfali et al., 2020; Wan et al., 2020). By regulating the aromatic hydrocarbon receptor/cytochrome P450 1A1 (CYP1A1) signaling pathway, taxifolin can significantly inhibit the proliferation, migration, invasion, and viability of gastric cancer cells (Xie et al., 2021). Similarly, the same effect of taxifolin has been observed on breast cancer by promoting mesenchymal-to-epithelial transition (EMT) through β-catenin signaling (Von Minckwitz et al., 2019).

Conclusion

MALDI-MSI was used for *in situ* detection and imaging of flavonoid distribution in litchi seeds for the first time. Overall, 15 flavonoids were successfully imaged. Among them, four (dihydrokaempferol, liquiritigenin, luteolin, and kaempferol) were distributed in the seed embryo, three (rutin, baicalin, and myricetin) were mainly found in the cotyledons, seven (quercetin, naringenin, isorhamnetin, daidzein, apigenin, catechin, and quercetin 3-β-D-glucoside) were enriched in both the embryo and cotyledons, and one (taxifolin) was mainly detected in the inner testa. Our MALDI-MSI results showed clear tissue distribution heterogeneity for the different flavonoid compounds in litchi seeds. Such information will be important for further study to understand the physiological and chemical functions of such flavonoid compounds. Furthermore, our study provides a basis for further improving the efficiency of extracting and utilizing bioactive compounds from litchi seeds.

Data availability statement

The original contributions presented in the study are included in the article/Supplementary Material. Further inquiries can be directed to the corresponding author.

Author contributions

Concepts: YL and XN. Design: ZW, FJ, and YL. Literature search: JW, ZZ, and YL. Data acquisition and analysis: ZW, XN, YL, and ZZ. Writing—original draft: YL, XN, and JW. Writing—review and editing: FJ, ZW, YL, and XN. Funding acquisition: YL, XN, and JW. Supervision: FJ and ZW. All authors contributed to the article and approved the submitted version.

Funding

This work was supported by grants from the fund of Qingdao Medical and Health Research Project (grant number: 2021-WJZD090).

Conflict of interest

The authors declare that the research was conducted in the absence of any commercial or financial relationships that could be construed as a potential conflict of interest.

Publisher's note

Supplementary material

The Supplementary Material for this article can be found online at: https://www.frontiersin.org/articles/10.3389/fpls.2023.1144449/full#supplementary-material

References

Amado, N. G., Predes, D., Fonseca, B. F., Cerqueira, D. M., Reis, A. H., Dudenhoeffer, A. C., et al. (2014). Isoquercitrin suppresses colon cancer cell growth *in vitro* by targeting the wnt/β-catenin signaling pathway. *J. Biol. Chem.* 289, 35456–35467. doi: 10.1074/jbc.M114.621599

An, J., Kim, S. H., Bahk, S., Vuong, U. T., Nguyen, N. T., Do, H. L., et al. (2021). Naringenin induces pathogen resistance against pseudomonas syringae through the activation of NPR1 in arabidopsis. *Front. Plant Sci.* 12. doi: 10.3389/fpls.2021.672552

Berger, A., Latimer, S., Stutts, L. R., Soubeyrand, E., Block, A. K., and Basset, G. J. (2022). Kaempferol as a precursor for ubiquinone (coenzyme q) biosynthesis: An atypical node between specialized metabolism and primary metabolism. *Curr. Opin. Plant Biol.* 66, 102165. doi: 10.1016/j.pbi.2021.102165

Berk, Ş., Kaya, S., Akkol, E. K., and Bardakçı, H. (2022). A comprehensive and current review on the role of flavonoids in lung cancer-experimental and theoretical approaches. *Phytomedicine* 98, 153938. doi: 10.1016/j.phymed.2022.153938

Bernini, R., and Velotti, F. (2021). Natural polyphenols as immunomodulators to rescue immune response homeostasis: Quercetin as a research model against severe COVID-19. *Molecules* 26. doi: 10.3390/molecules26195803

Bosse, M. A., Silva, M. B. D., Oliveira, N., Araujo, M. A., Rodrigues, C., Azevedo, J. P., et al. (2021). Physiological impact of flavonoids on nodulation and ureide metabolism in legume plants. *Plant Physiol. Biochem.* 166, 512–521. doi: 10.1016/j.plaphy.2021.06.007

Buer, C. S., Imin, N., and Djordjevic, M. A. (2010). Flavonoids: New roles for old molecules. *J. Integr. Plant Biol.* 52, 98–111. doi: 10.1111/j.1744-7909.2010.00905.x

Calderón-Montaño, J. M., Burgos-Morón, E., Pérez-Guerrero, C., and López-Lázaro, M. (2011). A review on the dietary flavonoid kaempferol. *Mini Rev. Med. Chem.* 11, 298–344. doi: 10.2174/138955711795305335

Casadonte, R., and Caprioli, R.M. (2011). Proteomic analysis of formalin-fixed paraffin-embedded tissue by MALDI imaging mass spectrometry. *Nat. Protoc.* 6, 1695–1709. doi: 10.1038/nprot.2011.388

Chen, A. Y., and Chen, Y. C. (2013). A review of the dietary flavonoid, kaempferol on human health and cancer chemoprevention. *Food Chem.* 138, 2099–2107. doi: 10.1016/j.foodchem.2012.11.139

Chen, J. H., Hou, N., Xv, X., Zhang, D., Fan, T. Q., Zhang, Q. X., et al. (2022a). Flavonoid synthesis and metabolism during the fruit development in hickory (Carya cathayensis). *Front. Plant Sci.* 13. doi: 10.3389/fpls.2022.896421

Chen, M., Xiao, J., El-Seedi, H. R., Woźniak, K. S., Daglia, M., Little, P. J., et al. (2022b). Kaempferol and atherosclerosis: From mechanism to medicine. *Crit. Rev. Food Sci. Nutr.* 1-19. doi: 10.1080/10408398.2022.2121261

Choi, S.-A., Lee, J. E., Kyung, M. J., Youn, J. H., Oh, J. B., and Whang, W. K. (2017). Anti-diabetic functional food with wasted litchi seed and standard of quality control. *Appl. Biol. Chem.* 60, 197–204. doi: 10.1007/s13765-017-0269-9

Ciumărnean, L., Milaciu, M. V., Runcan, O., Vesa Ș, C., Răchișan, A. L., Negrean, V., et al. (2020). The effects of flavonoids in cardiovascular diseases. *Molecules* 25. doi: 10.3390/molecules25184320

Deng, F., Aoki, M., and Yogo, Y. (2004). Effect of naringenin on the growth and lignin biosynthesis of gramineous plants. *Weed Biol. Manage.* 4, 49–55. doi: 10.1111/j.1445-6664.2003.00119.x

Dong, X., Huang, Y., Wang, Y., and He, X. (2019). Anti-inflammatory and antioxidant jasmonates and flavonoids from lychee seeds. *J. Funct. Foods* 54, 74–80. doi: 10.1016/j.jff.2018.12.040

Emanuele, S., Lauricella, M., Calvaruso, G., D'anneo, A., and Giuliano, M. (2017). Litchi chinensis as a functional food and a source of antitumor compounds: An overview and a description of biochemical pathways. *Nutrients* 9, 992. doi: 10.3390/nu9090992

Fan, X., Bai, J., Zhao, S., Hu, M., Sun, Y., Wang, B., et al. (2019). Evaluation of inhibitory effects of flavonoids on breast cancer resistance protein (BCRP): From library screening to biological evaluation to structure-activity relationship. *Toxicol. In Vitro* 61, 104642. doi: 10.1016/j.tiv.2019.104642

Ge, A., Liu, L., Deng, X., Luo, J., and Xu, Y. (2021). Exploring the mechanism of baicalin intervention in breast cancer based on MicroRNA microarrays and bioinformatics strategies. *Evid. Based Complement. Alternat. Med.* 2021, 7624415. doi: 10.1155/2021/7624415

Guo, Y., Ding, S. J., Ding, X., Liu, Z., Wang, J. L., Chen, Y., et al. (2022). Effects of selected flavonoids oncellproliferation and differentiation of porcine muscle stem cells for cultured meat production. *Food Res. Int.* 160, 111459. doi: 10.1016/j.foodres.2022.111459

Hu, F.-C., Chen, Z., Wang, X.-H., Wang, J.-B., Fan, H.-Y., Qin, Y.-H., et al. (2021). Construction of high-density SNP genetic maps and QTL mapping for dwarf-related traits in litchi chinensis sonn. *J. Integr. Agr.* 20, 2900–2913. doi: 10.1016/s2095-3119(20)63387-1

Huang, L., Tang, X., Zhang, W., Jiang, R., Chen, D., Zhang, J., et al. (2016). Imaging of endogenous metabolites of plant leaves by mass spectrometry based on laser activated electron tunneling. *Sci. Rep.* 6, 24164. doi: 10.1038/srep24164

Imran, M., Salehi, B., Sharifi-Rad, J., Aslam Gondal, T., Saeed, F., Imran, A., et al. (2019). Kaempferol: A key emphasis to its anticancer potential. *Molecules* 24. doi: 10.3390/molecules24122277

Iriti, M., Kubina, R., Cochis, A., Sorrentino, R., Varoni, E. M., Kabała-Dzik, A., et al. (2017). Rutin, a quercetin glycoside, restores chemosensitivity in human breast cancer cells. *Phytother. Res.* 31, 1529–1538. doi: 10.1002/ptr.5878

Jan, R., Khan, M., Asaf, S., Lubna,, Asif, S., and Kim, K. M. (2022). Bioactivity and therapeutic potential of kaempferol and quercetin: New insights for plant and human health. *Plants (Basel)* 11. doi: 10.3390/plants11192623

Ji, Y., Hu, W., Jin, Y., Yu, H., and Fang, J. (2021). Liquiritigenin exerts the anti-cancer role in oral cancer *via* inducing autophagy-related apoptosis through PI3K/AKT/mTOR pathway inhibition *in vitro* and *in vivo*. *Bioengineered* 12, 6070–6082. doi: 10.1080/21655979.2021.1971501

Jiang, C. K., Ma, J. Q., Liu, Y. F., Chen, J. D., Ni, D. J., and Chen, L. (2020). Identification and distribution of a single nucleotide polymorphism responsible for the catechin content in tea plants. *Hortic. Res.* 7, 24. doi: 10.1038/s41438-020-0247-y

Johnson, E. T., Ryu, S., Yi, H., Shin, B., Cheong, H., and Choi, G. (2001). Alteration of a single amino acid changes the substrate specificity of dihydroflavonol 4-reductase. *Plant J.* 25, 325–333. doi: 10.1046/j.1365-313x.2001.00962.x

Khan, H., Ullah, H., Martorell, M., Valdes, S. E., Belwal, T., Tejada, S., et al. (2021). Flavonoids nanoparticles in cancer: Treatment, prevention and clinical prospects. *Semin. Cancer Biol.* 69, 200–211. doi: 10.1016/j.semcancer.2019.07.023

Kong, N., Chen, X., Feng, J., Duan, T., Liu, S., Sun, X., et al. (2021). Baicalin induces ferroptosis in bladder cancer cells by downregulating FTH1. *Acta Pharm. Sin. B.* 11, 4045–4054. doi: 10.1016/j.apsb.2021.03.036

Li, H., Huang, D., Ma, Q., Qi, W., and Li, H. (2020). Factors influencing the technology adoption behaviours of litchi farmers in China. *Sustainability* 12, 271. doi: 10.3390/su12010271

Li, B., Neumann, E. K., Ge, J., Gao, W., Yang, H., Li, P., et al. (2018a). Interrogation of spatial metabolome of ginkgo biloba with high-resolution matrix-assisted laser desorption/ionization and laser desorption/ionization mass spectrometry imaging. *Plant Cell Environ.* 41, 2693–2703. doi: 10.1111/pce.13395

Li, Y., Zhang, T., and Chen, G. Y. (2018b). Flavonoids and colorectal cancer prevention. *Antioxidants (Basel)* 7. doi: 10.3390/antiox7120187

Liang, X., Hu, C., Liu, C., Yu, K., Zhang, J., and Jia, Y. (2020). Dihydrokaempferol (DHK) ameliorates severe acute pancreatitis (SAP) *via* Keap1/Nrf2 pathway. *Life Sci.* 261, 118340. doi: 10.1016/j.lfs.2020.118340

Liang, F., Zhang, H., Gao, H., Cheng, D., Zhang, N., Du, J., et al. (2021). Liquiritigenin decreases tumorigenesis by inhibiting DNMT activity and increasing BRCA1 transcriptional activity in triple-negative breast cancer. *Exp. Biol. Med. (Maywood)* 246, 459–466. doi: 10.1177/1535370220957255

Lin, Y., Shi, R., Wang, X., and Shen, H. M. (2008). Luteolin, a flavonoid with potential for cancer prevention and therapy. *Curr. Cancer Drug Targets* 8, 634–646. doi: 10.2174/156800908786241050

Liskova, A., Samec, M., Koklesova, L., Brockmueller, A., Zhai, K., Abdellatif, B., et al. (2021). Flavonoids as an effective sensitizer for anti-cancer therapy: Insights into multi-faceted mechanisms and applicability towards individualized patient profiles. *Epma. J.* 12, 155–176. doi: 10.1007/s13167-021-00242-5

Magne Nde, C. B., Zingue, S., Winter, E., Creczynski-Pasa, T. B., Michel, T., Fernandez, X., et al. (2015). Flavonoids, breast cancer chemopreventive and/or chemotherapeutic agents. *Curr. Med. Chem.* 22, 3434–3446. doi: 10.2174/0929867322666150729115321

Maleki, S. J., Crespo, J. F., and Cabanillas, B. (2019). Anti-inflammatory effects of flavonoids. *Food Chem.* 299, 125124. doi: 10.1016/j.foodchem.2019.125124

Martinez-Perez, C., Ward, C., Cook, G., Mullen, P., Mcphail, D., Harrison, D. J., et al. (2014). Novel flavonoids as anti-cancer agents: mechanisms of action and promise for their potential application in breast cancer. *Biochem. Soc. Trans.* 42, 1017–1023. doi: 10.1042/BST20140073

Mekawy, A. M. M., Abdelaziz, M. N., and Ueda, A. (2018). Apigenin pretreatment enhances growth and salinity tolerance of rice seedlings. *Plant Physiol. Biochem.* 130, 94–104. doi: 10.1016/j.plaphy.2018.06.036

Meng, H., Fu, G., Shen, J., Shen, K., Xu, Z., Wang, Y., et al. (2017). Ameliorative effect of daidzein on cisplatin-induced nephrotoxicity in mice *via* modulation of inflammation, oxidative stress, and cell death. *Oxid. Med. Cell. Longev.* 2017, 3140680. doi: 10.1155/2017/3140680

Miron, A., Aprotosoaie, A. C., Trifan, A., and Xiao, J. (2017). Flavonoids as modulators of metabolic enzymes and drug transporters. *Ann. N. Y. Acad. Sci.* 1398, 152–167. doi: 10.1111/nyas.13384

Mishra, C. B., Pandey, P., Sharma, R. D., Malik, M. Z., Mongre, R. K., Lynn, A. M., et al. (2021). Identifying the natural polyphenol catechin as a multi-targeted agent against SARS-CoV-2 for the plausible therapy of COVID-19: An integrated computational approach. *Brief Bioinform.* 22, 1346–1360. doi: 10.1093/bib/bbaa378

Ninfali, P., Panato, A., Bortolotti, F., Valentini, L., and Gobbi, P. (2020). Morphological analysis of the seeds of three pseudocereals by using light microscopy and ESEM-EDS. *Eur. J. Histochem.* 64. doi: 10.4081/ejh.2020.3075

Pan, H., Zhou, W., He, W., Liu, X., Ding, Q., Ling, L., et al. (2012). Genistein inhibits MDA-MB-231 triple-negative breast cancer cell growth by inhibiting NF-kappaB activity *via* the notch-1 pathway. *Int. J. Mol. Med.* 30, 337–343. doi: 10.3892/ijmm.2012.990

Park, K. I., Park, H. S., Nagappan, A., Hong, G. E., Lee, D. H., Kang, S. R., et al. (2012). Induction of the cell cycle arrest and apoptosis by flavonoids isolated from Korean citrus aurantium l. @ in non-small-cell lung cancer cells. *Food Chem.* 135, 2728–2735. doi: 10.1016/j.foodchem.2012.06.097

Peluso, I., Raguzzini, A., and Serafini, M. (2013). Effect of flavonoids on circulating levels of TNF-alpha and IL-6 in humans: a systematic review and meta-analysis. *Mol. Nutr. Food Res.* 57, 784–801. doi: 10.1002/mnfr.201200721

Peters, N. K., Frost, J. W., and Long, S. R. (1986). A plant flavone, luteolin, induces expression of rhizobium meliloti nodulation genes. *Science* 233, 977–980. doi: 10.1126/science.3738520

Piehowski, P. D., Zhu, Y., Bramer, L. M., Stratton, K. G., Zhao, R., Orton, D. J., et al. (2020). Automated mass spectrometry imaging of over 2000 proteins from tissue sections at 100-mum spatial resolution. *Nat. Commun.* 11, 8. doi: 10.1038/s41467-019-13858-z

Punia, S., and Kumar, M. (2021). Litchi (Litchi chinenis) seed: Nutritional profile, bioactivities, and its industrial applications. *Trends Food Sci. Technol.* 108, 58–70. doi: 10.1016/j.tifs.2020.12.005

Qin, L., Zhang, Y., Liu, Y., He, H., Han, M., Li, Y., et al. (2018). Recent advances in matrix-assisted laser desorption/ionisation mass spectrometry imaging (MALDI-MSI)

for *in situ* analysis of endogenous molecules in plants. *Phytochem. Anal.* 29, 351–364. doi: 10.1002/pca.2759

Rakha, A., Umar, N., Rabail, R., Butt, M. S., Kieliszek, M., Hassoun, A., et al. (2022). Anti-inflammatory and anti-allergic potential of dietary flavonoids: A review. *Biomed. Pharmacother.* 156, 113945. doi: 10.1016/j.biopha.2022.113945

Ren, J., Lu, Y., Qian, Y., Chen, B., Wu, T., and Ji, G. (2019). Recent progress regarding kaempferol for the treatment of various diseases (Review). *Exp. Ther. Med.* 18, 2759–2776. doi: 10.3892/etm.2019.7886

Shi, Y., Hu, H., Hao, Q., Wu, R., Wang, L., Qin, L., et al. (2022). Michler's ethylketone as a novel negative-ion matrix for the enhancement of lipid MALDI tissue imaging. *Chem. Commun. (Camb.)* 58, 633–636. doi: 10.1039/d1cc05718a

Shirley, B. W. (1998). Flavonoids in seeds and grains: Physiological function, agronomic importance and the genetics of biosynthesis. *Seed Sci. Res.* 8, 415–422. doi: 10.1017/s0960258500004372

Singh, P., Arif, Y., Bajguz, A., and Hayat, S. (2021). The role of quercetin in plants. *Plant Physiol. Biochem.* 166, 10–19. doi: 10.1016/j.plaphy.2021.05.023

Song, X., Tan, L., Wang, M., Ren, C., Guo, C., Yang, B., et al. (2021). Myricetin: A review of the most recent research. *Biomed. Pharmacother.* 134, 111017. doi: 10.1016/j.biopha.2020.111017

Soubeyrand, E., Johnson, T. S., Latimer, S., Block, A., Kim, J., Colquhoun, T. A., et al. (2018). The peroxidative cleavage of kaempferol contributes to the biosynthesis of the benzenoid moiety of ubiquinone in plants. *Plant Cell* 30, 2910–2921. doi: 10.1105/tpc.18.00688

Souza, R. P., Bonfim-Mendonca, P. S., Gimenes, F., Ratti, B. A., Kaplum, V., Bruschi, M. L., et al. (2017). Oxidative stress triggered by apigenin induces apoptosis in a comprehensive panel of human cervical cancer-derived cell lines. *Oxid. Med. Cell. Longev.* 2017, 1512745. doi: 10.1155/2017/1512745

Sudhakaran, M., Sardesai, S., and Doseff, A. I. (2019). Flavonoids: New frontier for immuno-regulation and breast cancer control. *Antioxidants (Basel)* 8. doi: 10.3390/antiox8040103

Sun, R., Hikosaka, S., Goto, E., Sawada, H., Saito, T., Kudo, T., et al. (2012). Effects of UV irradiation on plant growth and concentrations of four medicinal ingredients in Chinese licorice (Glycyrrhiza uralensis). *Acta Hortic.* 956, 643–648. doi: 10.17660/ActaHortic.2012.956.77

Surichan, S., Androutsopoulos, V. P., Sifakis, S., Koutala, E., Tsatsakis, A., Arroo, R. R., et al. (2012). Bioactivation of the citrus flavonoid nobiletin by CYP1 enzymes in MCF7 breast adenocarcinoma cells. *Food Chem. Toxicol.* 50, 3320–3328. doi: 10.1016/j.fct.2012.06.030

Suzuki, T., Morishita, T., Kim, S.-J., Park, S.-U., Woo, S.-H., Noda, T., et al. (2015). Physiological roles of rutin in the buckwheat plant. *Japan Agric. Res. Quarterly: JARQ* 49, 37–43. doi: 10.6090/jarq.49.37

Taira, S., Tokai, M., Kaneko, D., Katano, H., and Kawamura-Konishi, Y. (2015). Mass spectrometry imaging analysis of location of procymidone in cucumber samples. *J. Agric. Food Chem.* 63, 6109–6112. doi: 10.1021/acs.jafc.5b00957

Tang, Y., Yu, C., Wu, J., Chen, H., Zeng, Y., Wang, X., et al. (2018). Lychee seed extract protects against neuronal injury and improves cognitive function in rats with type II diabetes mellitus with cognitive impairment. *Int. J. Mol. Med.* 41, 251–263. doi: 10.3892/ijmm.2017.3245

Tautenhahn, R., Cho, K., Uritboonthai, W., Zhu, Z., Patti, G. J., and Siuzdak, G. (2012). An accelerated workflow for untargeted metabolomics using the METLIN database. *Nat. Biotechnol.* 30, 826–828. doi: 10.1038/nbt.2348

Van De Plas, R., Yang, J., Spraggins, J., and Caprioli, R. M. (2015). Image fusion of mass spectrometry and microscopy: A multimodality paradigm for molecular tissue mapping. *Nat. Methods* 12, 366–372. doi: 10.1038/nmeth.3296

Von Minckwitz, G., Huang, C. S., Mano, M. S., Loibl, S., Mamounas, E. P., Untch, M., et al. (2019). Trastuzumab emtansine for residual invasive HER2-positive breast cancer. *N. Engl. J. Med.* 380, 617–628. doi: 10.1056/NEJMoa1814017

Vue, B., Zhang, S., and Chen, Q. H. (2016). Flavonoids with therapeutic potential in prostate cancer. *Anticancer Agents Med. Chem.* 16, 1205–1229. doi: 10.2174/1871520615666151008122622

Wan, L., Lei, Y., Yan, L., Liu, Y., Pandey, M. K., Wan, X., et al. (2020). Transcriptome and metabolome reveal redirection of flavonoids in a white testa peanut mutant. *BMC Plant Biol.* 20, 161. doi: 10.1186/s12870-020-02383-7

Wang, J., Mao, J., Wang, R., Li, S., Wu, B., and Yuan, Y. (2020). Kaempferol protects against cerebral ischemia reperfusion injury through intervening oxidative and inflammatory stress induced apoptosis. *Front. Pharmacol.* 11. doi: 10.3389/fphar.2020.00424

Wang, X., Yang, Y., An, Y., and Fang, G. (2019). The mechanism of anticancer action and potential clinical use of kaempferol in the treatment of breast cancer. *Biomed. Pharmacother.* 117, 109086. doi: 10.1016/j.biopha.2019.109086

Wishart, D. S., Guo, A., Oler, E., Wang, F., Anjum, A., Peters, H., et al. (2022). HMDB 5.0: The human metabolome database for 2022. *Nucleic Acids Res.* 50, D622–D631. doi: 10.1093/nar/gkab1062

Wu, R., Qin, L., Chen, L., Ma, R., Chen, D., Liu, H., et al. (2021). Copper adhesive tape attached to the reverse side of a non-conductive glass slide to achieve protein MALDI-imaging in FFPE-tissue sections. *Chem. Commun. (Camb.)* 57, 10707–10710. doi: 10.1039/d1cc03629g

Xie, J., Pang, Y., and Wu, X. (2021). Taxifolin suppresses the malignant progression of gastric cancer by regulating the AhR/CYP1A1 signaling pathway. *Int. J. Mol. Med.* 48. doi: 10.3892/ijmm.2021.5030

Yang, L., Gao, Y., Bajpai, V. K., El-Kammar, H. A., Simal-Gandara, J., Cao, H., et al. (2021b). Advance toward isolation, extraction, metabolism and health benefits of kaempferol, a major dietary flavonoid with future perspectives. *Crit. Rev. Food Sci. Nutr.* 1–17. doi: 10.1080/10408398.2021.1980762

Yang, C., Song, J., Hwang, S., Choi, J., Song, G., and Lim, W. (2021a). Apigenin enhances apoptosis induction by 5-fluorouracil through regulation of thymidylate synthase in colorectal cancer cells. *Redox Biol.* 47, 102144. doi: 10.1016/j.redox.2021.102144

Yang, W., Xu, X., Li, Y., Wang, Y., Li, M., Wang, Y., et al. (2016). Rutin-mediated priming of plant resistance to three bacterial pathogens initiating the early SA signal pathway. *PLos One* 11, e0146910. doi: 10.1371/journal.pone.0146910

Yao, P., Gao, Y., Simal-Gandara, J., Farag, M. A., Chen, W., Yao, D., et al. (2021). Litchi (Litchi chinensis sonn.): A comprehensive review of phytochemistry, medicinal properties, and product development. *Food Funct.* 12, 9527–9548. doi: 10.1039/d1fo01148k

Yeon, M. J., Lee, M. H., Kim, D. H., Yang, J. Y., Woo, H. J., Kwon, H. J., et al. (2019). Anti-inflammatory effects of kaempferol on helicobacter pylori-induced inflammation. *Biosci. Biotechnol. Biochem.* 83, 166–173. doi: 10.1080/09168451.2018.1528140

Zaima, N., Goto-Inoue, N., Hayasaka, T., and Setou, M. (2010). Application of imaging mass spectrometry for the analysis of oryza sativa rice. *Rapid Commun. Mass Spectrom.* 24, 2723–2729. doi: 10.1002/rcm.4693

Zhang, H. W., Hu, J. J., Fu, R. Q., Liu, X., Zhang, Y. H., Li, J., et al. (2018). Flavonoids inhibit cell proliferation and induce apoptosis and autophagy through downregulation of PI3Kγ mediated PI3K/AKT/mTOR/p70S6K/ULK signaling pathway in human breast cancer cells. *Sci. Rep.* 8, 11255. doi: 10.1038/s41598-018-29308-7

Zhang, J., Hu, C., Li, X., Liang, L., Zhang, M., Chen, B., et al. (2021). Protective effect of dihydrokaempferol on acetaminophen-induced liver injury by activating the SIRT1 pathway. *Am. J. Chin. Med.* 49, 705–718. doi: 10.1142/S0192415X21500324

Zhao, L., Wang, K., Wang, K., Zhu, J., and Hu, Z. (2020). Nutrient components, health benefits, and safety of litchi (Litchi chinensis sonn.): A review. *Compr. Rev. Food Sci. Food Saf.* 19, 2139–2163. doi: 10.1111/1541-4337.12590

Zhao, F., Zhao, Z., Han, Y., Li, S., Liu, C., and Jia, K. (2021). Baicalin suppresses lung cancer growth phenotypes *via* miR-340-5p/NET1 axis. *Bioengineered* 12, 1699–1707. doi: 10.1080/21655979.2021.1922052

Zhu, X., Wang, H., Sun, J., Yang, B., Duan, X., and Jiang, Y. (2019). Pericarp and seed of litchi and longan fruits: Constituent, extraction, bioactive activity, and potential utilization. *J. Zhejiang Univ. Sci. B* 20, 503–512. doi: 10.1631/jzus.B1900161

frontiers | Frontiers in Plant Science

TYPE Original Research
PUBLISHED 06 April 2023
DOI 10.3389/fpls.2023.1144556

OPEN ACCESS

EDITED BY
Yinglang Wan,
Hainan University, China

REVIEWED BY
Zhi Chao,
Southern Medical University, China
Lixing Nie,
National Institutes for Food and Drug Control, China

*CORRESPONDENCE
Yu-Ping Yan
yanyuping2008@126.com
Yu-Guang Zheng
zyg314@163.com

†These authors have contributed equally to this work

SPECIALTY SECTION
This article was submitted to Technical Advances in Plant Science, a section of the journal Frontiers in Plant Science

RECEIVED 14 January 2023
ACCEPTED 10 March 2023
PUBLISHED 06 April 2023

CITATION
Liu P, Wang J-M, Guo H-C, Zhao M-W, Song Y-X, Guo H, Duan X-H, Yan Y-P and Zheng Y-G (2023) *In situ* detection and mass spectrometry imaging of protein-related metabolites in Bombyx batryticatus before and after frying with wheat bran. *Front. Plant Sci.* 14:1144556. doi: 10.3389/fpls.2023.1144556

In situ detection and mass spectrometry imaging of protein-related metabolites in Bombyx batryticatus before and after frying with wheat bran

Pai Liu[1,2†], Jie-Min Wang[1,2†], Hao-Chuan Guo[1], Meng-Wei Zhao[1], Yong-Xing Song[1], Hui Guo[1], Xu-Hong Duan[1,2], Yu-Ping Yan[1,2*] and Yu-Guang Zheng[1,2*]

[1]College of Pharmacy, Hebei University of Chinese Medicine, Shijiazhuang, Hebei, China, [2]Traditional Chinese Medicine Processing Technology Inheritance Base of the State Administration of Traditional Chinese Medicine, College of Pharmacy, Hebei University of Chinese Medicine, Shijiazhuang, Hebei, China

Bombyx batryticatus is derived from the dried larva of *Bombyx mori* Linnaeus infected by *Beauveria bassiana* (Bals.) Vuillant. Raw Bombyx batryticatus should be stir-fried before oral administration due to its irritation to the gastrointestinal tract. Nevertheless, it is still an arduous task to uncover the intrinsic mechanism of Bombyx batryticatus processing. In this study, we collected two types of Bombyx batryticatus, one being stir-fried and the other serving as a control. Then, an informative approach, which integrated matrix-assisted laser desorption/ionization mass spectrometry imaging (MALDI-MSI) with chemometrics analysis, was established to screen processing-associated markers and reveal *in situ* spatial distribution patterns of protein-related metabolites. After optimization of experimental conditions, 21 ions were initially detected from Bombyx batryticatus, including amino acids and peptides. In addition, 15 differential markers were screened by orthogonal projection to potential structure discriminant analysis (OPLS-DA), which were localized and visualized in the transverse section of Bombyx batryticatus by MSI. Eventually, it can be demonstrated that the stir-frying process reduces toxicity while potentially boosting specific biological activities of Bombyx batryticatus. In summary, the established strategy could not only clarify the chemical transformation of protein-related metabolites from Bombyx batryticatus before and after frying with wheat bran, but also reveal the significance of Chinese medicine processing technology.

KEYWORDS

MALDS-MSI, before and after frying, OPLS-DA, protein-related metabolites, Chinese medicine, Bombyx batryticatus

Introduction

Bombyx batryticatus is a famous Chinese medicine, which belongs to the dry bodies of the 4th and the 5th instar larvae of *Bombyx mori* Linnaeus infected (or artificially inoculated) with *Beauveria bassiana* (Bals.) Vuillant (Chinese Pharmacopoeia Commission, 2020). Bombyx batryticatus has a long history of clinical application in Chinese medicine, which was first recorded in the *Classic of Shennong Materia*. The main efficacy of Bombyx batryticatus is resolving phlegm and dispersing blood stasis, dispelling wind and settling shock. It is mainly used in the treatment of liver wind and phlegm, convulsion, infantile shock, tetanus, sore throat, and rubella pruritus (Wang et al., 2021a). The first-class Bombyx batryticatus has a hard texture, thick strips, white color and bright cross-section (Hu, 2017). Beauveria Batryticatus contains various chemical components, such as protein, amino acid, ammonium oxalate, enzymes, nucleoside bases, trace elements, etc. (Bai et al., 2018). The *Bombyx mori* feeds mainly on leaves of mulberry (*Morus alba* Linn.) throughout their life, absorbing, accumulating and metabolizing a variety of chemicals within their bodies. After invading the *Bombyx mori*, *Beauveria bassiana* proceed to multiply and grow based on the larva as a resource of nutrients, which was essentially a fermentation process by the fungus. Furthermore, the original components can be transformed into new components with higher activity in the form of hydroxylation, redox reaction, sulfonation, and hydrolysis of epoxide 4-O-methylglucoside (Xing et al., 2019). Accordingly, the bioactivities of Bombyx batryticatus are essentially derived from the co-action of *Bombyx mori*, mulberry leaves and *Beauveria bassiana* (Figure 1).

The processing of Chinese medicine is a unique pharmaceutical technology in China, which refers to the manufacturing process of stir-frying, roasting, carbonizing, steaming, etc., aiming to enhance efficacy and reduce toxicity (Li et al., 2020). There are two types of Bombyx batryticatus widely used in clinical applications, namely raw and fried forms. Bombyx batryticatus research has always focused on small molecular compounds with little protein-related metabolites involved in the past. For example, Wang et al. (2022) established a high performance liquid chromatography (HPLC) fingerprint combined with chemical pattern recognition technology to evaluate the quality of Bombyx batryticatus. A liquid chromatography-tandem mass spectrometry (LC-MS/MS) technology was used to qualitatively analyze the chemical constituents in water-soluble substances of Bombyx batryticatus (Wang et al., 2021b). Although several attempts have been made to elucidate the active metabolites in Bombyx batryticatus, the intrinsic transformation mechanisms of protein-related metabolites, which account for the largest proportion of endogenous components, from Bombyx batryticatus before and after frying are still unclear. Chinese medicine is a complex mixture with hundreds of chemical components. the active ingredients can be easily altered or lost, and the spatial distribution of various components in tissues is also severely damaged during processing, such as extraction, purification and enrichment, making it impossible to achieve *in situ* analysis of active ingredients (Wang et al., 2016). In recent years, matrix-assisted laser desorption/ionization mass spectrometry imaging (MALDI-MSI) has become an imaging technique for studying the composition and distribution of molecules or ions at the tissue or cellular level (Li et al., 2020), which is characterized with high sensitivity, high spatial resolution and high laser scanning speed (Zemaitis et al., 2022). Shu et al. (2010) performed MSI to confirm that ginsenosides were located more in the cortex and periderm than in the medulla of a lateral root of *Panax ginseng*. Li et al. (2021a) used MALDI-MSI combined with multiple matrixes to analyze spatial metabolomes on root sections of the two *Paeonia* species. Li et al. (2014) showed the distribution of major tissue-specific metabolites in the rhizome of *Glycyrrhiza glabra* (licorice) at cellular level by atmospheric pressure MALDI-MSI. However, this technique has not been applied to study the distribution of chemical components in tissues during processing Bombyx batryticatus.

In the present work, a mass spectrometry-based profiling and imaging strategy was established to reveal the chemical transformation of protein-related metabolites from Bombyx batryticatus before and after frying with wheat bran. To begin with, the chemical profiling of peptides and amino acids from raw and fried Bombyx batryticatus was achieved by identifying characteristic ion fragments and matching our in-built database. Subsequently, multivariate statistical analysis was applied to screen processing-related markers. Finally, MALDI-MSI was performed to testify the markers discovered and visualize their chemical transformation trajectories.

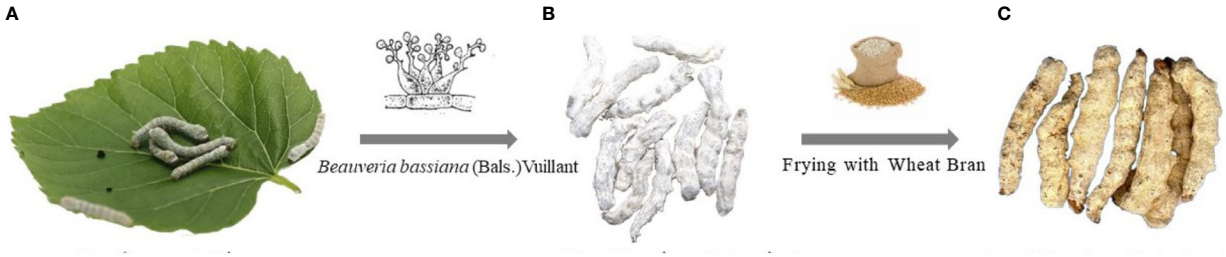

FIGURE 1
The formation of raw and fried Bombyx batryticatus. **(A)** Bombyx mori Linnaeus and mulberry leaves. **(B)** Raw Bombyx batryticatus. **(C)** Fried Bombyx batryticatus.

Materials and methods

Instruments and reagents

Instruments used in this study included Bruker Rapiflex MALDI-TOF/TOF mass spectrometer equipped with the FlexAnalysis data processing workstation (Bruker, Karlsruhe, Germany), GET-Sprayer (I) (HIT Co., Ltd., Beijing, China), Indium Tin Oxide (ITO) conductive slides (diagonal resistance ~40 Ω, Bruker, Karlsruhe, Germany), vacuum desiccator (Shanghai Yueyang Electronic Technology Co., Ltd., Shanghai, China), and cryomicrotome (Leica CM1950, Nussloch, Germany).

The following reagents were used in this study: methanol and acetonitrile (mass spectrometry pure, Merck, Darmstadt, Germany), optimum cutting temperature (OCT) embedding agent (Leica, Nussloch, Germany), and trifluoroacetic acid (TFA) (Sigma, St. Louis, MO, USA). Water was purified by a Milli-Q filtration system (Millipore, Billerica, MA, USA). A total of 26 compounds representing five different classes of bioactive components (e.g., amino acids, peptides, nucleosides, flavonoids, and others) were procured from the National Institutes of Food and Drug Control (Beijing, China) and used as reference compounds (Supplementary Table 1).

Sample preparation

Both raw Bombyx batryticatus (RBB) and fried Bombyx batryticatus (FBB) were purchased from Hebei Chenghai Tang Chinese Medicine Co., Shijiazhuang, Hebei Province, China. Morphological identification of Bombyx batryticatus was carried out by Professor Yu-Guang Zheng at the Processing Technology Innovation Center of Traditional Chinese Medicine (TCM), Shijiazhuang, Hebei Province. After the matrix application, three samples from the two types of Bombyx batryticatus were selected, and three biological replicates of each sample were performed. Bombyx batryticatus was placed in a freezing microtome at -25°C for 30 min and fixed to the microtome tray with OCT embedding agent. Frozen tissue sections of 20 µm in thickness were transferred to ITO conductive glass slides and vacuumed in a vacuum desiccator for 20 min.

Matrix and standard solution preparation

200mg control powder of 2-mercaptobenzothiazole (2-MBT) was weighed and dissolved in 10 ml of methanol-water (7:3) solution, followed by the addition of 0.1% trifluoroacetic acid (TFA) dropwise to promote ionization, and finally prepared into a matrix solution with a mass concentration of 20 mg/ml. The control solution of standard substances was prepared at 1.0 mg/ml. Then, 1 µl of the control solution was added dropwise to the Bruker ground steel target plate and dried in vacuum for 20 minutes until the sample spot was dry. After that, the matrix solution (1 µl) was added dropwise to cover the sample spot and dried in vacuum again until the solvent evaporated, followed by MALDI-MS analysis.

Matrix application

Vacuum-dried Bombyx batryticatus tissue sections were fixed in a matrix sprayer and matrix spraying was performed with 2-MBT. The spray program was performed for 8 cycles with a matrix flow rate of 0.075 mL/min, nozzle temperature at 60°C, nozzle travel speed of 800 mm/min, nozzle travel row spacing of 3 mm, and nozzle-sample row spacing of 3 cm. Tissue sections were prepared for the MALDI mass spectrometry analysis after spraying.

MALDI-TOF-MSI

Tissue sections of sprayed matrix were placed in a Bruker Rapiflex MALDI-TOF/TOF type mass spectrometer (Bruker, Karlsruhe, Germany) equipped with a smartbeamTM 3D laser for mass spectrometry imaging analysis. The wavelength was 355 nm at a sampling rate of 2.5 GS/s. MALDI mass spectrometry imaging was performed in a positive ion detection mode with a mass-to-charge ratio (m/z) ranging from 100 to 1500 and a spatial resolution of 100 µm for scanning samples.

MALDI-TOF-MS/MS

Peak values of precursor ions were obtained in the positive ionization and reflectron modes. Tandem mass spectrometry was performed in a LIFT mode with a mass tolerance of 0.05%. Precursor ions were accelerated at 7.5 kV under optimized ion-selective gating. The acceleration voltage of the LIFT unit was set to 19 kV. All mass spectra were analyzed with FlexAnalysis software 3.4 (https://softwaretopic.informer.com/). Default settings were used for baseline correction and smoothing.

Data analysis

For the mass spectrometry analysis, FlexAnalysis 3.4 software of Bruker (https://softwaretopic.informer.com/) was used for initial mass spectrum observation and processing. These extracted mass spectra were baseline subtracted, normalized, and recalibrated based on the total ion count (TIC) in the observed mass range. Ion screening was performed based on accurate mass-to-charge ratios from the literature and databases of METLIN (https://metlin.scripps.edu/) and HMDB (https://hmdb.ca). Three ion addition forms, i.e., $[M+H]^+$, $[M+Na]^+$, and $[M+K]^+$, were used to perform database search. Data sets were tabulated and imported into SIMCA 14 software (Umetrics, Malmo, Sweden) for multivariate statistical analyses, including principal component analysis (PCA), orthogonal projection to potential structure discriminant analysis (OPLS-DA) and hierarchical cluster analysis (HCA), to distinguish samples with different quality characteristics and identify potential quality-related markers. In order to further confirm the differential metabolites identified above, a Student's t-test analysis was conducted, which will be illustrated in the form of statistical tables (Supplementary Table 2).

Results

Chemical composition profile of Bombyx batryticatus before and after frying with wheat bran

In order to comprehensively, systematically and accurately identify the various types of active ingredients in raw Bombyx batryticatus and fried Bombyx batryticatus, we analyzed the characteristic ion fragmentation information of the standards, inferring the fragmentation patterns and suitable ionization conditions applicable to the ions of different components. Finally, the positive mode was adopted in the ranges of m/z 100-400 and m/z 400-800 for higher intensities and clearer fragmentation patterns to identify the ionic structure of different components. The representative overall average mass spectra are shown in Figure 2. There were 9 amino acid peaks and 12 peptide peaks identified from the transverse sections of Bombyx batryticatus by MS/MS fragmentation patterns of reference standards in conjunction with the precise mass-to-charge ratios, isotopic peaks, data from various literature and other databases (Supplementary Figure 1). We detected three main ionic adduct forms, i.e., $[M+H]^+$, $[M+Na]^+$, and $[M+K]^+$. Most amino acids had all been identified as $[M+H]^+$ form ions, while a large number of peptides were revealed to be sodium or potassium adducts (Table 1). Notably, owing to the extreme degradation and transformation of certain active ingredients in high-temperature environments, the contents of most active ingredients in fried Bombyx batryticatus, with the exception of some specific ingredients, were drastically reduced, although the varieties of compounds contained were essentially identical.

Multivariate statistical analysis of protein-related metabolites in raw Bombyx batryticatus and fried Bombyx batryticatus

The raw profile data of endogenous compounds detected were preprocessed including data filtering, area normalization, peak extraction and deconvolution *via* Bruker FlexAnalysis 3.4 software. After the standardization processing, the processed data were loaded into SIMCA-P 14 for further multivariate statistical analysis. Various samples of raw Bombyx batryticatus and fried Bombyx batryticatus were clearly separated into two unique clusters in the principal component analysis (PCA) score plots, indicating substantial distinction between the two treatment groups (Figure 3A). The R^2X (0.848) and Q^2 (0.691) values of the established PCA model demonstrated its superior fitness and prediction.

OPLS-DA was used to detect characteristic components that cause the differences in the product quality (Gennebäck et al., 2013). The OPLS-DA model clearly distinguished samples of raw Bombyx batryticatus and fried Bombyx batryticatus (Figure 3B). The cumulative statistic R^2X (0.768), model interpretation rate parameter R^2Y (0.993), and prediction ability parameter Q^2 (0.985) of the fitted model were all higher than 0.5, indicating that the established model is stable and reliable, and the prediction ability is strong. In addition, OPLS-DA model verification (permutation test n=200) was conducted, resulting in R^2 of 0.278 and Q^2 of -0.639 (Supplementary Figure 2). The values of R^2 and Q^2 were higher than those on the left side, and Q^2 intersected with the Y-axis on the negative half-axis, indicating that the model is reliable without any overfitting phenomenon.

Variable importance projection (VIP) can reflect the degree of contribution of ions to the model classification. Therefore,

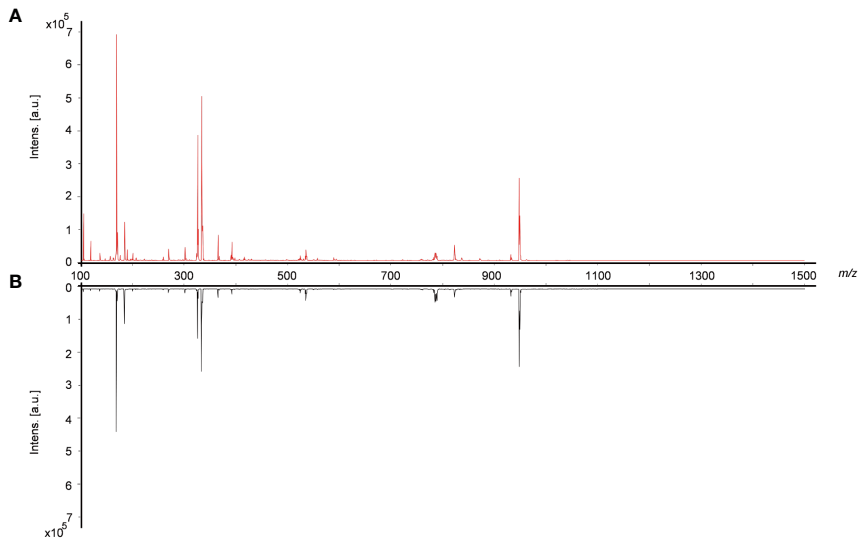

FIGURE 2
Typical overall average mass spectra obtained from cross sections of raw and fried Bombyx batryticatus by MALDI-TOF-MS in a positive mode. **(A)** Raw Bombyx batryticatus (red). **(B)** Fried Bombyx batryticatus (black).

TABLE 1 Amino acids and peptides detected in Bombyx batryticatus by MALDI-TOF-MSI and confirmed by MALDI-TOF-MS/MS.

Compound type	Identify	Molecular formula	Ion information		
			Adduct	m/z	Fragmentations
Amino acid	L-glutamic acid	$C_5H_9NO_4$	$[M+K]^+$	186.02	131.05, 130.05, 102.06 and 84.04
	L-proline	$C_5H_9NO_2$	$[M+H]^+$	116.07	70.07 and 68.05
	L-arginine	$C_6H_{14}N_4O_2$	$[M+H]^+$	175.12	158.09, 116.07 and 130.10
	L-tyrosine	$C_9H_{11}NO_3$	$[M+H]^+$	182.08	165.06, 147.04, 136.08 and 123.04
	L-lysine	$C_6H_{14}N_2O_2$	$[M+H]^+$	147.11	130.09, 101.11, 85.09 and 84.08
	Homoarginine	$C_7H_{16}N_4O_2$	$[M+H]^+$	189.14	187.40, 145.16, 151.24, 170.22 and 126.91
	γ-aminobutyric acid	$C_4H_9NO_2$	$[M+H]^+$	104.07	103.00, 83.92, 101.32, 58.51 and 73.21
	L-valine	$C_5H_{11}NO_2$	$[M+H]^+$	118.09	72.08, 59.05, 56.05 and 53.04
	Phosphatidylserine	$C_{42}H_{82}NO_{10}P$	$[M+Na]^+$	814.56	153.00, 281.25, 417.24, 773.53 and 774.54
Peptide	Beauvericin	$C_{45}H_{57}N_3O_9$	$[M+H]^+$	784.42	541.29, 362.19, 262.14 and 234.15
	Beauvericin A	$C_{46}H_{59}N_3O_9$	$[M+H]^+$	798.43	645.32, 545.26, 384.18 and 244.13
	Tenellin	$C_{21}H_{23}NO_5$	$[M+H]^+$	370.17	_
	Bassianolide	$C_{48}H_{84}N_4O_{12}$	$[M+K]^+$	947.57	682.47, 455.31, 328.21 and 228.16
	Beauverolide A	$C_{30}H_{47}N_3O_5$	$[M+Na]^+$	552.34	384.18, 266.13, 244.13 and 131.10
	Beauverolide B	$C_{31}H_{49}N_3O_5$	$[M+Na]^+$	566.36	_
	Beauverolide C	$C_{35}H_{49}N_3O_5$	$[M+H]^+$	592.38	_
	Beauveriolide I	$C_{27}H_{41}N_3O_5$	$[M+K]^+$	526.28	_
	Cyclo(D)-Pro-(D)-Val	$C_{10}H_{16}O_2N_2$	$[M+K]^+$	235.08	_
	Cyclo-(Ala-Pro)	$C_8H_{12}O_2N_2$	$[M+H]^+$	169.10	_
	Cyclo(Tyr-Val)	$C_{14}H_{18}N_2O_3$	$[M+K]^+$	301.10	235.32, 190.26, 136.10 and 107.18
	Cyclo(Ala-Tyr)	$C_{12}H_{14}N_2O_3$	$[M+Na]^+$	257.10	129.00, 136.00, 162.00, 207.00 and 235.00

differential marker components of amino acids and peptides from raw Bombyx batryticatus and fried Bombyx batryticatus were screened with VIP > 1 as a criterion for differential substances. The results for VIP > 1 included $[homoarginine+H]^+$ (m/z: 189.14, VIP=1.16), $[beauverolide\ C\ acid+H]^+$ (m/z: 592.38, VIP=1.16), $[cyclo(Tyr\text{-}Val)+K]^+$ (m/z: 301.10, VIP=1.16), $[\gamma\text{-}aminobutyric\ acid+H]^+$ (m/z: 104.07, VIP=1.16), $[bassianolide+K]^+$ (m/z: 947.57, VIP=1.16), $[L\text{-}tyrosine+H]^+$ (m/z:182.08, VIP=1.15), $[phosphatidylserine+Na]^+$ (m/z: 814.56, VIP=1.15), $[cyclo\text{-}(Ala\text{-}Pro)+H]^+$ (m/z: 169.10, VIP=1.15), $[beauverolide\ A+Na]^+$ (m/z: 552.34, VIP=1.11), $[tenellin+H]^+$ (m/z: 370.17, VIP=1.10), $[cyclo(Ala\text{-}Tyr)+Na]^+$ (m/z: 257.10, VIP=1.10), $[L\text{-}arginine+H]^+$ (m/z: 175.12, VIP=1.08), $[beauveriolide\ I+K]^+$ (m/z: 526.28, VIP=1.08), $[L\text{-}glutamic\ acid+K]^+$ (m/z: 186.02, VIP=1.05), and $[beauvericin+H]^+$ (m/z: 784.42, VIP=1.05) (Figure 3C). These ions were the major markers of raw Bombyx batryticatus and fried Bombyx batryticatus.

To reveal metabolic changes between raw Bombyx batryticatus and fried Bombyx batryticatus, a total of 21 protein-related metabolites were visualized in hierarchical clustering analysis (HCA). All data mean values are centralized before analysis, clustering by Euclidean rank and measuring distance by mean link. As shown in Figure 3D, each small rectangle in the heat map represents a differentiator, and the content of each metabolite is represented by a standardized range, with darker colors indicating higher metabolite levels. The cluster analysis plot of Bombyx batryticatus samples obviously indicated a division into two subgroups, a result consistent with the previous PCA and OPLS-DA analyses.

Spatial distribution of characteristic protein-related metabolites in raw Bombyx batryticatus and fried Bombyx batryticatus

MALDI-MSI is an advanced technique to unravel the spatiotemporal variations of the metabolic network of endogenous active ingredients in various tissues and layers of Bombyx batryticatus during the stir-frying process. To further investigate the spatial localization of the diverse metabolic pathways of the bioactive constituents in Bombyx batryticatus, the distribution of signature metabolites of proteins, i.e., peptides and amino acids, was explored in the various tissues. Histologically, the anatomical structure of Bombyx batryticatus was separated into

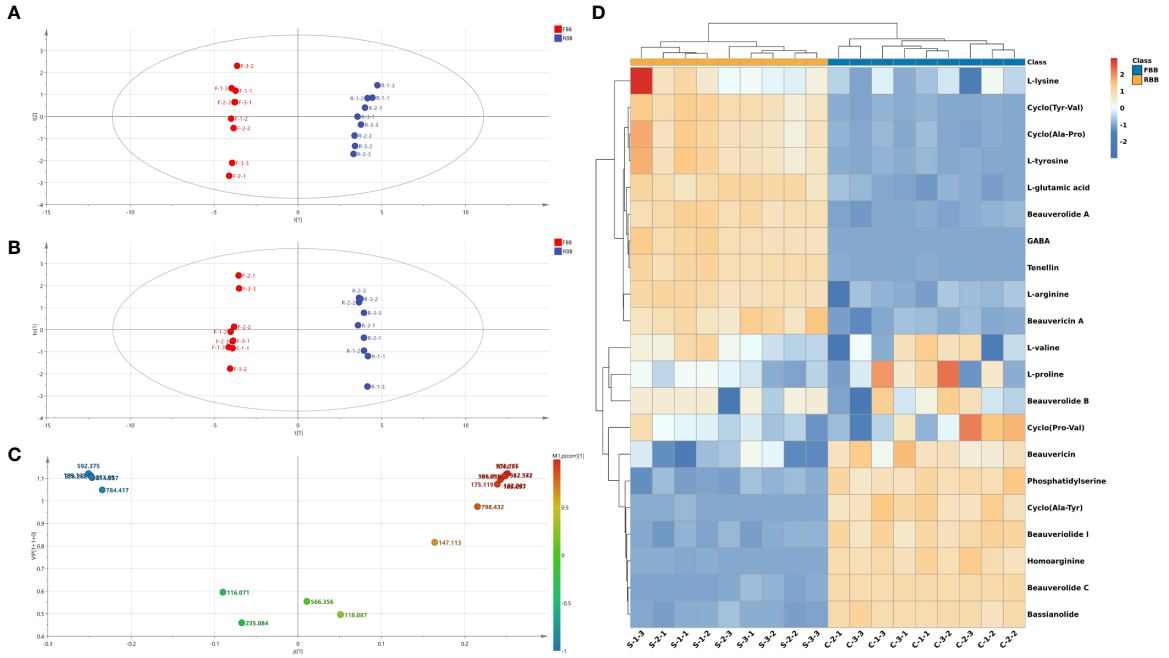

FIGURE 3
Multivariate statistical analysis of MALDI-TOF-MS data from raw and fried Bombyx batryticatus samples. **(A)** PCA score plot. **(B)** OPLS-DA score plot. **(C)** VIP diagram. **(D)** HCA heatmap.

silk gland, digestive tract, mesenchyme and integument from inside to outside (Figure 4).

Among all the compounds, the contents of peptides and amino acids accounted for the highest proportion, which existed in a variety of forms. Figure 5 illustrates the spatial distribution features of beauvericin (m/z 784.42) and bassianolide (m/z 947.57), two types of ring-shaped polypeptides, which were detected as the $[M+H]^+$ and $[M+K]^+$ ionic modes. Although they were both cyclic multi-peptide analogs, their distribution patterns were remarkably divergent. The former was more plentiful in the peripheral zone of the silk gland and the latter was more abundant in the epidermis layer of integument. Beauverolide was a large class of cyclic tricarboxylic acid peptide analogs with a variety of subtypes, such as beauverolide A, beauverolide C and beauverolide I. As determined from the ion signal distribution graphs in Figure 5, the peripheral tissue of the silk gland, mesenchyme and the digestive tract were the dominant

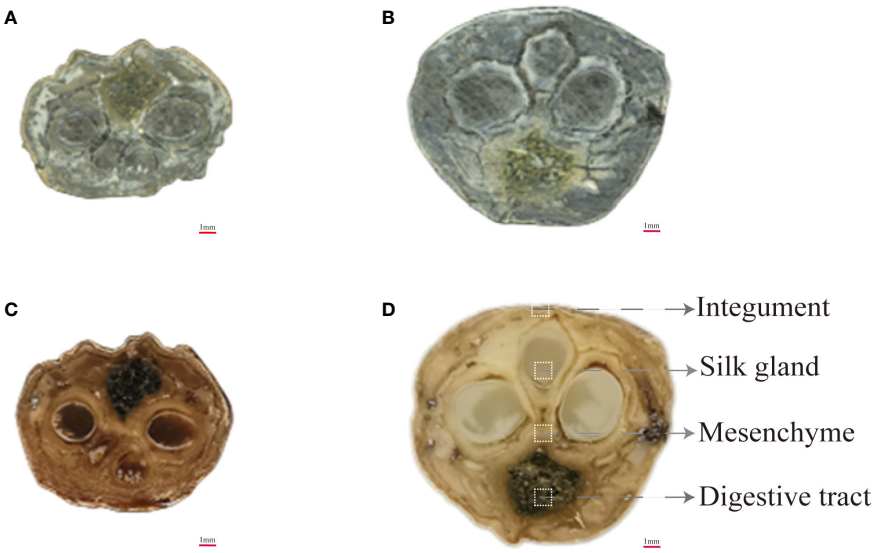

FIGURE 4
Cross-sectional optical images of raw and fried Bombyx batryticatus. **(A, B)** RBB. **(C, D)** FBB.

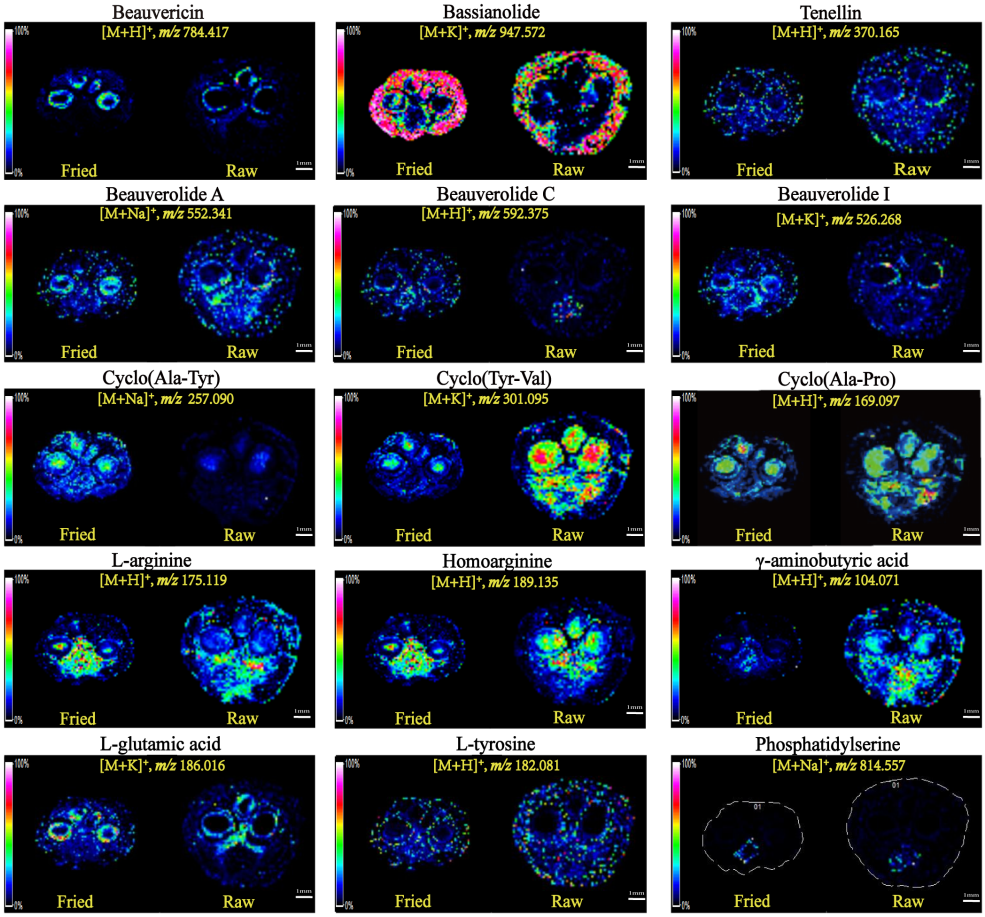

FIGURE 5
Mass spectrometry images of the ions of representative protein-related metabolites in the tissue sections of raw and fried Bombyx batryticatus.

concentration region for beauverolide A in the form of sodium adducts (m/z 552.34), beauverolide C in the form of proton adducts (m/z 592.38) and beauverolide I in the form of potassium adducts (m/z 526.28). It was evident from Figure 5 that the cyclic dipeptides cyclo(Ala-Tyr) (m/z 257.10), cyclo(Tyr-Val) (m/z 301.10) and cyclo(Ala-Pro) (m/z 169.10) were distributed in the silk gland, digestive tract and mesenchyme region primarily in the form of sodium, potassium and proton adducts, respectively. Notably, the distribution pattern of the proton adducts of tenellin (m/z 370.17) was accumulated in the area corresponding to almost all mesenchyme layers of Bombyx batryticatus. As a consequence of high-temperature stir-frying, the corresponding distribution areas of some certain cyclic dipeptides, such as cyclo(Tyr-Val), cyclo(Ala-Pro), beauverolide A, and tenellin, were reduced to a certain extent, accompanied by a dramatic decrease in the intensity of the detected ion signals. On the contrary, it was noteworthy that the abundance and distribution range of cyclo(Ala-Tyr), beauvericin, bassianolide, beauverolide C, and beauverolide I significantly increased in their respective regions (Table 2), which might imply that the latter was more thermally stable.

Amino acids, the most widely distributed chemical compounds in Bombyx batryticatus, were virtually present as proton adducts and exhibited a variable distribution in multiple areas. γ-aminobutyric acid (GABA), as a small non-protein amino acid, was an important inhibitory neurotransmitter of the central nervous system that existed widely in vertebrates, plants and microorganisms (Cifelli et al., 2021). L-arginine (m/z 175.12), homoarginine (m/z 189.14) and GABA (m/z 104.07) were more concentrated in the medial part of the silk gland and the digestive tract (Figure 5). In contrast, it was noted that a kind of amino acid was more plentiful in the peripheral region of the silk gland (Figure 5), which was ultimately characterized as L-glutamic acid (m/z 186.02), i.e., a kind of nonessential amino acid possessing the effect of treating hepatic coma. The distribution pattern of the proton adducts of L-tyrosine (m/z 182.08) was completely different from the above-mentioned localization of amino acids and accumulated at the area corresponding to almost all regions except the silk gland. Phosphatidylserine (m/z 814.56) appeared to have a clear tendency to distribute only in the central area of the digestive tract (Figure 5). Furthermore, it was noteworthy that the distribution areas of a considerable percentage of amino acids were shrunk to a large extent along with the content levels decreased significantly, whereas those of homoarginine increased substantially through the high-temperature processing in contrast (Table 2).

TABLE 2 Potential markers for the differentiation of raw Bombyx batryticatus and fried Bombyx batryticatus with their relative intensities and localization.

No	Compound	Chemical class	m/z	Existence in raw Bombyx batryticatus		Existence in fried Bombyx batryticatus	
				Intensities	Localization	Intensities	Localization
1	[Beauvericin+H]$^+$	Peptides	784.42	31383.56 ± 1931.12	silk gland	39474.44 ± 1122.59	Silk gland
2	[Bassianolide+K]$^+$	Peptides	947.57	165276.22 ± 3439.49	integument	222187.22 ± 2923.05	Integument
3	[Tenellin+H]$^+$	Peptides	370.17	1595.33 ± 72.81	mesenchyme	374.22 ± 20.61	Mesenchyme
4	[Beauverolide A+Na]$^+$	Peptides	552.34	1076.44 ± 47.65	mesenchyme, digestive tract	475.78 ± 28.69	Mesenchyme, Silk gland
5	[Beauverolide C+H]$^+$	Peptides	592.38	485.44 ± 64.85	digestive tract	1764.33 ± 28.01	Mesenchyme
6	[Beauveriolide I+K]$^+$	Peptides	526.28	431.67 ± 12.97	mesenchyme	647.89 ± 22.03	Mesenchyme
7	[Cyclo(Ala-Tyr)+Na]$^+$	Peptides	257.10	490.89 ± 34.28	silk gland	1641.11 ± 158.7	Silk gland
8	[Cyclo(Tyr-Val)+K]$^+$	Peptides	301.10	36395.67 ± 3488.47	silk gland, digestive tract	11948.11 ± 677.5	Silk gland
9	[Cyclo(Ala-Pro)+H]$^+$	Peptides	169.10	71155.78 ± 7863.57	silk gland, digestive tract	33003 ± 2057.84	Silk gland
10	[L-arginine+H]$^+$	Amino acids	175.12	17002.56 ± 258.74	silk gland, digestive tract	13264.11 ± 804.32	Digestive tract
11	[Homoarginine+H]$^+$	Amino acids	189.14	34114.78 ± 2136.17	digestive tract	332016.89 ± 26292.6	Silk gland, Digestive tract
12	[γ-aminobutyric acid+H]$^+$	Amino acids	104.07	135363.11 ± 8532.19	silk gland, digestive tract	8355.89 ± 235.28	Digestive tract
13	[L-glutamic acid+K]$^+$	Amino acids	186.02	2053 ± 28.22	mesenchyme	1704.67 ± 25.79	Mesenchyme
14	[L-tyrosine+H]$^+$	Amino acids	182.08	951.78 ± 119.21	mesenchyme	358.22 ± 19.33	Mesenchyme
15	[Phosphatidylserine+Na]$^+$	Amino acids	814.56	1047.89 ± 63.83	digestive tract	1724.44 ± 77.49	Digestive tract

Discussion

By integrating factors such as tissue integrity, data accuracy and detection sensitivity, we eventually set the section thickness of the tissue at 20 μm and the temperature at -25°. Further, in the pre-experiments for the extraction of active ingredients of Bombyx batryticatus we observed that more ionic peaks could be detected in the positive mode by spraying with 2-MBT as the matrix compared to the negative mode, possibly related to the spatial structure and ionization mode of the compounds. Therefore, we determined to choose the positive mode in our experiments.

The body of the authentic Bombyx batryticatus was white, straight, stiff, crisp, etc., among which the key characters that determined the quality of Bombyx batryticatus were the traits of silk gland in the cross section of Bombyx batryticatus after fracture. The transverse section of Bombyx batryticatus with the best curative properties was described as black, full and shiny like mirrors (Hu et al, 2017). By virtue of the *in situ* spatial distribution of 15 signature peptides and amino acids, we found that silk gland tissue was the enrichment region for the majority of active ingredients, demonstrating the spatial localization advantage of MSI over traditional analysis techniques. In the field of Chinese medicine research and development, silk gland could be regarded as the primary region for extracting the effective components of Bombyx batryticatus, so as to improve potency and reduce side effects.

Beauvericin is a cyclic tricarboxylic acid peptide, the essentially secondary metabolite secreted by *Beauveria bassiana* during the growing process as one of the most crucial active ingredients of the Bombyx batryticatus (Chen et al., 2019). We detected various types of beauvericin and its derivatives, such as beauvericin A, bassianolide and beauverolide A, which had pharmacological properties including antitumor (Zhan et al., 2007; Jiang et al., 2014; Wu et al., 2017), antibacterial (Kouri et al., 2005; Mei et al., 2009), antiviral, and anticonvulsant effects (Jiang et al., 2023). Cyclodipeptide is formed by the internal cyclization of two amino acids, with 2,5-diketopiperazine or 2,5-dioxypiperazine as its parent nucleus (Wei, 2020). There were several types of cyclic dipeptides identified by MALDI-MSI, such as cyclo(Tyr-Val) and cyclo(Ala-Pro), with the bioactivities of anti-tumor, neuroprotective, immune and metabolic regulatory, and anti-inflammatory effects (Qiang and Mei, 2014). It was revealed that some certain peptides and amino acids in stir-fried Bombyx batryticatus were elevated in specific regions by MSI, which might be attributed to the local degradation effect of proteins. Notably, we observed that the apparent increase in the abundance of beauvericin and bassianolide was accompanied by dramatic descents of cyclo(Tyr-Val) and cyclo(Ala-Pro). Such a tendency of variation in the content of peptides might greatly indicate the enhancement of antitumor, antiviral and anticonvulsant effects, as well as the decrease of antioxidant, neuroprotective, immune and metabolic regulatory activities.

GABA is an important active ingredient in mulberry leaves. It was reported that the intake of certain amounts of GABA had physiological effects, such as improving the quality of sleep, reducing toxic impairment of hepatocytes, and lowering blood

pressure (Nakamura et al., 2011). Arginine is involved in the ornithine cycle in the body, which facilitates the conversion of ammonia produced in the body into non-toxic urea for excretion, thereby reducing the blood ammonia concentration and correcting the acid-base balance in hepatic encephalopathy (Mangoni et al., 2019). Furthermore, homoarginine is a naturally occurring, non-protein-derived, cationic amino acid, which increases the availability of nitric oxide (NO), affecting endothelial function (Rodionov et al., 2021). Elevated levels of homoarginine could exert positive effects that were associated with cardiovascular protection, in terms of strengthening endothelial function, suppressing platelet aggregation and boosting insulin secretion (Kathrin et al., 2019). The results of our study demonstrated that significant decreases in arginine and GABA levels were accompanied by increased homoarginine content during the stir-frying process. The fried Bombyx batryticatus may not be as effective as raw Bombyx batryticatus in treating liver disease and neurotrophic effects, while it was more valuable in reducing the risk of cardiovascular disease (Kong et al., 2014; Zhao et al., 2018).

In recent years, it had been reported that the consumption of raw Bombyx batryticatus could sometimes trigger adverse reactions, probably due to the entry of foreign proteins into the body, which could lead to allergy and intense multi-organ syndromes through the immune mechanism, manifesting as respiratory obstruction, circulatory symptoms and abdominal pain as well as other type I allergic reactions. The allergen was also cross-reactive with the central nervous system, resulting in metabolic disorders and dysfunction of the central nervous system (Tu and Yu, 2012). Therefore, it was confirmed that the Bombyx batryticatus should be stir-fried with wheat bran before being applied to therapeutic purposes on account of the clinical experience from ancient Chinese medicine practitioners. As a matter of fact, this empirical medical theory was not fully accepted by the western medicine. Notably, it could be demonstrated from the rigorous data obtained in our study that fried Bombyx batryticatus had the following advantages over raw Bombyx batryticatus with reference to the relevant literature.

Above all, during the process of high-temperature frying, the energy absorbed by the protein exceeded the intermolecular interaction force, leading to the destruction of the spatial conformation in protein, followed by the rupture of the peptide chain, thus partially denaturing and inactivating the protein (Lin et al., 2020). The reduction of the animal protein and peptides in the fried Bombyx batryticatus moderated the irritation of the medicine applied to the patient, which was in accordance with the principles of processing (Ma et al., 2015). In addition, due to the breakage of the peptide bond by thermal oscillation during the stir-frying process, small molecule oligopeptides could be produced for oral absorption, solving the problem of low absorption rate of natural oligopeptides and the difficulty of industrialization, and providing an experimental basis for the development and utilization of the Bombyx batryticatus resources (Li et al., 2019).

Furthermore, the interaction between the excipients and the drug existed in the container because of substantial addition of wheat bran during the process of concoction. The surface of wheat bran was loose and porous with a higher surface area, reinforcing the adsorption activity. Meanwhile, wheat bran was rich in dietary fiber possessing an anti-oxidant effect. After being fried, there was plenty of dietary fiber remaining on the surface of the Bombyx batryticatus, which inhibited the biosynthesis of fungal toxins (Zhao et al., 2010). As a consequence of Maillard reaction on the Bombyx batryticatus during the stir-frying process, the epidermis of Bombyx batryticatus became golden in color with an aromatic smell, which promoted the digestive function and improves the therapy compliance of patients when taking medicine (Hu et al., 2016; Li et al., 2021b).

Conclusion

In this study, a high-resolution MALDI-MSI technique was applied to elucidate the *in situ* distribution of protein-related metabolites in the cross sections of raw and fried Bombyx batryticatus. Ultimately, 15 processing-related markers were screened and visualized in combination with OPLS-DA, which may have a significant impact on the research of the holistic chemical transformation mechanism of Bombyx batryticatus before and after frying with wheat bran.

Data availability statement

The original contributions presented in the study are included in the article/Supplementary Material. Further inquiries can be directed to the corresponding authors.

Author contributions

PL and J-MW performed the experiments and preparation of the draft manuscript. H-CG, M-WZ, and Y-XS analyzed the data. HG and X-HD prepared figures and tables. Y-PY project conceptualization, conceived, and designed the experiments. Y-GZ conceived and designed the experiments, and reviewed drafts of the paper. All authors contributed to the article and approved the submitted version.

Funding

This work was financially supported by the Scientific and Technological Research Projects of Colleges and Universities in Hebei Province (ZD2020111), the Innovation Team of Hebei Province Modern Agricultural Industry Technology System (HBCT2018060205 and HBCT2018060201), the S&T Program of Hebei (22326418D,19277637D, and H2022418001), and the Scientific Research Capability Improvement Project of Hebei University of Chinese Medicine (KTZ2019006 and KTY2019077).

Acknowledgments

Thanks to Professor Hongjie Li of the Institute of Crop Science, Chinese Academy of Agricultural Sciences for revising the language of the paper.

Conflict of interest

The authors declare that the research was conducted in the absence of any commercial or financial relationships that could be construed as a potential conflict of interest.

Publisher's note

All claims expressed in this article are solely those of the authors and do not necessarily represent those of their affiliated organizations, or those of the publisher, the editors and the reviewers. Any product that may be evaluated in this article, or claim that may be made by its manufacturer, is not guaranteed or endorsed by the publisher.

Supplementary material

The Supplementary Material for this article can be found online at: https://www.frontiersin.org/articles/10.3389/fpls.2023.1144556/full#supplementary-material

References

Bai, Y.-P., Zhao, Q., He, M.-X., Ye, X.-T., and Zhang, X.-Z. (2018). Extensive characterization and differential analysis of endogenous peptides from bombyx batryticatus using mass spectrometric approach. *J. Pharm. Biomed. Anal.* 163, 78–87. doi: 10.1016/j.jpba.2018.09.033

Chen, W.-W., Hu, M.-B., Peng, W., and Wu, C.-J. (2019). Research progress of effective ingredient beauvericin in the bombyx batryticatus. *China Pharm.* 30 (24), 3452–3456. doi: 10.6039/j.issn.1001-0408.2019.24.26

Chinese Pharmacopoeia Commission (2020). *Pharmacopoeia of the people's republic of China* Vol. Volume I (Beijing: China Medical Science Press).

Cifelli, P., Di, A.-S., Alfano, V., Morano, A., De, F.-E., Aronica, E., et al. (2021). Dissecting the molecular determinants of GABA receptors current rundown, a hallmark of refractory human epilepsy. *Brain Sci.* 11 (4), 441. doi: 10.3390/brainsci11040441

Gennebäck, N., Malm, L., Hellman, U., Waldenström, A., and Mörner, S. (2013). Using OPLS-DA to find new hypotheses in vast amounts of gene expression data - studying the progression of cardiac hypertrophy in the heart of aorta ligated rat. *Gene* 522 (1), 27–36. doi: 10.1016/j.gene.2013.03.018

Hu, M.-B. (2017). *The processing technology standardization and quality related research of bombyx batryticatus stir-fried with bran* (Chengdu: Chengdu University of Traditional Chinese Medicine).

Hu, B.-M., Liu, Y.-J., Xie, D.-S., Xiao, H., and Li, Y.-C. (2016). Maillard reaction in process of bombyx batryticatus stir-fried with bran. *J. Chin. Med. Mater.* 39 (10), 2221–2224. doi: 10.13863/j.issn1001-4454.2016.10.017

Hu, M.-B., Yu, Z.-J., Wang, J.-L., Fan, W.-X., Liu, Y.-J., Li, J.-H., et al. (2017). Traditional uses, origins, chemistry and pharmacology of bombyx batryticatus: A review. *Molecules* 22 (10), 1779. doi: 10.3390/molecules22101779

Jiang, Q., Wang, L.-N., Liu, Y., Liu, Q., Yang, R., and Zhang, Y.-Q. (2023). Research progress on processing history evolution, chemical constituents and pharmacological action of bombyx batryticatus. *China J. Chin. Mater. Med.* 1-13. doi: 10.19540/j.cnki.cjcmm.20230113.201

Jiang, X., Zhang, Z.-F., Chen, Y.-J., Cui, Z.-T., and Shi, L.-G. (2014). Structural elucidation and *in vitro* antitumor activity of a novel oligosaccharide from bombyx batryticatus. *Carbohydr. Polym.* 103, 434–441. doi: 10.1016/j.carbpol.2013.12.039

Kathrin, C., Doreen, S., Natalie, L., Lucie, C., Rainer, H.-B., Maxim, A., et al. (2019). Association of asymmetric dimethylarginine and diastolic dysfunction in patients with hypertrophic cardiomyopathy. *Biomolecules* 9 (7), 277. doi: 10.3390/biom9070277

Kong, Y., Xu, C., He, Z.-L., Zhou, Q.-M., Wang, J.-B., Li, Z.-Y., et al. (2014). A novel peptide inhibitor of platelet aggregation from stiff silkworm, bombyx batryticatus. *Peptides* 53, 70–78. doi: 10.1016/j.peptides.2013.12.004

Kouri, K., Duchen, M.-R., and Lemmens-Gruber, R. (2005). Effects of beauvericin on the metabolic state and ionic homeostasis of ventricular myocytes of the guinea pig. *Chem. Res. Toxicol.* 18, 1661–1668. doi: 10.1021/tx050096g

Li, B., Bhandari, D.-R., Janfelt, C., Römpp, A., and Spengler, B. (2014). Natural products in *Glycyrrhiza glabra* (licorice) rhizome imaged at the cellular level by atmospheric pressure matrix-assisted laser desorption/ionization tandem mass spectrometry imaging. *Plant Journal: Cell Mol. Biol.* 80, 161–171. doi: 10.1111/tpj.12608

Li, B., Ge, J.-Y., Liu, W., Hu, D.-J., and Li, P. (2021a). Unveiling spatial metabolome of *Paeonia suffruticosa* and *Paeonia lactiflora* roots using MALDI MS imaging. *New Phytol.* 231 (2), 892–902. doi: 10.1111/nph.17393

Li, J. F., Wang, Y. P., Bian, X. F., Zhang, H., and Sun, J. M. (2019). Anti-parkinson activity of bombyx batryticatus in vitro before and after processing based on thermal oscillation theory of peptide Bond. *Mod. Chin. Med.* 9, 1229–1235. doi: 10.13313/j.issn.1673-4890.20190215001

Li, M.-R., Wang, X.-Y., Han, L.-F., Jia, L., Liu, E., Li, Z., et al. (2020). Integration of multicomponent characterization, untargeted metabolomics and mass spectrometry imaging to unveil the holistic chemical transformations and key markers associated with wine steaming of ligustri lucidi fructus. *J. Chromatogr. A* 1624, 461228. doi: 10.1016/j.chroma.2020.461228

Li, Y.-L., Zhu, Y.-Z., Zheng, P.-H., Qu, Z.-Y., Zhang, H., Hou, W., et al. (2021b). Potentially harmful maillard reaction products in food and herb medicines. *J. Food Qual.* 2021, 1–11. doi: 10.1155/2021/1798936

Lin, L., Zhang, Y.-J., Li, Y., Fu, H.-Z., Hu, J.-H., Zhou, Y., et al. (2020). Identification of signature proteins of processed bombyx batryticatus by comparative proteomic analysis. *Int. J. Biol. Macromol.* 153, 289–296. doi: 10.1016/j.ijbiomac.2020.03.010

Ma, L., Wang, X., Ma, L., Wang, M.-Y., and Qiu, F. (2015). Scientific connotation of processing bombyx batryticatus under high temperature. *China J. Chin. Mater. Med.* 40 (23), 4629–4633. doi: 10.4268/cjcmm20152317

Mangoni, A. A., Rodionov, R. N., McEvoy, M., Zinellu, A., Carru, C., and Sotgia, S. (2019). New horizons in arginine metabolism, ageing and chronic disease states. *Age Ageing* 48, 776–782. doi: 10.1093/ageing/afz083

Mei, L., Zhang, L.-X., and Dai, R. (2009). An inhibition study of beauvericin on human and rat cytochrome p450 enzymes and its pharmacokinetics in rats. *J. Enzyme inhibit. med. Chem.* 24 (3), 753–762. doi: 10.1080/14756360802362041

Nakamura, Y., Hinoi, E., Takarada, T., Takahata, Y., Yamamoto, T., Fujita, H., et al. (2011). Positive regulation by gaba(b)r1 subunit of leptin expression through gene transactivation in adipocytes. *PloS One* 6 (5), e20167. doi: 10.1371/journal.pone.0020167

Qiang, W., and Mei, G. (2014). Research progress on antitumor activity of fungal cyclic dipeptides and their derivatives. *China Pharm.* 21, 2007–2010. doi: 10.6039/j.issn.1001-0408.2014.21.30

Rodionov, R.-N., Beyer-Westendorf, J., Bode-Boger, S.-M., Eggebrecht, L., Konstantinides, S., Martens-Lobenhoffer, J., et al. (2021). Homoarginine and methylarginines independently predict long-term outcome in patients presenting with suspicion of venous thromboembolism. *Sci. Rep.* 11, 9569. doi: 10.1038/s41598-021-88986-y

Shu, T., Ryuzo, I., Naohiko, Y., Issey, O., Manabu, S., Mitsuro, K., et al. (2010). Mass spectrometric imaging of ginsenosides localization in *Panax ginseng* root. *Am. J. Chin. Med.* 38 (3), 485–493. doi: 10.1142/S0192415X10008007

Tu, Y. D., and Yu, X. P. (2012). The clinical use of banbusa-lxilis in lung diseases and its side effects. *Shanghai J. Tradit. Chin. Med.* 46 (12), 64–66. doi: 10.16305/j.1007-1334.2012.12.021

Wang, S.-J., Bai, H.-R., Cai, Z.-W., Gao, D., Jiang, Y.-Y., Liu, J.-J., et al. (2016). MALDI imaging for the localization of saponins in root tissues and rapid differentiation of three *Panax* herbs. *Electrophoresis* 37 (13), 1956–1966. doi: 10.1002/elps.201600027

Wang, P.-L., Shang, E.-X., and Fan, X.-S. (2021a). Effect of san'ao decoction with scorpio and *bombyx batryticatus* on CVA mice model *via* airway inflammation and regulation of TRPA1/TRPV1/TRPV5 channels. *J. Ethnopharmacol.* 264, 113342. doi: 10.1016/j.jep.2020.113342

Wang, M., Wan, Z.-Y., Chen, H., Zhang, D.-L., Yu, W., Li, M., et al. (2022). Study on quality evaluation of bombyx batryticatus by chemical pattern recognition combined with HPLC fingerprint. *Natural Prod. Res. Dev.* 34, 203–212. doi: 10.16333/j.1001-6880.2022.2.004

Wang, S.-Q., Zhang, L.-R., Chen, W., Pan, Y.-Z., Zhou, F., Su, Z.-H., et al. (2021b). A study on fingerprint and common peaks identification of water-soluble components in bombyx batryticatus. *J. Clin. Med. Pract.* 25 (23), 53–57. doi: 10.7619/jcmp.20213009

Wei, G.-X. (2020). Research progress of cyclic dipeptides. *Contemp. Chem. Industry* 49 (2), 406–409. doi: 10.13840/j.cnki.cn21-1457/tq.2020.02.038

Wu, J.-Y., Sheikho, A., Ma, H., Li, T.-C., Zhao, Y.-Q., Zhao, Y.-L., et al. (2017). Molecular mechanisms of bombyx batryticatus ethanol extract inducing gastric cancer sgc-7901 cells apoptosis. *Cytotechnology* 69 (6), 875–883. doi: 10.1007/s10616-017-0102-7

Xing, D.-X., Shen, G.-W., Li, Q.-, Xiao, Y., Yang, Q., and Xia, Q.-Y. (2019). Quality formation mechanism of stiff silkworm, bombyx batryticatus using UPLC-Q-TOF-MS-based metabolomics. *Molecules* 24 (20), 3780. doi: 10.3390/molecules24203780

Zemaitis, K.-J., Veličković, D., Kew, W., Fort, K.-L., Reinhardt-Szyba, M., Pamreddy, A., et al. (2022). Enhanced spatial mapping of histone proteoforms in human kidney through MALDI-MSI by high-field UHMR-orbitrap detection. *Analytical Chem.* 94 (37), 12604–12613. doi: 10.1021/acs.analchem.2c01034

Zhan, J.-X., Burns, A.-M., Liu, M.-X., Faeth, S.-H., and Gunatilaka, A.-A. (2007). Search for cell motility and angiogenesis inhibitors with potential anticancer activity: beauvericin and other constituents of two endophytic strains of *Fusarium oxysporum*. *J. Natural Prod.* 70 (2), 227–232. doi: 10.1021/np060394t

Zhao, Q., Hao, L. J., Ma, X. L., Yuan, W. Y., and Guo, H. (2010). Study on thin layer chromatography differentiation and determination of six kinds of prepared bombyx batryticatus. *Liaoning J. Tradit. Chin. Med.* 12, 2421–2424. doi: 10.13192/j.ljtcm.2010.12.154.zhaoq.070

Zhao, Q., Jia, T.-Z., Cao, Q.-C., Tian, F., and Ying, W.-T. (2018). A crude 1-dnj extract from home made bombyx batryticatus inhibits diabetic cardiomyopathy-associated fibrosis in db/db mice and reduces protein n-glycosylation levels. *Int. J. Mol. Sci.* 19 (6), 1699. doi: 10.3390/ijms19061699

frontiers | Frontiers in Plant Science

TYPE Original Research
PUBLISHED 20 April 2023
DOI 10.3389/fpls.2023.1170947

OPEN ACCESS

EDITED BY
Xiaodong Wang,
Minzu University of China, China

REVIEWED BY
Liangyu Liu,
Capital Normal University, China
Yanping Jing,
Beijing Forestry University, China

*CORRESPONDENCE
Peisheng Mao
maops@cau.edu.cn

†These authors share first authorship

SPECIALTY SECTION
This article was submitted to Technical Advances in Plant Science, a section of the journal Frontiers in Plant Science

RECEIVED 07 March 2023
ACCEPTED 03 April 2023
PUBLISHED 20 April 2023

CITATION
Jia Z, Ou C, Sun S, Wang J, Liu J, Sun M, Ma W, Li M, Jia S and Mao P (2023) Integrating optical imaging techniques for a novel approach to evaluate Siberian wild rye seed maturity. *Front. Plant Sci.* 14:1170947. doi: 10.3389/fpls.2023.1170947

Integrating optical imaging techniques for a novel approach to evaluate Siberian wild rye seed maturity

Zhicheng Jia†, Chengming Ou†, Shoujiang Sun, Juan Wang, Jingyu Liu, Ming Sun, Wen Ma, Manli Li, Shangang Jia and Peisheng Mao*

College of Grassland Science and Technology, China Agricultural University, Beijing, China

Advances in optical imaging technology using rapid and non-destructive methods have led to improvements in the efficiency of seed quality detection. Accurately timing the harvest is crucial for maximizing the yield of higher-quality Siberian wild rye seeds by minimizing excessive shattering during harvesting. This research applied integrated optical imaging techniques and machine learning algorithms to develop different models for classifying Siberian wild rye seeds based on different maturity stages and grain positions. The multi-source fusion of morphological, multispectral, and autofluorescence data provided more comprehensive information but also increases the performance requirements of the equipment. Therefore, we employed three filtering algorithms, namely minimal joint mutual information maximization (JMIM), information gain, and Gini impurity, and set up two control methods (feature union and no-filtering) to assess the impact of retaining only 20% of the features on the model performance. Both JMIM and information gain revealed autofluorescence and morphological features (CIELab A, CIELab B, hue and saturation), with these two filtering algorithms showing shorter run times. Furthermore, a strong correlation was observed between shoot length and morphological and autofluorescence spectral features. Machine learning models based on linear discriminant analysis (LDA), random forests (RF) and support vector machines (SVM) showed high performance (>0.78 accuracies) in classifying seeds at different maturity stages. Furthermore, it was found that there was considerable variation in the different grain positions at the maturity stage, and the K-means approach was used to improve the model performance by 5.8%-9.24%. In conclusion, our study demonstrated that feature filtering algorithms combined with machine learning algorithms offer high performance and low cost in identifying seed maturity stages and that the application of k-means techniques for inconsistent maturity improves classification accuracy. Therefore, this technique could be employed classification of seed maturity and superior physiological quality for Siberian wild rye seeds.

KEYWORDS

Siberian wild rye seed, feature filtering, machine learning, integrating optical imaging, multispectral imaging, autofluorescence imaging, model updating

1 Introduction

The genus *Elymus* (L.), a member of the grass family (Poaceae), is the most widespread genus in the northern hemisphere, with approximately 150 species. Some species of *Elymus* exhibit remarkable resilience to biotic and abiotic stresses, including drought, cold, and disease. Siberian wild rye (*E. sibiricus* L.) is a notable representative with a wide distribution in the northern regions of Eurasia. Due to its broad adaptability, high cold tolerance, high nutritional value, palatability, and ease of cultivation, Siberian Wild rye has been widely used for grassland restoration and fodder production (Klebesadel, 1969; You et al., 2011; Xie et al., 2020). However, its seed yield remains relatively low, with only about 20% of its potential production being harvested. Research suggests that excessive shattering is a major factor contributing to this low seed yield, which has been confirmed by various studies (Yu et al., 2011; Zhao et al., 2012; Han et al., 2013; Zhao et al., 2015).

The traditional method of determining the optimum time to harvest Siberian wild rye seed relied on the subjective judgment of experienced farmers, which lacked objectivity and often resulted in sub-optimal yields. Meanwhile, to assess the physiological potential of Siberian wild rye seed at different maturity stages, conventional methods such as germination tests and physiological experiments were employed, which were both laborious and destructive (Rahman and Cho, 2016). With the rise of the modern seed industry and the growing demand for smart agriculture, these conventional methods have become increasingly inadequate to meet the needs of the industry. There is therefore an urgent need to develop a rapid, non-destructive, high-throughput method for identifying and classifying the maturity of Siberian wild rye seeds. Such a method would enable the modern seed industry to maximize yield and quality and meet the growing demand for high-quality seeds (Feng et al., 2019).

Biological imaging techniques, including X-ray, hyperspectral, multispectral, and autofluorescence optical technologies, have brought about significant changes in agricultural production and food quality. The multispectral imaging technology was a non-destructive technique that combined computer vision and spectroscopy to provide information on physical attributes such as texture, color, shape, size, and chemical composition (ElMasry et al., 2019; França-Silva et al., 2020). The main principle of the technique was based on the detection of different specific wavelengths produced by the varying physical structures and chemical compositions of objects. For example, multispectral imaging has been successfully used to identify variety genuineness and seeds quality, such as alfalfa (*Medicago sativa* L.) seeds (Yang et al., 2020; Jia et al., 2022), manioca (*Jatropha curcas* L.) seeds (Pinheiro et al., 2020), and spinach (*Spinacia oleracea* L.) seeds (Deleuran et al., 2013). The imaging technology allowed a better understanding of the seed maturation process and provided a research basis for the development of rapid, non-destructive, and high-throughput detection methods. The autofluorescence spectral imaging technique was based on the detection of fluorescence group signals in seeds that changed during maturation (Teixeira et al., 2016; Lima et al., 2017). With the advancement of optical imaging devices, integrated optical imaging devices had started to be applied in various fields such as food, medicine, and agriculture (Galletti et al., 2020; Wang et al., 2021).

In recent years, advanced imaging devices that integrate multi-optical components (multispectral, autofluorescence, hyperspectral, and RGB) can provide more comprehensive information and thus improve detection accuracy, but increase the dimensionality of the data and place higher demands on the computing equipment. The successive projection algorithm (SPA), a linear algorithm, is widely used to select important spectral bands in hyperspectral images (Tu et al., 2022). However, there are challenges with multi-source fused non-linear datasets, and to overcome this challenge, it was imperative to explore alternative feature selection methods that could reduce the dimensionality of the data, as high-dimensional data could lead to computational inefficiencies and prolong the training time of machine learning (ML) algorithms. For example, feature filtering algorithms such as minimal joint mutual information maximization (JMIM) (Kursa, 2018), information gain (Zawadzki and Kosinski, 2019), and Gini impurity (Bommert et al., 2020) have been shown to effectively reduce the dimensionality of high-dimensional data. However, current researches were mainly on individual datasets (França-Silva et al., 2020; Fu et al., 2023), while little research has been reported on the use of feature filtering algorithms on multi-source fused data.

2 Materials and methods

2.1 Sample materials

Samples were collected from Yuershan Ranch in Chengde City, Hebei Province, China. 100 spikelets were randomly selected from the field and stored in liquid nitrogen, and then transported to the laboratory for further analysis. These samples were stored in a refrigerator at minus 20 degrees Celsius for the determination of physiological indices. Additionally, 200 spikelets were air-dried and stored for germination testing and multispectral image acquiring. To ensure consistency among the samples, 4 - 6 spikelets were selected from the middle of the spike, and the 1st and 2nd seeds at the base of the spikelets were separated from the rest of the seeds and labeled as superior grain (SG) and inferior grain (IG) respectively. Samples were collected at the milk-ripe stage (MRS) (July 27), dough stage (DS) (August 7), and full-ripe stage (FRS) (August 13), and the dry weight, fresh weight, and moisture content are shown in Table 1.

2.2 Germination test

A germination experiment was carried out with Siberian wild rye seeds of uniform size. The experiment was repeated four times with 8 hours of light and 16 hours of darkness, with a light intensity of 66% and a fluctuating temperature of 15/25°C. Initial and final germination counts were made after 5 and 12 days respectively, and shoot and root length measurements were taken at the final germination count. The number of seeds with radicles greater

TABLE 1 The information of seed dry weight, fresh weight and water content at MRS, DS, and FRS.

Stages	Grain position	Fresh weight (mg/grain)	Dry weight (mg/grain)	Water content (%)
MRS	SG	8.06 ± 0.07a	3.85 ± 0.04b	52.20 ± 0.26b
MRS	IG	6.79 ± 0.02b	3.06 ± 0.04c	54.91 ± 0.55a
DS	SG	6.63 ± 0.06b	4.38 ± 0.04a	33.95 ± 0.83c
DS	IG	6.27 ± 0.02c	4.33 ± 0.06a	30.89 ± 0.95d
FRS	SG	5.29 ± 0.06d	4.38 ± 0.06a	17.32 ± 0.77e
FRS	IG	5.27 ± 0.08d	4.33 ± 0.04a	17.77 ± 0.45e

(± SD). Different lowercase letters indicated significant differences in Siberian wild rye seeds at different stages and grain positions at the P<0.05 level.

than 2 mm was recorded every 24 hours during the germination period. Finally, the germination percentage and the germination speed index were calculated.

$$\text{Germination percentage} = (G10/N) \times 100\,\% \quad (1)$$

$$\text{Germination speed index} = \sum(n/t) \quad (2)$$

Where *G10* was the number of normal seedlings at the last count, *N* was the total number of experimental seeds, *n* was the number of seed germination per day, and *t* was the number of days per germination.

2.3 Autofluorescence and multispectral imaging

Multispectral images were acquired from seeds using a VideometerLab4^{TM} device (Videometer A/S, Herlev, Denmark). The system incorporates a CCD chip with 19 wavelengths of high-powered light-emitting diodes (LEDs) arranged around the edge of the sphere at 365, 405, 430, 450, 470, 490, 515, 540, 570, 590, 630, 645, 660, 690, 780, 850, 880, 940, and 970 nm, ranging from ultraviolet (UV) to near-infrared (NIR), the led flashes continuously in a few seconds of scan time, producing monochrome images at 19 different wavelengths (2192 × 2192 pixels; 40 μm/pixel; 32 bits/pixel). And autofluorescence images were acquired by a mounted long-pass (LP) filter combined with different excitation wavelengths, which offers the following excitation-emission combinations: 365/400 nm, 365/500 nm, 405/500 nm, 430/500 nm, 450/500 nm, 630/700 nm, 645/700 nm, 660/700 nm.

2.4 Autofluorescence and multispectral image analysis

After acquiring the images, each seed was segmented from the background into a region of interest (ROI) using VideometerLab 3.14 software. All seeds were collected and added to a blob database, from which we extracted morphological features, multispectral features, and autofluorescence features of the seeds. A detailed description of the morphological features used in this study can be found in Table S1, while the multispectral features and autofluorescence features are described in section 2.3. The extracted multispectral and fluorescence features of individual ROI seeds represent the average reflected light intensity at each single wavelength calculated from all pixels in a single ROI image. In total, 42 features (cols) and 600 samples (rows) of data were used in this study. All three types of features for seeds were then collected in a matrix (X), associated with their corresponding stages and grain positions data (Y).

2.5 Data analysis

In this study, we conducted a comprehensive analysis of the morphological features, multispectral, and autofluorescence properties of Siberian wild rye seeds. To statistically evaluate differences among seed maturity stages and grain positions, we employed both Duncan's test and Student's t-test ($P< 0.05$). To reduce the number of features, we utilized three feature filtering methods: JMIM, information gain, and Gini impurity. We calculated the feature importance scores for all 42 features (Table S2), and based on these scores, we selected 20% as the threshold. This means that only 20% of the features were retained for further analysis. Furthermore, we included a features union approach (where filtering features of the three algorithms were fused using the union method) and a no-filtering group as control groups. Therefore, a total of five feature filtering methods were employed to analyze the data.

Principal component analysis (PCA), linear discriminant analysis (LDA), support vector machine (SVM), and random forest (RF) were applied in this study. PCA generally is used to reduce the dimensionality of the data as a mathematical technique by an orthogonal transformation of the initial data set into a new set of uncorrelated variables, the so-called principal components (PCs), where the first PC has the highest variance, the second PC has the second-highest variance, and so on. Thus, key information and potential data structure of high-dimensional data can be provided by PCs. LDA, a classical ML algorithm, calculates the optimal transformation (projection) by simultaneously minimizing the within-class distance and maximizing the between-class distance, resulting in maximum discrimination. SVM, a well-known kernel method, has been effectively used for multivariate function estimation or nonlinear classification by finding the optimal hyperplane to achieve segmentation of high-dimensional data (Cristianini and Shawe-Taylor, 2000).

In this study, we evaluated model performance for multiclass classification tasks using accuracy, area under curve (AUC), and Brier score (Brier, 1950). We implemented the LDA, RF, and SVM algorithms using the 'mlr3verse' R package (Lang and Schratz, 2021) in R 4.1 software. The PCA and K-means were implemented by 'FactoMineR' and 'cluster' R packages, respectively (Lê et al., 2008; Maechler et al., 2012). Additionally, we optimized the hyperparameters of the SVM and RF models using 5-fold cross-validation and the random search method. The optimized parameters were listed in Table S3, while the other parameters were set to their default values. The technology route for this study was illustrated in Figure 1.

3 Result

3.1 Effect of maturity and grain position of spikes on seed germination

The results indicate that there were differences in the quality of Siberian wild rye seeds at different maturity stages and grain positions. The analysis revealed that seeds from the MRS exhibited a greener color compared to those from the DS and FRS. However, there was no observable difference in the appearance of seeds from the DS and FRS. Moreover, there was no discernible distinction between seeds from different grain positions within the same maturity stage in terms of appearance (Figure 2A). Shoot length initially increased and then decreased as maturity increased, with the highest values observed in the DS-SG seeds, which were significantly higher than those of the other maturity stage seeds (P<0.05) (Figure 2B). Meanwhile, a gradual increase in root length was observed for both SG and IG samples as the maturity stage progressed (Figure 2C). Furthermore, the germination speed index of the SG was significantly higher than that of the IG seeds during the MRS and FRS (P<0.05) (Figure 2D). However, there were no significant differences in germination percentage among different maturity stages and grain positions, with germination percentages of all seeds consistently close to 100% (Figure 2E).

3.2 Morphological, multispectral, and autofluorescence data analysis

Fourteen morphological features were extracted from RGB images of seeds from three developmental stages and two grain positions. The probability density distribution trends of MRS seeds in saturation, CIELab A, and CIELab B were significantly different from those of seeds in the other two maturity stages (Figure 3). Our statistical analysis of the morphological features showed that the values of these three features were significantly lower than those of the other seeds, with the lowest value observed in IG seeds (P<0.05) (Table S4). On the other hand, the probability density distributions of seeds in the three maturity stages were not clearly differentiated for other morphological features.

Overall, the mean multispectral reflectance of seeds from different maturity stages and grain positions exhibited similar trends. We observed that the average reflectance increased as the wavelength increased (Figure 4A). Specifically, in the spectral range of 365 to 570 nm, seeds from the MRS-IG exhibited the highest reflectance, while seeds from the FRS-SG exhibited the lowest reflectance. In the NIR range (780 - 970 nm), we found that the multispectral reflectance of seeds from the MRS-SG was significantly higher compared to the other seed classes (P<0.05) (Table S5).

We further extracted eight autofluorescence spectra wavelengths, and the results showed that the autofluorescence spectra decreased progressively as the maturity of Siberian wild rye seeds increased. In particular, the average autofluorescence of SG was lower (or similar) than that of IG in the same maturity stage. Furthermore, the autofluorescence of MRS seeds was the highest in

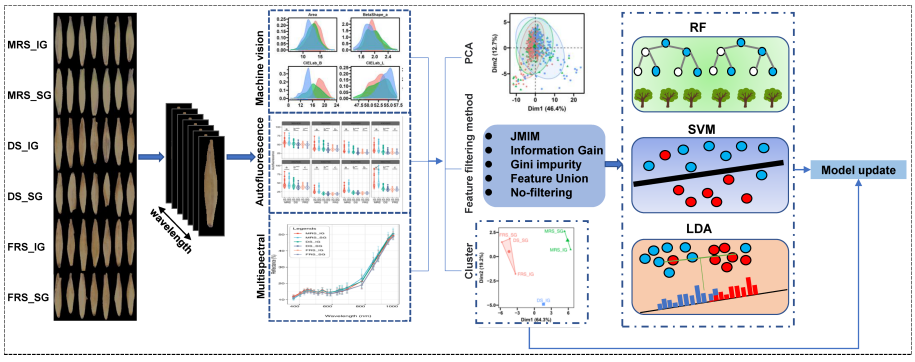

FIGURE 1
Technical route. RF, random forest; SVM, support vector machine; LDA, linear discriminant analysis. We obtained RGB images, multispectral images, and autofluorescence images of Siberian wild rye seeds at different maturity stages and grain positions using Vidoemeter equipment. Then, we segmented individual seeds from the background and extracted their morphological, multispectral, and autofluorescence features. Furthermore, we performed PCA and LDA exploratory analysis on the three types of features and their multi-source fusion data. We also selected three filtering algorithms, JMIM, information gain, and Gini impurity, and set two controls (feature fusion and non-filtered features) to filter the multi-source fusion data. Based on the filtered features, we built SVM, RF, and LDA models to differentiate different seed maturity stages. Additionally, we applied k-means clustering to reclassify seeds based on their maturity stages and grain positions, and updated the model to further improve its classification performance.

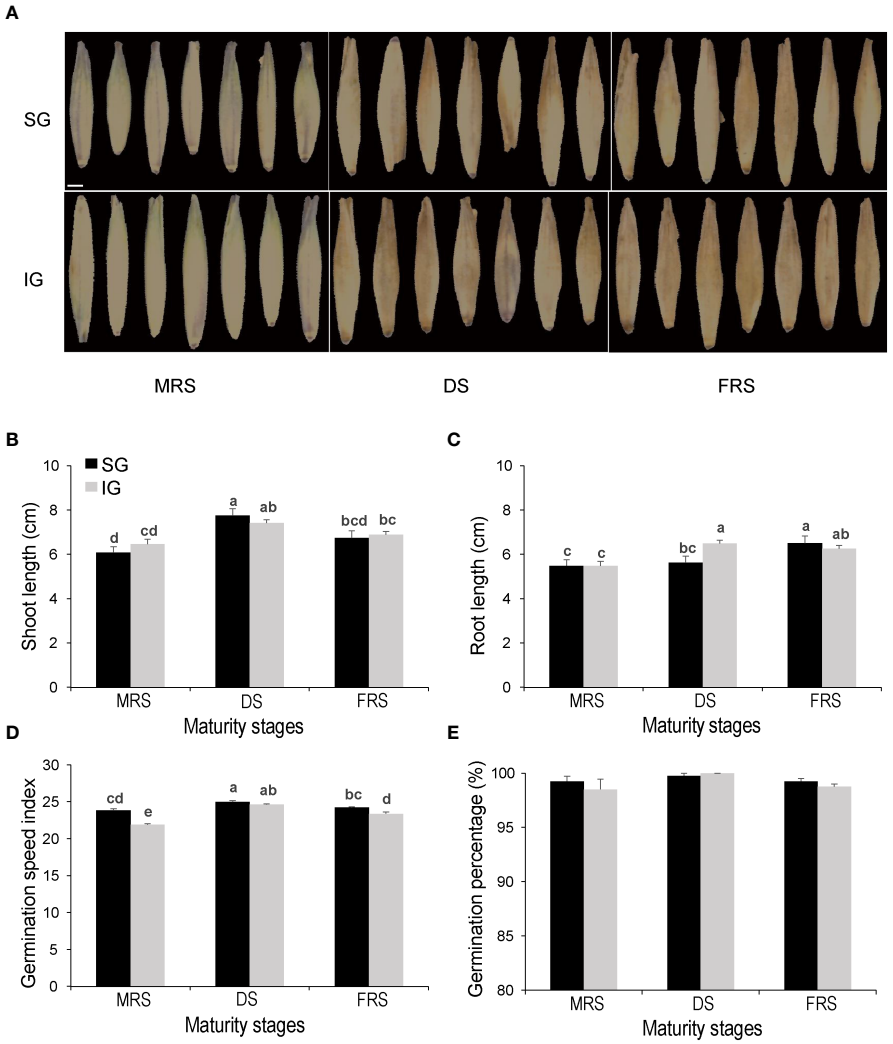

FIGURE 2
Germination and vigor tests, sorting of Siberian wild rye seeds at different developmental stages, and grain positions. **(A)** Seed images. **(B)** Shoot length. **(C)** Root length. **(D)** Germination speed index. **(E)** Germination percentage (%). Different lowercase letters indicate significant differences at different stages and grain positions at the P<0.05 level.

all eight autofluorescence bands. The MRS seeds were effectively detected at 365/400 nm, 365/500 nm, 405/500 nm, 430/500 nm, 450/500 nm, 630/700 nm, 645/700 nm, and 660/700 nm excitation-emission combinations, where 365/400 nm, 405/500nm, 430/500 nm, 450/500 nm, and 660/700 nm provided finer classifications for three maturity stage seeds (Figure 4B). For the SG and IG classifications at different maturity stages, the SG and IG seeds of DS could be distinguished by all autofluorescence bands. However, only 660/700 nm provided a stronger separation of IG and SG in MRS, and 365/400 nm in FRS allowed a clear classification of IG and SG seeds.

The results of the PCA analysis showed that the first two PCs for morphological features accounted for 50.5% of the total variation among developmental stages, with 28.4% for PC1 and 22.1% for PC2 (Figure 5A). In addition, for multispectral features, the first two PCs explained 72.6% and 23.8% of the variation, respectively (Figure 5B). The autofluorescence spectral features also showed a similar trend, with the first two PCs explaining 87.6% and 9.8% of the variance, respectively (Figure 5C). Furthermore, when all three features were considered, the first two PCs (46.4% for PC1 and 12.7% for PC2) accounted for a total of 59.1% of the original variance (Figure 5D). Despite the high variation explained by the first two PCs based on autofluorescence spectral features, no significant differences were observed between Siberian wild rye seeds at the three maturity stages.

We performed PCA on seed morphological, multispectral, and autofluorescence features for different grain positions at the same maturity stage. The results showed that the first two PCs for morphological features at the three developmental stages accounted for 49.33-51.2% of the total variation between grain positions, with 31.62-31.97% for PC1 and 17.47-19.58% for PC2, respectively (Figures 6A–C). For multispectral features, the first two PCs explained approximately 73% and 23% of the variance, respectively (Figures 6D–F). For autofluorescence spectral features, PC1 explained 92.4% of the variation during MRS, while PC1 explained 73.31-75.03% of the variation at different grain

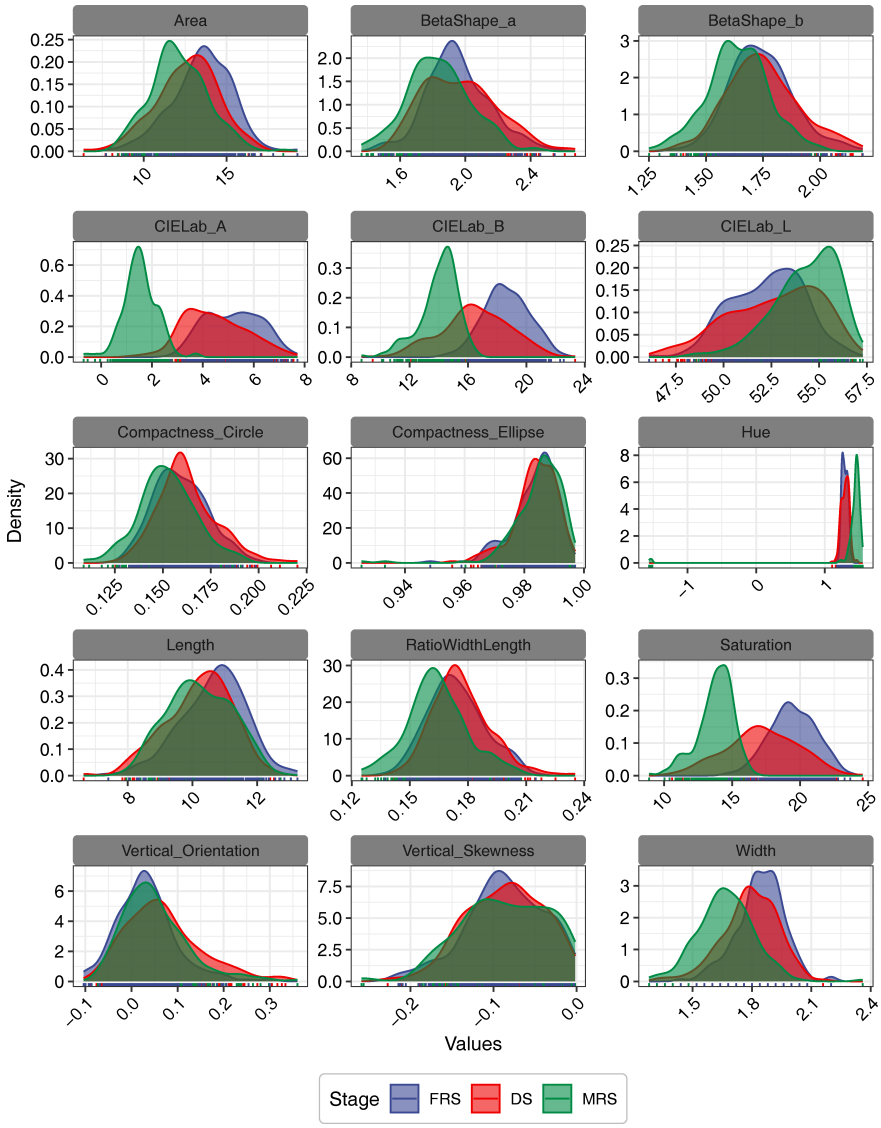

FIGURE 3
The probability density distributions of morphological features of Siberian wild rye seeds for different stages and grain positions.

positions for DS and FRS (Figures 6G–I). Furthermore, based on the combination of the three characters, the first two PCs (46.4% for PC1 and 12.7% for PC2) together explained about 48% of the original variation (Figures 6J–L). In summary, the different grain position seeds in the four datasets could not be completely distinguished; however, the different grain position seeds in MRS and DS did not completely overlap with each other compared to FRS.

The LDA results indicated that the first two LDs explained 92.96% and 7.04% of the variance in morphological traits, respectively. However, the limited variation between seeds of different developmental stages made it impossible to distinguish the three periods of Siberian wild rye based on LD1 and LD2 (Figure 7A). For multispectral features, the first two LDs accounted for 100% of the variance, and MRS seeds could be effectively separated in LD1 (Figure 7B). Similarly, for autofluorescence spectral features, the first two LDs explained 96.88% and 3.12% of the variance, respectively, but LD1 and LD2 were unable to separate seeds of the three periods of Siberian wild rye (Figure 7C). For multi-source fusion features, the first two LDs explained all of the variances, with LD1 and LD2 accounting for 92.16% and 7.84% of the variance, respectively. LD1 could completely distinguish MRS seeds, while LD2 could not separate DS and FRS seeds (Figure 7D). However, multi-source fused features could reveal more variation in seeds of Siberian wild rye at different maturity stages and could be employed as input features for the model.

3.3 Development of seed maturity models using multi-source fusion data and feature selection techniques

We applied three feature filtering methods (JMIM, information gain, and Gini impurity) to calculate feature importance scores for

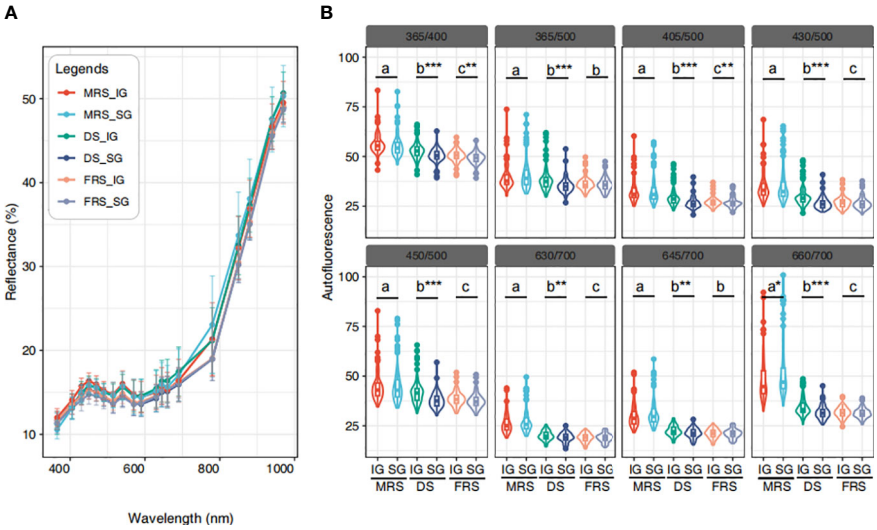

FIGURE 4
Spectral information of Siberian wild rye seeds. **(A)** Average multispectral reflectance of 19 wavelengths. **(B)** 8 autofluorescence wavelengths. The use of different colours was used to indicate differences in grain position at different maturity stages. The Duncan test was used to determine the significance of differences among maturity stages of Siberian wild rye seeds at the $P<0.05$ level, as indicated by the use of lowercase letters. In addition, Student's t-test was used to determine the significance of differences between grain positions within the same maturity period, as indicated by the use of symbols '*', '**', '***' or the absence of such symbols, respectively, denoting significance at $P<0.05$, $P<0.01$, $P<0.001$, and non-significance at $P>0.05$.

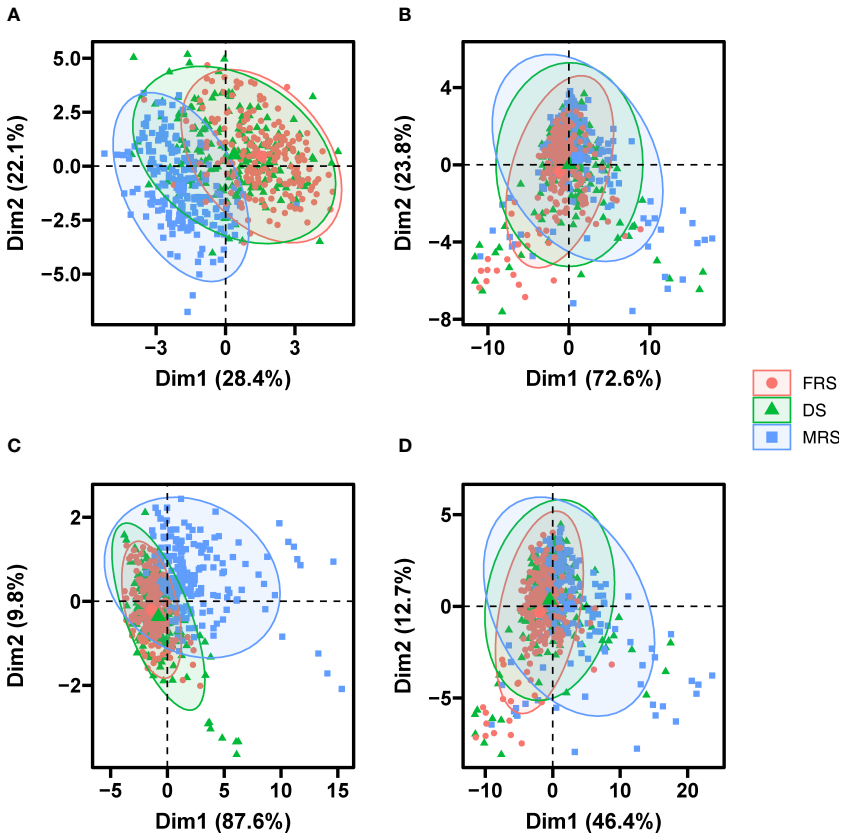

FIGURE 5
PCA score plot of seeds of different maturity stages and grain positions based morphological data **(A)**, multispectral data **(B)**, autofluorescence data **(C)**, and multi-source fusion data **(D)**.

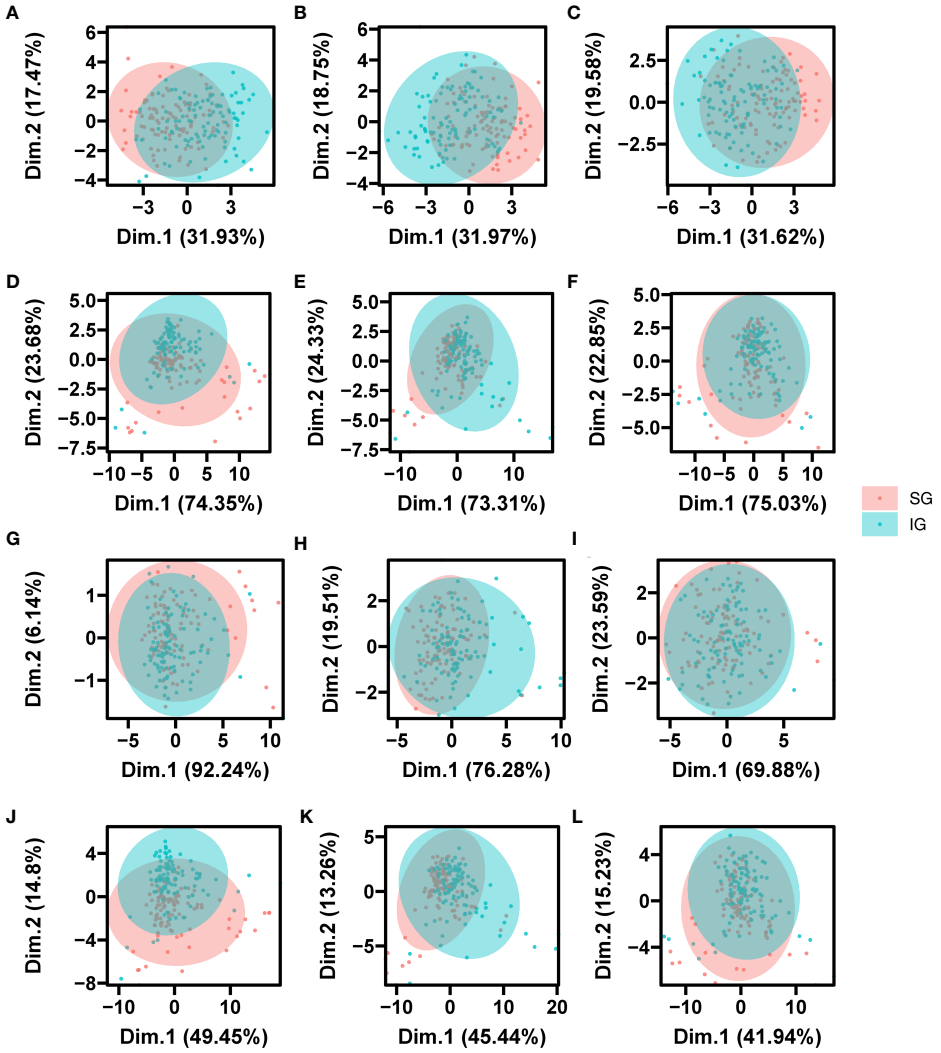

FIGURE 6
PCA score plot of grain position of seed based on the morphological data, the autofluorescence data, the multispectral data and multi-source fusion data. Figure **(A–C)** was morphological data, Figures **(D–F)** was autofluorescence data, **(G–I)** was multispectral data, and **(J–L)** was multi-source fusion data. Figures **(A, D, G, J)** were MRS; Figures **(B, E, H, K)** were DS; Figures **(C, F, I, L)** were FRS.

all features. The top 20% of features were found to have higher scores, with the first 9 features for JMIM and Gini impurity and the first 8 features for Information Gain exceeding the respective scores (Table S2). Further analysis of the top 20% of features showed that the retained 8 features for Information Gain were primarily morphological and autofluorescence spectral features, with CIELab A, hue, 660/700 nm, saturation, and CIELab B being the top 5 features. The results from the JMIM method also showed that the first two most important features were morphological, with CIELab A being prominent among them. In addition, the multispectral feature 660 nm was also an important feature filtered by JMIM. In contrast, the top-scoring features of the Gini impurity method consisted mainly of multispectral features and autofluorescence features, and the CIELab A feature was not among the important features identified (Figure 8). Furthermore, the JMIM and information gain methods shared 5 common features, while the Gini impurity method had 6 exclusive features. In addition, the three methods shared 2 features, namely saturation and 430/500 nm (Figure S1).

We also evaluated their computational efficiency by measuring their running times. The results showed that the JMIM and information gain methods had shorter running times of 0.01 and 0.03 s, respectively. On the other hand, the Gini impurity method had the longest running time of 12.64 s (Figure S2). These results provide insight into the computational efficiency of the three feature filtering methods, which could help in selecting the appropriate method for a particular application.

Further, we evaluated the performance of five datasets (three filtering algorithms, Union, and no-filtering) on LDA, RF, and SVM models (Figure 9). The results indicated that for the LDA model, the highest scores for accuracy, AUC, and Brier were achieved when the features were not filtered, with values of 0.94, 0.97, and 0.11, respectively. The feature fusion method was found to be the next best-performing method, while the remaining three methods

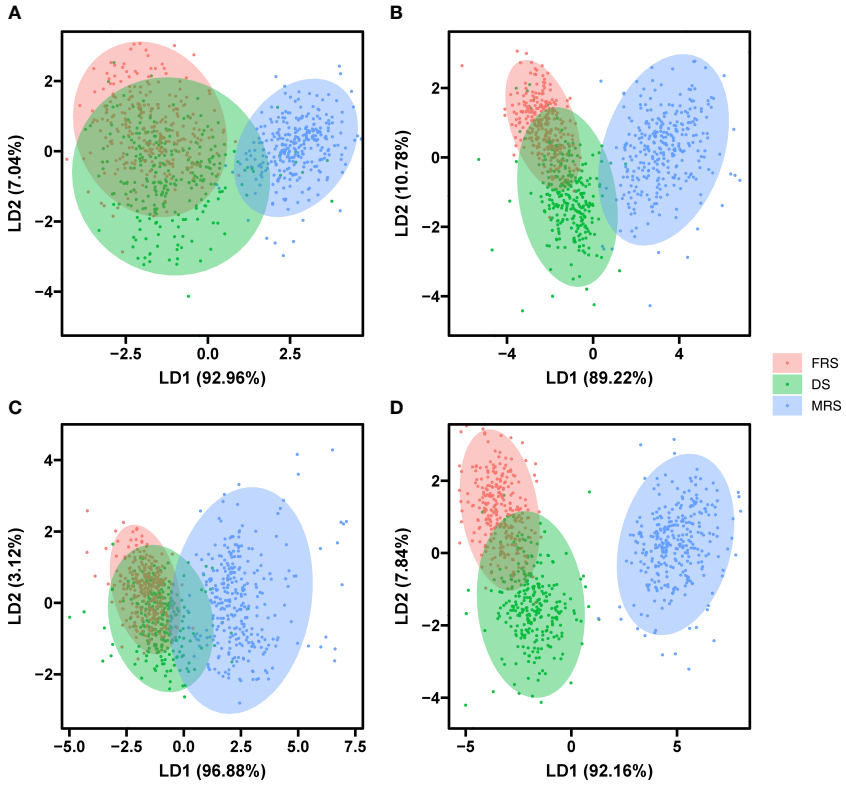

FIGURE 7
Two-dimensional biplot of LDA scores distinguishing seeds of three stage Siberian wildrye seeds based on morphological data **(A)**, multispectral data **(B)**, autofluorescence data **(C)**, and multi-source fusion data **(D)**.

demonstrated similar results. In the confusion matrix, MRS had the highest accuracy for seed identification, with an accuracy of approximately 1.00 under all five feature filtering strategies, while the DS had the lowest accuracy for seed detection (Table S6).

In the RF model, the feature fusion method had the best performance in terms of accuracy and AUC with values of 0.78 and 0.88, respectively, while the Gini impurity method had the lowest performance. However, the Brier scores were found to be similar across all five methods. The seed detection accuracy of MS was the highest, being greater than 0.96 in both the training and test sets, where the feature fusion-based method had the highest seed detection accuracy, followed by the JMIM method for the three stages (Table S7).

Lastly, for the SVM model, the AUC and Brier values were similar for both the feature fusion method and the no-filtering method, with the latter having the highest accuracy, while the Gini impurity method had the lowest value. The confusion matrix had the highest accuracy of seed detection without feature filtering, followed by the feature fusion method, while the JMIM and information gain methods had similar accuracies, both of which had about a 30% probability of identifying the DS seeds as FRS seeds (Table S8).

In summary, the results show that LDA consistently outperforms RF and SVM across all feature filtering methods, and we observe similar model performance using the feature fusion and JMIM methods, but JMIM has the shortest computation time.

An analysis of Pearson's correlations between 15 features, obtained by the fusion methods, and germination characteristics was performed (Figure 10). The results showed significant correlations ($P<0.05$) between the features, except 405 nm and vertical orientation. Notably, CIELab A and CIELab B exhibited a significant negative correlation with the remaining features, with the exception of saturation. Additionally, there was a significant positive correlation among the other features. Furthermore, it was found that shoot length was the only characteristic that was significantly correlated with the 15 features. Specifically, shoot length demonstrated a significant positive correlation with CIELab A, CIELab B, and saturation, and a significant negative correlation with 430/500 nm and 490 nm.

3.4 Validation and update of seed quality detection model based on multi-source fusion data

Due to the differences in SG and IG seeds at the same maturity stage, we applied k-means clustering techniques to improve model performance by reclassifying seeds at different stages and grain positions. The analysis showed that seeds of different maturity stages and grain positions were not grouped into one category based on maturity stage alone (Figure 11). Specifically, for the morphological data, seeds at different grain positions in the MRS

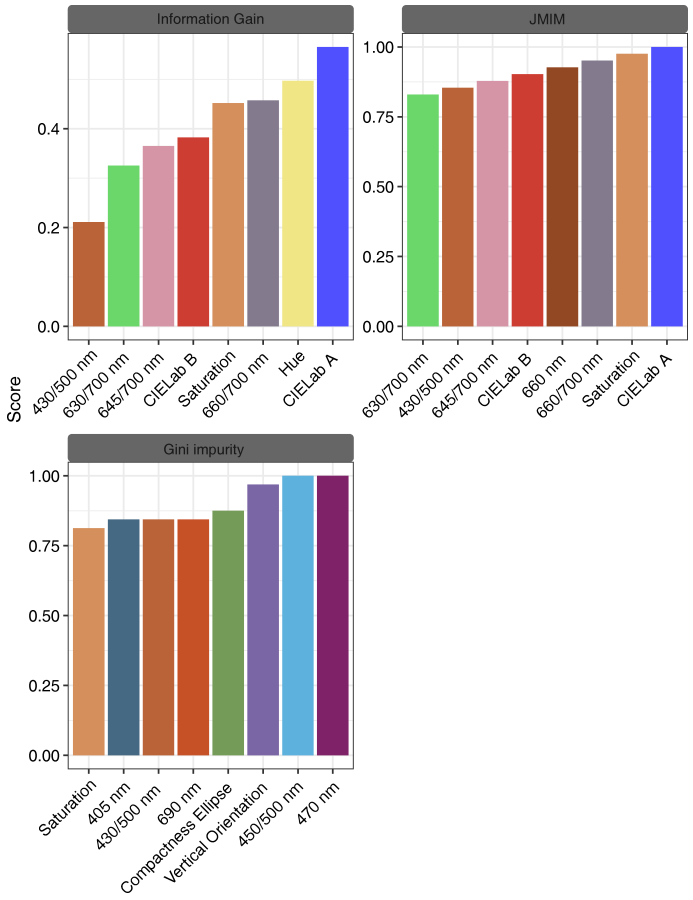

FIGURE 8
Feature importance scores of three feature filtering methods for information gain, JMIM, and Gini impurity.

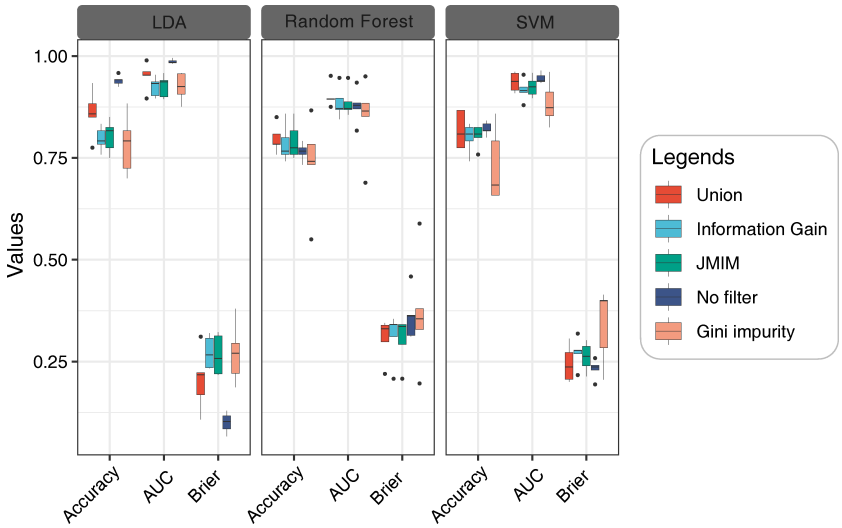

FIGURE 9
Model performance evaluation based on different feature filtering methods. From left to right are LDA, RF and SVM. Benchmark model performance with different filtering methods based on test set data using 5-fold cross-validation.

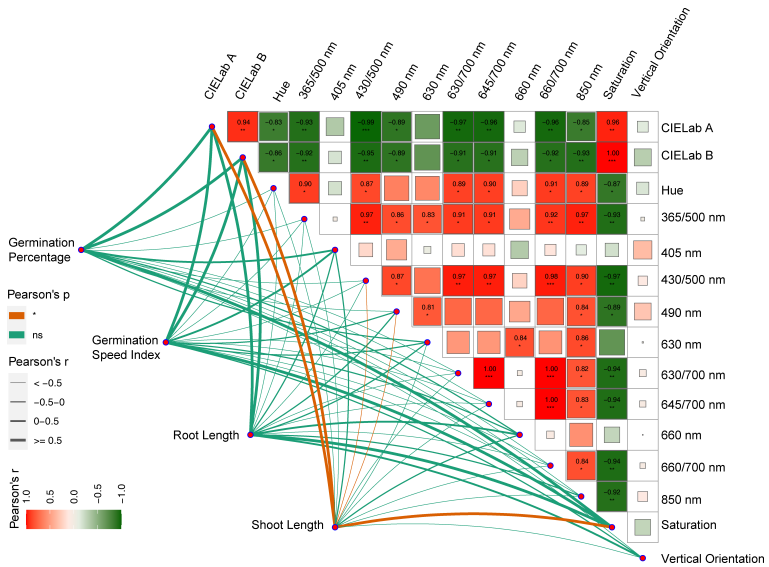

FIGURE 10
Pearson correlation coefficient of features based on the fusion of the three feature selection methods and Pearson correlation of germination indicators. The symbols '*', '**' and '***', indicate statistically significant correlation at P<0.05, P<0.01 and P<0.001 respectively, and ns indicates no correlation at P>0.05.

were grouped into one class, while the IG seeds on the DS and FRS were grouped into another class, and the SG seeds on the FRS and DS were grouped into a third class. For the multispectral data, the IG seeds from the MRS were grouped in a separate class, the SG seeds from the MRS and the IG from the DS were grouped in another class, and the SG seeds from the DS and the SG and IG from the FRS were grouped in a third class. Similarly, for the autofluorescence data, the SG and IG seeds on the MRS group were grouped in one class, the IG seeds on the DS group in another class, and the SG seeds on the DS group and the SG and IG seeds on the FRS group in a third class. The results were consistent with the multispectral data when multi-source fusion data were used. These results suggest that describing the quality of Siberian wild rye seed on the basis of maturity stage alone may not be sufficient and that intra-stage variation needs to be considered.

We employed K-means clustering based on feature fusion data, retaining only 20% of the original features, to improve the performance of the models. The results based on the test set showed a significant improvement in performance after reclassification (Figure 12). Specifically, the accuracy of the LDA model improved from 0.85 to 0.90, and the AUC improved from 0.95 to 0.97. In addition, the Brier score decreased from 0.20 to 0.14. Similarly, the accuracy of the RF model improved by 9.24% over the previous model to 0.87, and the AUC improved by 4.11%. The Brier score decreased from 0.27 to 0.20. The performance of the SVM model also improved, with the accuracy increasing from 0.83 to 0.89, and the AUC increasing by 2.63%. The Brier score decreased from 0.20 to 0.06.

In the confusion matrix, clust1 had the highest seed detection accuracy, followed by the detection accuracy of clust2, which was greater than 0.93 for all three models. Clust3 had the lowest detection accuracy, with the RF model having the lowest accuracy of 0.45 for its detection among the three models (Table S9).

Overall, these results suggest that label reclassification based on K-means clustering could substantially improve model performance for classifying seed maturity at different maturity stages and grain positions.

4 Discussion

Seed maturity is a crucial factor in improving the yield of Siberian wild rye, which is important for the sustainable development of animal husbandry and the improvement of degraded grasslands (Xie et al., 2015; Zhao et al., 2017). Delayed harvesting results in an 80% reduction in yield due to seed shattering (You et al., 2011), and traditionally, seed lots were sorted into different maturity fractions based on color, moisture content, and analysis of chlorophyll fluorescence signals (Jalink et al., 1998b; Ellis, 2019; Zhao et al., 2022). However, with advances in spectroscopy and computational technologies, non-destructive identification of seed characteristics is now possible through X-ray analysis (de Medeiros et al., 2020b), multispectral and hyperspectral image analysis (Xia et al., 2019), microtomography (Gomes-Junior et al., 2019), magnetic resonance (Melchinger et al., 2017), and other techniques. Recently, seed maturity analysis using multispectral imaging technology and ML methods has been applied to soybean (*Glycine max* L.) seed harvesting (Batista et al., 2022).

4.1 Seed maturity variation

Multispectral imaging has been demonstrated to be effective in differentiating seeds based on their morphological and spectral features (Hu et al., 2020). This study confirmed the morphological

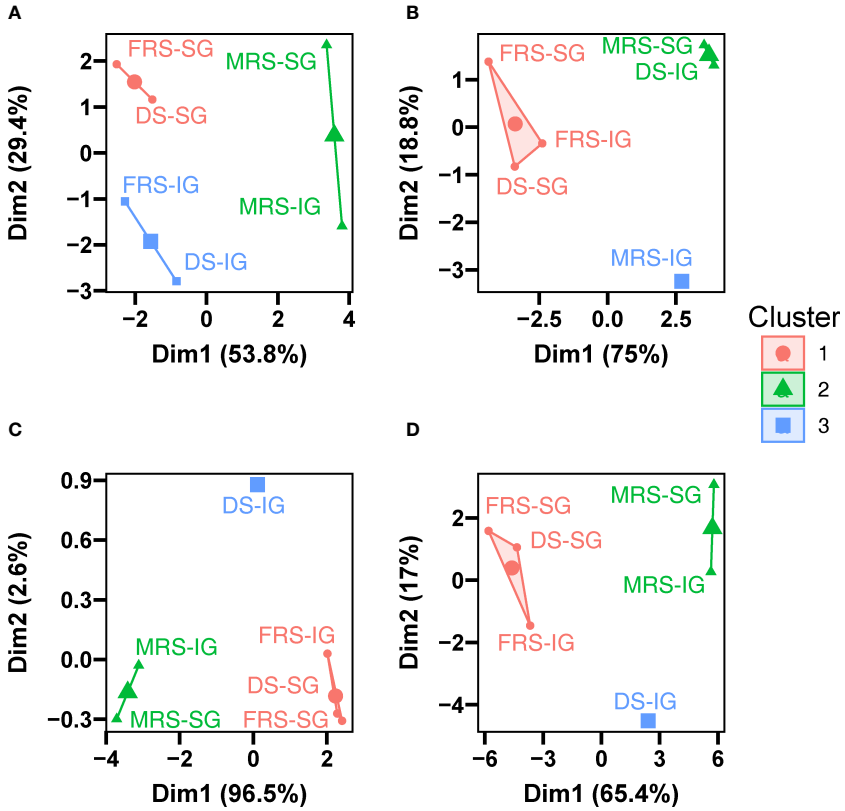

FIGURE 11
Two-dimensional biplot of seeds of different maturity stages and grain positions based on K-means clustering. **(A)** Morphological data, **(B)** multispectral data, **(C)** autofluorescence data, and **(D)** multi-source fusion data.

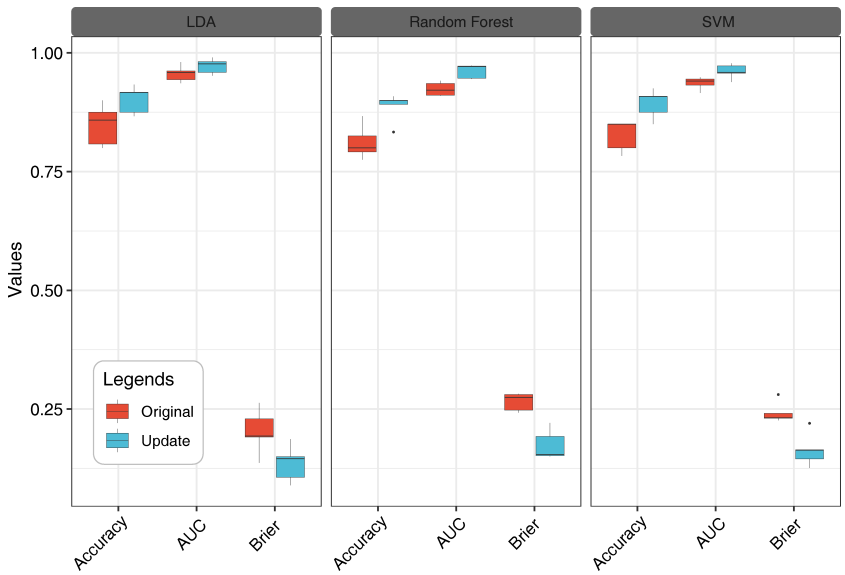

FIGURE 12
Accuracy of Siberian wild rye seed identification in three stages was improved by model update. Multi-source fusion data recognition models based on LDA, RF and SVM.

differences observed in previous reports during the maturation process of seeds (Zhang et al., 2022), where the projected area, length, and width of seeds increased with increasing maturity (Harada, 1997). However, these morphological traits were not sufficient to accurately determine seed maturity due to the differences between seeds with similar morphological features. The study showed that using saturation, CIELab A, and CIELab B probability density distribution trends, a combination of indicators that could considerably differentiate the maturity levels of Siberian wild rye seeds were identified. In addition, the study found that shoot length was positively correlated with CIELab A, CIELab B, and saturation, indicating its potential as an indicator to evaluate seed quality (Li and Chen, 2015).

Spectral information varies among species and varieties, as previous studies have shown (Zhang et al., 2012; Bao et al., 2019). In this study, we found that reflectance values were not uniform across seeds, although the spectral curves showed a similar trend. Immature seeds generally showed higher reflectance in the visible region of the spectrum due to changes in seed color and chlorophyll content (Boelt et al., 2018; ElMasry et al., 2019). The use of autofluorescence imaging was also found to be an effective tool for detecting fluorescent chemical compounds such as chlorophyll and lignin (Goggin and Steadman, 2012; Donaldson, 2020). Moreover, we found that excitation-emission combinations of 365/400 nm, 405/500 nm, 430/500 nm, 450/500 nm, and 660/700 nm provided clearer identification for three maturity stages seeds. This was consistent with previous researches (Jalink et al., 1998a; Kenanoglu et al., 2013; Donaldson and Williams, 2018). Furthermore, the use of supervised methods (LDA) was found to provide better results than unsupervised methods (PCA) in distinguishing seed maturity (Shrestha et al., 2016).

4.2 The feature filtering method could reduce the computational cost and time

In recent years, multispectral imaging designs have become more prevalent due to the shorter acquisition times required for image processing programs. This technology supports different LEDs light sources and allows for the precise stroboscopic timing needed to optimize and save images of each seed (ElMasry et al., 2019). Adjusting the light of each band individually can improve detection performance, making it crucial to select suitable features to improve training speed and reduce the operation cost of the model. While the SPA can reduce data dimension well in the hyperspectral spectrum, it may sacrifice accuracy as it relies on many linear relationships between the hyperspectral bands. Nonlinear relationships between self-fluorescence and morphological multivariate datasets require other methods to handle them. In this study, we used three filtering algorithms, we found that the feature filtering results of JMIM and information gain were similar in the first 20%, but different from Gini impurity as the latter relies on random forest models (Kursa, 2018; Zawadzki and Kosinski, 2019). Additionally, the running times of JMIM and information gain were substantially shorter than the Gini impurity, consistent with previous research (Bommert et al., 2020).

Feature filtering algorithms are increasingly used to improve ML models in the context of big data (Bommert et al., 2020). In this study, we applied three filtering algorithms to filter features, with no filtering and feature fusion as two comparison methods. Model performance was evaluated using these filtered features in LDA, RF, and SVM to automatically classify seed maturity. All models achieved accuracies greater than 0.78 and AUCs greater than 0.87, indicating that the classification process of Siberian wild rye seed maturity could be automated and provide reliable information on different maturity stages in a robust manner, similar to other studies (de Medeiros et al., 2020a; Barboza da Silva et al., 2021). Notably, feature filtering reduced the performance of the LDA model, while the unfiltered feature approach did not differ significantly from the other methods in RF and SVM. In addition, retaining the top 20% of features using filtering methods was found to be effective, but may result in a slight loss of accuracy. The feature fusion method outperformed other filtering methods such as information gain and Gini impurity, while the performance of JMIM was similar. The results obtained by combining different filtering methods could be used for key feature selection, and the optimal performance of the data training model was obtained under the JMIM filtering algorithm, which is consistent with previous research (Bommert et al., 2020).

4.3 The method based on K-means could improve the seed quality classification performance

The IG and SG seeds at the same maturity stage were varied reflecting on physiological, morphological, multispectral, and autofluorescence characteristics resulting in low model performance, this could be related to the low degree of domestication of Siberian wild rye. We re-classified 6 class seeds (3 stages×2 positions) into three clusters based on K-means. Interestingly, seeds at different grain positions varied in the same harvest time. IG matured later than SG about one week at the DS. Therefore, it may be inadequate to sort seed quality based on harvest time. Further, we found that the performance of the three models were improved by the model updating based on K-means clustering in Siberian wild rye seed quality classification. Moreover, this strategy could be employed to improve the performance of model recognition by applying it to other unknown maturity seeds not involved in model training. For instance, model performance was improved to identify other untested varieties by adding several untested corn varieties to the training data (Tu et al., 2022).

We have developed a fast, non-destructive, and high-throughput method to classify the maturity of Siberian wild rye seeds. This method could assist in determining the optimal harvest time in the field and is based on a feature filtering algorithm that can screen critical features, reducing equipment costs and training time. We could also develop low-cost instruments specifically for Siberian wild rye based on key features in the future. Compared to hyperspectral devices, our method was more cost-effective and flexible enough to train specific models for seed selection with unique features in different environments. Moreover, our feature filtering combined with machine learning algorithm could achieve

optimal performance with smaller samples and shorter training time, unlike deep learning algorithms that require extensive data, parameter tuning, and training time.

While temperature, precipitation, and light affect seed maturity and phenotypic traits, our study showed the significant potential of the seed maturity classification model within a growth environment. We could use k-means clustering with standard samples to assign specific maturity labels for seeds in different environments to improve the model's generalizability. In addition, future research could also enhance the accuracy and generalizability of this method by collecting seed samples from various growth environments.

5 Conclusion

In conclusion, our results demonstrated that integrated optical imaging technology has great potential for seed maturity identification in Siberian wild rye. The models based on multi-source fusion data showed wide applicability (>0.78 accuracies) and reduced the computing time and the cost of high-performance computing equipment. In addition, model updating based on K-means clustering could significantly improve model performance for seed maturity classification of plants with inconsistent maturity (low domestication).

Data availability statement

The original contributions presented in the study are included in the article/Supplementary Material. Further inquiries can be directed to the corresponding author.

Author contributions

PM conceived and designed the experiment. ZJ and CO performed the experiments and analyzed the data. SS, MS, JW, JL and WM contributed to the experiment. ZJ and CO wrote the paper, and SJ, ML, and PM revised the paper. All authors contributed to the article and approved the submitted version.

Funding

This research was supported by the earmarked fund for CARS (CARS-34) and R&D of seed coating technology for key pasture grasses in the Qinghai-Tibet Plateau.

Acknowledgments

We thank the staff at the trial site for their assistance in this work.

Conflict of interest

The authors declare that the research was conducted in the absence of any commercial or financial relationships that could be construed as a potential conflict of interest.

Publisher's note

All claims expressed in this article are solely those of the authors and do not necessarily represent those of their affiliated organizations, or those of the publisher, the editors and the reviewers. Any product that may be evaluated in this article, or claim that may be made by its manufacturer, is not guaranteed or endorsed by the publisher.

Supplementary material

The Supplementary Material for this article can be found online at: https://www.frontiersin.org/articles/10.3389/fpls.2023.1170947/full#supplementary-material

SUPPLEMENTARY FIGURE 1
Venn diagram based on information gain, Gini impurity, and JMIM feature filtering methods.

SUPPLEMENTARY FIGURE 2
Three feature filtering methods run time.

References

Bao, Y., Mi, C., Wu, N., Liu, F., and He, Y. (2019). Rapid classification of wheat grain varieties using hyperspectral imaging and chemometrics. *Appl. Sci.* 9, 4119. doi: 10.3390/app9194119

Barboza da Silva, C., Oliveira, N. M., de Carvalho, M. E. A., de Medeiros, A. D., de Lima Nogueira, M., and Dos Reis, A. R. (2021). Autofluorescence-spectral imaging as an innovative method for rapid, non-destructive and reliable assessing of soybean seed quality. *Sci. Rep.* 11, 17834. doi: 10.1038/s41598-021-97223-5

Batista, T. B., Mastrangelo, C. B., de Medeiros, A. D., Petronilio, A. C. P., Fonseca de Oliveira, G. R., dos Santos, I. L., et al. (2022). A reliable method to recognize soybean seed maturation stages based on autofluorescence-spectral imaging combined with machine learning algorithms. *Front. Plant Sci.* 13. doi: 10.3389/fpls.2022.914287

Boelt, B., Shrestha, S., Salimi, Z., Jørgensen, J. R., Nicolaisen, M., and Carstensen, J.M.(2018) Multispectral imaging–a new tool in seed quality assessment? *Seed Sci. Res.* 28, 222–228 doi: 10.1017/S0960258518000235

Bommert, A., Sun, X., Bischl, B., Rahnenführer, J., and Lang, M. (2020). Benchmark for filter methods for feature selection in high-dimensional classification data. *Comput. Stat. Data An.* 143, 106839. doi: 10.1016/j.csda.2019.106839

Brier, G. W. (1950). Verification of forecasts expressed in terms of probability. *Mon. Wea. Rev.* 78, 1–3. doi: 10.1175/1520-0493(1950)078<0001:VOFEIT>2.0.CO;2

Cristianini, N., and Shawe-Taylor, J. (2000). *An introduction to support vector machines and other kernel-based learning methods* (Cambridge, UK: Cambridge University Press). doi: 10.1017/CBO9780511801389

Deleuran, L. C., Olesen, M. H., and Boelt, B. (2013). Spinach seed quality: potential for combining seed size grading and chlorophyll fluorescence sorting. *Seed Sci. Res.* 23, 271–278. doi: 10.1017/S0960258513000202

de Medeiros, A. D., Capobiango, N. P., da Silva, J. M., da Silva, L. J., da Silva, C. B., and dos Santos Dias, D. C. F. (2020a). Interactive machine learning for soybean seed

and seedling quality classification. *Sci. Rep.* 10, 11267. doi: 10.1038/s41598-020-68273-y

de Medeiros, A. D., Pinheiro, D. T., Xavier, W. A., da Silva, L. J., and dos Santos Dias, D. C. F. (2020b). Quality classification of jatropha curcas seeds using radiographic images and machine learning. *Ind. Crop Prod.* 146, 112162. doi: 10.1016/j.indcrop.2020.112162

Donaldson, L. (2020). Autofluorescence in plants. *Molecules* 25, 2393. doi: 10.3390/molecules25102393

Donaldson, L., and Williams, N. (2018). Imaging and spectroscopy of natural fluorophores in pine needles. *Plants* 7, 10. doi: 10.3390/plants7010010

Ellis, R. H. (2019). Temporal patterns of seed quality development, decline, and timing of maximum quality during seed development and maturation. *Seed Sci. Res.* 29, 135–142. doi: 10.1017/S0960258519000102

ElMasry, G., Mandour, N., Al-Rejaie, S., Belin, E., and Rousseau, D. (2019). Recent applications of multispectral imaging in seed phenotyping and quality monitoring–an overview. *Sensors* 19, 1090. doi: 10.3390/s19051090

Feng, L., Zhu, S., Liu, F., He, Y., Bao, Y., and Zhang, C. (2019). Hyperspectral imaging for seed quality and safety inspection: a review. *Plant Methods* 15, 1–25. doi: 10.1186/s13007-019-0476-y

França-Silva, F., Rego, C. H. Q., Gomes-Junior, F. G., Moraes, M. H. D., de, A. D., and da Silva, C. B. (2020). Detection of drechslera avenae (*Eidam*) sharif [*Helminthosporium avenae* (eidam)] in black oat seeds (*Avena strigosa schreb*) using multispectral imaging. *Ah. S. Sens.* 20, 3343. doi: 10.3390/s20123343

Fu, X., Bai, M., Xu, Y., Wang, T., Hui, Z., and Hu, X. (2023). Cultivars identification of oat (*Avena sativa* L.) seed *via* multispectral imaging analysis. *Front. Plant Sci.* 14. doi: 10.3389/fpls.2023.1113535

Galletti, P. A., Carvalho, M. E., Hirai, W. Y., Brancaglioni, V. A., Arthur, V., and Barboza da Silva, C. (2020). Integrating optical imaging tools for rapid and non-invasive characterization of seed quality: tomato (*Solanum lycopersicum* L.) and carrot (*Daucus carota* L.) as study cases. *Front. Plant Sci.* 11. doi: 10.3389/fpls.2020.577851

Goggin, D. E., and Steadman, K. J. (2012). Blue and green are frequently seen: responses of seeds to short-and mid-wavelength light. *Seed Sci. Res.* 22, 27–35. doi: 10.1017/S0960258511000444

Gomes-Junior, F. G., Cicero, S. M., Vaz, C. M. P., and Lasso, P. R. O. (2019). X-Ray microtomography in comparison to radiographic analysis of mechanically damaged maize seeds and its effect on seed germination. *Acta Sci.-Agron.* 41, e42608. doi: 10.4025/actasciagron.v41i1.42608

Han, Y., Wang, X., Hu, T., Hannaway, D. B., Mao, P., Zhu, Z., et al. (2013). Effect of row spacing on seed yield and yield components of five cool-season grasses. *Crop Sci.* 53, 2623–2630. doi: 10.2135/cropsci2013.04.0222

Harada, J. J. (1997). *Cellular and molecular biology of plant seed development* (Germany: Springer-Verlag). doi: 10.1007/978-94-015-8909-3_15

Hu, X., Yang, L., and Zhang, Z. (2020). Non-destructive identification of single hard seed *via* multispectral imaging analysis in six legume species. *Plant Methods* 16, 1–13. doi: 10.1186/s13007-020-00659-5

Jalink, H., Frandas, A., Schoor, R., and Bino, J. B. (1998a). Chlorophyll fluorescence of the testa of brassica oleracea seeds as an indicator of seed maturity and seed quality. *Sci. Agr.* 55, 88–93. doi: 10.1590/S0103-90161998000500016

Jalink, H., van der Schoor, R., Frandas, A., van Pijlen, J. G., and Bino, R. J. (1998b). Chlorophyll fluorescence of brassica oleracea seeds as a non-destructive marker for seed maturity and seed performance. *Seed Sci. Res.* 8, 437–443. doi: 10.1017/S0960258500004402

Jia, Z., Sun, M., Ou, C., Sun, S., Mao, C., Hong, L., et al. (2022). Single seed identification in three *Medicago* species *via* multispectral imaging combined with stacking ensemble learning. *Sensors* 22, 7521. doi: 10.3390/s22197521

Kenanoglu, B. B., Demir, I., and Jalink, H. (2013). Chlorophyll fluorescence sorting method to improve quality of capsicum pepper seed lots produced from different maturity fruits. *HortScience* 48, 965–968. doi: 10.21273/HORTSCI.48.8.965

Klebesadel, L. J. (1969). Siberian Wildrye (*Elymus sibiricus* L.): agronomic characteristics of a potentially valuable forage and conservation grass for the north 1. *Agron. J.* 61, 855–859. doi: 10.2134/agronj1969.00021962006100060008x

Kursa, M. B. (2022). praznik: Tools for Information-Based Feature Selection and Scoring. Available at: https://CRAN.R-project.org/package=praznik.

Lang, M., and Schratz, P. (2022). Mlr3verse: Easily install and load the "mlr3" package family. Available at: https://CRAN.R-project.org/package=mlr3verse.

Lê, S., Josse, J., and Husson, F. (2008). FactoMineR: an r package for multivariate analysis. *J. Stat. Software* 25, 1–18. doi: 10.18637/jss.v025.i01

Li, Z., and Chen, Y. (2015). CIELAB colour space quantification-based evaluation of capsule development and seed vigour in *Nicotiana tabacum* l. *Chin. Tobacco Sci.* 36, 24–28. doi: 10.13496/j.issn.1007-5119.2015.04.004

Lima, J. J. P., Buitink, J., Lalanne, D., Rossi, R. F., Pelletier, S., da Silva, E. A. A., et al. (2017). Molecular characterization of the acquisition of longevity during seed maturation in soybean. *PloS One* 12, e0180282. doi: 10.1371/journal.pone.0180282

Maechler, M., Rousseeuw, P., Struyf, A., Hubert, M., and Hornik, K. (2012) *Cluster: cluster analysis basics and extensions*. Available at: https://lirias.kuleuven.be/3999459.

Melchinger, A. E., Munder, S., Mauch, F. J., Mirdita, V., Böhm, J., and Mueller, J. (2017). High-throughput platform for automated sorting and selection of single seeds based on time-domain nuclear magnetic resonance (TD-NMR) measurement of oil content. *Biosyst. Eng.* 164, 213–220. doi: 10.1016/j.biosystemseng.2017.10.011

Pinheiro, D. T., Medeiros, A. D., León, M. J. Z., Dias, D. C., dos, S., and da Silva, L. J. (2020). Physical and physiological quality of *Jatropha curcas* l. seeds at different maturity stages using image analysis. *Span. J. Agric. Res.* 18, 13. doi: 10.5424/sjar/2020183-16028

Rahman, A., and Cho, B.-K. (2016). Assessment of seed quality using non-destructive measurement techniques: a review. *Seed Sci. Res.* 26, 285–305. doi: 10.1017/S0960258516000234

Shrestha, S., Deleuran, L. C., and Gislum, R. (2016). Classification of different tomato seed cultivars by multispectral visible-near infrared spectroscopy and chemometrics. *J. Spectr. Imaging* 5, a1. doi: 10.1255/jsi.2016.a1

Teixeira, R. N., Ligterink, W., França-Neto, J., de, B., Hilhorst, H. W. M., and da Silva, E. A. A. (2016). Gene expression profiling of the green seed problem in soybean. *BMC Plant Biol.* 16, 1–15. doi: 10.1186/s12870-016-0729-0

Tu, K., Wen, S., Cheng, Y., Xu, Y., Pan, T., Hou, H., et al. (2022). A model for genuineness detection in genetically and phenotypically similar maize variety seeds based on hyperspectral imaging and machine learning. *Plant Methods* 18, 1–17. doi: 10.1186/s13007-022-00918-7

Wang, X., Zhang, H., Song, R., He, X., Mao, P., and Jia, S. (2021). Non-destructive identification of naturally aged alfalfa seeds *via* multispectral imaging analysis. *Sensors* 21, 5804. doi: 10.3390/s21175804

Xia, Y., Xu, Y., Li, J., Zhang, C., and Fan, S. (2019). Recent advances in emerging techniques for non-destructive detection of seed viability: a review. *Artif. Intell. Agric.* 1, 35–47. doi: 10.1016/j.aiia.2019.05.001

Xie, J., Zhao, Y., Yu, L., Liu, R., and Dou, Q. (2020). Molecular karyotyping of siberian wild rye (*Elymus sibiricus* L.) with oligonucleotide fluorescence *in situ* hybridization (FISH) probes. *PloS One* 15, e0227208. doi: 10.1371/journal.pone.0227208

Xie, W., Zhao, X., Zhang, J., Wang, Y., and Liu, W. (2015). Assessment of genetic diversity of siberian wild rye (*Elymus sibiricus* L.) germplasms with variation of seed shattering and implication for future genetic improvement. *Biochem. Syst. Ecol.* 58, 211–218. doi: 10.1016/j.bse.2014.12.006

Yang, L., Zhang, Z., and Hu, X. (2020). Cultivar discrimination of single alfalfa (*Medicago sativa* L.) seed *via* multispectral imaging combined with multivariate analysis. *Ah. S. Sens.* 20, 6575. doi: 10.3390/s20226575

You, M., Liu, J., Bai, S., Zhang, X., and Yan, J. (2011). Study on relationship of seed shattering, seed development and yield traits of *Elymus sibiricus* L. *Southwest China J. Agric. Sc.i* 24, 1256–1260. doi: 10.16213/j.cnki.scjas.2011.04.047

Yu, X., Zhu, P., and Mao, P. (2011). Effects of nitrogenous fertilizer and phosphorus fertilizer applications on roots and seed yield of *Elymus sibiricus*. *Acta Agrestia Sin.* 19, 637. doi: 10.11733/j.issn.1007-0435.2011.04.017

Zawadzki, Z., Kosinski, M., Slomczynski, K., Skrzypiec, D., and Schratz, P. (2021). FSelectorRcpp: "Rcpp" Implementation of "FSelector" entropy-based feature selection algorithms with a sparse matrix support. Available at: https://CRAN.R-project.org/package=FSelectorRcpp.

Zhang, X., Liu, F., He, Y., and Li, X. (2012). Application of hyperspectral imaging and chemometric calibrations for variety discrimination of maize seeds. *Ah. S. Sens.* 12, 17234–17246. doi: 10.3390/s121217234

Zhang, S., Zeng, H., Ji, W., Yi, K., Yang, S., Mao, P., et al. (2022). Non-destructive testing of alfalfa seed vigor based on multispectral imaging technology. *Sensors* 22, 2760. doi: 10.3390/s22072760

Zhao, P., Chu, L., Wang, K., Zhao, B., Li, Y., Yang, K., et al. (2022). Analyses on the pigment composition of different seed coat colors in adzuki bean. *Food Sci. Nutr.* 10, 2611–2619. doi: 10.1002/fsn3.2866

Zhao, X., Jiang, X., Zhao, K., Zhao, X., Yin, J., and Xie, W. (2015). Screening of germplasm with low seed shattering rate and evaluation on agronomic traits in *Elymus sibiricus* l. *J. Plant Genet. Resour.* 16, 691–699. doi: 10.13430/j.cnki.jpgr.2015.04.003

Zhao, L., WANG, M., and MAO, P. (2012). Selected nitrogen and phosphorus fertilizer applications affect seed yield, seed yield components and roots of *Elymus sibiricus*. *Acta Agrestia Sin.* 20, 662–668. doi: 10.11733/j.issn.1007-0435.2012.04.011

Zhao, X., Xie, W., Zhang, J., Zhang, Z., and Wang, Y. (2017). Histological characteristics, cell wall hydrolytic enzymes activity and candidate genes expression associated with seed shattering of *Elymus sibiricus* accessions. *Front. Plant Sci.* 8. doi: 10.3389/fpls.2017.00606

Frontiers in
Plant Science

Cultivates the science of plant biology and its applications

The most cited plant science journal, which advances our understanding of plant biology for sustainable food security, functional ecosystems and human health.

Discover the latest Research Topics

See more →

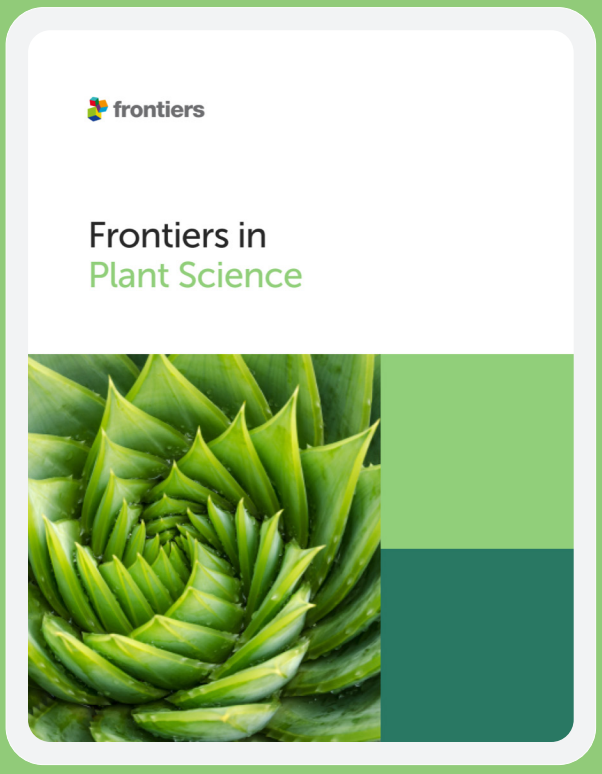

Frontiers

Avenue du Tribunal-Fédéral 34
1005 Lausanne, Switzerland
frontiersin.org

Contact us

+41 (0)21 510 17 00
frontiersin.org/about/contact